Università degli Studi di Torino
Scuola di Dottorato

Numerical Relativity completion and validation of an Effective-One-Body waveform model

Gunnar Markus Riemenschneider

Università degli Studi di Torino
Scuola di Dottorato

Dottorato in Fisica ed Astrofisica

Numerical Relativity completion and validation of an Effective-One-Body waveform model

Gunnar Markus Riemenschneider

Tutor: Dr. Alessandro Nagar
Co-tutor: Prof. Nicolao Fornengo

Abstract

Faithful, robust and fast waveform models are of critical importance to gravitational wave astronomy to allow for accurate and precise detection and analysis of the source. The dominant source of Gravitational Wave (GW) events observed to date is compact binary coalescence. Waveform models based on the Effective-One-Body (EOB) approach have been proven to be very powerful in their ability to combine analytical information from post-Newtonian theory, gravitational-self-force theory and more, in order to capture the full picture of merging binary systems. Purely analytical EOB models are however still of insufficient quality to be used in the detection and analysis of GW events. This thesis presents an introduction to the solution of this problem: The completion of EOB waveform models through Numerical Relativity (NR), on the example of non-precessing, non-eccentric Binary Black Hole (BBH) systems, utilizing the framework of the `TEOB` model. Once completed NR is further used to validate the model to ensure it meets the qualitative needs of GW data analysis.

The infrastructure of the `TEOB` model is introduced and discussed with a strong focus onto *analytical flexibilities* that can be used to capture missing information from NR waveforms. The analytical flexibilities of the `TEOB` model are made up of effective parameters that enter the Hamiltonian so as to modify both the orbital part (*i.e.* non-spinning) and the spin-orbit interaction between the orbital angular momentum and the black hole spins. The approximation of a quasi-circular inspiral is corrected effectively in the radiation reaction of the system by imposing NR fitted waveform characteristics. The model is completed with a phenomenological template fitted directly to NR to capture the merger and ringdown of the BBH system. In total 154 BBH-NR waveforms are combined to inform the `TEOB`. An additional 420 waveforms are used to validate the model. These waveforms span over a large part of the parameter space reaching mass-ratios $m_1/m_2 \leq 18$ and black hole spins of up to $|\vec{S}_{1,2}|/m_{1,2}^2 \leq 0.998$.

This calibration process is presented for three, successively improving avatars of the `TEOB` model. All models include improved analytical information, presenting an excellent opportunity to discuss the impact of analytical information onto the subsequent calibration to NR. Many important phenomenological features of the multipolar waveform is explored and discussed, in particular this includes several quasi-universal spin dependencies, simplifying direct fits of NR parameters greatly. The `TEOB` avatars discussed in this thesis are: Firstly, `TEOBResumS` is a model for the dominant, quadrupolar mode; Secondly, `TEOBiResumMultipoles` models BBH systems of non-rotating black holes, extending the calibration of the quadrupolar mode to a large set of 9 further subdominant modes; Finally, `TEOBiResumS_SM` extends the calibration of all but one subdominant mode to the full spin-range available of available NR waveforms. The fully calibrated models are all evaluated against the NR catalog. In many instances the model does not just meet but exceeds the quality demands for application in GW astronomy. However, this is not always possible to achieve with mere improvement of the NR calibration. For these cases the limits are investigated and discussed thoroughly.

Keywords: Effective-One-Body, Waveform models, Numerical Relativity, Binary Black Holes, Compact Binary Coalescence, Gravitational Waves.

Italian Abstract

Modelli di forme d'onda accurati, robusti e veloci sono di fondamentale importanza per l'astronomia delle onde gravitazionali. Essi consentono di ricavare informazioni precise sulla sorgente dei segnali rilevati. La fonte più importante degli eventi di onde gravitazionali osservati fino a oggi è la coalescenza di sistemi binari di oggetti compatti. I modelli di forme d'onda basati sull'approccio Effective-One-Body (EOB) si sono dimostrati molto importanti nella loro capacità di combinare informazioni analitiche della teoria post-newtoniana, della *gravitational self-force* e di altri approcci, al fine di riprodurre il quadro completo di sistemi binari coalescenti. I modelli EOB puramente analitici non sono tuttavia sufficientemente accurati per essere utilizzati nella rilevazione e nell'analisi di eventi di onde gravitazionali. Questa tesi presenta un'introduzione alla soluzione di questo problema: il completamento di modelli di forme d'onda EOB attraverso la Relatività Numerica (NR), con l'esempio di sistemi binari di buchi neri (BBH) quasi-circolari e senza precessione, utilizzando la struttura del modello `TEOB`. Una volta completato il modello, la relatività numerica viene utilizzata anche per convalidarlo in modo da garantire che esso soddisfi i requisiti necessari all'analisi dati dei segnali.

L'infrastruttura del modello `TEOB` viene introdotta e discussa con particolare attenzione alla *flessibilità analitica*, che può essere usata per incorporare le informazioni mancanti utilizzando forme d'onda numeriche. Le flessibilità analitiche del modello `TEOB` sono costituite da parametri efficaci che entrano nell'Hamiltoniana in modo da modificare sia la parte orbitale (i.e. non spinning) sia l'interazione spin-orbita tra il momento angolare orbitale e gli spin dei buchi neri. L'*inspiral* quasi-circolare viene corretto efficacemente nella reazione di radiazione del sistema imponendo delle caratteristiche fittate alle onde NR. L'onda è quindi completata da un modello fenomenologico fittato direttamente alla NR per riprodurre la coalescenza e il ringdown del sistema binario di buchi neri. In totale 154 forme d'onda BBH-NR vengono combinate per calibrare il modello `TEOB`. Ulteriori 420 forme d'onda vengono utilizzate per convalidarlo. Queste si estendono su gran parte dello spazio dei parametri raggiungendo rapporti di massa $m_1/m_2 \leq 18$ e spin del buco nero $|\vec{S}_{1,2}|/m_{1,2}^2 \leq 0.998$.

Questo processo di calibrazione viene presentato per tre successive iterazioni del modello `TEOB`. Ogni iterazione include maggiori informazioni analitiche, offrendo un'eccellente opportunità per discutere l'impatto di queste ultime sulla successiva calibrazione a NR. Molte importanti caratteristiche fenomenologiche della forma d'onda multipolare vengono esplorate e discusse: in particolare queste includono dipendenze quasi-universali dagli spin, che semplificano notevolmente i fit dei parametri NR. Le diverse formulazioni del modello `TEOB` discusse in questa tesi sono: in primo luogo `TEOBResumS`, un modello che include solamente il quadrupolo dominante; in secondo luogo, `TEOBiResumMultipoles`, che modellizza sistemi di buchi neri non rotanti, estendendo la calibrazione del modo quadrupolare ad altri 9 modi sottodominanti; infine, `TEOBiResumS_SM`, che estende la calibrazione di tutti i modi sottodominanti tranne uno all'intervallo di spin disponibile nelle forme d'onda NR. I modelli calibrati vengono dunque confrontati con l'intero catalogo di NR. In molti casi il modello non solo soddisfa, ma supera i requisiti di accuratezza per l'applicazione nell'astronomia delle onde gravitazionali. Tuttavia, questo non è sempre possibile, anche con il miglioramento della calibrazione alla NR. In questi casi, i limiti vengono studiati e discussi a fondo.

Glossary

Acronyms

GW	Gravitational Wave
GWA	Gravitational Wave Astronomy
EOB	Effective-One-Body
NR	Numerical Relativity
BBH	Binary Black Hole
BH	Black Hole
GR	General Relativity
CBC	Compact Binary Coalescence
NS	Neutron star
BNS	Binary Neutron Star
BHNS	Black Hole Neutron Star
PM	Post-Minkowskian
PN	Post-Newtonian
GSF	Gravitational-Self-Force
QNM	Quasi-Normal-Mode
IMR	Inspiral-Merger-Ringdown

Frequently used symbols

G	Newtons gravitational constant
c	the speed of light
M	total mass of the system, set to $M = 1$ commonly
m_i	mass of the i-th BH with the convention $m_1 \geq m_2$
X_i	mass-fraction of the i-th BH $X_i = m_i/M$
q	mass ratio $q = m_1/m_2 > 1$
ν	symmetric mass-ratio $\nu = m_1 m_2/M^2$
X_{12}	mass-fraction-difference $X_{12} = X_1 - X - 2$
S_i	spins of the i-th BH projected onto the orbital angular momentum
$\tilde{a}_i$	Kerr-spin parameters of the i-th BH $\tilde{a}_i = S_i/m_i$
χ_i	dimensionless spin of the i-th BH $\chi_i = S_i/m_i^2$
$\hat{a}_0$	sum of the effective Kerr-spin parameters $\hat{a}_0 = \tilde{a}_1 + \tilde{a}_2$
$\tilde{a}_{12}$	difference of the effective Kerr-spin parameters $\tilde{a}_{12} = \tilde{a}_1 - \tilde{a}_2$
$\hat{S}$	effective spin parameter $\hat{S} = \left(S_1 + S_2\right)/M^2$
$h_+, h_\times$	gravitational wave polarizations
h	the complex gravitational wave strain $h = h_+ - \mathrm{i}h_\times$
$h_{\ell m}$	multipolar waveform modes of h with $\ell \geq 2$ and $\lvert m\rvert \leq \ell$, see eq. (2.4)
$A_{\ell m},\ \phi_{\ell m}$	multipolar amplitude and phase $h_{\ell m} = A_{\ell m} e^{-\mathrm{i}\phi_{\ell m}}$
$\omega_{\ell m}$	multipolar frequency $\omega_{\ell m} = \dot{\phi}_{\ell m}$
$\Psi_{\ell m}$	Regge-Wheeler-Zerilli normalized waveform $\Psi_{\ell m} = h_{\ell m}/\sqrt{\left(\ell + 2\right)\left(\ell + 1\right)\ell\left(\ell - 1\right)}$
$\hat{h}_{\ell m}^{\mathrm{NQC}}$	NQC correction factor to the waveform, see Sec. 2.3.2

$\mathcal{R}$	the distance from the GW source to the observer
ι, ϕ	angular position of the observer relative to the source frame
$t,\ u$	time coordinate in the source frame (and inverse radius)
$F,\ \bar{F}$	faithfulness and unfaithfulness, see Sec. 2.1.1 and Appendix A
$t^{\rm peak}_{\ell m}$	the peak time of (ℓ, m) mode, $\max\left[A_{\ell m}\right] = A_{\ell m}\left(t^{\rm peak}_{\ell m}\right)$
$t^{\rm mrg}$	the merger time is given by the peak of the $(2,2)$ mode $t^{\rm mrg} = t^{\rm peak}_{22}$
$\Delta t_{\ell m}$	peak time shift of the (ℓ, m) mode relative to the $(2,2)$ mode, $\Delta t_{\ell m} \equiv t^{\rm peak}_{\ell m} - t^{\rm mrg}$
$\omega^{\rm peak}_{\ell m}$	(ℓ, m) frequency at the peak of the mode, $\omega^{\rm peak}_{\ell m} = \omega_{\ell m}\left(t^{\rm peak}_{\ell m}\right)$
$A^{\rm peak}_{\ell m}$	(ℓ, m) amplitude at the peak of the mode, $A^{\rm peak}_{\ell m} = A_{\ell m}\left(t^{\rm peak}_{\ell m}\right)$
$\omega^{\rm mrg}$	$(2,2)$ frequency at the peak of the mode, $\omega^{\rm mrg} = \omega_{22}\left(t^{\rm mrg}\right)$
$A^{\rm mrg}$	$(2,2)$ amplitude at the peak of the mode, $A^{\rm mrg} = A_{22}\left(t^{\rm mrg}\right)$
(G_S, G_{S_*})	gyro-gravitomagnetic ratios, see Sec. 2.3 and 4.1.1
$c_3^{A_{\ell m}}$	effective evolution parameter of the postpeak (ℓ, m) amplitude
$(c_3^{\phi_{\ell m}}, c_4^{\phi_{\ell m}})$	effective evolution parameter of the postpeak (ℓ, m) phase
$(\alpha_n^{\ell m}, \omega_n^{\ell m})$	inverse damping time and frequency of the n-th QNM
$\alpha_{21}^{\ell m}$	difference of the inverse damping times of the first and second QNM

Notation and Nomenclature

(q, χ_1, χ_2)	the triplet notation is often used to refer to a specific waveform
(ℓ, m)	the pair of integers is often used to refer to the multipole $h_{\ell m}$
merger	the merger, referred to as a concrete point in time, is the peak of the $(2,2)$ mode, as a physical phase it is sometimes referred to as the physical merging of the BBH
postmerger	the waveform past the merger is referred to as postmerger
postpeak	the waveform past the peak of a mode is also referred to as the postpeak waveform
inspiral	the inspiral phase is marked by a clear separation of the binary while they move along semi stable orbits
plunge	the radial, unstable plunge of the binary system preceding the merger
ringdown	the end-state of the evolution, during which the remnant BH is relaxing to a Kerr BH
NQC iteration	defined in Sec. 2.3.2, to ensure consistency between waveform and flux

Contents

List of Figures

List of Tables

Chapter 1

Introduction

Gravitational Waves (GWs) were first proposed by Albert Einstein in 1916 when he had discovered wave solutions to the linearized, weak-field equations of General Relativity (GR)[85]. Despite this early insight, the question of the physical relevance of GWs was to remain unclear for decades to come. Only in 1960, 44 years later, the first, direct GW detector was proposed by Joseph Weber [153]. Yet GWs proved too elusive and the first detection of the effects of GWs was only in 1981. Taylor and Weisberg showed that the energy loss of the binary pulsar system PSR B 1913+16 was consistent with the radiating off of GWs as predicted by GR[154].

The first *direct* detection of a GW event however did not succeed until fall of 2015, when on the 14th of September GW150914, a binary black hole (BBH) merger was detected in the first observational run of the two advanced LIGO detectors in Hanford and Livingston, USA [15], with the detector technology proposed by Rainer Weiss [155] in 1989. Thus, the era of gravitational wave astronomy had begun. In the following months two additional Compact Binary Coalescence (CBC) signals have been detected in the first observation run, ending on January 19th, 2017 [22]. During the second and first half of the third observing runs from November 30, 2016 to August 25, 2017 and April 1st, 2019, to October 1st, 2019, the advanced LIGO detectors were joined by the Virgo observatory in Cascina by Pisa in Italy and a total of 47 additional CBC events have been observed [22, 28].

GWs are unique among the different windows into the universe that can be observed. GWs are predominantly generated in cataclysmic events with the most extreme curvatures and the largest accelerations and are then carried off unperturbed through almost any medium. Therefore, direct observation of GWs allowed to test GR in the strong field regime directly. For a number of tests this has already been done for the observed CBC GW events (see *e.g.* Ref. [16, 24, 26, 27]).

GWs originating in CBC events have a further characteristic principle. The GW signal is dominated by the Chirp mass $\mathcal{M}$ [119]. Due to this special characteristic Bernard Schutz suggested that it was possible to extract both the redshift and the luminosity distance independently from a single observation [144]. Using CBC events as so called standard siren would then allow to directly measure Hubble constant from a single observation already. The constraints possibly arising from such an observation would be event stronger if the GW event could be observed together with an electromagnetic counterpart. Such an analysis has been indeed done using GW170817 the GW event which was also observed with an electromagnetic counterpart [21].

Observing BBH merger events allows to infer possible distributions of BHs through out spacetime in terms of mass and individual BH spins [25]. Through this it is possible to study formation mechanisms of BHs and alternative processes that cannot be observed directly but their effects might lead to the accumulation or transformation of BHs with specific spins and masses. E.g. the existence of axion-like particles was linked to a mechanism that would limit the maximum spin for a given mass of BH [35, 36].

These have been just some examples of the possible insights that can be gained by in the study of CBC events through GWs. A key ingredient in the works that have been cited so far is the use of a CBC waveform model. This model has to reliably reproduce the GW signature observed on earth for a given source configuration. Many factors impact a GW signal. They can generally be separated into extrinsic and intrinsic factors. The former relates the GW signal as generated in the source frame to the detector frame. These include the relative orientation of the source frame to the detector, distances, redshift and other details that are needed to project the emitted GW signature onto the detector response that can be observed[1]. These parameters are defined independent of the source.

The intrinsic parameters characterize the GW source through a model. In the definition of these parameters and all following equations, unless otherwise specified, geometric units $G = c = 1$ will be used. In the ideal case this model reconstructs the GW signal for a given set of parameters based on GR. While it is often useful to build a model that additionally reconstructs the underlying dynamics accurately, it is most important that the model output reproduces the GW signal on a phenomenological level to a high degree of accuracy. In the case of CBC systems a set of parameters is commonly used that is defined uniformly across models. These parameters are the total mass of a the binary system M, the individual masses of the BHs m_1, m_2 and their mass-ratio $q = m_1/m_2$ with the convention $m_1 \geq m_2$ (therefore $q \geq 1$ is true for all systems). Each BH can have a total spin $|\vec{S}_i|$ of up to m_i^2, with the index $i = 1, 2$ referring to the individual BHs unless otherwise stated. This limit to the spin is based on the cosmic censorship conjecture (see *e.g.* [152]). Further the binary motion in the most general case is not necessarily confined to a single plane and the orbits of a system can show non-zero eccentricity. If the two bodies are sufficiently close it is also necessary to account for their mass distributions. The case of a BH is however special. Israel *et al.* proved the *no-hair* theorem [62, 103, 104] for both Schwarzschild and Kerr metrics, showing that in these two cases no further parameters then mass and spin of the BH were necessary to fully characterize the metric fully[2]. Neutron Stars (NS) however are different and the momenta of their mass-distribution have to be considered.

Constructing such a model is however by no means an easy feat. Several sources of information are possible. The analytical approach has produced methods based on perturbation theory such as Post-Minkowskian (PM) and Post-Newtonian (PN) theory, expanding in powers of Newtons Gravitational constant G and the velocity of a body v relative to the speed of light c in powers of $(v/c)^2$ [119]. Gravitational Self-Force (GSF) approach computes perturbations in the mass-ratio q to the motion of a test-particle moving through an external Kerr metric [125, 141]. Finally BH perturbation theory can be used to identify dominant modes in the waveform. While each of these methods has a range in which it is very reliable they are not stable all over. Equations of motion

---

[1] See e.g. Chapter 7 of Ref. [119] for a discussion and derivation.

[2] A general mathematical proof of the *no-hair* theorem is still missing though, thus it would be more accurate to speak of the *no-hair* conjecture.

derived from PN theory are commonly unstable and accumulate too large errors. Even at small orders of PN theory a large amount of terms arise. But currently PN theory is even in the best of circumstances not able to fully predict the waveform of a CBC event through the inspiral, merger and ringdown. Thus analytical methods are powerful tools to construct models for the inspiral and potentially the ringdown of the system if the final state is known, but during the merger a different set of tolls is necessary to construct an adequate waveform model.

Numerical Relativity offers a potential solution to study the merging of two compact objects, but numerical solutions to the Einstein Equations prove to be very difficult even in the simplest of cases. The metric which defining the distance between two points is necessary to construct the grid and simultaneously the main goal of the computation. Thus, the general formalism is naturally quite involved and requires a large amount of study before it can be used [34, 43]. It is therefore not surprising that the first successful simulation of two BHs for the duration of a full orbit was indeed only achieved in 2003 [58]. Nowadays many large catalogs of NR waveforms exists and a variety of codes are capable of reliably generating waveforms for several orbits up until the merger and through the full ringdown. However, even the longest among them are not longer then a few hundred cycles and these simulations take several million CPU hours each (see *e.g.* [55]).

This leads to the current situation at hand. Both on the numerical and analytical side many useful sources of information exist that can be used to solve the problem of building a waveform model that robustly reproduces the GW signal as predicted by GR. On the analytical side the methods are not sufficiently stable and require a large amount of computational effort to be improved. On the numerical side it would be too costly to generate waveforms for arbitrary parameter combinations and length due to the excessive computational cost. A solution is necessary to combine the analytical sources of information in a reliable and robust manner, that can further include the necessary missing information that has not yet become available through analytical computations by extracting the difference from NR simulations. One such solution was introduced by Thibault Damour *et al.* in 1998: the Effective-One-Body (EOB) approach [60, 61, 71, 78]. In this setup the action describing the motion of two bodies is mapped onto the motion of a single body in an external metric. The large number of terms common in PN calculations are reduced to merely a handful. Over the years since then it was shown that the EOB approach was a robust and reliable resummation of the analytical information and currently the EOB approach is the foundation of most modern waveform models.

The focus of this thesis is set on the NR completion of EOB models. In particular the example of three EOB models of the `TEOB`-series. These models will be introduced with a strong focus on analytical parameters build into the models that are left free to be informed by NR simulations through fitting of several waveforms. Further once the calibration of the individual models is presented, the discussion is turned to the evaluation of the model on the basis of waveforms generated with NR. This will be done as follows. Chapter 2 introduces the EOB formalism from a conceptual framework and discusses the main theoretical context of this work. Chapter 3 focuses on introducing the reader to Numerical Relativity focusing primarily on the example of the SXS catalog [55]. Chapters 4 – 6 will discuss the different EOB models from the point of view of calibration as well as performance. Chapter 7 will discuss the potential application of the model discussed in chapter 6 in a non-standard context allowing for an interesting test of GR. This thesis is then concluded in chapter 8 through a general discussion of the results presented here.

During the preparation of this work several aspects of this work have been published already as short-author list articles and within the LIGO scientific, Virgo and KAGRA collaboration. The main results discussed in this thesis can be found in:

- A. Nagar, S. Bernuzzi, W. del Pozzo, **G. Riemenschneider** *et al.* "*Time-domain effective-one-body gravitational waveforms for coalescing compact binaries with nonprecessing spins, tides and self-spin effects*", published as Phys.Rev.D 98 (2018) 10, 104052. Hereafter referred to as Paper I.
- A. Nagar, , G. Pratten, **G. Riemenschneider** and R. Gamba "*Multipolar effective one body model for nonspinning black hole binaries*", published as Phys.Rev.D 101 (2020) 2, 024041. Hereafter referred to as Paper II.
- A. Nagar, **G. Riemenschneider** *et al.* "*Multipolar effective one body waveform model for spin-aligned black hole binaries*", published as Phys.Rev.D 102 (2020) 2, 024077. Hereafter referred to as Paper III.
- G. Carullo, **G. Riemenschneider**, Ka Wa Tsang *et al.* "*GW150914 peak frequency: a novel consistency test of strong-field General Relativity*", published as Class.Quant.Grav. 36 (2019) 10, 105009. Hereafter referred to as Paper IV.

Chapter 2

Gravitational Wave Astronomy and the Effective-One-Body approach

This chapter is devoted to an introductory waveform modeling for GW astronomy (GWA). The general framework of GWA is defined with respect to all necessary parameters important to consider for building waveform models from a general perspective and afterwards focused on CBC events, BBH in particular. The quality requirements for GWA are defined and the validation process is outlined. BBH systems are discussed and the choice to prioritize spin-aligned, non-eccentric BBH systems is motivated and their parameter space and general evolution are discussed.

The two-body problem of GR gives the starting point for a brief review of both analytical approximations and numerical solutions to the Einstein Equations given for coalescing BBH systems. The EOB approach is introduced to resum analytical information in a robust and reliable way. NR codes are used to generate BBH waveforms that can be used to complete and validate EOB waveform models.

This is discussed in detail by introducing the general framework of the `TEOB` Hamiltonian and how analytical and numerical information can be captured within this approach. The generation of the full EOBNR waveform is outlined first in detail, followed by a summary and including the completion of the waveform with phenomenological templates capturing the NR waveform of the merger-ringdown phase. The discussion of this chapter is concluded by an outline of this thesis.

2.1 Gravitational Wave Astronomy

The first thing to define in the context of GW astronomy is the GW strain h itself, following the definition given in Ref. [119]. The GW strain h contains two independent polarizations h_+ and $h_\times$[1]. Assuming a four-dimensional spacetime with the Cartesian coordinate system $\{t, x, y, z\}$, endowed with the flat Minkowski metric and mostly plus convention. A GW traveling along the z axis with the polarizations $h_{+,\times}$ would then impact the line element as follows:

$$ds^2 = -dt^2 + [1 + h_+]\, dx^2 + [1 - h_+]\, dy^2 + 2h_\times dxdy + dz^2 \tag{2.1}$$

---

[1] For a full introduction to the theory of GWs and the basic concepts of GW detectors the interested reader is referred to the excellent book by Michelle Maggiore [119].

The complex strain h is defined from these polarizations as

$$h \equiv h_+ - ih_\times \ . \tag{2.2}$$

The astute reader may have already noticed that the above definition of the GW polarization is done in the transverse-traceless gauge which will be used throughout this work [119]. Therefore, to detect a GW it is necessary to measure the effect of $h_{+,\times}$ on ds. This can be done with interferometric detectors based on the principles of a Michelson interferometer. The reader should note that this represents an essential difference to observations of electromagnetic radiation which is commonly detected through absorption of energy. The energy radiated off goes proportional to $1/\mathcal{R}^2$, with the distance $\mathcal{R}$. The GW strain however falls off proportional to $1/\mathcal{R}$ [119]. At the moment of preparation of this thesis four operational GW observatories exist that are sufficiently powerful to observe GWs originating in astrophysical CBC events. The two advanced LIGO detectors are located in Hanford, Washington, and Livingston, Louisiana, in the United States of America and have observed the first GW event GW150914 [15]. On August 14th, 2017, the Virgo detector in Cascina near Pisa, Italy, detected GW170814 jointly with the two LIGO detectors in the second observing run, making it the first three detector observation of a merging BBH system [10, 19]. On February 25th, 2020, the KAGRA detector, located in the Kamioka Observatory near the city of Hida, Japan, went online as well as the fourth GW detector capable of observing CBC events through GWs [4].

It is useful to consider how the effects of GWs traveling through a detector are measured and observed. Fig. 2.1 shows the systematic layout of advanced Virgo[2] at the beginning of the third observing run O3 [10]. The schematic setup is based on the principles of a Michelson interferometer as follows: A $25W$ laser with a wavelength of $1064nm$ is setup and send through a input mode cleaner and sent into an equal 50% beam splitter which separates the beam into two orthogonal arms. Each arm consists of an optical Fabry-Perot cavity between two mirrors acting as test-masses, three kilometers apart. After passing through the arms several times the beam is then recombined at the beam splitter and sent to a photo-diode detector. The signal reaching the photo diode is tuned to be as close as possible to total destructive interference. A gravitational wave passing through the plane of the detector would then oscillate between elongating one arm while shortening the other and the reverse. As a result the photo diode would detect a change in the signal observed which is directly correlated to the GW polarizations $h+, \times$. The detector response function, relating the physical GW event to the observed interference pattern, depends primarily on the geometry of the detector and the relative position of the source in the detector frame[3].

While it is possible to detect the presence of GWs with a singular detector it is very difficult to obtain any form of sky localization without the addition of at least one further detector. Which is in turn greatly improved through the addition of a third detector as can be seen on the example of GW170814 [19]. Commonly an increased number of detectors additionally increases the statistical significance of any GW event. Especially in the case of faint GW signals additional detectors would be very useful to improve the total Signal-to Noise-Ratio (SNR) ρ of the signal, which as a function of the individual detector SNR ρ_k goes as $\rho = \sqrt{\sum_k \rho_k^2}$ with k being summed over all detectors.

---

[2] While there are many noteworthy differences between the LIGO and KAGRA detectors compared to the Virgo detector the operational principle is identical for all and thus the Virgo detector will suffice as an example.

[3] A derivation of an example detector response function can be found in chapter 9 of Ref. [119].

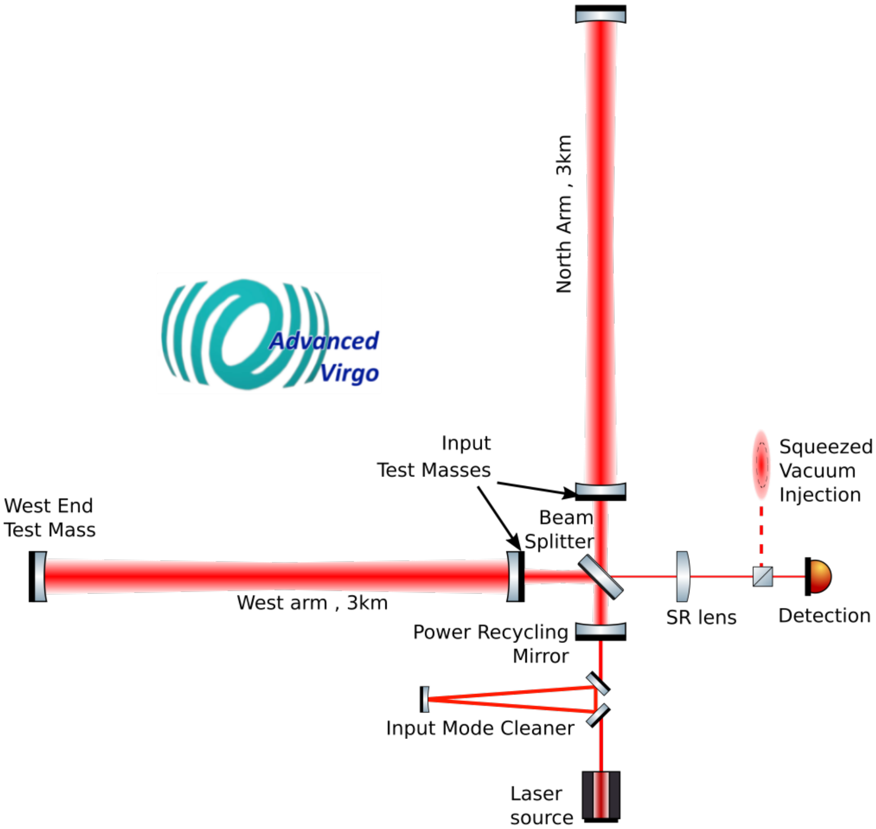

Figure 2.1: The schematic layout of the advanced Virgo detector at the beginning of the third observing run O3. For a more detailed discussion of interferometric GW detectors see *e.g.* Ref. [9, 10] or chapter 9 of Ref. [119]. [Picture source: [10]]

In the context of GW astronomy there are a list of variables that strongly influence the signal which are however independent of the source observed. These parameters are commonly referred to as *extrinsic* opposed to the *intrinsic* ones describing the system within the framework given by a specific model. The extrinsic parameters are mainly related to the three dimensional orientation of the source relative to the detector frames. The distance can be measured in both redshift and luminosity distance simultaneously[4]. The GW strain goes as

$$h \propto \mathcal{R}^{-1}, \tag{2.3}$$

see *e.g.* [119]. To fully capture the relative orientation of the source to the detector four angles are necessary. Two pairs of azimuthal and longitudinal angles (ι, ϕ). The first pair describing the position of the source relative to the detector frame and the second describing the direction of the detector relative to the source frame[5]. Within this thesis, unless stated explicitly otherwise, (ι, ϕ) will refer to the position of the detector relative to the source frame.

In principle, the parameters (ι, ϕ) can be defined independent of any knowledge of the source

---

[4] As mentioned in the previous chapter, this specific property allows GW signals to be used as standard sirens, especially systems as clean and well controlled as CBC events [144].

[5] the second pair of angles will always be necessary since spherically symmetric sources are excluded by Birkhoff's Theorem [151].

and are technically extrinsic. While they naturally do not impact the waveform that is generated at the source, they do have a great impact on the signal observed. To account for the dependence on (ι, ϕ) the complex waveform h is decomposed into multipoles following Ref. [56] as

$$h\left(M, t, \mathcal{R}, \iota, \phi\right) = \frac{M}{\mathcal{R}} \sum_{\ell=2}^{\infty} \sum_{m=-\ell}^{m=\ell} h_{\ell m}\left(t - \mathcal{R}\right) \; {}^{-2}Y_{\ell m}\left(\iota, \phi\right) \; . \tag{2.4}$$

The expansion coefficients are the complex functions $h_{\ell m}$, which depend on the retarded time $t - \mathcal{R}$ at the separation $\mathcal{R}$ from the source while of course also depending the intrinsic parameters of the underlying waveform model. The dependency on M and the remaining dependency on $\mathcal{R}$ are factored out[6]. The expansion basis is given by the $s = -2$ spin-weighted spherical harmonics ${}^{-2}Y_{\ell m}\left(\iota, \phi\right)$ given in terms of the Wigner d-functions is

$$ {}^{s}Y_{\ell m}\left(\iota, \phi\right) = (-1)^s \sqrt{\frac{2\ell + 1}{4\pi}} d^{\ell}_{m,s}(\iota) e^{im\phi} \tag{2.5}$$

$$\textit{with} \;\; d^{\ell}_{m,s}(\iota) = \sum_{k=k_1}^{k_2} \frac{(-1)^k \left[(\ell+m)!(\ell-m)!(\ell+s)!(\ell-s)!\right]^{1/2}}{(\ell+m-k)!(\ell-s-k)!k!(k+s-m)!} \times \left(\cos\left(\frac{\iota}{2}\right)\right)^{2\ell+m-s-2k} \left(\sin\left(\frac{\iota}{2}\right)\right)^{2k+s-m} \; , \tag{2.6}$$

with $k_1 = max(0, m-s)$ and $k_2 = min(\ell+m, \ell-s)$ [56]. The monopole and dipole radiation, corresponding to $\ell = 0, 1$ are 0 for all possible sources (see *e.g.* [119]). As can be seen from eq. (2.4) there are $2\ell + 1$ multipoles for each value of $\ell \geq 2$. This number of multipoles $h_{\ell m}$ can however be reduced due to the identity

$$h_{\ell m} = (-1)^{\ell} \, h^{*}_{\ell -m}, \tag{2.7}$$

where * denotes the complex conjugation, reducing the number of independent multipoles to $\ell + 1$ for each value of $\ell \geq 2$. In the case of concrete waveform models this assumption is often build into the model and only $h_{\ell m}$ with $m \geq 0$ are generated while the remaining ones are obtained with the above identity. Unless specified otherwise the discussion in this thesis will always restrict itself to $m \geq 0$. In the case of waveforms generated with NR codes all multipoles are typically given. To simplify the modeling of each multipole $h_{\ell m}$ a further separation into amplitude $A_{\ell m}$, phase $\phi_{\ell m}$ and frequency $\omega_{\ell m}$ is done as

$$h_{\ell m} = A_{\ell m} \cdot e^{-i\phi_{\ell m}} \; , \tag{2.8}$$

$$\omega_{\ell m} \equiv \dot{\phi}_{\ell m} \; , \tag{2.9}$$

where the notation $\dot{(..)} \equiv \partial_t(..)$ was used. While in principle an infinite number of multipoles contribute to the GW signal, in the case of CBC events, a general hierarchy exists between the magnitude of the different multipoles. For any given value of ℓ the largest multipole is given by $m = \ell$ and the magnitude of the $A_{\ell m}$ decreases with m until $m = 0$. Comparing two different $\ell = m$ multipoles shows that magnitude of $A_{\ell m}$ increases as ℓ decreases[7]. Therefor, the most

---

[6] The fact that the total mass of the system can be factored out is a consequence of the scale free nature of the Einstein Equations in vacuum without a cosmological constant and will be discussed later in this chapter.

[7] This can be seen in Paper II and III, where the individual amplitudes are compared for the different multipoles

dominant mode generated during a CBC event is the $(\ell, m) = (2, 2)$ mode[8] combined with the $(2, -2)$ mode. Further, the reader should note that for example the relative magnitude of $A_{\ell m}$ between $(\ell, m) = (2, 1)$ and the $(3, 3)$ depends on the binary in question. In some cases one will find $A_{21} > A_{33}$, or possibly the reverse. In some cases the two amplitudes will be of comparable magnitude. In fact in some cases the relative contribution to h of these two amplitudes can change with the position of the observer relative to the observed binary system.

2.1.1 Comparing waveforms: The Match and the Unfaithfulness

Thus, the main outputs of the waveform models needed for GW astronomy are the $h_{\ell m}$ coefficient functions that then allow a reconstruction of h. Once h is reconstructed it can be projected onto the detector frame and the detector response function can be computed that allows to compare the generated waveform h with the data observed by a given detector. The natural follow up question is how to compare the waveform generated by a given model to a realistic data set containing a specific realization of noise in addition to the physical signal. To answer this question the match $\mathcal{M}$ is introduced. $\mathcal{M}$ is the normalized inner product of two waveforms in the frequency domain weighted against the noise of the detector under consideration. The characterization of the detector noise in the frequency domain is given by the Power Spectral Density (PSD) commonly denoted by S_n given as a function of the physical frequency f (See App. A for further discussion on the PSD). The inner product of two waveforms h_I and h_J is then given as

$$\langle h_I, h_J \rangle \equiv 4\Re\left[\int_{f_{\min}}^{\infty} \frac{\tilde{h}_I(f)\tilde{h}_J^*(f)}{S_n(f)}\, df\right] , \tag{2.10}$$

where $\Re[\dots]$ denotes the real part, $\tilde{h}$ denotes the Fourier transform of h and $f_{\min}$ denotes the minimal frequency for which both waveform are defined or a minimum cut-off frequency defined by a specific experimental context. The norm of a waveform and the match $\mathcal{M}$ can then be defined as

$$||h|| \equiv \sqrt{\langle h, h \rangle}, \tag{2.11}$$

$$\mathcal{M}(h_I, h_J) \equiv \max_{t_0,\phi_0} \frac{\langle h_I, h_J \rangle}{||h_I|| \cdot ||h_J||}, \tag{2.12}$$

where $\max_{t_0,\phi_0}$ denotes the maximization with respect to an initial time shift t_0 and phase shift ϕ_0. A few observations can be made from eq. (2.10) – (2.12). (i) The match is normalized and therefor can be 1 at most. (ii) The norm $||h||$ is often referred to as the Signal-to-Noise Ratio (SNR) in the experimental context. (iii) A match close to 1 between two waveforms would then imply $h_I \approx h_J$ with respect to the detector while a smaller match would indicate measurable differences. Eq. (2.10) indicates that the PSD S_n is compared to quantities that are quadratic in the GW strain. It is therefor useful to consider the strain noise spectrum which is given by $\sqrt{S_n(f)}$. The design sensitivities for advanced LIGO [5], advanced Virgo [10] and KAGRA [3] are shown in Fig. 2.2.

---

at their respective peak. As an explicit example it is additionally useful to consider the test-particle data presented in [90].

[8] For many GW events of the first two observing runs, O1 and O2, an accurate model representing the h_{22} was sufficient to obtain a thorough analysis of the data [22].

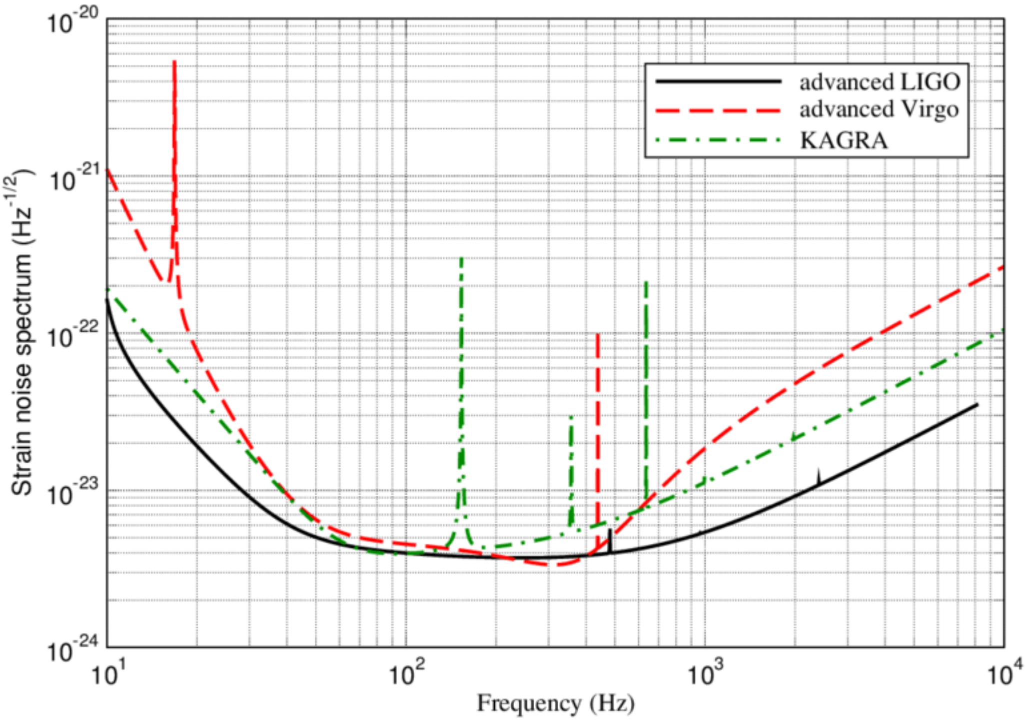

Figure 2.2: Strain noise spectral density estimated by the design sensitivity [146] given for the advanced LIGO, advanced Virgo and KAGRA design as a function of the physical frequency. [Picture source: [146]]

Each GW event that accumulates sufficient SNR can then be detected and analyzed[9].

Equipped with the definition of the inner product and the match $\mathcal{M}$ it is now possible to turn to the Parameter Estimation (PE) process. But first it is necessary to define the relative probability: Given a set of assumptions B, the probability of the statements A to be true is defined as $p(A|B)$. The aim of the PE process is then to perform a Bayesian Inference Analysis to obtain the posterior density distribution $p(\vartheta|data)$, with ϑ being an element of the space of all possible combinations of extrinsic and intrinsic parameters Θ [44, 106]. Examples of such an analysis can be found with each detected and analyzed GW event, see *e.g.* [22, 28]. The posterior can then be estimated from Bayes theorem as

$$p(\vartheta|data) = \frac{\mathcal{L}(data|\vartheta) \cdot p(\vartheta)}{p(data)}, \tag{2.13}$$

where $\mathcal{L}(data|\vartheta)$ is the likelihood function and $p(\vartheta)$ is the prior distribution. The probability of the data $p(data)$ is a general normalizing constant and as only the shape of the integral has a physical meaning, it is possible to normalize it to 1, fixing $p(data)$. The main constraint of $p(\vartheta)$ are the domains of validation and definition of the waveform model used to perform the analysis. Additionally, it is possible to chose $p(\vartheta)$ such that this impacts the resulting posterior (see *e.g.* Ref. [106] for a discussion). The likelihood function is commonly obtained as follows. Given an observed signal d_k with the index k denoting each detector that has recorded a signal. Given a waveform model, the waveform for the k-th detector generated is then denoted by $h\left(\vartheta_k\right)$. Then it

---

[9] The reader should note however that these are strongly idealized curves and a number or additional small and large noise spikes complicate the analysis. Further it is not always possible to reach level of performance. For a more detailed information on observed GW data and the detector performance one should see *e.g.* Ref. [2].

is possible to estimate the likelihood function as

$$\mathcal{L}(data|\vartheta) \propto \exp\left\{ -\frac{1}{k_{\max}} \sum_k \langle h\left(\vartheta_k\right) - d_k, h\left(\vartheta_k\right) - d_k \rangle \right\} \ , \tag{2.14}$$

where $k_{\max}$ denotes the total number of detectors. To evaluate the right-hand side of this expression several methods can be used. In practice most common ones are nested sampling or Markov-Chain-Monte-Carlo integration [22, 28]. For a waveform model to be usable in such an analysis two conditions must be met: (i) It needs to be possible to evaluate to model very quickly on time scales of about $\sim 0.1s$. The analysis of most GW events observed in practice demands models to be evaluated around 10^6 to 10^7 times [13, 22]. (ii) the model needs to be robust and smooth. In practice this means that small changes in ϑ correspond to small changes in $h_{\ell m}$.

It is useful to compare the maxima of $\mathcal{L}(data|\vartheta)$ and $\mathcal{M}_k\left(d_k, h(\vartheta_k)\right)$[10]. Following from their respective definitions above it stands to reason that if a GW event is present in the data d_k that the combination of parameters ϑ that maximizes $\mathcal{L}(data|\vartheta)$ will correspond to the ϑ_k that maximize $\mathcal{M}\left(d_k, h(\vartheta_k)\right)$. This observation can now be used to define the currently most used quality estimate for waveform models: The faithfulness F and the unfaithfulness $\bar{F}$. The faithfulness F is computed in the same way as the match[11]. Within this work the following distinction will be made. The match $\mathcal{M}$ will always compare a waveform model with observed data. This obviously necessitates that all *extrinsic* and *intrinsic* parameters are set to precise values on the side of the waveform model and the projection of the generated waveform into the detector frame. The faithfulness on the other hand will be used to compare two different waveforms that both aim to model GR. Therefor, as the projection of the waveform strain polarizations $h_{+,\times}$ is known exactly, it is not necessary to test for various combinations of the *extrinsic* parameters. Thus faithfulness and it's complement the unfaithfulness are given as

$$F(h_I, h_J) \equiv \mathcal{M}(h_I, h_J), \tag{2.15}$$

$$\bar{F}(h_I, h_J) \equiv 1 - F(h_I, h_J) \ . \tag{2.16}$$

Alternatively, the notation $\bar{F}_{IJ} \equiv \bar{F}(h_I, h_J)$ or $F_{IJ} \equiv F(h_I, h_J)$ will be used. While both the unfaithfulness and the faithfulness will be used in this thesis the primary focus is on the unfaithfulness since it is more efficient in most cases to compare numbers close to 0 as opposed to 1. Generally, in this thesis two computations of the unfaithfulness are distinguished. First, mode-by-mode comparisons for which $h_{\ell m}$ is compared directly for two different models, in particular h_{22} as the most dominant mode is often the first focus of such an analysis. Alternatively, if the aim is to compute the performance of the full waveform h it is necessary to vary the computation of $\bar{F}$ with respect to (ι, ϕ). $\bar{F}$ can either be minimized (corresponding to F being maximized) with respect to the (ι, ϕ) or it can be evaluated over a grid. Both approaches are useful to study the performance of a waveform model and will be used and discussed in a practical context in chapter 5 and 6. The computation

---

[10] The reader should note that while $\mathcal{L}(data|\vartheta)$ contains information of all detectors, this is not true for $\mathcal{M}_k\left(d_k, h(\vartheta_k)\right)$ which is given for each detector k individually due to the dependence on the detector specific PSD. Further note a slight abuse of notation since ϑ_k in principle contains the initial relative time and phase shifts (t_0, ϕ_0) which are maximized in the computation of the match.

[11] In fact it is common in the literature that match (mismatch) and faithfulness (unfaithfulness) are used interchangeably.

of the unfaithfulness together with some technical aspects is summarized in Appendix A.

2.1.2 Quality demands and estimation of waveforms

Assuming a catalog of perfect waveforms that exactly represent GR is given. With this perfect catalog it would then be possible to compute $\bar{F}$ between the catalog and a waveform model. The generated distribution $\bar{F}(\vartheta_{intrinsic})$ would therefor represent the error of the waveform model. As in any realistic case this error will not be zero it is important to estimate what level of accuracy and precision are necessary for the model to produce reliable results in application to real data. A thorough discussion of this question can be found in Refs. [88, 112]. A good heuristic that can be derived from their discussion is this: Assume a GW event detected with an SNR ρ. Then to ensure that the analysis of the signal is reliable and the detection loss is reasonable the error should be capped as

$$\max\left[\bar{F}(\vartheta_{intrinsic})\right] \lessapprox \frac{1}{\rho} \,. \tag{2.17}$$

Common practice for second generation GW detectors such as advanced LIGO, advanced Virgo and KAGRA, these bounds are set to < 0.03 at minimum, but ideally < 0.01 (see *e.g.* [53] or Paper I – III). In summary, the goal of waveform modeling is ultimately, given a catalog that accurately and precisely represents GR over the parameter space of GW-CBC events, to build a model such that one can reach $\max\left[\bar{F}(\vartheta_{intrinsic})\right] < 0.03$ or even better $\max\left[\bar{F}(\vartheta_{intrinsic})\right] < 0.01$ over the entire catalog. This discussion of $\bar{F}$ is amended by several practical details in Appendix A.

Within this thesis one of the main points of focus will be on using NR waveforms generated with different codes to estimate the quality of such waveform models and on how those waveform models can be improved utilizing the information contained in a catalog of NR waveforms. The catalog of NR waveforms will be discussed in chapter 3, while the discussion of the improvement and quality analysis of three waveform models will be presented in chapters 4 – 6. Further two additional notes should be made here:(i) the reader should note that the unfaithfulness is very useful to compare two waveforms within a given experimental context and probe them for relevant differences. To find the cause of said differences it is however more efficient to compare two waveforms directly in the time domain, after aligning them to minimize the phase difference in a reasonable frequency interval. In practice this method will be used heavily throughout chapters 3 – 6 to demonstrate agreement or disagreement between waveforms. The frequency intervals chosen are always given to allow the reproduction of the results.

(ii) While these methods can be used to access the quality of a given waveform model it is still important to point out that these methods of estimating the quality of a waveform model are not the best possible way to ensure that no pathological effects are present in the model even though they might not be exhibited in this waveform model. Some additional simple methods to explore the stability and reliability of a waveform model will be explored in practice in the later chapters 3 – 6. In principle the best test to determine if a model adequately represents the prediction of GR is to perform an injection study [31, 37, 99, 143]. During an injection study a waveform, assumed to reliably represent GR for a given set of parameters ϑ is projected into a combination of detectors and to each signal a single realization of the detector noise is added. Thus one obtains the set $d_k^{injection}(\vartheta)$. This data can then be treated as a possible real event and a PE algorithm can be applied. If the model can accurately recover several combinations of ϑ it can be considered ready and reliable. In principle it would be possible to use real GW event data that has been analyzed already by trusted models, however such a setup would be less controlled and also would limit the parameter space to the parameter combinations that have been observed so far. Especially models that aim to increase the range of the parameter space covered it is advisable to validate the model through injection studies to estimate possible biases that would be exhibited in the application to observed GW events.

2.2 The two-body problem and the EOB approach

The discussion so far aimed to outline the two major aspects that set the context for waveform model development. First, the model needs to produce h or the individual $h_{\ell m}$ for a set of *intrinsic* parameters $\vartheta_{intrinsic}$. Secondly, given a catalog of waveforms representing the prediction of GR it is then necessary to test and develop the waveform model until it meets the first quality demand: Namely, that the maximum of $\bar{F}$ computed over the parameter space covered by the catalog of GR waveforms.

So far the focus was set most generally on the case of building a waveform model and only partially focused in on relevant only to CBC systems. In the following, the discussion will turn exclusively to the problem of a BBH systems emitting GW. First, an introduction to the two-body problem will be given. The discussion will then focus on the analytical methods capable of studying BBH systems. In particular, PM, PN and Gravitational-Self-Force (GSF) theory. These theories however will prove insufficient to form the basis of a robust waveform model. The introduction of the EOB approach allowed to combine the analytical information into a robust and reliable framework. Many choices are involved in constructing an EOB model and it is not self-evident which is superior to the others. Further, even given the wealth of information that can be found in PM, PN and GSF theory, it is not sufficiently to model a BBH system to the above stated quality demands all the way through merger to the final state. Therefor more information is needed. Additionally, purely from the analytical framework it is not possible to construct a reliable target catalog of waveforms that accurately represent GR. To solve these two problems the discussion will then turn to NR. NR waveforms will be discussed both as a source of missing information and as a catalog of waveforms representing GR. NR is however not perfect and the uncertainty of the NR catalog has been estimated and accounted for when NR waveform catalogs are utilized for the building of GR waveform models.

2.2.1 The two-body problem of GR: Binary Black Holes

Once a BBH system has formed four stages of evolution will follow. First, the *inspiral* during which the two BHs are bound gravitationally. The two BHs orbit each other while slowly emitting GWs and steadily increasing the frequency at which they orbit each other getting slightly closer to each other with every orbit. This process is extremely slow. Typically time spans of the order of 10^9 to 10^{10} years or even longer can be expected for astrophysical, relevant sources observable with second generation GW detectors such as advanced LIGO, advanced Virgo and KAGRA [64, 119, 120].

The second step of the evolution of a BBH system is the *plunge* (see *e.g.* [61]). The plunge marks the end of the inspiral of a BBH systems. After a sufficiently long inspiral the two BHs

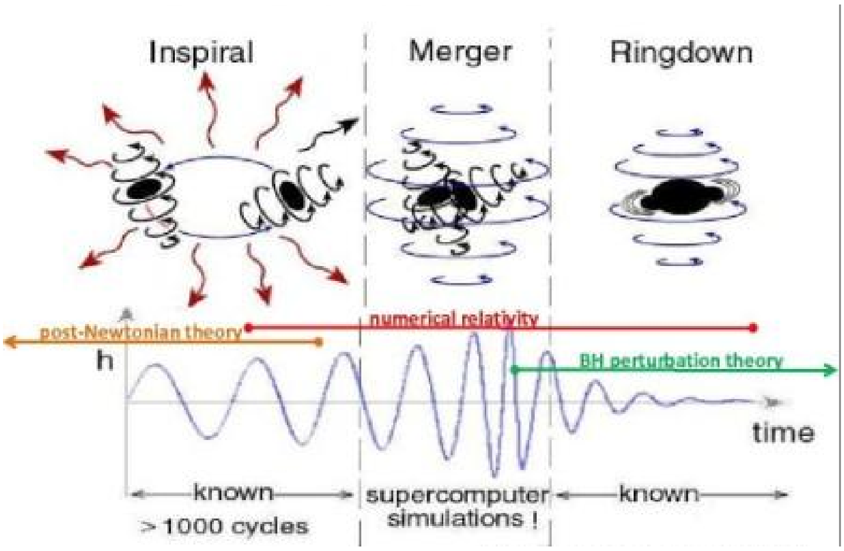

Figure 2.3: The three phases of BBH coalescence: inspiral, merger and ringdown. Matched with the ranges of validity for the three sources of information about the BBH coalescence. Post-Newtonian Theory, Numerical Relativity and Black Hole perturbation theory. [Picture credits: Kip Thorne]

will have gotten close enough to each other that any further emission of GWs will push them so close together that the semi-stable inspiral will transition into an unstable radial plunge and a successive head-on collision of the two BHs: The *merger*, the third step of the BBH evolution. In the context of a test-particle orbiting a BH[12] the transition from the inspiral to the plunge occurs at the Innermost-Stable-Circular Orbit [64].

The plunge and the merger are the most extreme stages of the BBH evolution and consequently also the peak of the GW luminosity lies within this stage. The end of the merger is marked by the formation of a final BH in a perturbed state. This exited BH will then enter the *ringdown* phase and emit GWs through Quasi-Normal-Modes (QNM) [47] until it has reached the state of a relaxed Kerr BH. Once the BBH system has reached this state the evolution will be considered over.

The reader should note that while from a modeling point of view the addition of the plunge phase can be useful as it is dynamically different from both the inspiral and merger, it is not always treated as a different phase. This can be seen *e.g.* in the fact that a waveform model that covers the full range of the BBH evolution is commonly referred to as an Inspiral-Merger-Ringdown (IMR) waveform model. A schematic example of an IMR waveform is shown in Fig. 2.3. Additionally, it shows schematically the different theories that allow the study of BBH systems and their approximate range of validity throughout the evolution of the system. In chapter 1 a brief introduction to the *intrinsic* parameters describing a BBH system was given. The discussion will now return to this list of parameters, extend them and expand on some general considerations. Additionally, the motivation to focus on waveform models with following constraints will be reviewed and discussed: (i) The motion of the BBH system be constrained to a singular plane of motion with constant BH spins perpendicular to the plane of motion. (ii) The BBH system should have vanishing eccentricity.

The first thing to note when considering to build BBH systems is that the spacetime describing

---

[12] A test-particle orbiting a BH can be interpreted as a BBH system with one BH being several hundred to a thousand times larger than the smaller one.

their full IMR evolution will solve the *Einstein Equations* in vacuum given as

$$G_{ab} = 0 \tag{2.18}$$

where G_{ab} is the Einstein Tensor and a, b are spacetime indices defined with respect to a suitable four dimensional coordinate system [152]. While it might not be obvious at first sight, but the Einstein Equations in vacuum are special due to the absence of any physical scale. This scale free nature thus would imply that the scale would have to be set by the BBH system and one can find that indeed the total mass M of the BBH system can be scaled out without loss of generality [34, 43][13]. In practice this allows to set $M = 1$ while preparing any computing any waveform. M can then be reintroduced through dimensional analysis together with Newtons gravitational constant G and the speed of light c, which are set to 1 as well.

While M sets the overall scale of the system, just as important are the individual masses of the BHs m_1, m_2 and their mass-ratio $q = m_1/m_2$ with the convention $m_1 \geq m_2$ (therefore $q \geq 1$ is true for all systems). As a matter of fact it can be seen that the GW emission of a BBH system is dominated by the mass-ratio at leading order. More precisely the GW strain h is directly proportional to the symmetric mass-ratio ν given as

$$\nu = \frac{m_1 m_2}{(m_1 + m_2)^2} \ . \tag{2.19}$$

It can easily be seen that the case of $m_1 = m_2$ implies $\nu = 1/4$. While the case of $m_1 \gg m_2$ is equivalent to $\nu \approx 0$. Each BH has additionally a spin given by the 3-vector $\vec{S}_i$, with the index $i = 1, 2$ referring to the individual BHs unless otherwise stated. The cosmic censorship conjecture implies then that $|\vec{S}_i| \leq m_i^2$ [152]. The properties of the BH spins $\vec{S}_i$ and masses m_i are defined for each BH individually. To fully classify the trajectory of both BHs their initial positions and 3-momenta are given by the 3-vectors $\vec{x}_i$ and $\vec{p}_i$ at an initial time t_0. Based on the *no-hair* theorem, proven by Israel *et al.* [62, 103, 104][14], both BHs are thus fully characterized. The reader should note that the determination of the BH mass, BH spins and the linear momentum are by no means trivial in a general setup. One way to reliably determine these quantities is the ADM formalism (see e.g. [43]) [15].

Earlier it was pointed out that within this thesis the focus is on BBH waveform models with two constraints. The first constraint is relatively easy to justify: In a BBH system only the total

---

[13] The reader should note that this scale invariance will not be a true in the general case. For any GW source for which effects of a non-zero Cosmological Constant or matter play a role the invariance would be explicitly broken.

[14] For completion the reader should note two things: (i) The no-hair theorem generally allows for the BH to carry electrical charge. As most BHs are assumed to neutralize on very fast time scales relative to the length of an inspiral of the order of 10^9 years or even more, it is reasonable to neglect the electric charge (see *e.g.* Ref. [64] for a discussion of charges BHs). (ii) Israel *et al.* have proven the no-hair theorem in the context of static BHs while for the full dynamical case the proof of the no-hair theorem is still undiscovered. However, no violation of the no-hair theorem has been observed experimentally or numerically.

[15] Within the ADM formalism masses and angular momenta are given locally as integrals over the three dimensional volume segments $\sum$. Through Stokes Theorem these integrals can alternatively be expressed as integrals of the boundary of $\sum$. Especially in a NR setup can this formulation be useful. The moving puncture method for example "removes" the interior of the BH and therefor an integration over the full volume would not be possible (see *e.g.* Ref. [43]).

angular momentum $\vec{J}$ is conserved and given by

$$\vec{J} = \vec{L} + \vec{S}_1 + \vec{S}_2 + \vec{J}_{\mathrm{GW}} \tag{2.20}$$

where $\vec{L}$ is the orbital angular momentum and $\vec{J}_{\mathrm{GW}}$ the total angular momentum carried by GWs emitted by the system. It can be shown in EOB models with general spin vectors that this will lead to a precessing dynamics of $\vec{L}$, $\vec{S}_1$ and $\vec{S}_2$ (see *e.g.* Refs. [33, 71]). When observing the concrete equations of motions directly it is noticeable that the time derivatives of $\vec{S}_1$, $\vec{S}_2$ and $\hat{L} \equiv \vec{L}/||\vec{L}||$, where $||\vec{L}||$ denotes the norm of $\vec{L}$, are all linear combination of cross-products between each other. Consequently, if the 3-vectors $\hat{L}$, $\vec{S}_1$ and $\vec{S}_2$ will be parallel, they will also be constants of motion during the inspiral phase. This alone would not necessarily justify the restriction to this special case, but it has been pointed out in Ref. [71] that the GW signals of BBH systems with both BH spins aligned with $\hat{L}$ (*i.e.* $\hat{L} \cdot \vec{S}_i > 0$) will produce a larger GW strain h and therefor will be easier to detect. Thus, it is a reasonable strategy to first focus on waveform models with spins parallel to $\hat{L}$.

Turning now to the initial position and momentum vectors. Within the framework of this all work will be done in the Center-of-Mass frame. In the discussion it was established that $\hat{L}$ is a constant of motion and therefor $\vec{x}_i$ and $\vec{p}_i$ have to be in the plane perpendicular to $\hat{L}$. The most general orbit in a two dimensional plane would be given by the semi-major axis a and an eccentricity ε. Due to the emission of GWs both a and ε will be time-dependent. Applying the quadrupole formula to the motion of a BBH system the time derivative of ε is given as

$$\dot{\varepsilon} = -\frac{304}{15}\frac{G^3 m_1 m_2 M}{c^5 a^4}\frac{\varepsilon}{(1-\varepsilon^2)^{5/2}}\left(1 + \frac{121}{304}\varepsilon^2\right) \tag{2.21}$$

with M, G and c left explicit (see *e.g.* chapter 4 of Ref. [119] for a derivation). As can be seen $\dot{\varepsilon}$ is negative and becomes proportional to ε in the limit of $\varepsilon \ll 1$. This phenomena is generally referred to as circularization of compact binary systems. As most observed BBH systems have evolved for thousands of cycles and more it is likely that by the time they get close to merger and become detectable with GW observatories they will have been fully circularized. As the inclusion of eccentricity would further complicate any GW model it is reasonable to first construct a working model without it.

It is useful to now summarize and conclude the discussion of the BBH parameter space relevant for this thesis. Each individual BH is given through it's mass m_i and the spin $\vec{S}_i$, which is parallel to the orbital angular momentum $\vec{L}$. The direction of $\vec{L}$ is given by $\hat{L}$ and is constant throughout the evolution of the BBH system. The source frame is defined as the coordinate system t, x, y, z. The origin is $x = y = z = 0$ is chosen to coincide with the Center of Mass (CoM). The coordinate t is chosen to be time-like. $\hat{L}$ is chosen to coincide with the positive z-axis[16] and thus the motion of the BBH system is constrained to the $z = 0$ plane. As the eccentricity $\varepsilon = 0$ is imposed, the motion of the BBH system will ba succession of circularized orbits driven to smaller and smaller radii by the emission of GWs until the two BHs merge to a final BH. It is easy to see that in this setup the radial separation of the two BHs will monotonically together with the orbital angular momentum

---

[16] This can be assumed without loss of generality as the transformation $\hat{L} \to -\hat{L}$ would change the waveform as $h_{\ell m} \to h_{\ell,-m}$ as can be seen from explicitly evaluating eq. (2.5).

while the orbital frequency does increase.

As the total mass $m_1 + m_2 = M = 1$ can be scaled out only the ratio of the masses $q = m_1/m_2$ (with the convention $m_1 \geq m_2$ follows that $q \geq 1$) and the spins $S_i = \vec{S}_i \cdot \hat{L}$ of the two BHs determine the evolution of the BBH system uniquely. The parameter q is commonly used to denote the mass-ratio. For example the overwhelming majority of the waveforms used in Paper I were generated for integer values of q and the interpretation is intuitively accessible. With the exception of the extreme mass-ratio limit (*e.g.* $q \gg 1$) it however has no large dynamical impact. More commonly used is the symmetric mass-ratio ν defined in eq. (2.19) as $\nu = m_1 m_2/M^2$, going from 0 (test-particle limit) to 1/4 (equal-mass case). As will be seen later many important aspects of the dynamics scale directly with ν, *e.g.* the GW strain generated by a BBH system $h \propto \nu$. Often it will be useful to work with the fractions of the individual BH masses $X_i \equiv m_i/M$. Their difference $X_{12} \equiv X_1 - X_2$ can be obtained from the symmetric mass-ratio as $X_{12} = \sqrt{1 - 4\nu}$. The BH spins S_i are on the other hand some of the most meaningful variables if combined. As will be shown in chapters 4 and 6 the spin-dependence of many important waveform parameters can effectively modeled as a function of a single linear combination of S_1 and S_2. However, their maximal range depends on q as each of them is limited to be at most m_i^2. Thus it is useful to express them in terms of the dimensionless spin variables $\chi_i \equiv S_i/m_i^2$ which go from -1 to 1 for all values of q. The spins S_i are related to the Kerr spins of the BHs as $a_i \equiv S_i/m_i$. Within this thesis the notation (q, χ_1, χ_2) will often be used to refer to a specific BBH system.

2.2.2 Analytical methods and the Effective-One-Body approach

So far the discussion derived the context in which the problem of waveform model building is defined: To construct a model that can generate a set of $h_{\ell m}$ for a reasonable range of combinations of (q, χ_1, χ_2) ($q \geq 1$ and $|\chi_i| < 1$) usable in the computation of $\mathcal{L}(data|\vartheta)$ as discussed above. Especially, keeping in mind that the waveform model has to be smooth and robust as well as fast to evaluate.

Starting with these goals in mind the natural place to start is with the analytical methods provided. In the context of this work three major analytical approximation methods have been used to inform the inspiral-plunge sector of the `TEOB`-series of waveform models: (i) PN theory expands the metric dynamics as a series of the inverse speed of light $1/c$, often relative to a typical velocity v of the system as v/c, it is thus a low velocity approximation. The leading order is given in the case of a BBH system by Newtons law of Gravity and the Einstein Quadrupole Formula (see *e.g.* Refs. [51, 119, 138] for a review). (ii) The PM approach represents an expansion in powers of Newtons gravitational constant G around flat Minkowskian space time and can be seen as a low curvature approximation (a review of PM theory can be found in Refs. [51, 119, 138]). (iii) GSF theory computes the corrections of the motion of a small mass around a BH in powers of the inverse mass-ratio ($1/q$) and thus is a large-mass-ratio approximation (see *e.g.* Refs. [40, 139, 148] for a review).

All three are important sources in building BBH waveform models. However already on the level of leading order computations for a Binary system it can be seen that a the BHs during the plunge and merger move with velocities comparable to the speed of light, the the curvature of the metric will be a significant deviation from the Minkowski metric and that the most important signals will be of comparable mass BBH systems (recall that $h \propto \nu$). Therefor, it is no surprise that neither of the methods have produced stable and reliable results for BBH dynamics in the late inspiral-plunge regime. In the late 1990s this problem was still unsolved and debated. The solution to this problem was presented in the EOB approach developed, after an example in quantum electro dynamics, by Thibault Damour *et al.* [60, 61, 71, 78] in 1998. Through direct comparison of the PN Hamiltonian describing a BBH system onto that of a point-mass moving in an external metric it was possible to resummate many hundreds of terms into a small number of exact coefficients that captured the information of the PN expansion in a stable and accurate manner. Since then the EOB formalism has become the commonly used standard and most modern waveform models are based on the EOB approach[17]. The interested reader is referred to the above named reviews and books for more details and discussion of PN, PM and GSF theory and their subsequent mapping into the EOB picture. As neither computation and mapping are subject to this thesis no further discussion will be given and the results of the mapping will merely be presented when it is meaningful but this thesis does not aim to give a full overview of these topics. The focus of this thesis starts at the end of the mapping into the EOB picture. While there is a great wealth of analytical information available already it is still not enough to satisfy the general quality demands for GW astronomy discussed above. Further even if the models would reliably predict the waveform it would still be only accurate for the inspiral-plunge phase as most models are conceptually not necessarily to capture the merger of the BBH system. This missing information can be captured through the fitting of effective parameters to NR.

2.2.3 Numerical Relativity

In 2003 the first evolution of a BBH system over a full orbit succeeded [58, 140]. Since then NR has developed greatly. Since then many catalogs[18] of NR simulation describing the evolution of a BBH system over several orbits through inspiral, plunge, merger and ringdown have been achieved (see Refs. [34, 43] for an introductory review of the topic of NR).

NR catalogs serve a dual role within waveform model building. On the one hand they are currently the best option to obtain exact solutions of the Einstein Equations for merging BHs starting in the late inspiral, through the plunge and merger to the ringdown. Therefor they are the natural choice to be used as a "target" catalog. On the other hand they are a useful source of information that can complete a waveform model through the incorporation of effective degrees of freedom that are calibrated to reduce the unfaithfulness $\bar{F}$ between the NR catalog and the waveform model. Still NR has a finite error. This error in some cases can be managed and estimated to an accurate degree. One example of this are the waveforms generated by the `BAM` code [101, 108, 109]. `BAM` is a finite difference code. As the error scales with the grid size it is possible to obtain a reasonable measure of the uncertainty by comparing different resolutions. With a sufficient number of successive waveforms generated for different grid size parameters in the domain of convergence allow one to extrapolate the error to infinite resolution, though this is computationally extremely costly. The `SXS` code however is based on spectral methods [7, 55]. While in a finite difference code a given difference between grid size parameters corresponds linearly to the local resolution of

---

[17] This can be seen *e.g.* by the list of waveform models used in the analyses presented with the first and second GWTC [22, 28]

[18] Some examples of such Catalogs based on individual codes are NINJA [31, 37], NRAR [99], Georgia Tech [105] and RIT [96, 97]. In this thesis however only two catalogs of NR waveforms are used `BAM` [101, 108, 109] and `SXS` [7, 55].

the spacetime, this is not the case for codes generated with the spectral approximations. In the later case it can be that a significant increase in the grid size parameter has almost no effect on the actual grid size and vice versa. Therefor it is not necessarily as useful to compare different grid size parameters for finite-difference methods.

Estimating the error of NR waveforms is therefor no simple task in itself. To ensure that the waveforms faithfully represent GR a general threefold strategy is commonly employed. First, a given waveform is evaluated on an individual basis. The waveform can be inspected visually for indicators of nonphysical or pathological behavior and if a second resolution is available the two are compared. Secondly, the waveform is compared to other waveforms with similar but slightly different parameters (q, χ_1, χ_2) expecting that similar parameters will lead to similar waveforms. Finally, the results of different codes can be compared, based on the assumption that it is unlikely that different codes would diverge from GR in a similar manner on both a qualitative and quantitative level. Largely, along all strategies a good agreement and stable behavior is found it is highly unlikely to expect that the NR waveforms do not represent GR with reasonable faithfulness.

Within this thesis two waveform catalogs, `SXS` and `BAM`, are used as the main sources of NR information used in this thesis and will be reviewed and discussed in chapter 3. Once their uncertainties are under control they will be used to complete several incarnations of the `TEOB` model in chapters 4 – 6.

2.3 `TEOB` infrastructure

The discussion will now turn to the basic structure of the `TEOB` model and how both analytical and numerical information can be incorporated in the model. This infrastructure is common among all three incarnations of the `TEOB` model discussed in this thesis. These are `TEOBResumS` a model for h_{22} for the entire parameter space (q, χ_1, χ_2) (Paper I), `TEOBiResumMultipoles` a model for several multipoles $h_{\ell m}$ over the non-spinning sector exploring the application of the modeling techniques employed for `TEOBResumS` for subdominant modes (Paper II), and `TEOBiResumS_SM` an extension of `TEOBiResumMultipoles` to the spinning sector for a subset of the $h_{\ell m}$, combined with a significant performance upgrade with respect to the h_{22} of `TEOBResumS` (Paper III).

2.3.1 `TEOB` Hamiltonian and Equations of motion

The first point of discussion is the `TEOB` Hamiltonian and the corresponding equations of motions, laying the basis for the model with respect to the inspiral and plunge until the first peak of the multipole $h_{\ell m}$. The `TEOB` Hamiltonian can be best understood as a deformation of a test-particle moving on the background of a spinning Kerr BH, with the deformation parameter given by the symmetric mass-ratio ν. The Kerr-limit (*i.e.* the evolution of a test-particle falling into a spinning BH) is reached as ν goes to 0 and the deformation of the Kerr-Hamiltonian is maximized in the equal-mass case when $\nu = 1/4$.

Generally in the PN context it is possible to separate the conservative dynamics from the dissipative radiation reaction by PN order. Even powers of v/c are referred to as integer PN orders while half integer PN orders refer to odd powers of v/c. In summary the the term $(v/c)^n$ correction with respect to the leading order is commonly referred to as the $n/2$ PN order. As can be seen by explicit PN computations integer PN expansion terms contribute to the conservative dynamics, while half-integer PN expansion terms contribute to the dissipative radiation reaction [119][19]. This allows the separation of the Hamiltonian into H_{EOB} capturing the conservative dynamics of the system and the radiation reaction force $\mathcal{F}$ (entering the equations of motion directly), which can both are obtained from the mapping of the two-body dynamics onto the EOB picture.

The relative dynamics are evolved using dimensionless, phase-space variables $(r, p_r, \varphi, p_\varphi)$[20], corresponding to polar coordinates in the equatorial plane $\theta = \pi/2$. r is given as the relative separation with its conjugate momentum, p_r is replaced by $p_{r_*} = (A/B)^{1/2}\, p_r$, with respect to the "tortoise" (dimensionless) radial coordinate $r_* = \int dr (A/B)^{-1/2}$, where A and B are the EOB potentials. The A and B potentials are the first vessels to account for analytical information. Commonly the A potential is defined explicitly, obtained from PN theory, and the B potential is then obtained from the product AB, fixed in the `TEOB` framework. Within the `TEOB` framework the A potential is closest associated with the orbital dynamics[21]. The concrete forms of the A and B potentials are introduced in Sec. 4.1.1 for `TEOBResumS` and in Sec. 5.2.1 for `TEOBiResumMultipoles` and `TEOBiResumS_SM`.

The dimensionless phase-space variables are related to the dimensionful ones $(R, P_R, \varphi, P_\varphi)$ as

$$r = \frac{R}{GM}, \quad p_{r_*} = \frac{P_{R_*}}{\mu}, \quad p_\varphi = \frac{P_\varphi}{\mu G M}, \quad t = \frac{T}{GM}. \tag{2.22}$$

The spin variables (S_1, S_2) defined within the two-body BBH picture are mapped onto the EOB spin variables as

$$S = S_1 + S_2, \quad S_* = \frac{M_2}{M_1} S_1 + \frac{M_1}{M_2} S_2. \tag{2.23}$$

The EOB Hamiltonian H_{EOB} is rescaled by $\mu = M\nu$ and expressed as

$$\hat{H}_{\mathrm{EOB}} = \frac{H_{\mathrm{EOB}}}{\mu} = \frac{1}{\nu}\sqrt{1 + 2\nu\left(\hat{H}_{\mathrm{eff}} - 1\right)}, \tag{2.24}$$

with

$$\hat{H}_{\mathrm{eff}} = \hat{H}_{\mathrm{eff}}^{\mathrm{orb}} + p_\varphi\left(G_S \hat{S} + G_{S_*} \hat{S}_*\right), \tag{2.25}$$

$$\hat{H}_{\mathrm{eff}}^{\mathrm{orb}} = \sqrt{p_{r_*}^2 + A\left(1 + \frac{p_\varphi^2}{r_c^2} + z_3 \frac{p_{r_*}^4}{r_c^2}\right)}. \tag{2.26}$$

First, the reader should note the reappearance of the A potential in the Hamiltonian, one of the main vessels of analytical and NR information. Further, the coefficient z_3 is given as $z_3 = 2\nu(4 - 3\nu)$. The variables $\hat{S} \equiv S/M^2$ and $\hat{S}_* \equiv S_*/M^2$ are rescaled dimensionless expressions of the above

---

[19] While for lower order terms this separation has a valid physical interpretation this is no longer true for higher PN orders [51].

[20] To simplify the discussion in the previous section p_φ was not defined explicitly. The relationship to $\vec{L}$ is given as $\vec{L} = p_\varphi \hat{L}$.

[21] The reader should note two things: (i) "Orbital" is a general reference to the orbital angular momentum $\vec{L}$. "Orbital dynamics" therefor refers to the aspect of the underlying dynamics driven by $\vec{L}$. In practice this is sector of the model is informed based with the non-spinning ($\chi_{1,2} = 0$) sector and is therefor a function of ν (or q). (ii) While the A potential of `TEOBResumS` does not depend explicitly on the spins it depends implicitly on the spins variables as can be seen in Sec. 4.1.1. For `TEOBiResumMultipoles` and `TEOBiResumS_SM` this dependence on the spin has been removed to improve the performance.

mentioned EOB spin variables. The centrifugal radius r_c was introduced into the `TEOB` framework in Ref. [76] including next-to-leading (NLO) spin-spin terms [91] and is given as

$$r_c^2 = r^2 + \hat{a}_0^2\left(1 + \frac{2}{r}\right) + \delta\hat{a}^2, \tag{2.27}$$

here $\hat{a}_0$ refers to the dimensionless effective Kerr parameter given as

$$\hat{a}_0 \equiv \hat{S} + \hat{S}_* = X_1\chi_1 + X_2\chi_2 = \tilde{a}_1 + \tilde{a}_2\ . \tag{2.28}$$

The NLO spin-spin contribution is given by $\delta\hat{a}^2$ presented in Refs. [39, 76] as

$$\delta\hat{a}^2 = \frac{1}{r}\left\{\frac{5}{4}(\tilde{a}_1 - \tilde{a}_2)\hat{a}_0 X_{12} - \left(\frac{5}{4} + \frac{\nu}{2}\right)\hat{a}_0^2 + \left(\frac{1}{2} + 2\nu\right)\tilde{a}_1\tilde{a}_2\right\}. \tag{2.29}$$

The gyro-gravitomagnetic ratios G_S and G_{S_*} are formally coefficient functions of the EOB spins onto the orbital angular momentum and capture the strength of the spin-orbit coupling. These are the second major vessel for analytical and numerical information. The are given explicitly in Sec. 4.1.1 and are used consistently for all three `TEOB` incarnations. Based on Refs. [76, 127] the models presented here are incorporating next-to-next-to-leading order (NNLO) spin orbit coupling [92]. The Damour-Jaranowski-Schäfer gauge is fixed and as a result (G_S, G_{S_*}) depend exclusively on $(r, p_{r_*}^2)$ and *not* on the angular momentum p_φ [80, 127]. The Hamilton's equations for the `TEOB` Hamiltonian are thus simplified and given in compact form as

$$\frac{d\varphi}{dt} = \Omega = \frac{\partial\hat{H}_{\rm EOB}}{\partial p_\varphi}, \tag{2.30a}$$

$$\frac{dr}{dt} = \left(\frac{A}{B}\right)^{1/2}\frac{\partial\hat{H}_{\rm EOB}}{\partial p_{r_*}}, \tag{2.30b}$$

$$\frac{dp_\varphi}{dt} = \hat{\mathcal{F}}_\varphi, \tag{2.30c}$$

$$\frac{dp_{r_*}}{dt} = -\left(\frac{A}{B}\right)^{1/2}\frac{\partial\hat{H}_{\rm EOB}}{\partial r}, \tag{2.30d}$$

which in turn can be expanded to

$$\frac{d\varphi}{dt} = \Omega = \frac{1}{\nu\hat{H}_{\rm EOB}\hat{H}_{\rm eff}^{\rm orb}}\left[A\frac{p_\varphi}{r_c^2} + \hat{H}_{\rm eff}^{\rm orb}\big(G_S\hat{S} + G_{S_*}\hat{S}_*\big)\right], \tag{2.31a}$$

$$\frac{dr}{dt} = \left(\frac{A}{B}\right)^{1/2}\frac{1}{\nu\hat{H}_{\rm EOB}\hat{H}_{\rm eff}^{\rm orb}}\left[p_{r_*}\left(1 + 2z_3\frac{A}{r_c^2}p_{r_*}^2\right) + \hat{H}_{\rm eff}^{\rm orb}p_\varphi\left(\frac{\partial G_S}{\partial p_{r_*}}\hat{S} + \frac{\partial G_{S_*}}{\partial p_{r_*}}\hat{S}_*\right)\right], \tag{2.31b}$$

$$\frac{dp_\varphi}{dt} = \hat{\mathcal{F}}_\varphi, \tag{2.31c}$$

$$\frac{dp_{r_*}}{dt} = -\left(\frac{A}{B}\right)^{1/2}\frac{1}{2\nu\hat{H}_{\rm EOB}\hat{H}_{\rm eff}^{\rm orb}}\left[A' + p_\varphi^2\left(\frac{A}{r_c^2}\right)' + z_3\,p_{r_*}^4\left(\frac{A}{r_c^2}\right)' + 2\hat{H}_{\rm eff}^{\rm orb}p_\varphi\Big(G_S'\hat{S} + G_{S_*}'\hat{S}_*\Big)\right], \tag{2.31d}$$

where the notation $(\cdots)' \equiv \partial_r(\cdots)$ implies the spatial derivative with respect to r. Similar to $H_{\rm EOB}$, $\mathcal{F}$ is similarly rescaled by μ as $\hat{\mathcal{F}}_\varphi \equiv \mathcal{F}_\varphi/\mu$. Note that μ is constant for a given waveform and thus the rescaling has no impact on the equations of motion. The radiation reaction force $\mathcal{F}$ in the general case is made up of two components $\hat{\mathcal{F}}_\varphi$ and $\hat{\mathcal{F}}_{r_*}$. However, following previous works the choice $\hat{\mathcal{F}}_{r_*} = 0$ is made or all models discussed in this thesis [76][22]. Further note that the horizon absorption is included to leading order in the radiation reaction (see Eqs. (97)-(98) of [76]). The initial data for the `TEOB` equations of motion are generated with the post-post-adiabatic (2PA) initial data [75, 82] for all waveform computations presented in this thesis. The reader should note that Ref. [128] greatly improved upon the post-adiabatic concept and these methods can be included into all models presented here without any negative impact[23].

2.3.2 The `TEOB` waveform and Next-to-Quasi-Circular corrections

The radiation reaction force $\hat{\mathcal{F}}_\varphi$ incorporates the back reaction of the emission of GWs onto the the system. $\hat{\mathcal{F}}_\varphi$ is obtained from the summation over all available multipoles $h_{\ell m}$. These $h_{\ell m}$ are expressed through a special factorization and resummation presented originally in Ref. [81]. The explicit form of $\mathcal{F}_\varphi$ is given in Ref. [76] as

$$\hat{\mathcal{F}}_\varphi = -\frac{1}{8\pi} \sum_{l=2}^{8} \sum_{m=1}^{l} m^2 \Omega \left| (\mathcal{R}/M)\, h_{lm} \right|^2 , \tag{2.32}$$

where Ω is the frequency of h and $(\mathcal{R}/M)$ reintroduces the dependence on distance and total system mass scaled out in the definition of $h_{\ell m}$. The factorized and resummed $h_{\ell m}$ are introduced in the form presented in Refs. [76, 81, 137]. In the notation of [76], this factorization is given as

$$h_{\ell m} = h_{\ell m}^{(N,\epsilon)} \hat{S}_{\rm eff}^{(\epsilon)} \hat{h}_{\ell m}^{\rm tail} f_{\ell m} \hat{h}_{\ell m}^{\rm NQC} , \tag{2.33}$$

with ϵ denoting the parity of $\ell + m$, $h_{\ell m}^{(N,\epsilon)}$ is the Newtonian (or leading-order) contribution, $\hat{S}_{\rm eff}^{(\epsilon)}$ the effective source factor, $\hat{h}_{\ell m}^{\rm tail}$ the tail factor, $f_{\ell m}$ the residual amplitude correction and $\hat{h}_{\ell m}^{\rm NQC}$ the next-to-quasi-circular (NQC) correction factor. The explicit expressions of the individual factors of $h_{\ell m}$ form the third vessel for analytical and numerical information to be included into the `TEOB` model. The waveform is however different from both the A potential and the gyro-gravitomagnetic ratios. In both of the latter, as can be seen in Sec. 4.1.1, the function is taken to the highest available order from analytical computations (the A-potential from PN theory, while (G_S, G_{S_*}) are informed by GSF theory) and the next-to-highest-available-order term is taken to be an effective parameter that is fitted against (q, χ_1, χ_2). The factors up to $\hat{h}_{\ell m}^{\rm NQC}$ are computed within PN theory. The factor $\hat{h}_{\ell m}^{\rm NQC}$ accounts for possibly missing information of the remaining factors while simultaneously accounting for the radial radiation reaction $\hat{\mathcal{F}}_{r_*} = 0$. While $\hat{\mathcal{F}}_{r_*} = 0$ is a good approximation in the circularized inspiral, this breaks down once the binary transitions into the near-radial plunge. Therefor $\hat{h}_{\ell m}^{\rm NQC}$ explicitly depends on the radial momentum and it's derivatives [74]. This allows the generation of waveforms up till the peak of the individual multipole. Each $\hat{h}_{\ell m}^{\rm NQC}$ depends on 4 parameters that are extracted by comparison between the generated waveform and the NR waveform. While $\hat{h}_{\ell m}^{\rm NQC}$

---

[22] This choice can be easily justified by the observation that the radial motion will be very slow while the angular motion will dominate in the case of BBH system with zero eccentricity. For a model with eccentricity this needs to be then included.

[23] The post-adiabatic approach presented in Ref. [128] actually solves also another problem as it greatly reduces the evaluation time of the `TEOB` equations of motion and thus allow a full waveform to be of the order of $0.1ms$ and thus meeting the computation time requirement of GW astronomy.

is defined and can be calculated for each (ℓ, m), only $\hat{h}_{22}^{\mathrm{NQC}}$ contributes to $\hat{\mathcal{F}}_\varphi$ for all three model incarnations. Thus the accuracy and precision demands for the $(2,2)$ mode are much higher. While in principle also the NQC of any of the subdominant modes can be included into the NQC at the stage of consideration within this thesis, this has not yet been done. See Chap. 5 and references listed there for a further discussion on this topic.

The NQC factor is modeled as

$$\hat{h}_{\ell m}^{\mathrm{NQC}} = (1 + a_1^{\ell m} n_1^{\ell m} + a_2^{\ell m} n_2^{\ell m}) e^{\mathrm{i}(b_1^{\ell m} n_3^{\ell m} + b_2^{\ell m} n_4^{\ell m})} \ . \tag{2.34}$$

The coefficients $(a_1^{\ell m}, a_2^{\ell m}, b_1^{\ell m}, b_2^{\ell m})$ are determined by imposing the waveform amplitude, frequency and their derivatives around the peak of the waveform. The coefficient basis $(n_1^{\ell m}, n_2^{\ell m}, n_3^{\ell m}, n_4^{\ell m})$ is given in terms of the radial momentum and its derivatives. The NQC for the $(2,2)$ mode are introduced in Ref. [76]. Paper II expands the NQC basis $(n_1^{\ell m}, n_2^{\ell m}, n_3^{\ell m}, n_4^{\ell m})$ for `TEOBiResumMultipoles` and `TEOBiResumS_SM` to include the subdominant modes as well.

The NQC basis $(n_1^{22}, n_2^{22}, n_3^{22}, n_4^{22})$ of `TEOBResumS` is given as

$$n_1^{22} = \left(\frac{p_{r_*}}{r\Omega}\right)^2 \tag{2.35a}$$

$$n_2^{22} = \frac{(\ddot{r})^{(0)}}{r\Omega^2}, \tag{2.35b}$$

$$n_3^{22} = \frac{p_{r_*}}{r\Omega}, \tag{2.35c}$$

$$n_4^{22} = p_{r_*} r\Omega = n_1'(r\Omega)^2. \tag{2.35d}$$

The superscript (0) in the definition of n_2 refers to the evaluation of the second time derivative of r along the conservative dynamics, *i.e.* this implies that the equations of motion are used with $\mathcal{F} = 0$ imposed (see the Appendix of [82] for a discussion and motivation of this choice).

The NQC bases of the subdominant modes beyond the $(\ell, m) = (2,2)$ are modifications of the n_i^{22}. These are chosen by experience as they provided more stable and accurate results over the parameter space. The NQC basis of the $(2,1)$ mode has been chosen separately from the remaining modes as

$$n_1^{21} = n_1^{22}, \tag{2.36a}$$

$$n_2^{21} = n_1^{22}\Omega^{2/3}, \tag{2.36b}$$

$$n_3^{21} = n_3^{22}, \tag{2.36c}$$

$$n_4^{21} = n_3^{22}\Omega^{2/3}, \tag{2.36d}$$

while for all modes with $\ell \geq 3$ the basis was uniformly chosen to be

$$n_1^{\ell m} = n_1^{22}, \tag{2.37a}$$

$$n_2^{\ell m} = n_2^{22}, \tag{2.37b}$$

$$n_3^{\ell m} = n_3^{22}, \tag{2.37c}$$

$$n_4^{\ell m} = n_3^{22}\Omega^{2/3}. \tag{2.37d}$$

As the modelization of the NQC is now given it remains to describe the determination process of the NQC parameters $(a_1^{\ell m}, a_2^{\ell m}, b_1^{\ell m}, b_2^{\ell m})$. This is done by imposing $\left\{\hat{A}^{\rm NQC}_{\ell m}, \dot{\hat{A}}^{\rm NQC}_{\ell m}, \omega^{\rm NQC}_{\ell m}, \dot{\omega}^{\rm NQC}_{\ell m}\right\}$ extracted from NR onto the EOB waveforms. This generates a system of four coupled linear equations that can be solved for the NQC parameters. The superscript $^{\rm NQC}$ refers to the NQC extraction time defined below for both NR and EOB[24]. It is now necessary to point out the notation. Commonly $A_{\ell m}$ refers to the amplitude of the strain multipole $h_{\ell m}$, with $\hat{h}_{\ell m} \equiv h_{\ell m}/\nu$ being the ν rescaled waveform strain corresponding to the amplitude $\hat{A}_{\ell m}$[25]. This is different in the case of $\hat{A}^{\rm NQC}_{\ell m}$ and $\dot{\hat{A}}^{\rm NQC}_{\ell m}$ (with a slight abuse of notation), which refer to the amplitude of the Regge-Wheeler normalized strain waveform $\hat{\Psi}_{\ell m} \equiv \hat{h}_{\ell m}/\sqrt{(\ell+2)(\ell+1)\ell(\ell-1)}$ and thus $(\hat{A}^{\rm NQC}_{\ell m}, \dot{\hat{A}}^{\rm NQC}_{\ell m})$ are obtained from $\hat{A}^{\rm NQC}_{\ell m} \equiv \left|\hat{\Psi}_{\ell m}(t^{\rm NQC})\right|$.

As the NQC are meant to correct the waveform during the plunge-merger phase and allow to capture the neglected effect of the radial contribution to the radiation reaction. Therefor the NQC are extracted at the peak of the merger. However, as the derivative of the amplitude is 0 at peak it is advisable to extract them slightly after the peak. On the NR side the NQC extraction point is therefor chose to be

$$t^{\rm NR}_{{\rm NQC}_{\ell m}} = t^{\rm peak_{NR}}_{\ell m} + 2M \ , \tag{2.38}$$

where $t^{\rm peak_{NR}}_{\ell m}$ refers to the time at which $A_{\ell m}$ reaches its maximum, the peak. While for h_{22} this is a unique definition as the waveform has only a singular peak this is not necessarily the case for the subdominant modes. As can be shown from the study of perturbations around a BH, the appropriate basis for the multipole expansion around a BH is the spheroidal harmonic base (see *e.g.* Ref. [47]). This will necessarily lead to a complicated multi-peak structure in the merger-ringdown phase for the subdominant multipoles as will be discussed explicitly in chapter 5 and 6.

Moving to the `TEOB` side one finds that the determination of the time coordinate to impose the NQC is by far not as simple as for NR, as the waveform without the NQC corrections is incomplete, which is especially significant in the late inspiral-plunge phase where the NQC are meant to be imposed. To solve this problem the following approach was developed in Ref. [76] which is given as

$$t^{\rm EOB}_{{\rm NQC}_{\ell m}} = t^{\rm peak}_{\Omega_{\rm orb}} - \Delta t_{\rm NQC} + \Delta t_{\ell m} \ , \tag{2.39}$$

where $\Delta t_{\ell m}$ refers to the time shift between the peak of $h_{\ell m}$ and h_{22} given as

$$\Delta t_{\ell m} \equiv t^{\rm peak}_{\ell m} - t^{\rm mrg} \ , \tag{2.40}$$

where $t^{\rm mrg}$ is the time of merger, the peak of h_{22}, and is fitted directly to NR. $\Omega_{\rm orb}$ refers to the *pure orbital frequency* (see Eq. (100) of Ref. [76]) and is derived from Eq. (2.31a) above, as

$$\Omega_{\rm orb} \equiv \frac{1}{H_{\rm EOB}} \frac{\partial \hat{H}^{\rm eff}_{\rm orb}}{\partial p_\varphi} = \frac{p_\varphi u_c^2 A}{H_{\rm EOB} \hat{H}^{\rm eff}_{\rm orb}}, \tag{2.41}$$

where $u_c = 1/r_c$ is the inverse centrifugal radius. $\Delta t_{\rm NQC} = 1$ is set by hand. In the case of large

---

[24] Within this thesis it is common practice to denote a variable with a given superscript to refer to the variable taken at a specific time.

[25] Within discussions of the `TEOB` model this is the most common definition. Within the discussion of `TEOBiResumMultipoles` and `TEOBiResumS_SM` this notation will however be adapted to simplify the notation and will be pointed out directly.

mass-ratios and a large spins of the heavier BH χ_1, however, $\Delta t_{\rm NQC} = 4$ was needed to ensure a stable determination of the NQC which will be discussed for `TEOBResumS` explicitly (see Sec. 4.4).

With the definition of the NQC extraction time on both the NR and `TEOB` side it is now possible to set the system of four equations that allow the determination of (a_1, a_2, b_1, b_2) as

$$\hat{A}^{\rm EOB}_{\ell m}\left(t^{\rm EOB}_{{\rm NQC}_{\ell m}}\right) = \hat{A}^{\rm NR}_{\ell m}\left(t^{\rm NR}_{{\rm NQC}_{\ell m}}\right) \,, \tag{2.42a}$$

$$\dot{\hat{A}}^{\rm EOB}_{\ell m}\left(t^{\rm EOB}_{{\rm NQC}_{\ell m}}\right) = \dot{\hat{A}}^{\rm NR}_{\ell m}\left(t^{\rm NR}_{{\rm NQC}_{\ell m}}\right) \,, \tag{2.42b}$$

$$\omega^{\rm EOB}_{\ell m}\left(t^{\rm EOB}_{{\rm NQC}_{\ell m}}\right) = \omega^{\rm NR}_{\ell m}\left(t^{\rm NR}_{{\rm NQC}_{\ell m}}\right) \,, \tag{2.42c}$$

$$\dot{\omega}^{\rm EOB}_{\ell m}\left(t^{\rm EOB}_{{\rm NQC}_{\ell m}}\right) = \dot{\omega}^{\rm NR}_{\ell m}\left(t^{\rm NR}_{{\rm NQC}_{\ell m}}\right) \,. \tag{2.42d}$$

As the extraction of the NQC parameters is now defined formally, it is now necessary to elaborate the practical approach to their determination:

(i) The equations of motion are integrated while the NQC parameters are set to $(a_1^{\ell m}, a_2^{\ell m}, b_1^{\ell m}, b_2^{\ell m}) = (0,0,0,0)$. Once the full waveform is integrated and once $t^{\rm EOB}_{{\rm NQC}_{\ell m}}$ has been passed, $(a_1^{\ell m}, a_2^{\ell m}, b_1^{\ell m}, b_2^{\ell m})$ are computed.

(ii) The equations of motion are reintegrated with (a_1^{22}, a_2^{22}) taken from the previous step and the remaining ones set to zero as they have no impact on the radiation reaction. Once $t^{\rm EOB}_{{\rm NQC}_{\ell m}}$ has been passed again, $(a_1^{\ell m}, a_2^{\ell m}, b_1^{\ell m}, b_2^{\ell m})$ are computed and compared to the parameters with which the waveform has been integrated.

(iii) Step (ii) is repeated until the NQC parameters (a_1^{22}, a_2^{22}) converged. Typically, this occurs after four to five iterations at the latest. However, several very large positive spins will demand seven or more iterations.

This concludes the introduction to the `TEOB` infrastructure used for the generation of the $h_{\ell m}$ multipoles until their respective peaks. In brief summary, the `TEOB` Hamiltonian was introduced together with a list of parameters and functions that can be used to account for information from analytical approximations and numerical solutions to the Einstein Equations.

2.3.3 The full `TEOB` Hamiltonian waveform

As the full infrastructure is defined it is now useful to summarize and briefly reflect on the Hamiltonian driven model with respect to the individual building blocks, how they impact the waveform generated and how they are informed:

(i) The A-potential in the `TEOB` picture represents the dependence of the dynamics on the orbital angular momentum and depends explicitly only on ν and not directly on the spins $\chi_{1,2}$[26]. It is primarily informed by PN theory and completed through the addition of a single effective parameter. This parameter is fitted, as a function of ν, to NR and thus represents effectively the difference between the PN prediction and GR as captured within the NR framework.

---

[26] This is not fully correct in fact. A residual dependency on the spins can be introduced through a redefinition of the function in terms of the centrifugal radius. This is however only done in `TEOBResumS` and dropped later on.

The calibration of the dynamics of the orbital angular momentum is generally done in the non-spinning sector $\chi_{1,2} = 0$. The A-potential will be discussed in Sec. 4.1.1 and Sec. 5.2.1.

(ii) The gyro-gravitomagnetic ratios (G_S, G_{S_*}) are similarly given as an expansion in PN powers of v/c but obtained from GSF theory. An effective parameter is introduced to capture the missing information going beyond the GSF computation. However, there is a major difference with respect to the calibration of the A-potential to NR. The calibration of the A potential in the `TEOB`-picture si fixed by the waveforms in the non-spinning sector and thus independent of any particular form or coefficient incorporated into (G_S, G_{S_*}). This is not true for the later as the calibration of (G_S, G_{S_*}) does depend on the A potential. This will explicitly be discussed in Sec. 4.1.1.

(iii) The analytical waveform $h_{\ell m}$ is obtained from PN theory, factorized and resummed. While the factorization is strongly motivated by general physical considerations, the resummation is chosen to solely to improve the performance of the waveform model. This is generally done through comparing different resummations to NR and optimizing for the most robust agreement. The impact of the resummation can be seen for example when comparing the performance of h_{22} between `TEOBResumS` and `TEOBiResumS_SM`, where the latter utilizes an updated and improved resummation. The waveform will be discussed at several points throughout chapters 4 – 6. The discussion will however in manner aim at completeness with respect to the analytical waveform and be limited to the aspects directly impacting the work discussed in this thesis.

(iv) The NQC correction factor $\hat{h}^{\rm NQC}_{\ell m}$ is introduced to account for the constraint $\mathcal{F}_{r_*} = 0$ and limitations in the analytical waveform. The NQC parameters $(a_1^{\ell m}, a_2^{\ell m}, b_1^{\ell m}, b_2^{\ell m})$ are combined with a functional basis depending on the radial momentum and it's derivatives. The equality between `TEOB` and NR is imposed at the NQC extraction point around the peak of the multipole. This allows to obtain the NQC parameters if the NQC extraction point $\left\{\hat{A}^{\rm NQC}_{\ell m}, \dot{\hat{A}}^{\rm NQC}_{\ell m}, \omega^{\rm NQC}_{\ell m}, \dot{\omega}^{\rm NQC}_{\ell m}\right\}$ is given. The NQC parameters are then iterated upon until (a_1^{22}, a_2^{22}) converge to ensure the consistency between radiation reaction and the waveform h_{22}. In principle it is also possible to fit (a_1^{22}, a_2^{22}) so that one could use them as a suitable first-guess values giving an acceptable waveform with a single iteration. While this is in principle always possible to obtain a fit, it is quite challenging to do so over the full three dimensional parameter space (q, χ_1, χ_2). For `TEOBResumS` it was not possible to obtain such a fit as the NQC had to account for relatively large effects that have not been accounted for by the analytical waveform. Through the improved resummation it was possible to obtain such fits over the full three dimensional parameter space for `TEOBiResumS_SM`.

(v) The peak-time shift $\Delta t_{\ell m}$ is one of the necessary ingredients to determine $t^{\rm EOB}_{{\rm NQC}_{\ell m}}$ for the subdominant modes. Further, $t^{\rm EOB}_{{\rm NQC}_{\ell m}}$ marks the transition point from the Hamiltonian driven waveform to the phenomenological template waveforms. Thus, $\Delta t_{\ell m}$ gains additional importance for the subdominant modes. As it generally can be extracted from NR directly, it is fitted as such.

The discussion will now turn to the extension of the waveform beyond the peak by the introduction of a phenomenological postpeak-ringdown templates that can be fitted to NR and be attached to the `TEOB` inspiral-plunge-merger waveform obtained form integrating the equations of motion.

2.3.4 Phenomenological Merger-Ringdown waveform templates

Ref. [77] introduced an approach to fit an NR waveform from the peak onward against NR after factoring out leading order behavior of the remnant BH. This model was expanded first to a larger section of the parameter space in Refs. [83] and Paper I, while Paper II and Paper III expanded it to subdominant modes. Modified versions of this model have been adopted in Ref. [53, 70] as well. The basic setup of the model is as follows: First, the leading order QNM [47] behavior is factored out and the next-to-leading-order QNM decay time are imposed. Secondly, the factored waveform is separated into phase and amplitude which are fitted independent of each other. The reader should note that Ref. [77] is dealing exclusively with the h_{22} mode. The template about to be discussed represents the straight forward generalization to generic multipoles.

As the fit is done from the peak onward exploiting the QNM behavior of the remnant BH it is useful to define a new time coordinate τ with $\tau \geq 0$ given as a function of the time t as

$$\tau \equiv \frac{t - t_{\ell m}^{\text{peak}}}{M_{\text{BH}}} \,, \tag{2.43}$$

where M_{BH} refers to the mass-fraction of the remnant BH with respect to the total mass M. Note that τ differs for each multipole, despite this dependency not being acknowledged explicitly through a set of indices $_{\ell m}$. As all parameters used in this section need to carry these indices they are omitted. Once the fitted parameters are introduced they will be given explicitly with indices $_{\ell m}$.

Starting with the complex frequency of the fundamental QNM as $\sigma_1 \equiv \alpha_1 + \mathrm{i}\omega_1$, made up of the inverse damping time α_1 and the frequency ω_1[27], the QNM-factorized waveform $\bar{h}(\tau)$ is given as

$$\bar{h}\left(\tau\right) \equiv e^{\sigma_1 \tau + \mathrm{i}\phi_0} \hat{h}\left(\tau\right). \tag{2.44}$$

The amplitude and phase are then obtained through

$$\bar{h}(\tau) = A_{\bar{h}}(\tau) e^{\mathrm{i}\phi_{\bar{h}}(\tau)}, \tag{2.45}$$

fitted to the templates

$$A_{\bar{h}}(\tau) = c_1^A \tanh\left(c_2^A \tau + c_3^A\right) + c_4^A, \tag{2.46}$$

$$\phi_{\bar{h}}(\tau) = -c_1^\phi \ln\left(\frac{1 + c_3^\phi e^{-c_2^\phi \tau} + c_4^\phi e^{-2c_2^\phi \tau}}{1 + c_3^\phi + c_4^\phi}\right). \tag{2.47}$$

Prior to the fit five conditions are imposed. The peak ν normalized amplitude $\hat{A}^{\text{peak}}$ and frequency ω^{peak}, together with a vanishing derivative of the amplitude, are imposed at $\tau = 0$. The decay behavior of the next-to-leading-order inverse damping time are imposed on both the phase and

---

[27] This notation deviates from the more standard notation where the QNM parameters are commonly denoted as *e.g.* $\omega_{\ell mn}$. When dealing only with the $(2,2)$ mode the multipolar index is omitted. And to be consistent with prior notation with the EOB literature the fundamental QNM is denoted by 1 instead of 0. Consequently, the first overtone is denoted with 2.

amplitude. These conditions are then explicitly given as

$$c_2^A = \frac{1}{2}\alpha_{21}, \tag{2.48}$$

$$c_4^A = \hat{A}^{\rm peak} - c_1^A \tanh\left(c_3^A\right), \tag{2.49}$$

$$c_1^A = \hat{A}^{\rm peak}\alpha_1 \frac{\cosh^2\left(c_3^A\right)}{c_2^A}, \tag{2.50}$$

$$c_1^\phi = \Delta\omega \frac{1 + c_3^\phi + c_4^\phi}{c_2^\phi\left(c_3^\phi + 2c_4^\phi\right)}, \tag{2.51}$$

$$c_2^\phi = \alpha_{21}, \tag{2.52}$$

with $\Delta\omega = \omega_1 - M_{\rm BH}\omega^{\rm peak}$, and $\alpha_{21} \equiv \alpha_2 - \alpha_1$, the difference between the inverse damping times of the first overtone (α_2) and the fundamental mode (α_1). This leaves the three parameters $\left(c_3^A, c_3^\phi, c_4^\phi\right)$ free and thus can be fitted to NR. First, in a *primary* fit these parameters are extracted from NR while in a secondary *global* fit the individual *primary* fits are interpolated across (q, χ_1, χ_2). It is useful to highlight a few points:

(i) The dominant indicator of the fit performance is the accuracy of the fits capturing the peak amplitude $\hat{A}^{\rm peak}$ and frequency $\omega^{\rm peak}$. These parameters capture the peak behavior and the overall scale of the waveform. Inaccuracies of these fits will lead, if large enough, to pathological waveforms.

(ii) The QNM parameters can be fitted with high precision and accuracy against the dimensionless spin χ_f of the final BH. In practice, χ_f is obtained through the fit presented in Ref. [107], given as a function of (q, χ_1, χ_2). Thus reducing the fit-dimensionality from three to one combined with a gain in both accuracy and precision.

(iii) The effective parameters $(c_3^A, c_3^\phi, c_4^\phi)$ capture the transition from the peak to the ringdown regime. Their behavior is generally very sensitive to noise in NR waveforms used in their determination. Further, it is in many cases possible to capture the waveform accurately even with differences between *global* and *primary* fit that are similar in magnitude to the *primary*, which is not necessarily surprising as they enter the waveform non-linearly. This is however not generally true. The proper measure of their performance is accuracy and precision of the reconstructed waveform amplitude and frequency.

(iv) In some cases it will become evident that the amplitude template Eq. (2.46) is not sufficiently flexible to account for the NR behavior accurately. In particular for the extreme-mass-ratio limit and for multipoles this limitation will become evident. An improvement of the template represents a possible avenue for future work.

2.4 Thesis outline

This chapter introduced the reader to the basic concepts of GW astronomy in a strongly simplified manner to allow a definition of the quality goals of waveform model building. Starting with the two-body problem the `TEOB` framework was introduced and the focus on spin-aligned, non-eccentric

BBH systems was motivated. This chapter will now be concluded by briefly discussing Papers I – IV and outlining their results in the context of this thesis. The discussion will be focused around two major aspects important when building waveform models for GW astronomy: Firstly, completing analytically defined waveform models using NR waveform catalogs. Secondly, the validation of waveform models such that they can be used within the practical framework of GW astronomy. This discussion will then be concluded by a brief review of a non-standard application of waveform models in GW astronomy.

Paper I In Ref. [135] `TEOBResumS` is introduced. `TEOBResumS` is a full CBC waveform model for BBH, Black Hole-Neutron Star (BHNS) and Binary Neutron Star (BNS) systems. For BHNS and BNS systems the waveform is constrained to the inspiral. In the BBH sector the model generates the full h_{22}, inspiral-plunge-merger-ringdown waveform for spin-aligned binaries without eccentricity. The model is fully calibrated to NR, in all aspects of the `TEOB` setup discussed above relevant for $(\ell, m) = (2, 2)$. The NR waveform catalog used contains 135 `SXS` waveforms generated with `SpEC`, 19 waveforms obtained with `BAM` and a list of waveforms of a test-particle falling into Kerr BHs with various spins covering the interval $(-0.99, 0.999)$. The calibration of the model exploits analytically motivated spin variables to allow the effective and accurate fitting over the full (q, χ_1, χ_2) parameter space with a two-dimensional fit. Exploring the model performance with respect to the NR catalog Paper I showed that, with the exception of a single `BAM` waveform $(8, +0.85, +0.85)$[28], the model shows an excellent agreement with NR. Outside the parameter space covered by NR the robustness of the model is explored and improved to grantee a stable, non-pathological waveform all over. Several technical aspects of the model are discussed explicitly. A `C++` implementation of the code is introduced. This code is then used in an analysis of GW150914, proving the readiness of `TEOBResumS` for GW astronomy by example.

Paper II In Ref. [133] `TEOBiResumMultipoles` introduced which, similarly to `TEOBResumS`, is based on the `TEOB` infrastructure introduced above. The changes with respect to `TEOBResumS` can be seen in an updated A-potential and an improved resummation of the waveform and represents an extension of `TEOBResumS` to include all modes with $m \geq 1$ for $\ell = 2, 3, 4$ and the $(5, 5)$ mode. However, `TEOBiResumMultipoles` models the non-spinning sector exclusively. Therefor the NR catalog used in Paper I is limited to the non-spinning waveforms. These are the waveform of a test-particle falling along circularized orbits into a Schwarzschild BH together with 16 `SXS` and 3 `BAM` waveforms. Several aspects of incorporating subdominant modes are discussed and applied. This in particular includes the computation of the unfaithfulness $\bar{F}$ for the full strain h, for which the position of the detector relative to the source frame needs to be included.

Paper III In Ref. [134] `TEOBiResumS_SM` is introduced, extending a selective number of the multipoles covered by `TEOBiResumMultipoles` to the spinning sector. The `SXS` catalog is extended to include 555 waveforms of aligned-spin, non-eccentric BBH systems. The uncertainty of these waveforms is discussed and analyzed. This additionally includes an improved version of the

---

[28] The reader should note that with waveform was not used in the calibration of `TEOBResumS` as the waveform was not sufficiently stable and did not allow an accurate determination of the NQC. In Paper III with an improved resummation of the waveform and a newly generated waveform at higher resolution, one finds excellent agreement between `TEOBiResumS_SM` and this waveform.

h_{22} showing that with an improved resummation of the analytical waveform it is possible to resolve the issues that have been present in `TEOBResumS`. The subdominant modes are compared in detail to NR. A peculiar dip in the NR waveform amplitude of the $m = 1$ modes, pointed out in Ref. [70], was discussed and it was shown that the `TEOBiResumS_SM` waveform predicts and models this effect accurately.

Paper IV In Ref. [63] an alternative application of `TEOBiResumS_SM` is discussed. The article proposes a test of GR as follows: Given a GW event of a BBH, it is possible to locally reconstruct the peak of the GW waveform strain using the `BayesWave` method. A model, such as `TEOBiResumS_SM`, can then be used to fit the signal and give an alternative prediction of the peak waveform strain. The BBH signal can be fitted over the entire IMR waveform or merely over the inspiral by imposing a frequency cut-off. As `TEOBiResumS_SM` represents the waveform as predicted by GR any significant disagreement between the reconstructed peaks, given by `TEOBiResumS_SM` and the `BayesWave` method would thus be a direct violation of General Relativity. This test of GR was then applied to GW150914, showing no deviation from GR.

The foundation of using NR information to complete or validate a waveform model is an understanding of the different formats of NR waveforms and an estimate of their uncertainty. This will be the focus of Chapter 3. The `SXS` and `BAM` waveform catalogs are reviewed and summarized. The error of the `SXS` waveform catalog is explored in more detail. Several pathological aspects of NR waveforms are discussed and explored. Additionally, several aspects of waveform extraction and post-processing are discussed. This discussion covers the NR catalogs used in Papers I – III.

In Chapter 4, the discussion will turn to introducing `TEOBResumS` and its BBH sector as presented in Paper I. The discussion will focus on the NR completion of the model and performance evaluation. The robustness of the model outside the domain of calibration is estimated and methods aimed to improve that stability are presented.

Following the results and discussion of Paper II, Chapter 5 will discuss `TEOBiResumMultipoles`. The differences between the general multipolar case and the exclusive dominant mode analysis are discussed in both model calibration and validation. The comparison of `TEOBiResumMultipoles` the non-spinning waveforms used in Paper II is thus used as a case study to demonstrate the increased complexities.

Chapter 6, based on Paper III, is devoted to `TEOBiResumS_SM` and the calibration of subdominant modes in the spinning case. The discussion will cover several quantities that have been fitted to inform the waveform and compare the full NR catalog available with `TEOBiResumS_SM`. As only part of the catalog was used to inform `TEOBiResumS_SM` it is useful to explore the model outside the domain of calibration yet still covered by NR. A peculiar feature of the $m = 1$ modes, that has been observed for the $(2, 1)$ in Ref. [70] from the perspective of NR, is discussed and shown to be accurately reproduced by `TEOBiResumS_SM`. Additionally a fit of the NQC parameters (a_1^{22}, a_2^{22}) is reviewed, allowing a fast and accurate implementation of `TEOBiResumS_SM`.

Chapter 7 will focus on the test of GR presented in Paper IV and briefly review the possible prospects and future applications of it. This thesis is concluded, in Chapter 8, with a summary and discussion of the individual topics and results presented in this thesis, especially from the context of the two major topics of this thesis: (i) The completion of waveform models with NR and (ii) the validation of waveform models with NR, all focused on the aim set to use the models in the context of GW astronomy.

Chapter 3

Numerical Relativity Catalog

This chapter is devoted to the Binary Black Hole (BBH), Numerical Relativity (NR) catalog used in the following chapters and in the major publications associated with this thesis. The focus will be set on the basics needed to use NR waveforms to inform the `TEOB` infrastructure presented in the previous chapter. The waveforms have been generated with three codes. First, a set of high precision waveforms of a test particles falling into Kerr BHs along circularized orbits, generated with the code presented in Ref. [90]. Second, 555 waveforms taken from the `SXS` catalog [7], generated with SpEC [49, 59, 67, 68, 98, 111, 115–117, 126, 142]. The most recent version of the `SXS` catalog, as considered for this work, was presented in Ref. [55], covering massratios $1 \leq q \leq 10$. Third, 19 waveforms generated with the `BAM` code [101, 108, 109], with massratios $2 \leq q \leq 18$ with spin parameters $\|\chi_{1,2}| \leq 0.85$.

Several important aspects of NR waveforms are discussed in this chapter. First the format is set into context with respect to the two-body problem. Important aspects of meta-data files are reviewed. The numerical waveform extraction is discussed. Characteristic waveform parameters, already mentioned in chapter 2, are defined explicitly and put into the context of their impact on the calibration and validation of the `TEOB` waveform models.

The overall catalog of waveforms is discussed with respect to their parameter space coverage. The uncertainties of the `SXS` waveform catalog is assessed on an individual basis. Several aspects when considering subdominant modes are reviewed and discussed.

3.1 NR waveforms and data formats

Generally speaking NR[1] is based on the $3 + 1$ decomposition of the Einstein Equations (following a similar argument presented in Ref. [43]): Given the Einstein Tensor G_{ab}, the Christoffel Connection Γ^a_{bc}, the partial derivatives over time ∂_t and with respect to space ∂_i. One finds that the Bianchi Identity $\nabla_b G^{ab} = 0$, with the covariant derivative operator ∇_b, implies

$$\partial_t G^{a0} = -\partial_i G^{ai} - G^{bc}\Gamma^a_{bc} - G^{ab}\Gamma^c_{bc} \ , \tag{3.1}$$

---

[1] Here only a brief introduction will be given to illustrate the most important aspect needed for the use of NR in calibrating and validating waveform models. The reader interested in a thorough introduction to the field of NR is referred to Refs. [34, 43].

where the indices a, b, c run over the full four dimensional spacetime indices $0, 1, 2, 3$, while the indices i, j only run over the three spatial indices $1, 2, 3$. The right-hand side of eq. (3.1) has at most second order derivatives with respect to the time. Thus, it can be seen that G^{a0} has at most first order derivatives with respect to the time. This observation allows to separate the full Einstein Equations into four constraint equations as

$$G^{a0} = 8\pi T^{a0} \tag{3.2}$$

with the energy momentum tensor T^{ab}, and into six evolution equations as

$$G^{ij} = 8\pi T^{ij} \ . \tag{3.3}$$

The initial data for the NR simulation is obtained by solving eq. (3.2), for the metric tensor g_{ab} projected onto a three-dimensional, space-like hypersurface Ξ_0 and thus separated into the induced metric on Ξ_0 and a set of parameters extrinsic with respect to Ξ_0. This $3 + 1$ decomposition of the metric is then evolved with eq. (3.3) to generate a one-parameter family Ξ_t along the time-like 0 coordinate t. For each value of t the hypersurface Ξ_t is endowed with $3 + 1$ decomposition of the metric with respect to that hypersurface[2]. In the idealized case eq. (3.2) would be solved exactly and evolved without any numerical truncation error or other limitations along eq. (3.3). In such a case all parameters would be set explicitly within the initial data. However, in practice this approach is not recommendable. Commonly when a code starts evolving a set of initial data will the simulated system will undergo a transition during which it will emit a large burst of seemingly chaotic GWs leading the system to relax into a stable GR orbit. This burst of radiation is called the initial state radiation. While largely it is reasonable to assume that GWs emitted by the system are not significantly impacting the masses m_i and spins $\vec{S}_i$ of the BHs, this is not strictly true for the initial state radiation. Thus, all binary parameters that are assumed to be constant during the evolution should be extracted only once the initial state radiation has left the system.

The astute reader might have noticed a large difference between NR and analytical approximation methods. In the analytical setup it is trivial to chose the desired combination of parameters (q, χ_1, χ_2) as they are explicit variables. These are how ever not naturally defined in the context of NR which is most naturally described in terms of the family of Ξ_t and the induced $3 + 1$ decomposition of the metric onto each hypersurface. This comes with the obvious advantage that the NR waveform, if the resolutions lies in the domain of convergence, represents full GR without any need to individually model a phenomena to ensure that it is captured accurately. The downside is however that it is difficult to extract the quantities which can be defined in a very precise manner in the analytical context. One side to this are the masses and spins of the BHs. Another side is the extraction of GWs and their extrapolation to the observer. Thus the question is when and how are the relevant parameters defined. One option is the ADM formalism, reviewed in Ref. [43], can be used to compute masses and angular momenta. Several other methods are possible [3]. GWs are however more difficult as they are part of the metric, but they can be distinguished from the comparably static background through a frequency filter (see *e.g.* Ref. [119]).

---

[2] Naturally, this is a tremendously oversimplified picture of NR. As it took until 2003 for the first BBH system to be evolved for a single cycle [58]. Today, waveforms with hundreds of cycles before the merger can be evolved until the final state is reached (see *e.g.* Ref. [7]).

[3] See Ref. [7] for what is practically used in the `SXS` catalog.

Metadata While it is useful to understand these details, it is not necessary to be in a position to apply them before using NR data. Commonly all important parameters needed to use NR waveform are given in `metadata` files. In publicly available catalogs they are released with the waveform data directly (see *e.g.* the public release of the `SXS` catalog [7]). It is now useful to go over a list of parameters given in the `metadata` for `SXS` waveforms and a brief review of how they relate to the `TEOB` parameters discussed in Sec. 2.2:

(i) The identification code of BBH-NR waveforms within the `SXS` catalog commonly reads `SXS:BBH:xxxx` with the four-digit integer number *xxxx* uniquely identifying the simulation. This is in particular important as there are waveforms that have similar parameters (q, χ_1, χ_2) which differ on a more subtle level. Possible differences include the waveform length, resolutions available, version of the code used or the generation of the initial data.

(ii) The relaxation time t_0 is the time at which the initial state radiation has left the system (See e.g. Sec. 2.2.2 of [55].).

(iii) $X_i = m_i/M$: the masses of the i-th BH as fractions of the total mass M. As already pointed out the individual masses are not directly relevant as all necessary information is captured by their ratio. However, within this thesis the convention $m_1 \geq m_2$ is chosen, which is not universally used by all NR waveform catalogs. The transformation $BH_1 \leftrightarrow BH_2$ does not affect any of the physical processes involved but it is only an exact symmetry of the system if both BHs are equal in mass and spin. Thus it does create a number of sign changes for variables defined in the previous chapter (*e.g.* $X_{12} \to -X_{12}$) and for the waveform multipoles $h_{\ell m}$[4]. Typically, the `metadata` file contains several masses for each BH which do not necessarily agree. In line with previous discussion in this chapter it is recommended to use quantities that are defined at or around t_0.

(iv) $\vec{\chi}_i$ or $\vec{S}_i/M^2$: the dimensionless or dimensionful (normalized to the total mass of the BBH system M) spin vector of the i-th BH[5]. Their relation is given as $m_i^2\vec{\chi}_i/M^2 = \vec{S}_i/M^2$. Recall that within this thesis the focus is exclusively onto BBH systems with spins parallel to the orbital angular momentum[6]. Within this thesis the spins extracted at the relaxation time $t = t_0$ are used. In the previous chapter the spin variable χ_i was introduced, which can also be expressed as $\chi_i = |\vec{\chi}_i|$.

(v) The eccentricity ε. Following the discussion in Sec. 2.2 it is reasonable to assume that all astrophysical binaries have been circularized through the emission of GWs, thus motivating to primarily focus on the case of $\varepsilon = 0$. This is however rarely achieved exactly in NR simulations. Therefor an upper bound on the eccentricity has to be chosen. Within this thesis the exclusion bound for a waveform was set around $\varepsilon \sim 5 \times 10^{-3}$.

---

[4] Both BHs are confined to the $z = 0$ plane and therefor the rotation $\phi \to \phi + \pi$ would be equivalent to $BH_1 \leftrightarrow BH_2$ in their effect on the $h_{\ell m}$. Following from eq. (2.4) – (2.5) the multipoles would transform as $h_{\ell m} \to (-1)^m h_{\ell m}$.

[5] The reader should note that the coordinate system chosen in this work naturally agrees with the `SXS` catalog [7], this convention is however not uniform among all NR catalogs by default. Therefor care must be taken when extracting information of the spin from a given `metadata` file. Further, if the BH masses have been interchanged to ensure $m_1 \geq m_2$ then this must be done for the spins as well.

[6] See the discussion in Sec. 2.2 for the motivation.

(vi) $(M_{\mathrm{BH}}, \vec{\chi}_f)$: The mass and spin of the remnant BH, the final state of the BBH evolution as described in Sec. 2.2, normalized to the total mass M. These parameters are particularly impactful in the description of the phenomenological *merger-ringdown* waveform as they determine the time-scale and dominant frequency and damping time of the *ringdown* part of the signal.

Waveform extraction From the perspective of BBH waveform model building the most important output of NR simulations are the GW strain polarizations $h_{+,\times}$, which defined through their effect on the metric as introduced in chapter 2. From them it is possible to construct the complex GW strain $h = h_+ - ih_\times$ which can be split into $h_{\ell m}$ following eq. (2.4). In practice it is quite complicated to separate h from the background metric. Most methods rely on the fact that it is possible to *e.g.* separate the slowly changing background from the rapidly moving GW strain[7]. For test-particle waveforms h is computed directly, either through high level analytical approximations or through the fact that the background Kerr metric is known exactly. `BAM` waveforms are extracted at several radii [101, 108, 109]. When comparing different extractions of waveforms it is important that if the waveform is extracted too close to the center of mass the waveform will show large systematic error since it could not be accurately separated from the background. If the extraction radius is too large the waveform will show finite-size effects from reflections off the boundary. The `SXS` catalog provides the waveform extracted at the outer-most-extraction-radius as well, but also waveforms that have been extracted at finite radius and extrapolated with polynomials of different order to future null infinity[8]. The extracted GW signal is fitted over several radii as a polynomial of the inverse radial distance to the source $1/\mathcal{R}$. The polynomial order is designated by $N = 1, 2, 3, 4$. As the extraction of the GW signal already has factored out the leading order radial dependence $1/\mathcal{R}$ it is easy to see that only the constant polynomial term survives at future null infinity [7, 55]. The $(2, 2)$ mode is taken with $N = 3$ extrapolation if no other modes are included in the particular computation. Otherwise all modes are extrapolated with $N = 2$. This choice and the motivation for it will be discussed below in Sec. 3.4.

Characteristic parameters Before turning to the catalog itself it is useful to define on the NR side explicitly several parameters that are used in the calibration and validation of `TEOB` models.

(i) $\hat{A}_{\ell m} \equiv A_{\ell m}/\nu$: The amplitude of the (ℓ, m) mode, scaled with the symmetric mass-ratio.

(ii) $t^{\mathrm{peak}}_{\ell m}$: The time of the peak of $\hat{A}_{\ell m}$ given as $\hat{A}_{\ell m}\left(t = t^{\mathrm{peak}}_{\ell m}\right) = max\left[\hat{A}_{\ell m}\right]$. In this thesis the notation $(..)^{\mathrm{peak}}_{\ell m} \equiv (..)_{\ell m}\left(t = t^{\mathrm{peak}}_{\ell m}\right)$ will be used frequently. Especially, the amplitude and frequency at the peaks of the individual multipoles are important in fitting the phenomenological *merger-ringdown* templates.

(iii) $t^{\mathrm{mrg}} \equiv t^{\mathrm{peak}}_{22}$: Within `TEOB` literature the merger is often given a slightly dual meaning. On the one hand it refers generally to the phase in which the two BHs merge to form the final BH. On the other hand if it is used to refer to a concrete time it refers to the peak of the

---

[7] see chapter 1 of Ref. [119] for a general discussion, while a more technical introduction for applications in NR can be found in Section 9.4 of Ref. [43]. For details of the GW extraction used for a specific code it is always necessary to refer to the code documentation or the article introducing the catalog, which for the `SXS` catalog can be found in Refs. [7, 55].

[8] See *e.g.* chapter 11 of Ref. [151] for a definition.

dominant $(2, 2)$ mode, $t^{\rm mrg}$. Similar to the peak-time a superscript is used to simplify notation as $(..)^{\rm mrg} \equiv (..)\,(t = t^{\rm mrg})$.

(iv) $\Delta t_{\ell m} \equiv t^{\rm peak}_{\ell m} - t^{\rm mrg}$: The relative time shift of the peak of the (ℓ, m) mode with respect to the merger. As was discussed in Sec.2.3.2, $\Delta t_{\ell m}$ is used in imposing the NQC and thus indirectly ensures that the relative position of the amplitude peaks agree with NR.

(v) $N_{\rm orb}$: The number of orbits the system goes through between $t = t_0$ and $t_{\rm mrg}$. Even though $N_{\rm orb}$, with slightly different definition, is given in most cases as the part of the `metadata`, it is useful to have a universal definition that can ba applied to an arbitrary waveform. Formally, $N_{\rm orb} = |\phi^{\rm mrg}_{22} - \phi_{22}(t = t_0)|/(4\pi)$, with $\phi_{\ell m}$ defined in Sec. 2.1, is used in this thesis.

(vi) $\delta\phi^{\rm NR}_{{\rm mrg}_{\ell m}} \equiv (\phi^{\rm mrg}_{\ell m} - \phi_{\ell m}(t = t_0))_{\rm LevH} - (\phi^{\rm mrg}_{\ell m} - \phi_{\ell m}(t = t_0))_{\rm LevM}$: The accumulated phase difference at merger between the highest resolution LevH and the second highest resolution LevM, computed for $(\ell, m) = (2, 2)$ for all `SXS` waveforms for which a second resolution is publicly available.

(vii) $\bar{F}_{\rm LevH/LevM}$: The $(\ell, m) = (2, 2)$ NR/NR unfaithfulness, defined in eq. (A.12). Computed for all `SXS` waveforms for which a second resolution is publicly available. A thorough discussion of $\bar{F}_{\rm LevH/LevM}$ over the `SXS` catalog is given in below in Sec. 3.3.1.

In case of possible confusion the superscript $^{\rm NR}$ or $^{\rm EOB}$ will be added to clarify the notation. In cases in which it is assumed to be clear the superscript will be dropped to simplify the notation.

3.2 Catalog overview

The discussion will now turn to the catalog of NR waveforms used in this work and the parameter space covered by the different sub catalogs. Within this work 555 `SXS` [55][9] and 19 `BAM` [101, 108, 109] waveforms merging BBH systems of comparable masses, aligned spins and with small eccentricity are used. Additionally, a set of test-particle waveforms is used, which describe a test-particle falling into a Kerr BH along circularized orbits [90]. These have been generated with dimensionless spin parameters of the central Kerr BH χ_1 going from -0.99 up to 0.999. The reader should note that the sign of χ_1 represents the relative alignment with the orbital angular momentum. The full catalog of `SXS` and `BAM` waveforms is summarized in Tab. 3.1. The NR waveform catalog has been separated into two sets. The *Calibration* and *Validation* set primarily used as their name implies in the building of `TEOB` waveform models[10].

Calibration set The *Calibration* set consists of 135 `SXS` and all 19 `BAM` waveforms. These waveforms have been used to inform all three models: `TEOBResumS`, `TEOBiResumMultipoles` and `TEOBiResumS_SM`. The 135 `SXS` waveforms consist of (i) 19 non-spinning (Tab. F.14), (ii) 38 spinning, equal-mass (Tab. F.1) and (iii) 78 spinning, unequal mass BBH waveforms (Tab. F.2 – F.3).

---

[9] The reader should note that the publicly available `SXS` catalog contains many more waveforms. However, the ones presented here are all the waveforms with BH spins parallel to the orbital angular momentum and sufficiently small eccentricity.

[10] The reader should note that the TP waveforms are excluded from these considerations as they have been used solely to inform the model and stabilize the extrapolation to large mass-ratios. Nonetheless, the waveforms lie outside the domain of validity of all waveform models discussed in this work.

	Parameter interval ranges		Waveform count #		$\langle N_{\mathrm{orb}}\rangle$	$\bar{F}_{\mathrm{LevH/LevM}}$	
	$q \equiv m_1/m_2$	$\chi_{1,2}$	total	with LevM		$\bar{F}^{\max}_{\mathrm{NR/NR}}$	$\langle \bar{F}^{\max}_{\mathrm{NR/NR}}\rangle$
Calibration set							
`SXS`	$[1.0,\ 10.0]$	0	19	18	21.98	0.075%	0.0092%
	$[1.0,\ 1.0]$	$[-0.95, 0.9942]$	38	37	22.77	0.22%	0.020%
	$[1.3,\ 8.0]$	$[-0.9, 0.96]$	78	73	25.09	0.11%	0.0088%
`BAM`	$[4.0,\ 18.0]$	0	3	–	8.11	$< 0.1\%$	$< 0.1\%$
	$[2.0,\ 18.0]$	$[-0.85, 0.85]$	16	–	11.13	$< 0.1\%$	$< 0.1\%$
Validation set							
`SXS`	$[1.0,\ 10.0]$	0	61	46	24.99	0.066%	0.0051%
	$[1.0,\ 1.16]$	$[-0.97, 0.998]$	79	77	20.29	0.0093%	0.0029%
	$[1.17,\ 8.0]$	$[-0.9, 0.95]$	275	254	20.07	0.056%	0.0052%
long `SXS`	$[1.41,\ 1.83]$	$[-0.5, 0.5]$	5	5	144.05	1.52%	0.98%

Table 3.1: This table lists the sub-catalogs of NR data from both `SXS` and `BAM` catalog. From left to right, the columns report: origin; interval of parameters covered for the mass ratio q and the spins $\chi_{1,2}$; total number of waveforms in the particular sub-catalog; the number of `SXS` data with a second resolution LevM available; the average waveform length expressed in number of orbits, $\langle N_{\mathrm{orb}}\rangle$, counted here between the relaxation time (i.e., after the initial-state radiation) and the waveform amplitude peak; the absolute maximum $\bar{F}^{\max}_{\mathrm{NR/NR}}$ and the average of the individual maxima $\langle \bar{F}^{\max}_{\mathrm{NR/NR}}\rangle$ of the unfaithfulness $\bar{F}_{\mathrm{NR/NR}}$ computed between the highest, LevH, and second highest, LevM, resolutions. See section 3.3.1 for further discussion of the unfaithfulness.

For all three sets sufficiently many waveforms have been published with at least one additional resolution. Thus, it is possible to infer the accuracy of the waveforms that have been published without a second resolution. See Sec. 3.3 for the presentation and discussion of the uncertainty estimation. The 19 non-spinning waveforms cover mass-ratios $1 \leq q \leq 10$. The 38 equal-mass BBH have spins $-0.95 \leq \chi_{1,2} \leq +0.9942$. The 78 spinning, unequal-mass BBH waveforms contain in particular three waveforms with highly relativistic spins: `SXS:BBH:0306` $(1.3, +0.96, -0.9)$; `SXS:BBH:0208` $(5, -0.9, 0)$; and `SXS:BBH:1375` $(8, -0.9, 0)$. The spin range for $q = 2$ and $q = 3$ is very well covered with spins $-0.87 \leq \chi_{1,2} \leq 0.87$. For mass-ratios $3 < q \leq 8$ the spins remain in the range $-0.6 \leq \chi_{1,2} \leq 0.6$. The `BAM` waveforms consist of three non-spinning BBH systems, with mass-ratios $q = 4,\ 10$ and 18, and 16 spinning BBH systems. The latter contain five waveforms with large mass-ratios and highly relativistic spins: $(8, +0.85, +0.85)$, $(8, +0.8, 0)$,$(8, -0.85, -0.85)$,$(18, +0.8, 0)$ and $(18, -0.8, 0)$, thus extending the parameter space, complementing the `SXS` sub-catalogs above.

Validation set The *Validation* set consists of 420 `SXS` waveforms that have been made publicly available with Ref. [55]. These include 61 non-spinning waveforms with mass-ratios $1 \leq q \leq 10$ (Tab. F.14 – F.15), refining the coverage of this region given in the *Calibration* set. Of the remaining 359 waveforms five have a very long inspiral with an average of 144.05 cycles. While the waveforms in the *Calibration* set have been almost exclusively waveforms with integer or half-integer mass-ratios, this is no longer the case for these waveforms. The waveforms have been separated into two groups as $\nu > 0.2485$ and $\nu \leq 0.2485$ which corresponds approximately to $q < 1.17$ and $q \geq 1.17$. This split is motivated by the fact that while the $q = 1$ can be modeled very well, in practice however it is used very rarely or almost never. On the other hand waveforms with a mass-ratio approximately equal one are used very often, thus it is useful to treat waveforms with $\nu > 0.2485$ from a modeling perspective as equal mass. The set of approximately, equal-mass BBH waveforms contains 79 waveforms and extends the the range of spins covered to $-0.97 \leq \chi_{1,2} \leq +0.998$ (Tab. F.5 – F.6). The remaining waveforms cover the spin range $-0.9 \leq \chi_{1,2} \leq +0.95$ and go up to mass-ratios $q = 8 \;\Leftrightarrow\; \nu = 8/81$ (Tab. F.7 – F.12)[11].

3.3 Estimating NR uncertainties: `SXS` catalog

When comparing waveform models to NR it is important to have an estimate of NR uncertainties. Several possible sources of uncertainty for NR waveforms can be relevant. (i) Finite-Resolution; (ii) Waveform extraction; And (iii) systematic errors. As there exist several methods of waveform extraction these can be compared to limit any uncertainty due to the extraction method. Systematic errors can be limited by comparing waveforms generated by different codes. For NR-codes build upon finite difference methods it is possible to do a convergence study and extrapolate observable quantities to infinite resolution. However, even for the simplest of NR simulations a full convergence study would be too inefficient with respect to computing resources. Two possible routes to minimize the uncertainty exist under such circumstances. First, conservative estimates can be made from studying differences between two waveforms with sufficiently high resolution. Second, if comparing NR waveforms, generated with different codes, gives a good agreement it is reasonable to assume that the waveform is physical as it is unlikely that different errors would be similar in effect to each other and produce such an agreement. Within this work the discussion will focus on the former solution and consider the differences between the highest, available resolutions, while the using partially the latter option as well through the inclusion of a second catalog with slightly overlapping parameter space coverage.

`BAM` waveform uncertainties have been studied and analyzed in the publishing article [109]. Based upon the analysis presented there a conservative estimate on the uncertainty is that an unfaithfulness larger then 0.5% is a meaningful disagreement to the NR waveform. Similarly, uncertainties of the Test-Particle waveforms are discussed in Ref. [90]. As uncertainties of the Test-Particle waveforms are orders of magnitude smaller then those of `SXS` and `BAM` waveform they can be neglected within this work.

With the most recent update to the `SXS` catalog Ref. [55] an updated discussion of the unfaithfulness between the two highest levels of resolution has been presented. As `SXS` waveforms are generated with `SpEC`, a spectral code, it is not possible to directly determine a convergence order between two different levels of resolution. Further, due to the adaptive refinement used in `SpEC` it might be the case that the two highest levels of resolution for a given waveform are very close, while others might be very far apart. Nonetheless, differences between the two highest levels of resolution can be used as a conservative estimate on the uncertainty.

3.3.1 `SXS` catalog: NR-NR mismatch

We will now review the computation of the $(2,2)$ mode $\bar{F}^{\rm max}_{\rm NR/NR}$ for the 510 `SXS` waveforms for which a second resolution exists. The unfaithfulness was introduced in Sec. 2.1 and further technical

---

[11] The reader should note that the validation set as presented and discussed in Paper III contained additional 40 waveforms, for which the spin of the secondary BH had a non-zero component transverse to the orbital angular momentum. All affected figures and numbers have been redone. The results and discussion presented in this thesis remain unaffected by this error.

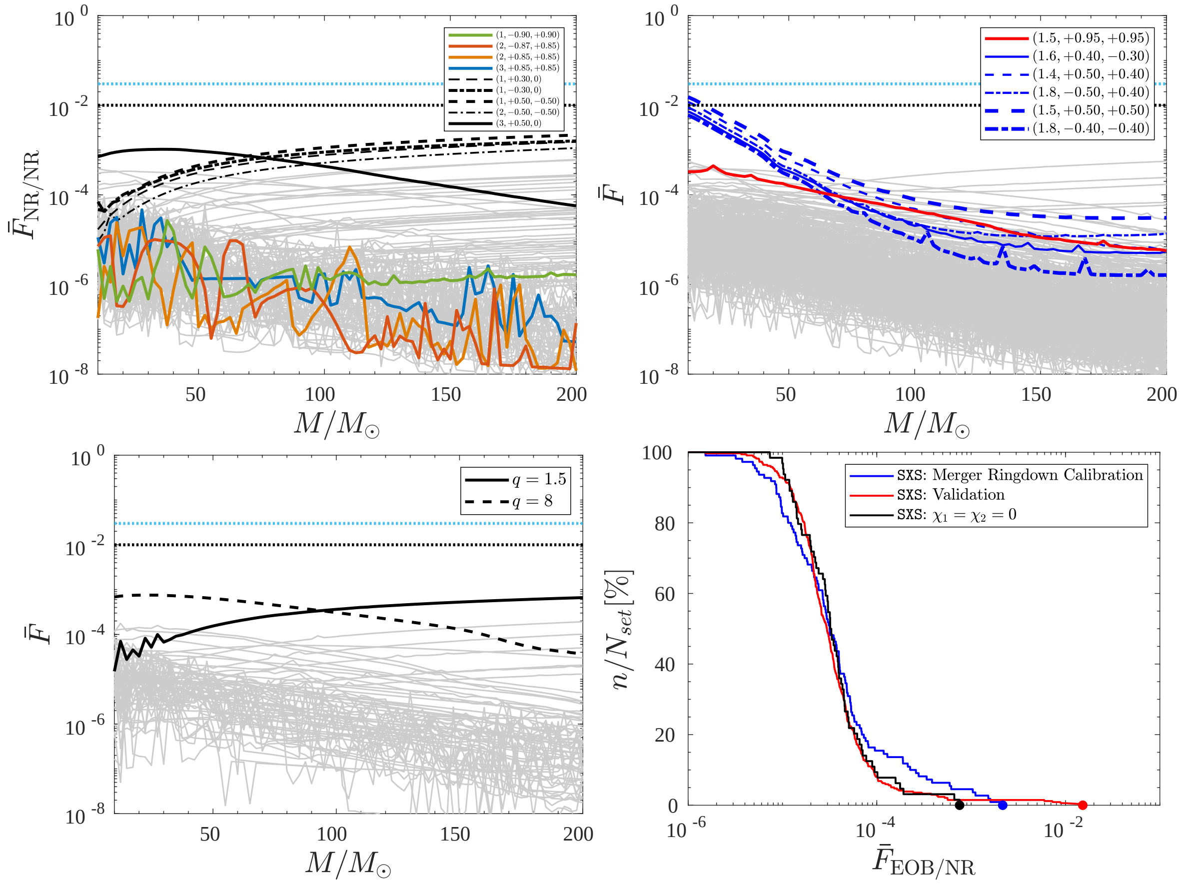

Figure 3.1: NR/NR unfaithfulness uncertainty computed from Eq. (A.12) between the highest and next to highest resolution for each `SXS` waveform for which the second highest resolution is available. (Top left) The spinning-sector of the *calibration* set. The 110 spinning waveforms used to inform `TEOBResumS` and `TEOBiResumS_SM`. (Top right) The spinning-sector of the *validation* set. 336 spinning datasets released and discussed in Ref. [55] and used in Paper III. (Bottom left) The combined non-spinning sector of both the *calibration* and *validation* set. 64 waveforms for which a second resolution is available. (Bottom right) The global summary of $\bar{F}^{\rm max}_{\rm NR/NR}$ for all 510 `SXS` BBH-NR simulations for which a secondary resolution is available. The fraction (expressed in %) $n/N_{\rm set}$ compared for each value of $\bar{F}$, where n gives the number of waveforms for which $\bar{F}^{\rm max}_{\rm NR/NR} \geq \bar{F}$ holds, divided by the total number of waveforms given with a second resolution $N_{\rm set}$. The PSD used in this computation was presented in Ref. [11]. The unfaithfulness was always computed over the maximum frequency range for which the individual NR waveforms are free of systematic features and have a reasonably large amplitude (typically once the amplitude falls 3 orders of magnitude with respect to the peak the waveform is cut.).

details are given in Appendix A. The computation results are shown in Fig. 3.1. The top-left panel shows the *Calibration* sets spinning sector. In black are highlighted the waveforms which reach an unfaithfulness of at least 10^{-3}. The waveforms marked in color represent four particularly interesting cases from the perspective of waveform model building. All four show highly relativistic spins and probe two important aspects of waveform phenomenology. Large spins both aligned with the angular momentum or anti-aligned relative to each other. This convention has already been adopted in Paper I. The top-right shows the *Validations* sets spinning waveforms. For all waveforms $\bar{F}^{\rm max}_{\rm NR/NR}$ never exceeds 10^{-3} with the exception of 5 waveforms an average length of 144.05 orbits before merger. For system masses of approximately $50M_\odot$ and below they show a very large $\bar{F}^{\rm max}_{\rm NR/NR}$

up to and above the 1% mark[12]. The bottom-left panel shows the non-spinning waveforms of both *Calibration* and *Validation* set. Only two waveforms ever reach values of $\bar{F}^{\rm max}_{\rm NR/NR} \sim 10^{-3}$ and are marked in black. The bottom-right panel shows as summary the cumulative curves corresponding to the three previous plots. The plot shows the fraction (expressed in %) $n/N_{\rm set}$, where $N_{\rm set}$ is the total number of waveforms in a given NR-waveform set and n is the number of waveforms, in the same set, that, given a value $\bar{F}$, have $\bar{F}^{\rm max}_{\rm NR/NR} \geq \bar{F}$. As can be seen the majority of waveforms reach $\bar{F}^{\rm max}_{\rm NR/NR} < 10^{-4}$. Only a few waveforms reach $\bar{F}^{\rm max}_{\rm NR/NR} > 10^{-3}$. Summarizing these results one can make an estimate of the uncertainty for the `SXS` catalog. To remain very conservative the uncertainty of $\bar{F}$ is estimated to be globally at the 0.5% level. This choice is made to prevent over fitting of the NR-informed parameters, although it will be seen that very often a much better EOB/NR agreement arises naturally.

All `SXS` waveforms have been given with all multipoles up to and including $\ell = 8$. The analysis of the NR-NR unfaithfulness of subdominant modes was however omitted within this work. The `SXS` collaboration recommends as a general rule of thumb that any mode with an amplitude of less then 10^{-5} of the dominant $\ell = m = 2$ mode should not be trusted [7].

Alternatively, there are some ways to gain a non-quantitative impression of the uncertainty. As mentioned above the comparison with waveforms obtained from different codes is an option as it is unlikely that their respective errors produce quantitatively comparable effects. Once a waveform model is sufficiently calibrated, and in some cases such as the very early *inspiral* even without explicit calibration to NR, can be used to indicate errors on a qualitative level as will be demonstrated below. Lastly, a comparison of waveforms with similar spins and mass-ratios can be used based on the principle that small changes in (q, χ_1, χ_2) should correspond to small changes in $h_{\ell m}$.

3.4 `SXS` waveform extraction of subdominant modes

The `SXS` h_{22} multipolar waveforms have been extrapolated with $N = 3$ for all applications within this thesis. In Paper I and Paper III no issues arose and no unphysical phenomena have shown up during any analysis of the `SXS` data. In Paper II, however a peculiar effect was discovered. As the bottom panel of Fig. 3.2 shows[13], the unfaithfulness (maximized with respect to the observer position (ι, ϕ)) between `TEOBiResumMultipoles` and the `SXS` waveforms consistently increased for larger masses if the waveforms were nearly-equal-mass. Fig. 3.2 illustrates these issues further. In the top-panel $N = 2$ and $N = 3$ extrapolation are compared for `SXS:BBH:0194`, $q = 1.518$ waveform, demonstrating that the $N = 3$ extrapolation of Ψ_{44} indeed shows a noticeable offset relative to the $N = 2$ extrapolation and `TEOBiResumMultipoles`. Additionally, noticeable is that the bottom panel shows that the effect of the extrapolation is almost negligible once the mass-ratio is sufficiently large.

This effect was pointed out already in previous works. Ref. [70] noted that the $N = 3$ extrapolation does indeed introduce pathological features into the waveform. When the waveform extrapolation method was introduced in Ref. [54] it was pointed out that an ill-chosen polynomial order N can introduce pathological features into the waveform. Lower orders N are advisable in

---

[12] The interested reader is referred to Sec. III C and Sec. IV A of Paper III where a brief discussion is given individually and in reference to `TEOBiResumS_SM`.

[13] This analysis was carried out by Geraint Pratten.

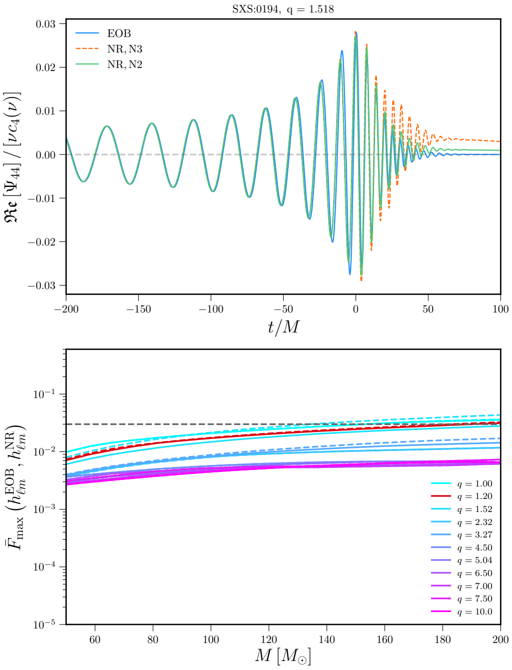

Figure 3.2: The fully calibrated `TEOBiResumMultipoles` can be used to understand phenomenological issues in the SXS-NR waveforms. Following the discussion in the main text it is useful to demonstrate the pathological features introduced into the waveform for near-equal-mass waveforms. The top panel shows a comparison on the level of the real part of $\Psi_{44}/\nu c_4(\nu)$, the RWZ-normalized waveform, between `TEOBiResumMultipoles`(solid blue) and `SXS:BBH:0194`, a $q = 1.518$ waveform, where $c_4(\nu) = 1 - 3\nu$. `SXS:BBH:0194` is given extrapolated with $N = 3$ (dashed orange) and $N = 2$ (solid green). While $N = 2$ and `TEOBiResumMultipoles` show a good agreement, the $N = 3$ extrapolation shows a systematic offset relative to `TEOBiResumMultipoles` and $N = 2$. The bottom panel shows $\bar{F}_{\rm EOB/NR}$ between `TEOBiResumMultipoles` and several SXS waveforms extrapolated with $N = 2$ (solid) and $N = 3$ (dashed). While for near-equal-mass waveforms the choice of N clearly shows an impact, this effect decreases as q increases and for the largest values of $q = 10$ is almost imperceptive.

for the merger and ringdown phase, while larger orders of N are recommended for the study of the inspiral. Therefor $N = 2$ was chosen for the study of subdominant modes, similar to Ref. [70].

The reader should note that while the angular dependence for which the worst cases is achieved is not explicitly stated in Fig. 3.2, for most waveforms it is the near-edge-on case for which the contribution of the $(2, 2)$ mode is minimal. Further, it is useful to recall that under the exchange of the two BHs the waveforms transform as $h_{\ell m} \Leftrightarrow (-1)^m h_{\ell,-m}$. In the equal-mass case one finds however that the exchange of the two BHs is an exact symmetry of the system, implying all multipoles with odd m vanish in the equal-mass (equal-spin as well, generally speaking) case exactly. The leading order Newtonian factor, stated explicitly in Sec. 5.2.3, indicates further that m odd modes smoothly approach zero as they approach the equal-mass case and only develop meaningfully once ν is sufficiently away from the equal-mass case. Thus, as the $(4, 4)$ mode is at least the third most dominant mode in the nearly-equal-mass case it seems only natural that any issue in the NR or `TEOB` waveform would become more important as the equal-mass-case is approached. The discussion on possible future improvements with this regard are left to chapter 5 and 8.

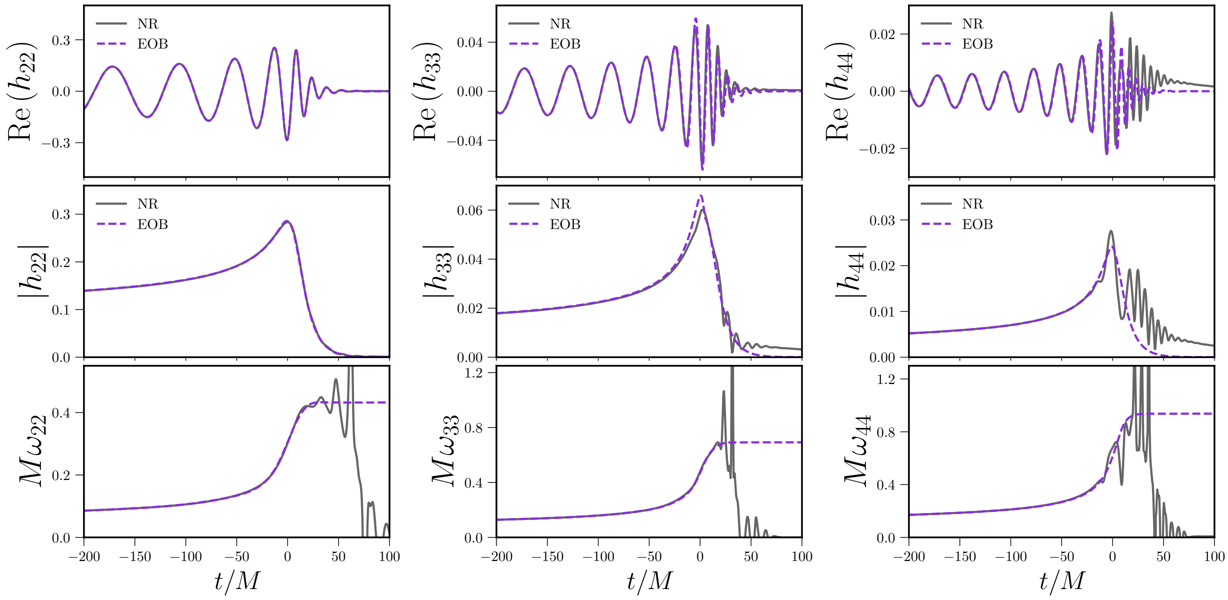

Figure 3.3: A comparison of `SXS:BBH:0039`(solid black), $(3, -0.5, 0)$, compared to `TEOBiResumS_SM` (dashed purple). The waveform was extracted with $N = 2$. From top to bottom the rows show the strain $h_{\ell m}$, the strain amplitude $A_{\ell m}$ and the frequency $M\omega_{\ell m}$ (where the scale given by the total mass is left explicit). From left to right the columns show the $(2, 2)$, $(3, 3)$ and $(4, 4)$ modes. As can be seen both the $(2, 2)$ and $(3, 3)$ mode show a reasonable agreement between NR and `TEOBiResumS_SM`. The $(4, 4)$ mode shows clear unphysical behavior for both A_{44} and $M\omega_{44}$ around the peak of the mode. A_{44} shows strong unphysical oscillations around it's peak, coinciding with similarly pathological features in $M\omega_{44}$. Thus, it can be assumed that any unfaithfulness computation that would involve h_{44} would likely not lead to any insight that could be useful in improving or validating a waveform model.

3.5 Pathological behavior of subdominant modes

As the $(4, 4)$ mode can impact the unfaithfulness significant through pathological effects in the non-spinning sector it was only prudent to continue the search for possible pathological issues in the spinning sector as well. Following the discussion of Paper II and III, the spinning sector similarly explored looking for numerical noise and systematics in the NR data that can lead to a degradation in the mismatches. As will be discussed in Chapter 6 thoroughly (see Fig. 6.8),the worst-case unfaithfulness are typically found near edge-on cases, for which the contribution of the $(2, 2)$-mode are minimized. Especially, for mass ratios near $q \sim 1$, where the odd-m multipoles are suppressed. As mentioned above in these cases the most dominant contribution to the waveform are the $(4, 4)$ and the $(3, 2)$ mode. However, Fig. 3.3 demonstrates by example that the $(4, 4)$ mode of many NR datasets can often show pathological behaviors, especially when focusing in on the *merger-ringdown* segment of the waveform. In particular, general theory predicts that the frequency of the $(4, 4)$ mode should increase monotonically, yet it oscillates strongly around it peak of the waveform. Similarly in the amplitude un-physical, non-monotonic features can be made out. These effects are sufficient to cause large unfaithfulness that cannot be used to indicate any quality issues within any waveform model calibrated to this data. To minimize these issues waveforms that show pathological features similar to Fig. 3.3 are discarded.

3.5.1 Extracting derivatives of subdominant modes from NR

For the $(2,2)$ mode, the waveform and all derivatives are sufficiently clean to determine all quantities and achieve a sufficient performance all over the parameter space. For the subdominant modes, as demonstrated above, this is not necessarily always the case. Thus, all individual points of the waveform $h_{\ell m}$, *e.g.* $A_{\ell m}^{\mathrm{peak}}$ and $\omega_{\ell m}^{\mathrm{peak}}$, are extracted with the `MATLAB` function `spline`. When the noise becomes too large to obtain an accurate numerical derivative the `MATLAB` function `smooth` is used to employ a Savitzky-Golay filter with a third degree polynomial to the data starting at $h_{\ell m}$ and all subsequently derived quantities until the target quantity is sufficiently smooth to obtain an accurately extracted data point. This process has however the danger that it could lead to unphysical data that might potentially heavily influenced by the filtering process. Thus, the filter parameters are applied conservatively with a focus to only reduce noise in the derivative without impacting the underlying functional form.

Chapter 4

The dominant $(2, 2)$ mode: `TEOBResumS`

The Effective-One-Body (EOB) approach to the general relativistic two-body problem was first introduced by Thibault Damour *et al.* [60, 61, 71, 78]. At its core the EOB represents a resummation of relative PN dynamics of two coalescing point masses. This resummation is marked by stability and reliability even in the strong-field, high-velocity regime and, thus, can be used to model CBC events up to merger. Several models to generate Gravitational Waveforms for CBC events have been developed with the help of EOB methods and formalism. The three most prominent families of models that came from this are the `TEOB`-series, which is the focus of this thesis, and the `SEOBNR`-series [38, 53, 70, 121, 136]. Additionally, the `IMRPhenom`-series [86, 87, 108–110, 114] uses EOB waveforms for calibration to improve the inspiral.

In chapter 2, two important topics have been discussed. First, for a model to be used in GWA it is necessary that it reproduces $h_{\ell m}$, or h to be more precise, with an unfaithfulness, with respect to a given target catalog of NR waveforms, that should never exceed 3% and ideally stay below 1%. Secondly, the introduction to the `TEOB` model infrastructure was given, including the definition of different vessels that able to hold analytical information from PN, GSF or PM theory. Chapter 3, discussed the full NR waveform catalog available in this work. Within this chapter it will be sufficient to focus the discussion on the *calibration* set. With this understanding of the previous two chapters it is now possible to discuss the calibration and validation of `TEOBResumS`. `TEOBResumS` was introduced in Paper I and is a model focused on the $(\ell, m) = (2, 2)$ mode. Thus, it is in fact the simplest model that will be discussed in this thesis from the point of view of NR calibration. Several of the methods used in the NR completion of `TEOBResumS` are general to the `TEOB` infrastructure. Thus, both `TEOBiResumMultipoles` (Chapter 5) and `TEOBiResumS_SM` (Chapter 6) will expand on these methods only in a limited manner, but rather focus on important details.

4.1 `TEOBResumS` Hamiltonian and waveform

Starting from the `TEOB` infrastructure set up in Sec. 2.3 three main choices must be made. First, the A-potential must be chosen. Second, the gyro-gravitomagnetic ratios (G_S, G_{S_*}) have to be chosen. Third, the resummed and factorized waveform must be specified. Both the A-potential and (G_S, G_{S_*}) are discussed in detail in Sec. 4.1.1, including the introduction of effective PN parameter capable of capturing missing information through fitting GR.

The factorized[1] and resummed was is taken from Refs. [76, 81, 137]. The waveform is often referred to not just as $h_{\ell m}$ but also through the Regge-Wheeler-Zerilli (RWZ) normalization $\Psi_{lm} = (\mathcal{R}/M)h_{lm}/\sqrt{(l+2)(l+1)l(l-1)}$. Within this chapter the notation of $\hat{(\ldots)} = (\ldots)/\nu$ is used at several points for $h_{\ell m}$, Ψ_{lm} and $A_{\ell m}$.

4.1.1 EOB potentials and gyro-gravitomagnetic functions

The EOB potentials A and B, and the gyro-gravitomagnetic functions G_S and G_{S_*} are informed by state-of-the-art PN and GSF computations[2]. The A-function as computed by PN theory is given as

$$A^{PN}_{orb}(u_c,\nu) = 1 - 2u_c + 2\nu u_c^3 + \nu a_4 u_c^4 + \nu\left(a_5^c + a_5^{\log}\right)u_c^5 + \nu\left(a_6^c + a_6^{\log}\right)u_c^6 \tag{4.1}$$

with $a_4 = \frac{94}{3} - \frac{41}{32}\pi^2$ [78, 79]. The logarithmic coefficients are known from analytical computations [41, 42, 52, 72] as

$$a_5^{\log} = \frac{64}{5}, \qquad a_6^{\log} = -\frac{7004}{105} - \frac{144}{5}\nu. \tag{4.2}$$

Similar to Ref. [82], `TEOBResumS` fixes a_5^c to the value $a_5^c = 23.5$ [32, 42, 48] by hand. The PN results are resummed with a Padé approximate in u_c as

$$A_{orb}(u_c,\nu) = P^1_5\left[A^{PN}_{orb}\right](u_c) \tag{4.3}$$

and enters the full A-function of H^{orb}_{eff} through

$$A\left(r,\nu,S_1,S_2\right) = \left[A_{orb}(u_c,\nu)\frac{1+2u_c}{1+2u}\right]_{u_c(u,S_1,S_2)}. \tag{4.4}$$

The parameter a_6^c is introduced to `TEOBResumS` without being fixed by analytical computation results and, thus, takes on the role of an effective PN parameter capable of modifying the A-potential at the first undetermined PN order. As such it has a different physical interpretation then the other parameters, which can be given independent from each other. a_6^c on the other hand is an effective representation of all terms entering the A-function at higher PN order, represented effectively at 5PN order and thus it depends on both the PN orders included, the parameters not included and the resummation (see Sec. 4.2.3).

The B-potential can then be determined through the general relationship to the A-potential [76],

$$AB = \frac{r^2}{r_c^2}\frac{1}{1 + 6\nu u_c^2 + 2\left(26 - 3\nu\right)\nu u_c^3}. \tag{4.5}$$

The quantities G_S and G_{S_*} entering the spin-orbit sector of the model are the gyro-gravitomagnetic ratios and determine the strength of the spin-orbit coupling. The gyro-gravitomagnetic functions G_S and $G_{S_\star}$ are given at next-to-next-to-leading order (NNLO) [92]. The Damour-Jaranowski-Schäfer gauge [80, 127], is fixed so that (G_S, G_{S_*}) only depend explicitly on $(r, p^2_{r_*})$ and *not* on

---

[1] Following the factorization scheme presented in Sec.2.3.2.

[2] This section follows closely Paper I, Sec. II A.

the angular momentum p_φ. G_S and $G_{S_\star}$ are resummed by an inverse Taylor expansion, with the test-particle limit factored out

$$G_S = \frac{2uu_c^2}{1 + c_{10}u_c + c_{20}u_c^2 + c_{30}u_c^3 + c_{02}p_{r_\star}^2 + c_{12}u_c p_{r_\star}^2 + c_{04}p_{r_\star}^4} \tag{4.6}$$

$$G_{S_\star} = \frac{\frac{3}{2}u_c^3}{1 + c_{10}^\star u_c + c_{20}^\star u_c^2 + c_{30}^\star u_c^3 + c_{40}^\star u_c^4 + c_{02}^\star p_{r_\star}^2 + c_{12}^\star u_c p_{r_\star}^2 + c_{04}^\star p_{r_\star}^4} \tag{4.7}$$

Similar to a_6^c, the coefficients c_{30} and $c_{30}^\star$ are not fixed by analytical computations but through a free parameter c_3 as

$$c_{30} = \nu c_3 \tag{4.8}$$

$$c_{30}^\star = \frac{135}{32}\nu c_3. \tag{4.9}$$

The remaining parameters are given in Ref. [76]. Again, different from the analytically determined parameters, the meaning of c_3 is less straight forward. Additionally to the dependence on the parameters included, as well as the ones not included and the resummation and factorization of the waveform, c_3 also depends on the the calibration of a_6^c. Thus, the calibration can not be done independently, but must be done hierarchically. Similarly to a_6^c it is thus an effective representation of all the higher PN terms that are not included, as well as an additional correction to the effect a_6^c has on the spin evolution. Further, an important difference to keep in mind is that given a specific choice of c_3 the denominator of either G_S or $G_{S_\star}$ can become 0 or close to 0. Thus, c_3 needs to be chosen with care and thoroughly checked across the parameter space to ensure the absence of a divergence.

4.2 Numerical Relativity fits

The discussion will now turn to the calibration of the *analytical flexibility* of `TEOBResumS`. The calibration is partly taken from Refs. [76, 131, 132], which preceded Paper I, as selective aspects calibration of `TEOBResumS` did not require an update. However, they are still reviewed to introduce the reader to the concepts involved in the determination of these quantities.

4.2.1 Analytical flexibility of `TEOBResumS`

Starting from the `TEOB` infrastructure given in Sec. 2.3 and followed up by the prior discussion in this chapter, several points of *analytical flexibility* in `TEOBResumS` have been introduced, which can be used to capture NR information and complete the model. Briefly summarized they are:

(i) The effective parameter a_6^c introduced at fifth PN order to the A-potential.

(ii) The effective parameter c_3 introduced at NNNLO into the gyro-gravitomagnetic functions G_S and G_{S_*}.

(iii) The Phenomenological *merger-ringdown* template consisting of

  (a) the amplitude and frequency at merger $\{\hat{A}_{22}^{\rm mrg}, \omega_{22}^{\rm mrg}\}$,

(b) the three parameters $(c_3^{A_{22}}, c_3^{\phi_{22}}, c_4^{\phi_{22}})$ characterizing the evolution between merger and ringdown,

(c) the ringdown QNM parameters $\{\alpha_1^{22}, \alpha_2^{22}, \omega_1^{22}\}$.

(iv) The NQC extraction points $\left\{\hat{A}_{22}^{\rm NQC}, \dot{\hat{A}}_{22}^{\rm NQC}, \omega_{22}^{\rm NQC}, \dot{\omega}_{22}^{\rm NQC}\right\}$ used in the iterative determination of $(a_1^{22}, a_2^{22}, b_1^{22}, b_2^{22})$.

In the following discussion will highlight several ways to improve the fits that have been proven by experience. We will review structures that have been useful in obtaining a good quality fits.

4.2.2 Implementation errors and waveform calibration

As errors in the implementation of a model are always possible, and have been to some extent discussed in Paper I, it is useful now to briefly review this on the example of `TEOBResumS`. While some aspects of the *analytical flexibility* are defined in a way independent of the model such as the *merger-ringdown* template and the NQC extraction points, others are not. Examples in `TEOBResumS` are first and foremost a_6^c and c_3. Should the model be implemented with an error while these are determined this would of course also impact their calibration. However, if the faulty implementation only affects the waveform to a small quantitative degree, it is possible that these parameters can correct for this error. In such a situation it is important to note that the potential for correcting errors through such means is limited.

As discussed in Paper I, a coding error in the `TEOBResumS Matlab` numerical implementation was found. This error has affected, though marginally, the spin-dependent sector of the model from it's conception in 2014 [76, 84, 131, 132]. The leading order factor of $\ell = 5$, $m =$ odd multipolar waveform amplitudes was missing the contribution of the factor $X_{12} = \sqrt{1-4\nu}$, which entered squared into the radiation reaction force $\hat{\mathcal{F}}_\varphi$. Especially, in the nearly-equal-mass case when $X_{12}^2 \approx 0$ this effect can have a significant impact. Once this error was corrected a new determination of c_3 was in order. Further, in previous `TEOB` avatars $\Delta t_{\rm NQC}$ was fitted for $\chi_1 = \chi_2 > 0.85$, as discussed in Ref. [131] [see also Sec. IIIC of Ref. [132], Eqs. (24)-(25) therein]. Through this correction $\Delta t_{\rm NQC} = 1$ could be chosen also in the large, aligned spin region[3].

4.2.3 Effective Post-Newtonian coefficients

The discussion will now focus on the fits of the effective PN coefficient a_6^c and the NNNLO effective spin-orbit parameter c_3. The previous versions of these fits were presented in Refs. [131, 132]. The fit of a_6^c has been found to perform sufficiently well to not warrant an update in Paper I. However, due to the implementation error, discussed in the previous section, a new determination of c_3 was necessary[4]. In general the two fits should be done in a hierarchical manner to avoid complication. As c_3 does not impact the waveform if $\chi_1 = \chi_2 = 0$, the fit of a_6^c should be done first using non-spinning waveforms. The fit of c_3 should then follow up to complete the spinning sector. By this design, a_6^c is only a function of ν while c_3 depends on ν as well as the individual spin $\tilde{a}_{1,2}$. Further, it is useful to note that any change in a_6^c would require a new determination of c_3, while the reverse is not the case.

---

[3] However, as will be discussed in Sec. 4.4, it is necessary to modify $\Delta t_{\rm NQC}$ for large mass-ratios and large negative spins.

[4] This fit has been done by Dr. Alessandro Nagar.

Table 4.1: $c_3^{\text{first guess}}$ is chosen by hand to obtain a good agreement between `TEOB` and NR during the late inspiral. As can be seen from the functional form of $(G_S, G_{S_\star})$, c_3 enters the denominator and thus is inversely proportional to it's effect onto the magnitude of $(G_S, G_{S_\star})$. A larger value of c_3, thus, makes the spin-orbit-coupling more attractive while a smaller value makes it more repulsive. These are then compared to the value c_3^{fit} obtained from the interpolating fit over all waveforms listed. The spin-variable $\hat{S}$ is given in the last column, as it has been proven to be a useful characterization of quantities at merger, see Sec. 4.2.4.

#	(q, χ_A, χ_B)	$c_3^{\text{first guess}}$	c_3^{fit}	$\Delta c_3/c_3^{\text{fit}}[\%]$	$\hat{S}$
1	$(1, -0.95, -0.95)$	93.0	92.31	0.75	-0.4750
2	$(1, -0.90, -0.90)$	89.0	89.44	-0.49	-0.4500
3	$(1, -0.80, -0.80)$	83.0	83.78	-0.93	-0.4000
4	$(1, -0.60, -0.60)$	73.5	72.83	0.92	-0.3000
5	$(1, -0.44, -0.44)$	64	64.45	-0.70	-0.2200
6	$(1, +0.20, +0.20)$	35	34.85	0.43	$+0.1000$
7	$(1, +0.60, +0.60)$	20.5	20.17	1.64	$+0.3000$
8	$(1, +0.80, +0.80)$	13.5	14.15	-4.59	$+0.4000$
9	$(1, +0.90, +0.90)$	11.5	11.52	-0.17	$+0.4500$
10	$(1, +0.99, +0.99)$	9.5	9.39	1.17	$+0.4950$
11	$(1, +0.994, +0.994)$	9.5	9.30	2.15	$+0.4970$
12	$(1, -0.50, 0)$	61.5	56.62	8.62	-0.1250
13	$(1, +0.90, 0)$	25.5	22.33	14.20	$+0.2250$
14	$(1, +0.90, +0.50)$	17.0	15.73	8.07	$+0.3500$
15	$(1, +0.50, 0)$	32.0	31.20	2.56	$+0.1250$
16	$(1.5, -0.50, 0$	62.0	57.97	6.95	-0.1800
17	$(2, +0.60, 0)$	29.0	26.71	8.57	$+0.2\bar{6}$
18	$(2, +0.85, +0.85)$	15.0	14.92	0.54	$+0.47\bar{2}$
19	$(3, -0.50, 0)$	63.0	61.15	3.03	-0.28125
20	$(3, -0.50, -0.50)$	70.5	66.63	5.81	-0.3125
21	$(3, +0.50, 0)$	28.0	28.02	-0.07	$+0.28125$
22	$(3, +0.50, +0.50)$	26.5	24.44	8.43	$+0.3125$
23	$(3, +0.85, +0.85)$	16.5	14.38	14.74	$+0.53125$
24	$(5, -0.50, 0)$	62.0	59.84	3.61	$-0.347\bar{2}$
25	$(5, +0.50, 0)$	30.5	29.01	5.14	$+0.347\bar{2}$
26	$(8, -0.50, 0)$	57.0	56.48	0.92	-0.3951
27	$(8, +0.50, 0)$	35.0	33.68	3.92	$+0.3951$

Obtaining the values of a_6^c and c_3 for a given NR waveform would in principle be possible by fit, but that is not necessary. Due to the very stable resummation of both the A-potential and the gyro-gravitomagnetic ratios (G_S, G_{S_*}), the tolerance for error in both parameters is relatively large. A deviation of $\mathcal{O}(1)$ could be without impact on unfaithfulness or phasing. Therefor the values of a_6^c and c_3 for the individual NR waveforms have been chosen by hand. This choice was primarily driven by the need to achieve a good phasing between `TEOBResumS` and that particular NR waveform and to remain conservative and only minimally modify the A-potential or (G_S, G_{S_*}). The parameter is tuned until the accumulated dephasing at merger between `TEOBResumS` and NR is comparable to the NR error, which can be estimated by comparing the two highest resolutions available. The interpolating fits have been done using `MATHEMATICA`.

The fit of a_6^c used within `TEOBResumS`, presented in Ref. [76] is given by

$$a_6^c(\nu) = 3097.3\nu^2 - 1330.6\nu + 81.38\ . \tag{4.10}$$

The improved fit of $c_3(\tilde{a}_1, \tilde{a}_2, \nu)$ was calibrated by a set of 27 `SXS` BBH-NR simulations (see Tab. 4.1). The determination of $c_3(\tilde{a}_1, \tilde{a}_2, \nu)$ in practice is done as follows. The fit of a_6^c is held fixed. The initial estimates of $c_3^{\text{first guess}}$ are given for all 27 `SXS` waveforms in Tab. 4.1 The new and improved fit of c_3 was chosen to be of similar form as the one chosen in Ref. [132]. Explicitly, the fit is done using the template

$$c_3(\tilde{a}_1, \tilde{a}_2, \nu) = \ p_0 \frac{1 + n_1 \hat{a}_0 + n_2 \hat{a}_0^2}{1 + d_1 \hat{a}_0} + \left(p_1\nu + p_2\nu^2 + p_3\nu^3\right) \hat{a}_0 \sqrt{1 - 4\nu} + p_4\left(\tilde{a}_1 - \tilde{a}_2\right)\nu^2, \tag{4.11}$$

where

$$p_0 = 43.371638, \tag{4.12a}$$
$$n_1 = -1.174839, \tag{4.12b}$$
$$n_2 = 0.354064, \tag{4.12c}$$
$$d_1 = -0.151961, \tag{4.12d}$$
$$p_1 = 929.579, \tag{4.12e}$$
$$p_2 = -9178.87, \tag{4.12f}$$
$$p_3 = 23632.3, \tag{4.12g}$$
$$p_4 = -104.891. \tag{4.12h}$$

As can be seen in Tab. 4.1, where the values of c_3 obtained from the fit and relative differences, the error of c_3 gets up to almost 15%. While this does impact the relative dephasing between `TEOBResumS` and NR, those are not the relevant measures of accuracy with which this fit should be judged. Ultimately, the fit quality can only be estimated by computing the EOB/NR unfaithfulness or directly comparing the waveforms in the time-domain.

Hypothetically, it is possible that the calibration of c_3, as it is limited to such a small parameter space and limited functional form, is not yet the best that can be done. Thus, Eq. (4.11) is modified. A single, quadratic term in $\hat{a}_0$ is added with the explicit form $p_5\nu\hat{a}_0^2\sqrt{1-4\nu}$, with the fitting coefficient p_5. The modified c_3 fit coefficients are $(p_1, p_2, p_3, p_4, p_5) = (917.59, -8754.35, 20591.0, -78.95, 83.40)$. By explicit computation it can be checked that the second fit does improve the agreement with the individual values of $c_3^{\text{first guess}}$. It remains to be seen how this impacts the comparison of `TEOBResumS` and NR on the levels of unfaithfulness. This question will be discussed explicitly in Sec. 4.3.

4.2.4 Merger amplitude and frequency

The merger-ringdown template applied to the $(2,2)$ mode is often referred to as the postmerger-ringdown template. This name refers to *the* merger being defined as $t_{\text{mrg}} \equiv t_{22}^{\text{peak}}$, the peak of the dominant quadrupolar mode. The starting point of the postmerger are therefor the first variables to be fitted: The $(2,2)$ mode amplitude $\hat{A}^{\rm mrg}$ and frequency $\omega^{\rm mrg}$ at merger,

$$\hat{A}^{\rm mrg} = \frac{A_{22}\left(t = t_{\rm mrg}\right)}{\nu} \tag{4.13}$$

$$\omega^{\rm mrg} = \omega_{22}\left(t = t_{\rm mrg}\right) \ . \tag{4.14}$$

These fits are of key importance to obtain a robust and reliable postmerger-ringdown waveform, as they do enter as overall scale factors into the phenomenological waveform template introduced in Sec. 2.3.4.

When fitting the spin-dependence $\hat{A}^{\rm mrg}$ it is useful to consider the leading order behavior of the waveform, which within the EOB formalism is factorization and resummed following Refs. [76, 81, 137]. Starting from the analytical waveform $\hat{A}^{\rm mrg}$ is factorized as

$$\hat{A}^{\rm mrg} = \hat{A}^{\rm mrg}_{\rm orb}\hat{A}^{\rm SO}_{\rm LO}\hat{\hat{A}}^{\rm mrg}_{\rm S}. \tag{4.15}$$

In this equation, $\hat{A}^{\rm mrg}_{\rm orb}$ is the nonspinning (or orbital) contribution solely dependent on ν. The factor $\hat{A}^{\rm SO}_{\rm LO}$, heuristically based on the analytical waveform, is chosen to extract leading order behavior and simplify the fit of $\hat{\hat{A}}^{\rm mrg}_{\rm S}$, the remnant spin-dependent factor. The orbital contribution is modeled as a quadratic polynomial in ν as

$$\hat{A}^{\rm mrg}_{\rm orb} = c_0^{\hat{A}^{\rm mrg}_{\rm orb}} + c_1^{\hat{A}^{\rm mrg}_{\rm orb}}\nu + c_2^{\hat{A}^{\rm mrg}_{\rm orb}}\nu^2. \tag{4.16}$$

In principle it would have been possible to impose the test-particle limit [90] directly onto $c_0^{\hat{A}^{\rm mrg}_{\rm orb}}$, however, in this fit it was not done explicitly. Yet their agreement is still within 1%. To simplify the extrapolation to larger mass ratios both `TEOBiResumMultipoles` and `TEOBiResumS_SM` heavily exploit the high level of accuracy and precision present in the test-particle data available, as will be discussed in Chapter 5 and Chapter 6. The $(2,2)$ spin-dependence at leading order is motivated by the analytical waveform (see e.g. Eq. (16) of [123]) and can be written as

$$\hat{A}^{\rm SO}_{\rm LO} = 1 - \left(\hat{a}_0 + \frac{1}{3}X_{12}\tilde{a}_{12}\right)x^{3/2}_{\rm mrg}. \tag{4.17}$$

Where the spin variable $\tilde{a}_{12} \equiv \tilde{a}_1 - \tilde{a}_2$ is used. The frequency $x_{\rm mrg} \equiv \left(\omega^{\rm mrg}_{22}/2\right)^{2/3}$ is a slight approximation. The variable is generally given as $x = \Omega^{2/3}$. The frequency of the binary motion Ω however does not relate directly to $\omega_{22}/2$, but only approximately. As can be seen in [81] explicitly, ω_{22} does receive a correction from the tail factor of the waveform $\hat{h}^{\rm tail}_{\ell m}$, which is in fact most relevant when the frequency gets increases close to the merger. Yet, even with this approximation it is possible to fit $\hat{\hat{A}}^{\rm mrg}_{\rm S}$ with remarkable simplicity. To this end it is useful to define $\hat{a}_{\rm eff} \equiv \hat{a}_0 + X_{12}\tilde{a}_{12}/3$ as an effective spin variable. As can be seen in comparing the top-right to the top-left panel Fig. 4.1, this parameterization is clearly superior to the structure of a simple fit against $(\hat{a}_0, \nu)$ as employed in previous avatars of the `TEOB` model [83, 132]. The remnant spin dependence is then fitted as

$$\hat{\hat{A}}^{\rm mrg}_{\rm S} = \frac{1 - n^{\hat{\hat{A}}}(\nu)\hat{a}_{\rm eff}}{1 - d^{\hat{\hat{A}}}(\nu)\hat{a}_{\rm eff}}, \tag{4.18}$$

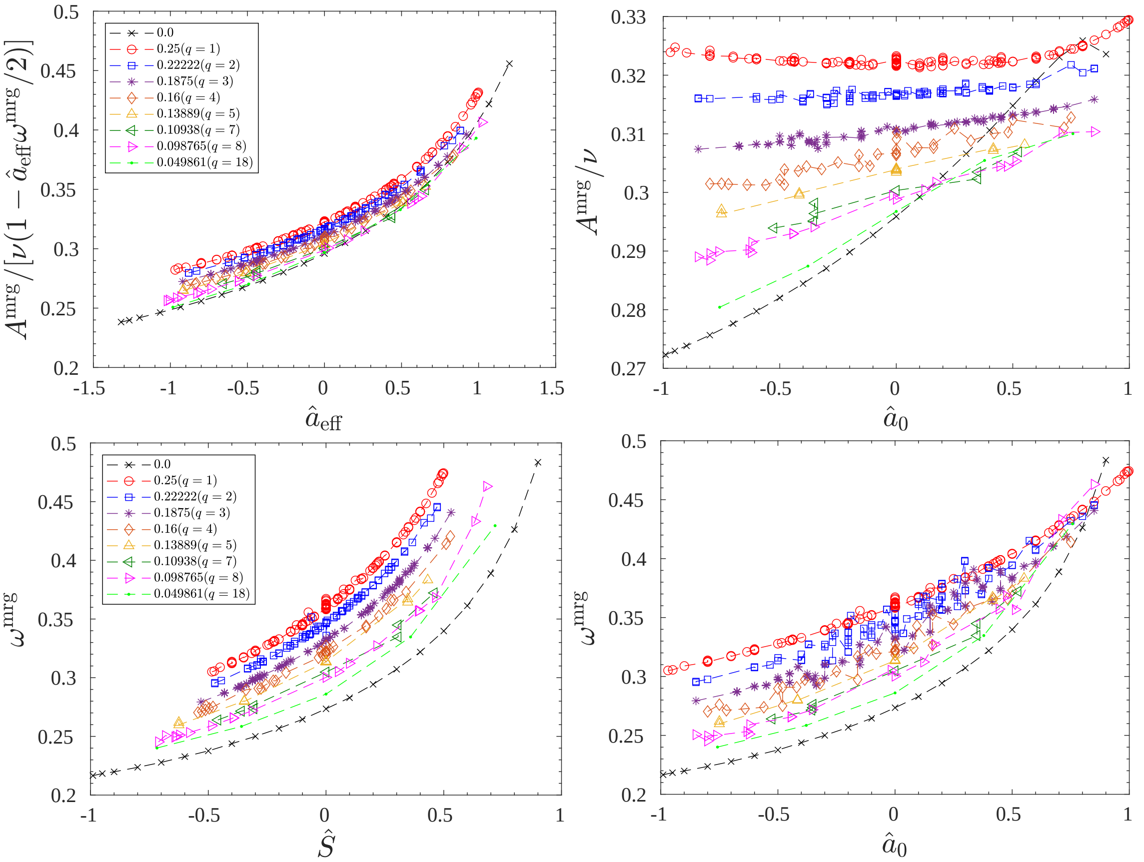

Figure 4.1: The quasi-universal structures exploited to obtain fits of $\{\hat{A}^{\rm mrg}, \omega^{\rm mrg}\}$ are plotted (top-left and bottom-left respectively). These are shown in a side-by-side comparison to the structure used in previous works, versus the effective EOB Kerr parameter $\hat{a}_0$ (top-right and bottom-right) [83, 132]. In each plot all waveforms with a given mass-ratio form a line. The mass-ratios plotted are $q = 1$ (red), $q = 2$ (blue), $q = 3$ (purple), $q = 4$ (brown), $q = 5$ (yellow), $q = 7$ (dark green) , $q = 8$ (magenta), $q = 18$ (light green) and the test-particle limit (black). Comparing (top-left) $\hat{A}^{\rm mrg}$ normalized to the leading-order, spin-orbit contribution plotted versus $\hat{a}_{\rm eff}$ to (top-right) $\hat{A}^{\rm mrg}$ versus $\hat{a}_0$ the differences appear quite noteworthy. All mass-ratios as a function of $\hat{a}_0$ show oscillations as well as an individual behavior. While this is not the case for the mass-ratios as a function of $\hat{a}_{\rm eff}$, where all mass-ratios are quasi-parallel and show a similar, only slightly shifted behavior with almost no scattering, presenting an optimal starting point to obtain a fit. $\omega^{\rm mrg}$ is plotted against $\hat{S} = (S_1 + S_2)/M^2$ (bottom-left) and the standard effective Kerr parameter $\hat{a}_0 = \hat{S} + \hat{S}_*$ (bottom-right). As discussed in the main text, the simplification is quite remarkable and thus allows a very straightforward approach to fitting the spin-dependence. Yet, the origin of this structure remains unclear.

where $(n^{\hat{\hat{A}}}, d^{\hat{\hat{A}}})$ are modeled at quadratic order in X_{12}, which is given explicitly as

$$n^{\hat{\hat{A}}}(\nu) \equiv n^{\hat{A}^{\rm mrg}_{\rm spin}}_{\nu=1/4} + n^{\hat{A}^{\rm mrg}_{\rm spin}}_{1} X_{12} + n^{\hat{A}^{\rm mrg}_{\rm spin}}_{2} (X_{12})^2 \,, \tag{4.19}$$

$$d^{\hat{\hat{A}}}(\nu) \equiv d^{\hat{A}^{\rm mrg}_{\rm spin}}_{\nu=1/4} + d^{\hat{A}^{\rm mrg}_{\rm spin}}_{1} X_{12} + d^{\hat{A}^{\rm mrg}_{\rm spin}}_{2} (X_{12})^2 \,. \tag{4.20}$$

The reader should note that $\hat{\hat{A}}^{\rm mrg}_{\rm S}$ was fitted in two steps. First, $\left\{ n^{\hat{A}^{\rm mrg}_{\rm spin}}_{\nu=1/4}, d^{\hat{A}^{\rm mrg}_{\rm spin}}_{\nu=1/4} \right\}$ were fitted with the equal-mass data. The fit-results were then imposed and the extrapolation coefficients proportional to X_{12} and X_{12}^2 were determined with the remaining `SXS` and `BAM` data of the *calibration* set. All fitted coefficients are listed in the left column of Tab. B.2.

The next target to be fitted is the merger frequency $\omega^{\rm mrg}$ of the $(2,2)$ mode. As in the case of the amplitude, previous works employed a simple fit against $(\hat{a}_0, \nu)$ [83, 132]. This however

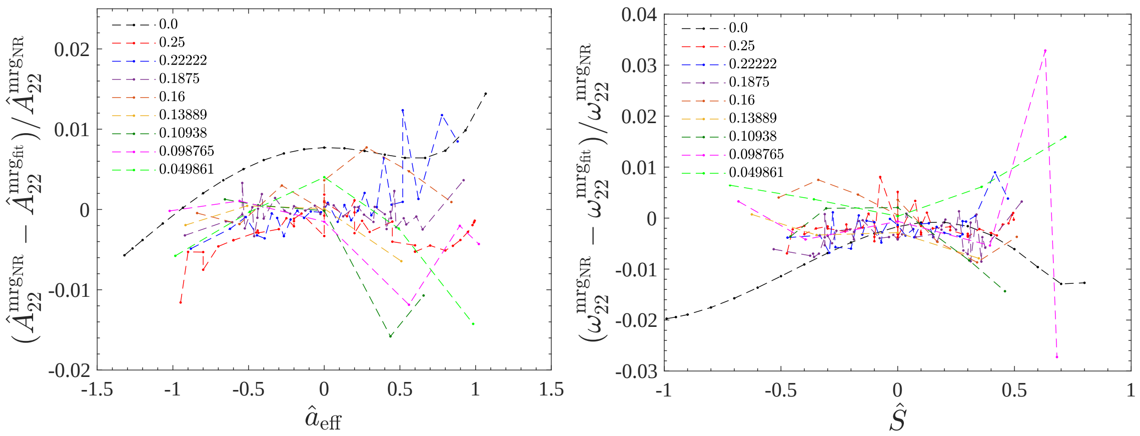

Figure 4.2: The fractional error of the fits for $\hat{A}^{\mathrm{mrg}}$ (left) and ω^{mrg} (right) with respect to the *calibration* set, at the state of Paper I including the faulty $(8, +0.85, +0.85)$ waveform, is shown. The individual lines highlight the respective mass-ratios and are marked explicitly with the symmetric mass-ratio ν. The mass-ratios given are $q = 1$ (red), $q = 2$ (blue), $q = 3$ (purple), $q = 4$ (brown), $q = 5$ (yellow), $q = 7$ (dark green) , $q = 8$ (magenta), $q = 18$ (light green) and the test-particle limit (black). The fit coefficients are given in Tab. B.2 and are evaluated along eq. (4.15) – (4.24).

proved insufficient in capturing the behavior of the amplitude for large oppositely aligned spins with comparably small values of $\hat{a}_0$. In Fig. 4.1 (bottom left) a solution to this problem is shown, that does avoid the introduction of a fully three-dimensional fit. ω^{mrg}, extracted from NR[5], is plotted versus the effective spin variable $\hat{S} \equiv (S_1 + S_2)/M^2$. First, comparing the behavior of the individual mass-ratios shown versus $\hat{S}$ (bottom left) and versus $\hat{a}_0$ (bottom right of Fig. 4.1), it is evident that the oscillations of each curve reduces drastically. This can be seen in particular for $q = 2,\ 3$ and 4 data which oscillates heavily as a function of $\hat{a}_0$. Further, it can be seen by eye that plotted versus $\hat{S}$ all mass-ratios show qualitatively the same behavior of an approximate fourth order polynomial, shifted vertically relative to each other. This simple structure is very useful in obtaining an accurate fit of the merger frequency as will be exploited below. While it is still an open question what the origin of this behavior is, it is possible to give a brief argument to explore a connection to the EOB framework.

Starting from the approximation $\omega_{22}^{\mathrm{mrg}} \simeq 2\Omega$, (which as mentioned above is not perfect, yet in the case of large, positive spins $\hat{S}$ it is quite reliable) for $u = u_{\mathrm{mrg}}$, ω^{mrg} can be approximated as

$$\omega_{22}^{\mathrm{mrg}} \simeq 2 \left[\frac{A u_c^2 p_\varphi^{\mathrm{mrg}}}{H_{\mathrm{EOB}} \hat{H}_{\mathrm{eff}}^{\mathrm{orb}}} + H_{\mathrm{EOB}}^{-1} \left(G_S \hat{S} + G_{S_*} \hat{S}_* \right) \right] . \tag{4.21}$$

The reader should first note that u_c, as introduced in Sec. 2.3, only depends on the spin through even-parity powers of $\hat{a}_0 = \hat{S} + \hat{S}_*$. Further, looking at the functional form of $\hat{S}_*$ it is easy to see that $\hat{S} = \hat{S}_*$ in the $q = 1$ and the test-particle limit, thus, it seems natural that the dependency on $\hat{S}$ would dominate the systems. However, when departing from the equal-mass case to the $q \neq 1$ region it becomes less straight forward to find a plausible explanation for this behavior. Nonetheless, Fig. 4.1 does indicate that $\hat{S}_*$ does not contribute significantly to ω^{mrg}. Paper I continues the discussion through exploring an expansion of eq. (4.21) in powers of $\hat{S}$ and $\hat{S}_*$, yet

---

[5] The reader should note that while this is a remarkable result, it cannot be obtained blindly from NR, as a small number of waveforms have to be discarded following the principle that small changes in (q, χ_1, χ_2) only cause small changes in the amplitude and frequency.

without arriving at a concrete justification. For now, the simplified scaling is quite remarkable and will be exploited in the determination of a global fit. To do so, a template in factorized form is chosen as

$$\omega^{\rm mrg} = \omega^{\rm mrg}_{\rm orb}\left(\nu\right)\omega^{\rm mrg}_{\rm S}\left(\hat{S}, X_{12}\right), \tag{4.22}$$

with the orbital factor $\omega^{\rm mrg}_{\rm orb}$ fitted to a quadratic function in ν,

$$\omega^{\rm mrg}_{\rm orb}\left(\nu\right) = c_0^{\omega^{\rm mrg}_{\rm orb}} + c_1^{\omega^{\rm mrg}_{\rm orb}}\nu + c_2^{\omega^{\rm mrg}_{\rm orb}}\nu^2. \tag{4.23}$$

The functional form of $\hat{A}^{\rm mrg}_{\rm S}$ of eq. (4.18) is kept for $\omega^{\rm mrg}_{\rm S}$, but the spin-variable is $\hat{S}$ as spin variable

$$\omega^{\rm mrg}_{\rm S} = \frac{1 - n^{\omega}(\nu)\hat{S}}{1 - d^{\omega}(\nu)\hat{S}}\;. \tag{4.24}$$

The functions (n^{ω}, d^{ω}) are identically chosen to eq. (4.19) – (4.20). The $\nu = 1/4$ factor is fitted first, followed up by the fitting of the coefficients proportional to X_{12} and X_{12}^2. All coefficients are given in the right column of Table B.2. While the first exploratory fits of $\omega^{\rm mrg}$ were assumed to necessitate a full three-dimensional fit to accurately capture the NR behavior, this was indeed not necessary due to the discovery of the simple behavior as a function of $\hat{S}$. To estimate its performance, the fit was compared with the full *calibration* set of data available, at the time of publication of Paper I. The fractional differences are displayed in Fig. 4.2. It is useful to point towards the disagreement between the `BAM` waveforms $(8, 0.8, 0)$ and $(8, 0.85, 0.85)$ that was present at the time. As these two waveforms are very similar, one would expect that they would behave in a similar manner. Yet, this is not the case for $(8, 0.85, 0.85)$. While $(8, 0.8, 0)$ continues to follow the trend of similar waveforms, $(8, 0.85, 0.85)$ actually shows a decrease in the merger frequency. Thus, by the principle of consistency between similar waveforms $(8, 0.85, 0.85)$ was excluded from the NR calibration of `TEOBResumS`. As became evident after publishing Paper I, the NR waveform of $(8, 0.85, 0.85)$ was generated with insufficient resolution and a waveform with increased resolution was generated. In fact, this updated waveform will motivate an improved fit of the merger amplitude and frequency in chapter 6. Additionally, the updated waveform $(8, 0.85, 0.85)$, together with a majority of the *validation* generated for approximately integer mass-ratios has been included in Fig. 4.1.

4.2.5 Next-to-Quasi-Circular corrections

Once the peak of the $(2, 2)$ mode is fitted it is ideal to move directly to the NQC extraction point. These are given by the NR waveform taken at the point $t_{\rm NQC} \equiv t_{\rm mrg} + 2M$, following the setup in Sec. 2.3.2. From each `SXS` and `BAM` NR data set the quantities $\left\{\hat{A}^{\rm NQC}_{22}, \dot{\hat{A}}^{\rm NQC}_{22}, \omega^{\rm NQC}_{22}, \dot{\omega}^{\rm NQC}_{22}\right\}$ are extracted and fitted globally. These are then used to determine the NQC parameters defined in Sec. 2.3.2.

For $\ell = m = 2$ mode a very high level of accuracy is necessary, as it is the only multipole for which the NQC parameters enter the radiation reaction, eq. (2.32). While inaccuracies for the subdominant multipoles are leaving the remainder of the model untouched, even a small inaccuracy can lead to the failure of the iterative determination of the NQC parameters (a_1^{22}, a_2^{22}) to converge. Especially, for the equal- and almost equal-mass region $(q < 4)$ a very accurate fit is necessary. In

Appendix B.1 the fits of the equal mass region, eq. (B.1) and the nearly-equal-mass $1 < q < 4$ region, eq. (B.2) are given. The former is fitted with quartic polynomials, while the latter is fitted with cubic polynomials in $\hat{a}_0$. While these fits are done very well for regions with an excellent NR coverage, their extrapolation outside the domain of calibration is usually very poor. Any attempt to build a singular fit starting from this structure will lead to pathological behavior for large mass-ratios, where the NR coverage is thin. Therefor, both `TEOBResumS` and `TEOBiResumS_SM` have been designed to only update the fits in the region of $q \geq 4$ as needed for the $\ell = m = 2$ mode.

Another point to note when fitting the NQC it is useful to use a template similar to that utilized for the fits of the merger amplitude and frequency. This is to ensure that outside the domain of calibration the waveform is robust and shows no pathological behavior. The robustness of the waveform outside the domain of calibration will be discussed further in Sec. 4.4.

The discussion will now turn to updating the fit of the $q \geq 4$ region. $\hat{A}_{22}^{\rm NQC}$ employs the factorization of $\hat{A}^{\rm mrg}$ as

$$\hat{A}_{22}^{\rm NQC} = \hat{A}_{\rm orb}^{\rm NQC} \hat{A}_{\rm LO}^{\rm SO} \hat{A}_{\rm S}^{\rm NQC}. \tag{4.25}$$

The leading-order, spin-orbit contribution $\hat{A}_{\rm LO}^{\rm SO}$ is given by eq. (4.17) as well, however with a slight difference using $x_{\rm NQC} \equiv \left(\omega_{22}^{\rm NQC}/2\right)^{2/3}$ to ensure consistency. The nonspinning (orbital) contribution $\hat{A}_{\rm orb}^{\rm NQC}$ is fitted with an additional cubic term in ν as

$$\hat{A}_{\rm orb}^{\rm NQC} = c_3^{\hat{A}_{\rm orb}^{\rm NQC}} \nu^3 + c_2^{\hat{A}_{\rm orb}^{\rm NQC}} \nu^2 + c_1^{\hat{A}_{\rm orb}^{\rm NQC}} \nu + c_0^{\hat{A}_{\rm orb}^{\rm NQC}}. \tag{4.26}$$

The beyond leading-order spin dependence is then captured by fitting $\hat{A}_{\rm S}^{\rm NQC}$ first to the $q = 1$ data and followed up by the extrapolation to higher mass-ratios as

$$\hat{A}_{\rm S}^{\rm NQC} = \frac{1 - n_S^{\rm NQC} \hat{a}_{\rm eff}}{1 - d_S^{\rm NQC} \hat{a}_{\rm eff}}, \tag{4.27}$$

with $(n_S^{\rm NQC}, d_S^{\rm NQC})$ both given by second-order polynomials in X_{12} as defined in eq. (4.19) – (4.20). All coefficients are listed in the top-left column of Table B.1.

The derivative of the amplitude $\dot{\hat{A}}_{22}^{\rm NQC}$ is particularly difficult, as it is very close to 0 it is highly sensitive to numerical noise. Thus, after several attempts to build a construction that would allow to increase the robustness of $\dot{\hat{A}}_{22}^{\rm NQC}$ this form was chosen:

$$\dot{\hat{A}}_{22}^{\rm NQC} = \omega_{22}^{\rm NQC} \left[\dot{\hat{A}}_{\rm orb}^{\rm NQC}(\nu) + \dot{\hat{A}}_{S}^{\rm NQC}(\hat{a}_{\rm eff}, X_{12})\right]. \tag{4.28}$$

A rational function, linear in both denominator and numerator as a function of ν is fitted to capture the non-spinning behavior as

$$\dot{\hat{A}}_{\rm orb}^{\rm NQC}(\nu) = -\frac{N_0^{\dot{\hat{A}}_{\rm orb}^{\rm NQC}} + N_1^{\dot{\hat{A}}_{\rm orb}^{\rm NQC}} \nu}{1 + D_1^{\dot{\hat{A}}_{\rm orb}^{\rm NQC}} \nu}. \tag{4.29}$$

A rational function in the effective-amplitude-spin variable $\hat{a}_{\rm eff}$ is also chosen to capture the spin dependence of $\dot{A}^{\mathrm{NQC}}_{22}$ as

$$\dot{A}^{\mathrm{NQC}}_{S} = \frac{n^{\dot{A}_{\mathrm{NQC}}}\hat{a}_{\mathrm{eff}}}{1 + d^{\dot{A}_{\mathrm{NQC}}}\hat{a}_{\mathrm{eff}}}. \tag{4.30}$$

Again, quadratic polynomials in X_{12} are used to capture $(n^{\dot{A}_{\mathrm{NQC}}}, d^{\dot{A}_{\mathrm{NQC}}})$. First, the functions are calibrated to the equal-mass case and then extrapolated to the $X_{12} \neq 0$ region. The explicit values of the coefficients are listed in the top-right column of Table B.1.

The NQC frequency is to be fitted next. A factorization and choice of spin-variable, inspired by the merger-quasi-universal behavior of the merger frequency, are made as

$$\omega^{\mathrm{NQC}}_{22}\left(\nu; \hat{S}\right) = M\omega^{\mathrm{NQC}}_{\mathrm{orb}}\left(\nu\right)\omega^{\mathrm{NQC}}_{S}\left(\hat{S}, X_{12}\right). \tag{4.31}$$

The non-spinning contribution is fitted at quadratic order by a polynomial in ν as

$$\omega^{\mathrm{NQC}}_{\mathrm{orb}}\left(\nu\right) = c_0^{\omega^{\mathrm{NQC}}_{\mathrm{orb}}} + c_1^{\omega^{\mathrm{NQC}}_{\mathrm{orb}}}\nu + c_2^{\omega^{\mathrm{NQC}}_{\mathrm{orb}}}\nu^2. \tag{4.32}$$

Continuing to follow the principle of consistency between the merger and NQC the spin-factor is fitted by a rational function in $\hat{S}$ as

$$\omega^{\mathrm{NQC}}_{S} = \frac{1 - n^{\omega^{\mathrm{NQC}}}(\nu)\hat{S}}{1 - d^{\omega^{\mathrm{NQC}}}(\nu)\hat{S}}. \tag{4.33}$$

Following the typical procedure $(n^{\omega^{\mathrm{NQC}}}, d^{\omega^{\mathrm{NQC}}})$ are, as for the amplitude, quadratic functions of X_{12}. The first fit is done with respect to the equal-mass data and followed by the extrapolation into the unequal-mass region. The functions are defined in eq. (4.19) – (4.20). The coefficients are listed in the bottom-left column of Table B.1.

The typical factorization of the orbital and spin-dependence into a hierarchical structure is also done for the time derivative of the frequency as

$$\dot{\omega}^{\mathrm{NQC}}_{22} = \dot{\omega}^{\mathrm{NQC}}_{\mathrm{orb}}\left(\nu\right)\dot{\omega}^{\mathrm{NQC}}_{S}\left(\hat{S}, X_{12}\right). \tag{4.34}$$

The non-spinning part is fitted to a rational function of linear order in ν for both numerator and denominator as

$$\dot{\omega}^{\mathrm{NQC}}_{\mathrm{orb}}\left(\nu\right) = \frac{N_0^{\dot{\omega}^{\mathrm{NQC}}_{\mathrm{orb}}} + N_1^{\dot{\omega}^{\mathrm{NQC}}_{\mathrm{orb}}}\nu}{1 + D_1^{\dot{\omega}^{\mathrm{NQC}}_{\mathrm{orb}}}\nu}. \tag{4.35}$$

$\hat{S}$ also proved useful here as the spin-dependence as a quadratic polynomial in $\hat{S}$ through

$$\dot{\omega}^{\mathrm{NQC}}_{S}\left(\hat{S};\, X_{12}\right) = 1 + a_{\dot{\omega}^{\mathrm{NQC}}}\left(\nu\right)\hat{S} + b_{\dot{\omega}^{\mathrm{NQC}}}\left(\nu\right)\hat{S}^2. \tag{4.36}$$

Where again the coefficients $(a_{\dot{\omega}^{\mathrm{NQC}}}, b_{\dot{\omega}^{\mathrm{NQC}}})$ are represented, as above, with quadratic functions of X_{12}, fitted to the equal-mass data then extrapolated to the unequal-mass-case. The corresponding coefficients are listed in the bottom column of Tab. B.1. The astute reader will have noticed that even though none of these fits are meant for usage in the equal-mass case[6] yet all four are fitted directly to the equal-mass data. The reason for this is two-fold. First, the amplitude and frequency at merger are fitted in such a way and thus to ensure consistency it is necessary to do the same for the NQC amplitude and frequency. However, this does not justify to handle the derivatives in a similar manner. The reason can be found once different waveforms fits are compared with respect to stability to numerical noise, extrapolation and possible pathological features. What is found is that if a one-dimensional fit is imposed directly, this stabilizes the fit and improves it's quality. Thus, while it might not be intuitive to calibrate the fit in such a manner, it yet produces the best results.

4.2.6 Ringdown

To fit $Y = \left\{\omega_1^{22}, \alpha_1^{22}, \alpha_2^{22}\right\}$ it is useful to consider their origin as BH perturbation modes. As such they are functions only of the dimensionless spin of the remnant BH $\chi_{\mathrm{f}} \equiv J_{\mathrm{f}}/M_{\mathrm{f}}^2$. The dimensionless spin of the final BH however was fitted with excellent accuracy and precision by Jimenez-Forteza et al. [107] for merging BBH systems. Thus, to avoid unnecessary complications $\left\{\omega_1^{22}, \alpha_1^{22}, \alpha_2^{22}\right\}$ are fitted directly against χ_{f}, which is in turn reproduced using the above mentioned fit as a function $\chi_{\mathrm{f}} = \chi_{\mathrm{f}}\left(q, \chi_1, \chi_2\right)$. These fits are informed by data interpolated from publicly available tables given by Berti et al. [46, 47]. The $\chi_{\mathrm{f}} = 0$ limit is factored out and each parameter is fitted by a rational function to third order of χ_{f} in both denominator and numerator as

$$Y\left(\chi_f\right) = Y_0 \, \frac{1 + b_1^Y \chi_f + b_2^Y \chi_f^2 + b_3^Y \chi_f^3}{1 + c_1^Y \chi_f + c_2^Y \chi_f^2 + c_3^Y \chi_f^3}, \tag{4.37}$$

The fitted coefficients are listed in Tab. B.3.

4.2.7 Postmerger evolution

The evolution parameters of the phenomenological merger-ringdown template are defined in Sec. 2.3.4. They connect the peak of the mode to the later stages of the ringdown during which only the fundamental QNM is contributing to the GW strain. To fit them, first the GW strain is rescaled with respect to the fundamental QNM, separated into amplitude and frequency, and then the derivative of the amplitude at peak is set to 0, the peak amplitude and frequency as well as the dominant QNM behavior are imposed on the templates. Once prepared as such, they are fitted first individually to the `SXS` and `BAM` NR waveform data and interpolated globally in a second step. The templates are given in eq. (2.46) and eq. (2.47) and on the level of the primary fit they have been fitted to the time interval from the peak of the mode for $4\tau_1^{22} = 4/\alpha_1^{22}$, four times the damping time of the fundamental QNM. As will be discussed partially in the next chapters $4\tau_1^{\ell m}$ is sufficient to obtain such a fit and the choice of the fitting interval length needs to be made consistently as in the case of noise multipoles the effects of the noise are more and more significant. The three parameters $Y = \left\{c_3^{A_{22}}, c_3^{\phi_{22}}, c_4^{\phi_{22}}\right\}$ are fitted with the template

$$Y(\nu;\, \hat{S}) = b_0^Y(\nu) + b_1^Y\left(X_{12}\right)\hat{S} + b_2^Y\left(X_{12}\right)\hat{S}^2 + b_3^Y\left(X_{12}\right)\hat{S}^3 + b_4^Y\left(X_{12}\right)\hat{S}^4. \tag{4.38}$$

---

[6] Recall that the NQC for $q < 4$ are given by the fits originally presented in Refs. [131, 132].

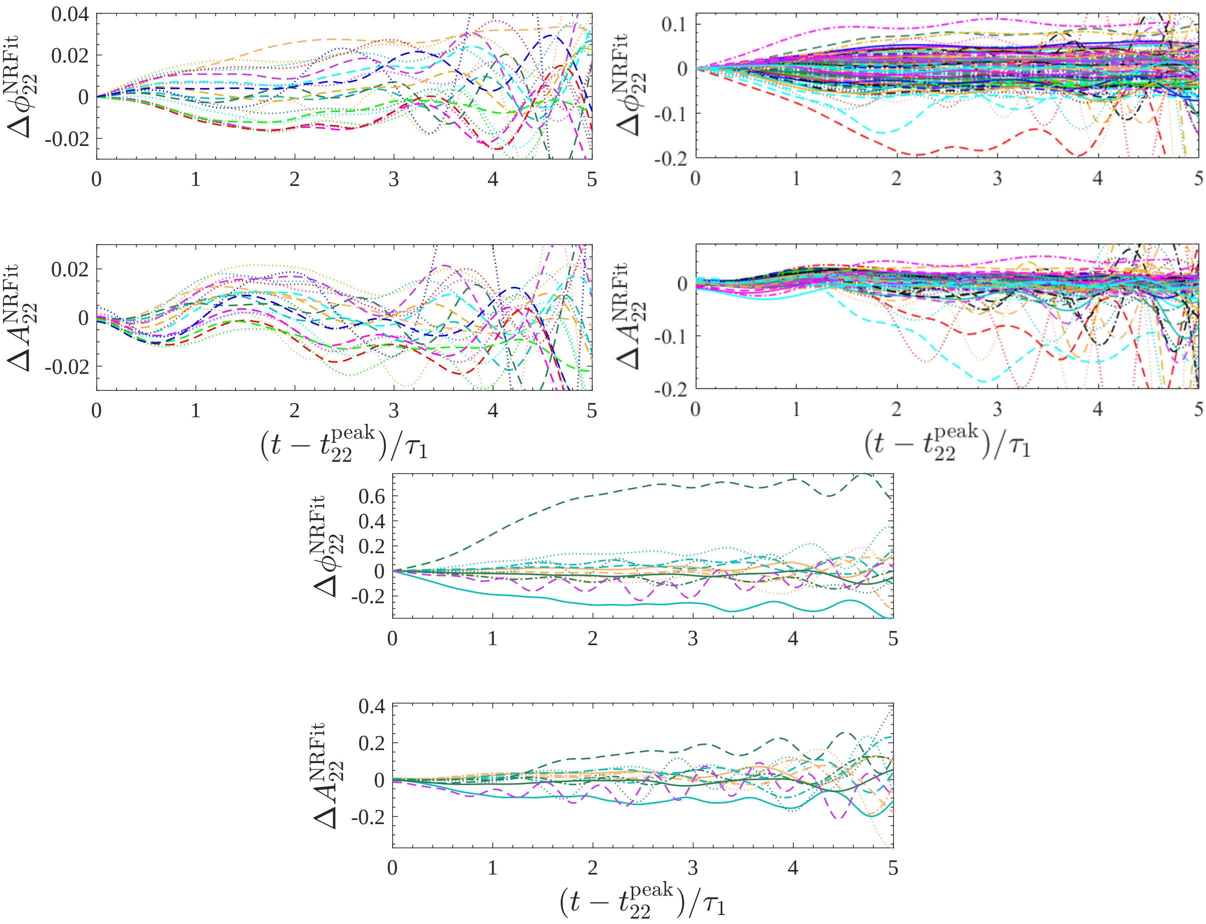

Figure 4.3: The performance of the $(2,2)$ mode postmerger-ringdown template waveforms. The top row shows the phase error $\Delta\phi_{22}^{\rm NRFit} \equiv \phi_{22}^{\rm NR} - \phi_{22}^{\rm fit}$, while the bottom row shows the fractional error of the amplitude $\Delta A_{22}^{\rm NRFit} \equiv (A_{22}^{\rm NR} - A_{22}^{\rm fit})/A_{22}^{\rm NR}$. The panels show: (top-left) The non-spinning `SXS` waveforms. (top-right) The spinning `SXS` waveforms. And (bottom) the spinning `BAM` waveforms. The time is shifted to the peak such $t_{22}^{\rm peak} = 0$ and normalized to the damping time of the fundamental QNM given as $\tau_1 \equiv M_{\rm BH}/\alpha_1$.

Even though the hierarchical nature of the fit is not highlighted for this template, it is still done in such a manner. The orbital and equal-mass contribution are fitted one-dimensionally each. The extrapolation to higher mass-ratios is done through coefficients proportional to X_{12}. The coefficients of the fit are listed in Tab. B.4. The reader should note that the effective spin $\hat{S}$ was exploited here again for the phase, while the amplitude parameter $Y = c_3^{A_{22}}$ was fitted with $\hat{a}_{\rm eff}$. Even though, other than for the frequency and amplitude this structure cannot be observed directly when looking at the data for $Y = \left\{c_3^{A_{22}}, c_3^{\phi_{22}}, c_4^{\phi_{22}}\right\}$. These spin-variables do not simplify the structure presented by the individual mass-ratios as it was for the frequency in Fig. 4.1. Yet, as will be shown in the next section, the performance of the template when using these variables is improved.

4.2.8 *Merger-ringdown*-ringdown template performance

In the discussion above fits of the individual parameters making up the postmerger template have been presented. Before the focus is shifted to the comparison of the full `TEOBResumS` model with NR, it is useful to consider the performance of the postmerger template. Two quantities are relevant when evaluating the template performance on an NR waveform. These are $\Delta\phi_{22}^{\rm NRFit} \equiv \phi_{22}^{\rm NR} - \phi_{22}^{\rm fit}$ and $\Delta A_{22}^{\rm NRFit} \equiv (A_{22}^{\rm NR} - A_{22}^{\rm fit})/A_{22}^{\rm NR}$ which are plotted in Fig. 4.3 for (from top-left over top-right to bottom) the non-spinning `SXS` waveforms, the spinning `SXS` waveforms and the `BAM` waveforms. The top row shows $\Delta\phi_{22}^{\rm NRFit}$ while the bottom row shows $\Delta A_{22}^{\rm NRFit}$. Typically, a good agreement between the template and the NR would be constituted by $\left\|\Delta\phi_{22}^{\rm NRFit}\right\| < 0.2$ and $\left\|\Delta A_{22}^{\rm NRFit}\right\| < 0.1$.

The only two significant outliers beyond this limit can be found in the right plot presenting the `BAM` data. These are $(8, 0.8, 0)$ (light blue, solid) and $(8, 0.85, 0.85)$ (green, dashed). As already discussed above the `BAM` waveform $(8, 0.85, 0.85)$ did show a divergence from waveforms of similar parameters therefor this outlier is not that difficult. Still it will be shown below (see Sec. 4.3) that through an improved NR calibration this behavior could in principle be captured, but this in fact does push the boundaries of what can captured with the analytical flexibilities of the `TEOB` infrastructure as will be discussed below. As will be further shown in chapter 6, once an improved waveform with heightened resolution was available, the postmerger as well as many other parts of the NR calibration have been redone and while the overall quality only improved slightly the main goal of these improvements is achieved as `TEOBiResumS_SM` does indeed show excellent agreement with `BAM` $(8, 0.85, 0.85)$.

4.3 EOB/NR comparison and the unfaithfulness

When comparing a waveform model to a large catalog of NR it is useful to start the analysis by computing the unfaithfulness $\bar{F}$ between the model and the full catalog. Recall that for second generation GW detectors such as advanced LIGO and advanced Virgo the aim is to have an EOB/NR faithfulness, computed with respect to the advanced LIGO PSD [8], of $F > 97\%$ at minimum, but ideally $F > 99\%$ [88, 112]. Similar standards have been applied for *e.g.* `SEOBNRv4` [53].

Unfaithfulness of `TEOBResumS` vs. `SXS`: Now that `TEOBResumS` is fully calibrated to NR it is necessary to access if it meets the requirements for GWA. To this end the unfaithfulness was computed between `TEOBResumS` and the `SXS` and `BAM` data contained in the *calibration* set, defined in Sec. 3.2. Fig. 4.4 (top-left) shows the $\bar{F}$ computation of `TEOBResumS` and `SXS` for the total mass varied between 10 and $200 M_\odot$. The maximum unfaithfulness reached is $\max(\bar{F}) \lesssim 2.7 \times 10^{-3}$ with the exception of a single outlier $(3, +0.85, +0.85)$, `SXS:BBH:0293`, reaching a maximum of $\max(\bar{F}) = 7.1 \times 10^{-3}$. This is a clear improvement over the previous implementation of the `TEOB` avatar presented in Ref.v [132] (see Fig. 7 therein) and well below both the 3% (light-blue, dotted, horizontal line) and the ideal limit of 1% (black, dotted, horizontal line). Thus, clearly meeting the quality requirement for GWA[7]

Unfaithfulness, the outlier `SXS` $(3, +0.85, +0.85)$: Even though `SXS:BBH:0293` $(3, +0.85, +0.85)$ does not violate the 1% bound, it does exceed the NR-NR unfaithfulness computed for the `SXS` data, shown in the top-left panel of Fig. 3.1, which never exceeds 10^{-4} for `SXS:BBH:0293`, even when this is reduced to the conservative estimate of 0.5%. Thus, it is still worth to investigate the origin of the differences. When checking c_3 of #23 of Tab. 4.1 it becomes plausible that the difference between $c_3^{\rm firstguess} = 16.5$ and $c_3^{\rm fit} = 14.38$ is potentially responsible for the increased unfaithfulness. To access

---

[7] While this is a very good result and, at the time, was the lowest max $\left[\max(\bar{F})\right]$ ever achieved by a comparison of an EOB model to the `SXS` catalog presented. This however only the first part of preparing a model for practical use in GWA. Paper I further presents a stand-alone C-implementation of `TEOBResumS` and an example analysis of GW150914, proving that the model is ready for application real data analysis.

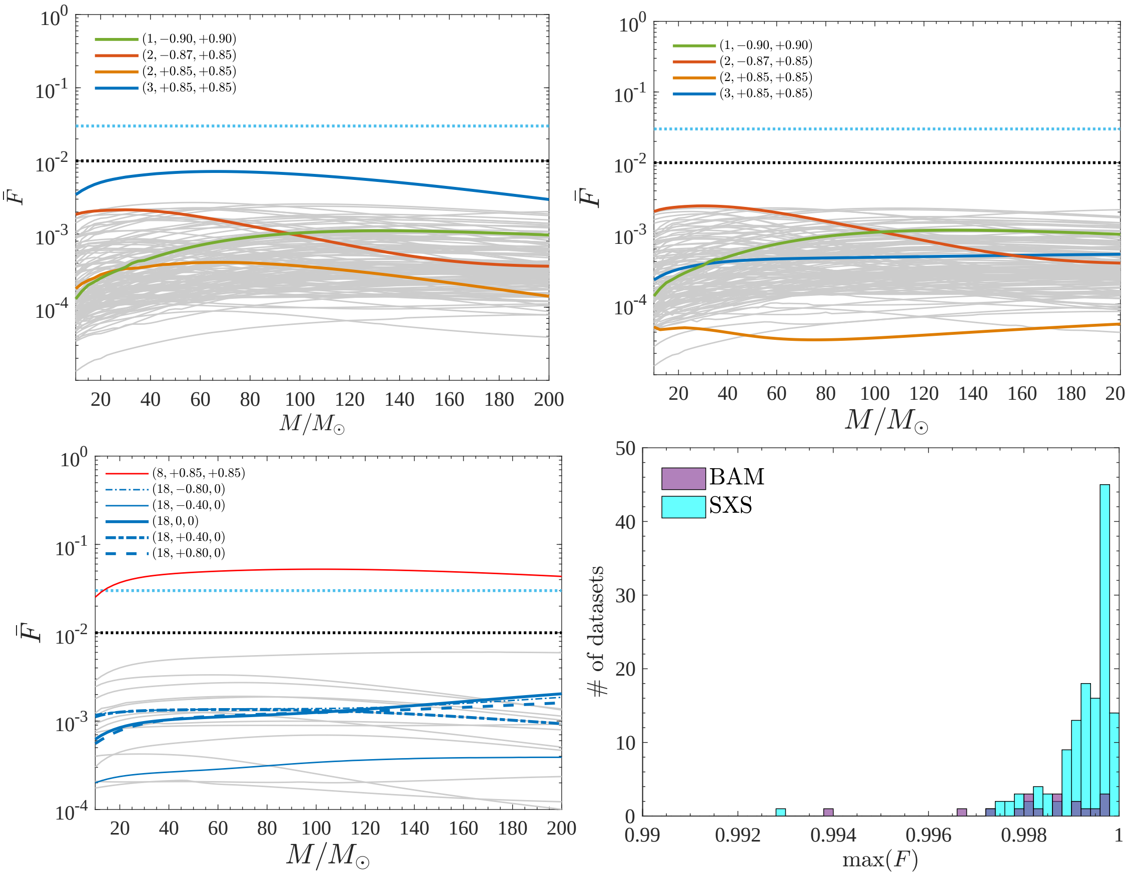

Figure 4.4: The unfaithfulness $\bar{F}_{\mathrm{EOB/NR}}$, eq. (A.12), `TEOBResumS` vs the *calibration* set of `SXS` and `BAM` waveforms. The unfaithfulness was computed with PSD [8]. (Top-left) `TEOBResumS`, implemented using the c_3 modeled after eq. (4.11), compared to the *calibration* set of SXS data, both spinning and non-spinning waveforms. The unfaithfulness never reaches the 1% limit. With the exception of a single waveform $\max(\bar{F}) \lesssim 2.5 \times 10^{-3}$ is achieved all over the SXS *calibration* set. For `SXS:BBH:0293`, $(q, \chi_1, \chi_2) = (3, +0.85, +0.85)$, $\max(\bar{F}) \simeq 7.1 \times 10^{-3}$ is found. (Top-right) $\bar{F}$ computed over the same set of `SXS` waveforms against `TEOBResumS`. The representation of c_3 has however been modified with an additional term proportional to $\nu \hat{a}_0^2 \sqrt{1-4\nu}$ in the functional form added to Eq. (4.11). One finds $\max(\bar{F}) < 2.5 \times 10^{-3}$ all over. (Bottom-left) $\bar{F}_{\mathrm{EOB/NR}}$ computed of `TEOBResumS` and `BAM` presented in Refs. [101, 108, 109]. c_3 is modeled by the fitting template eq. (4.11). (Bottom-right) Global picture of the maximum value of the EOB/NR faithfulness F, Eq. (A.12) over SXS and `BAM` NR data, corresponding to the plots in the top-left and bottom-left. The only outlier above 1% or 3%, $(8, +0.85, +0.85)$, is omitted from the figure.

the potential improvement from a stronger fit of c_3 , the functional form of the template eq. (4.11) is modified in the unequal-mass through the introduction of a *quadratic* in $\hat{a}_0$, taking the form $p_5 \nu \hat{a}_0^2 \sqrt{1-4\nu}$, introducing the fitting coefficient p_5. The updated fit is given in Sec. 4.2.3. Once the fit is calibrated, the unfaithfulness between the `SXS` waveforms and `TEOBResumS` is recomputed and shown in Fig. 4.4 (top-right). Two things are especially noteworthy. First, $\max(\bar{F}) < 2.5 \times 10^{-3}$ is reached all over the `SXS`-*calibration* set. Further, $(3, +0.85, +0.85)$ lies now at $\max(\bar{F}) = 5 \times 10^{-4}$, a remarkably good agreement, while still above the corresponding value of $\bar{F}_{\mathrm{NR/NR}}$, it is well below the conservative estimate of the uncertainty. While it might seem tempting based on these results to simply chose the improved fit of c_3 it can be seen that for larger mass-ratios the fit of c_3 this fit diverges and would require further waveforms to inform it to remain stable in the large-mass-ratio region of the parameter space. Thus, for now the conservative approach is chosen and as will be discussed below an alternative route to improvement of `TEOBResumS` will be outlined, that will come

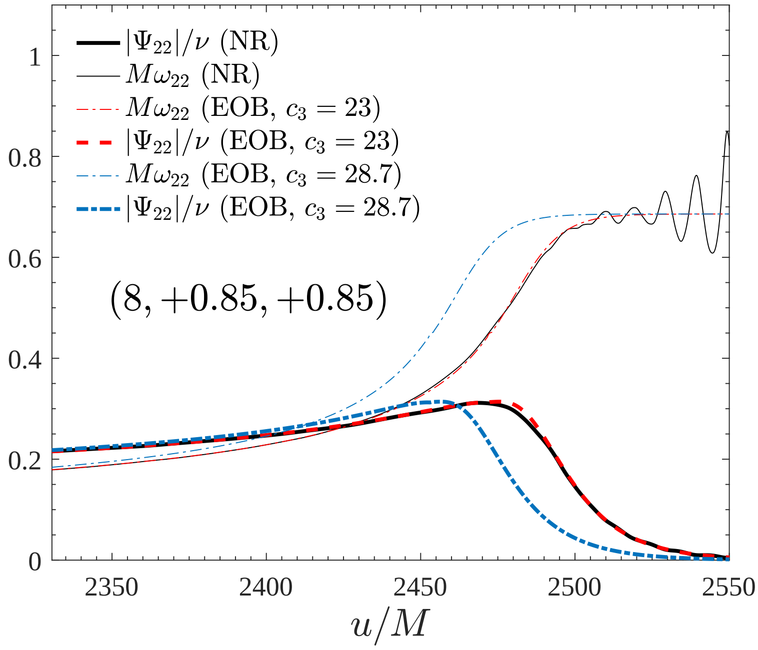

Figure 4.5: The `BAM` catalog gave an excellent opportunity to test the modelization in the large-mass-ratio and large spin region. In particular the extrapolation of c_3 can be tested and improved greatly through the addition of the `BAM` catalog. At the time of Paper I, with an insufficiently accurate version of `BAM` $(8, +0.85, +0.85)$, it was shown that an improvement of $c_3 = 28.7$ down corrected to $c_3 = 23$ indeed lowers the unfaithfulness from going up to 5.2% down to $\bar{F} \simeq 1.3 \times 10^{-3}$. This figure shows explicitly the time domain comparison between the `TEOBResumS` and `BAM` $(8, +0.85, +0.85)$, with `TEOBResumS` evaluated for both $c_3 = 28.7$ and $c_3 = 23$, aligned with the `BAM` waveform in the frequency interval $[0.2, 0.35]$. This frequency interval is very close to merger and in principle it would be necessary to determine c_3 accurately it would be necessary to align in a much lower frequency interval. However, $c_3 = 23$ is actually very close to the limit at which the NQC corrections can still be applied consistently, as any smaller values of c_3 would lead to the iterative determination of the NQC (introduced in Sec. 2.3.2) to diverge. Thus, to keep in line with the conservative mindset employed in the calibration of `TEOB` models an improvement of the analytical baseline will be necessary before improving the model.

to fruition in `TEOBiResumS_SM`, solving these issues as will be shown in chapter 6.

Unfaithfulness: `TEOBResumS` vs. `BAM`: The bottom-left panel of Fig. 4.4 shows the unfaithfulness computed between `TEOBResumS` and the `BAM` catalog. While the $q = 2$ and $q = 4$ waveforms overlap with the `SXS` coverage, the $q = 8$ and $q = 18$ spinning waveforms significantly extend the parameter space coverage of spinning waveforms. While for most waveforms an excellent agreement between NR and `TEOBResumS` is found, this is not the case for the `BAM` waveforms $(8, +0.85, +0.85)$ configuration, that yields a very NR/EOB disagreement of $\max(\bar{F}) \simeq 5.2\%$. As mentioned in the discussion above at several points, this waveform was at the time of Paper I not sufficiently accurate even though it was already once improved relative to a waveform included in the previous analysis presented in Ref. [132]. Yet this inaccuracy of the `BAM` waveform was not sufficient to justify this large a value of the unfaithfulness. Thus an investigation of the origin behind this disagreement is needed.

Unfaithfulness, the outlier `BAM` $(8, +0.85, +0.85)$: The origin of the increased unfaithfulness lies within an inaccuracy of the inspiral-plunge waveform of `TEOBResumS`. On the other hand, the NR-calibrated description of NQC and postmerger-ringdown waveform, even though, not informed by `BAM` $(8, +0.85, +0.85$ still captures the waveform accurately. Fig. 4.5 illustrates this point more clearly through comparing `TEOBResumS`(blue, dash-dotted, lines) to the NR (black) waveform as well as modified `TEOBResumS` waveform for which the fit value of $c_3 \approx 28.7$ was replaced by $c_3 = 23$ (red). The `TEOBResumS` waveforms have been aligned to the NR counterpart in the frequency interval $[0.2, 0.35]$, of the late inspiral-plunge region. Even though the alignment was done so close to merger the `TEOBResumS` (blue) shows a significant departure from the NR, while the modified value of c_3 does indeed lead to an almost perfectly accurate agreement with NR. This can be reproduced on the level of unfaithfulness as $\bar{F} \simeq 1.3 \times 10^{-3}$ with an improved value of c_3. While this seems to require an update in the NR calibration, two arguments stand against it. (i) The `BAM` $(8, +0.85, +0.85)$ does show indicators of being insufficient accuracy and precision. Therefor, it should not be included in the NR calibration. (ii) The improved value of c_3 is in fact almost at the boundary at which the NQC correction parameters $\left(a_1^{22}, a_2^{22}\right)$ do converge. Any further reduction in c_3 would lead to divergent NQC corrections. This indicates that the NR calibration is at the limit of what it can be used for. Therefor, Paper I concluded with leaving this for future work and in fact chapter 6 (following the results presented in Paper III) will show that including the improved factorization and resummation of the waveform presented in Refs. [123, 129] indeed addresses this issue sufficiently, producing an excellent agreement between `TEOBiResumS_SM` and `BAM` $(8, +0.85, +0.85)$.

Unfaithfulness, Summary: A global representation of the unfaithfulness computation is given as a histogram in Fig. 4.4 (bottom-right), showing the maximal faithfulness over the `SXS` and `BAM` excluding `BAM` $(8, +0.85, +0.85)$ to keep the plot informative. It is useful to highlight the results of the unfaithfulness computation and insights about the analysis:

(i) The unfaithfulness is a powerful tool to identify disagreements between NR and `TEOBResumS` . Yet, it is ill-suited to be used to identify the problem, while an analysis in the time-domain will often prove to be more insightful to identify the problem. It is then useful to compute the unfaithfulness to confirm the origin of the problem.

(ii) The unfaithfulness all over the `SXS`-*calibration* set is in very good agreement reaching $\bar{F} \lesssim 2.7 \times 10^{-3}$ with the exception of a single outlier, not breaching the 1% bound. This single outlier indicates a need for further improvement of the analytical information included in the model.

(iii) For the `BAM` catalog a similar result is reached[8]. The outlier `BAM` $(8, +0.85, +0.85)$ is however far stronger.

(iv) Following the analysis of `BAM` $(8, +0.85, +0.85)$ in Fig. 4.5 an improvement of the analytical baseline information incorporated into `TEOBResumS` is motivated and it is pointed out that the the improved factorized and resummed waveform of Ref. [123] represents a possible path forward. Once included the improved waveform will indeed solve this problem as will be discussed in chapter 6.

---

[8] The astute reader may have noticed a single `BAM` waveform above the 0.4% limit set as the goal over the `BAM` catalog. This unfaithfulness corresponds to $(8, +0.8, 0)$ and does indeed not produce any further insight other then confirming the analysis of `BAM` $(8, +0.85, +0.85)$, which indicates an improved analytical baseline becomes necessary and is thus omitted from the discussion as an explicit outlier, even though technically speaking it is one.

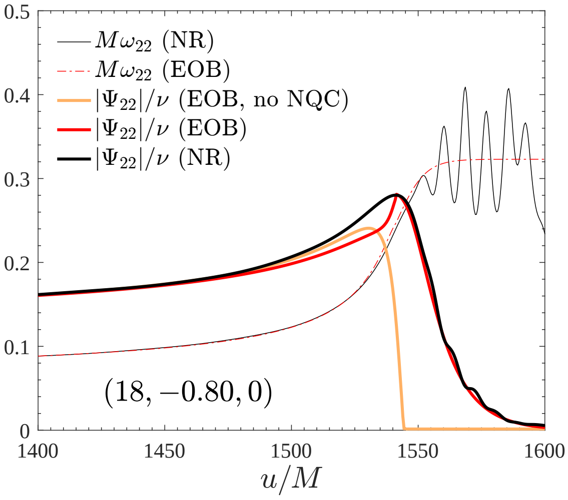

Figure 4.6: During a more thorough comparison of `TEOBResumS` and the `BAM` catalog a peculiar feature appears. For `BAM` $(18, -0.80, 0)$, the `TEOBResumS` waveform shows a peculiar unphysical feature. As the full EOB waveform shows a dip and sudden rise around the peak of the amplitude appears, even though the waveform prior to inclusion of the NQC does not repeat this feature. As the frequency is not impacted by this it is not surprising that this does not show up as an effect in the unfaithfulness, y is not impacted Frequency and amplitude comparison between `TEOBResumS` and `BAM` for $(18, -0.80, 0)$. The full waveform amplitude develops a slightly unphysical feature due to the action of the NQC parameters. The frequency (as well as $\bar{F}$) is unaffected by this.

Beyond the unfaithfulness: Even though the unfaithfulness analysis was clearly useful it is still necessary to study the waveform further. Fig. 4.6 illustrates one such effect that, due to lack of impact on the frequency, does not show as an increase in the unfaithfulness. As can be seen the `TEOBResumS` waveform (red) compared with `BAM` $(18, -0.80, 0)$ (black) shows a peculiar, unphysical dip in the amplitude close to merger. Looking at the `TEOBResumS` waveform prior to the application of the NQC (orange) it can be seen that this pathological feature of the amplitude originates in the NQC correction. Further investigation shows that the orbital EOB frequency Ω indeed becomes zero close to merger. When computing the individual contributions to Ω it was found that (G_S, G_{S_*}), defined in Sec. 4.1.1, becomes very large and negative if both spins are large and anti-aligned with respect to the orbital angular momentum. Now it is important to note that in the case of a test-particle plunging into a Kerr-BH with large anti-aligned spins the orbital frequency does indeed change sign as the dragging of the frame of the test-particle dominates close to the merger. This is however not the case here. Thus, it is useful to briefly outline the source of this issue without going to deep into it.

When Ref. [76] first defined the `TEOB` infrastructure, (G_S, G_{S_*}) where expressed as functions of the inverse centrifugal radius $1/r_c$ as opposed to merely the inverse radius $1/r$ (see Eqs. (36)-(37) of [76]). After reversing this change it can be seen that the frequency Ω does in fact remain positive in this region. As this effect does not have large practical implications for the use of `TEOBResumS` it does not yet warrant to change the model at this stage, which in turn prevents the necessity for a full recalibration to NR. Rather the effect on the amplitude will be explored and the robustness in the large-mass-ratio, large-anti-aligned-spins region will be explored in Sec. 4.4. Further, it will be shown that a modification of Δt_{NQC} does indeed improve the robustness of the waveform at merger.

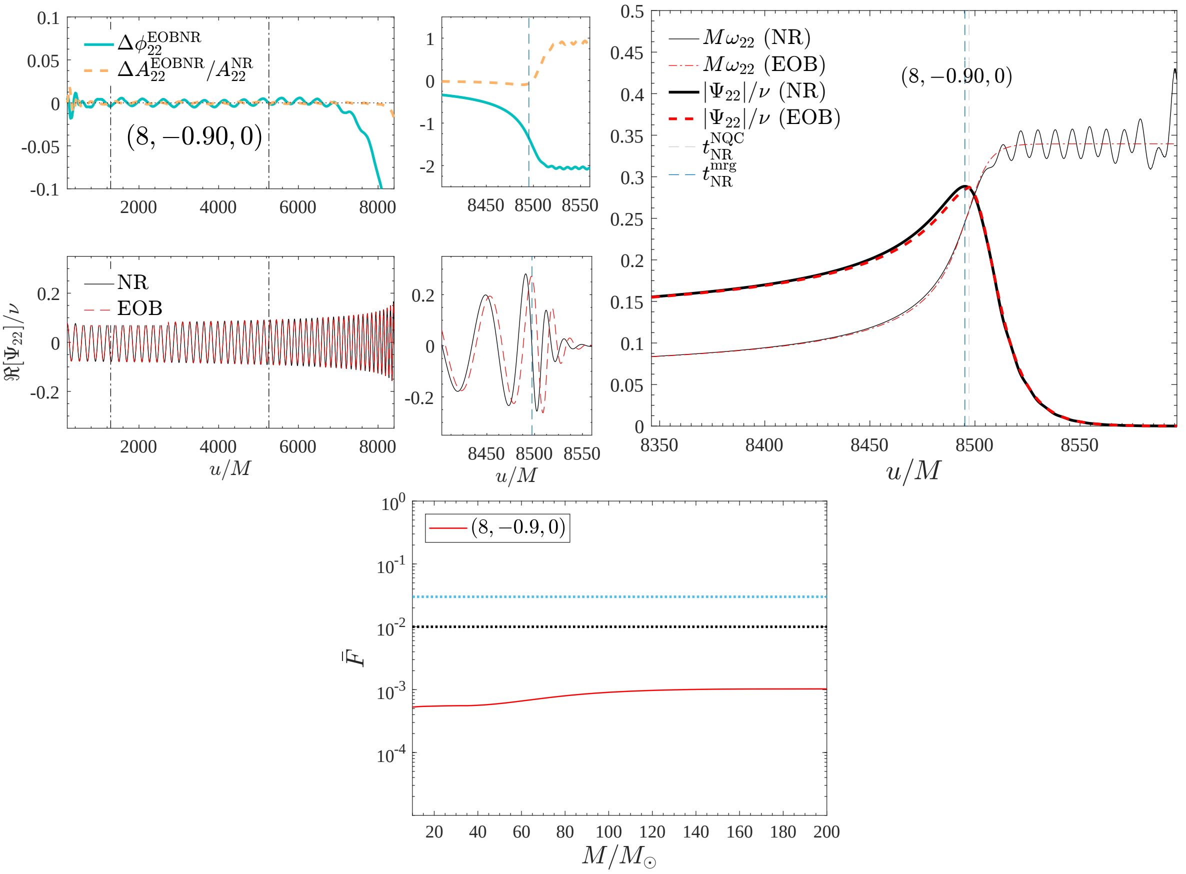

Figure 4.7: The waveform `SXS:BBH:1375`, $(8,-0.9,0)$, is a remarkably accurate waveform and thus it is worth taking a closer look at the performance compared between `TEOBResumS` and `SXS` for this waveform. The waveforms are compared on the level of phasing with vertical lines marking the alignment in the inspiral (top-left), amplitude and frequency around merger, aligned in the frequency interval $[0.2, 0.3]$ close to merger (top-right) and the unfaithfulness (bottom). The alignment of the waveforms in the early inspiral leads to an accumulated dephasing of -1.3 rad at the NR $(2,2)$ mode waveform peak. The unfaithfulness reaches $\max(\bar{F}) = 1.027\times10^{-3}$. All over `TEOBResumS` and `SXS:BBH:1375` show an excellent agreement. It stands out however that the postmerger is not perfectly captured, as can be observed in the middle panel. This is due to the fact that currently, model does not account for the beating between positive and negative frequency QNMs. An example of how to implement this feature can be found for the test-particle limit in Ref. [45].

4.3.1 An extreme BBH configuration: $(8,-0.90,0)$

During the preparation of Paper I, a new high precision `SXS` waveform was published: `SXS:BBH:1375` describing a BBH system with $(q,\chi_1,\chi_2) = (8,-0.90,0)$ [100]. Aside from it's exceptional quality it is remarkable for two reasons from the perspective taken in Paper I. First, with an effective spin of $\hat{S} = -0.7111$ it is slightly more relativistic than `BAM` $(8,-0.85,-0.85)$ with $\hat{S} = -0.6821$ (see Tab. F.4). Secondly, while this is a marginal shift it is a marginal shift in a highly relativistic region therefor granting a useful additional point to test `TEOBResumS` in a region where the modeling of the analytical baseline is particularly challenging[9]. It is instructive to now compare the `TEOBResumS` with the `SXS` waveform thoroughly to introduce the reader to several aspects of such a comparison.

The full comparison of `TEOBResumS` and `SXS:BBH:1375` is shown in Fig. 4.7. The top-left panel shows the comparison of the phasing and amplitude, the alignment region marked by vertical black-dashed lines. The light-blue line represents the phase difference between `TEOBResumS` and `SXS`

---

[9] As mentioned above and as will be discussed in Sec. 4.4, the region of large mass-ratios and large spins anti-aligned with respect ot the orbital angular momentum.

waveform, showing a slight oscillation around zero. Inspecting the parameters further shows that `SXS:BBH:1375` has a slight residual eccentricity $\sim 1.1 \times 10^{-3}$. This is of course to be expected as in an any NR setup it is next to impossible generate eccentricity-free waveforms on a consistent basis. Yet this is different in the analytical setup of the `TEOB` model. The initial data is generated with the 2PA approximation [75, 82] generating almost completely eccentricity-free waveforms. Further, one notices that the departure of the phase difference from the oscillation around zero during the late inspiral and the plunge, indicating a slightly slower plunge of the `TEOBResumS` system with respect to the NR system. A possible physical interpretation might be that the prediction of the `TEOBResumS` spin-orbit coupling is too low. This could be captured through a modification of c_3[10].

The top-right panel of Fig. 4.7 shows the comparison of the amplitude and frequency around the merger aligned in the frequency interval $[0.2, 0.3]$. An alignment in a frequency window so close to the merger is often useful to access the behavior of the two waveforms around merger as the accumulated dephasing often distorts the picture if both waveforms are aligned in the early inspiral. Even though this waveform lies outside the domain of calibration of both NQC and postmerger, both waveforms agree very well on the level of amplitude as well as frequency. An additional phenomenon that can be observed in this waveform is the beating between positive and negative frequency QNMs, well known in the test-particle limit for Kerr-BHs with large anti-aligned spins [45], creating oscillations in the ringdown of the NR waveform. Finally, the unfaithfulness is presented in the bottom panel of Fig. 4.7. As can be seen by eye the agreement is excellent. The unfaithfulness, reaching $\max(\bar{F}) = 1.027 \times 10^{-3}$, is well below the 1% limit and the conservative NR uncertainty of 0.5%. Reiterating that even though a dephasing of 1 red occurs if aligned in the inspiral this disagreement is not of concern for the practical application of the model.

In summary, four observations can be made:

(i) The postmerger template performed very well in comparison to `SXS:BBH:1375`. While the parameters used in the template would not necessarily improve through the inclusion of this waveform it might stabilize the extrapolation to higher mass-ratios with spins anti-aligned to the orbital angular momentum.

(ii) As the ringdown is a very clean example of beating between positive and negative frequency quasi-normal-modes [45] this waveform will be useful to explore extensions of the postmerger template.

(iii) Despite the small eccentricity this waveform can be used to inform NR quantities related to the spinning sector of the inspiral, e.g. c_3.

(iv) As the subdominant modes are very clean and accurate as well it is likely that many fits of subdominant mode parameters will benefit strongly from the inclusion of this waveform.

4.4 Waveform robustness outside the domain of calibration

The fits of both NQC and postmerger, the peak in particular, have been done in similar fashion. The same spin variables have been used consistently for quantities depending on whether they

---

[10] However, the reader should note that this disagreement is perfectly within the acceptable margin of error for the application in any physical context.

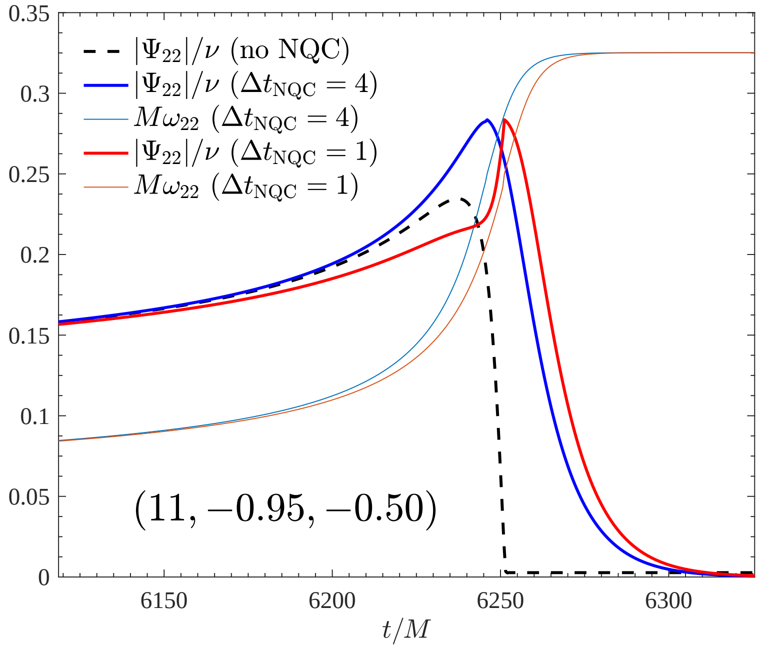

Figure 4.8: $(q,\chi_1,\chi_2) = (11,-0.95,-0.50)$ lies well within the region for which $\Delta t_{\rm NQC} = 4$ (blue) is used instead of $\Delta t_{\rm NQC} = 1$ (red), given by eq. (4.39)-(4.40). As can be seen the choice of $\Delta t_{\rm NQC} = 4$ allows for a smooth transition between the inspiral-plunge waveform and the postmerger template, avoiding the unphysical feature in the amplitude, present if $\Delta t_{\rm NQC} = 1$ is used.

were associated to the amplitude or the frequency. Amplitude and frequency at peak used identical templates for the spin-dependence as the NQC amplitude and frequency, ensuring a similar behavior asymptotically by design. These choice lead to a remarkable stable and robust extrapolation outside the domain of calibration. Here, the robustness of the waveform is tested for large mass-ratios (up to $q \leq 20$) and large spin magnitudes both aligned and anti-aligned with respect to the orbital angular momentum. However, it is important to point out that in particular in the case of large-aligned spins the NQC correction parameters become large and diverge during the iterative determination, thus, only a first determination of the NQC is possible in these cases. Similar behavior could already be observed when comparing `TEOBResumS` to `BAM` $(8, +0.85, +0.85)$, where the NQC parameters became of order 10, limiting the choice of c_3 for which the NQC parameter can be iterated upon for consistency between flux and waveform.

Pathological features in the amplitude: As was already observed for $(18, -0.8, 0)$, the waveform shows pathological features in the amplitude for mass-ratios $q \geq 8$ and large, anti-aligned spins. The origin was already pointed out to lie in the crossing of the frequency through zero and becoming negative during shortly before the merger for these waveforms. An example of this behavior is shown in Fig. 4.8 for $(11, -0.95, -0.50)$. While the frequency no significant issues, the amplitude clearly demonstrates an unphysical and pathological behavior. Similarly, to `BAM` $(18, -0.8, 0)$, the *bare* EOB-waveform amplitude is clean and without any clear and present issues that might cause this effect prior to the addition of the NQC correction factor. It was verified explicitly that Ω crosses zero for this case, confirming the origin of this unphysical feature. As mentioned above the appropriate solution of this problem is a modification of the spin-orbit sector of the Hamiltonian, yet this would require for the inspiral to be recalibrated and retested, which due to the limited practical impact of this pathology would be unwarranted for `TEOBResumS`, but to be remembered for

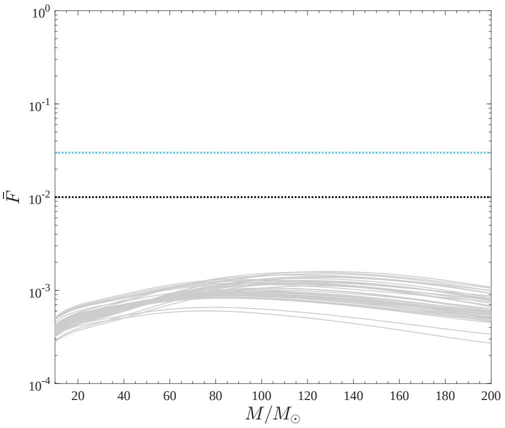

Figure 4.9: The transition, defined in eq. (4.39)-(4.40), introduces a jump between $\Delta t_{\rm NQC} = 1$ and $\Delta t_{\rm NQC} = 4$. This jump has potentially the effect that a small change in the parameters could potentially create a disproportionate jump in the waveform. Thus, it is necessary to access the error introduced by this transition. To this end the unfaithfulness between waveforms along the border is computed. One waveform each is generated with $\Delta t_{\rm NQC} = 1$ and $\Delta t_{\rm NQC} = 4$ and their unfaithfulness is plotted against the typical mass-spectrum from $10M_\odot$ to $200M_\odot$.

future models. A pragmatic solution to this problem can however be found in replacing $\Delta t_{\rm NQC} = 1$ with the increased value $\Delta t_{\rm NQC} = 4$ for the problematic waveforms. Several further configurations showed this pathology as well and it was possible to identify the region in which it occurs. A two-step boundary was taken around this area and at the boundary $\Delta t_{\rm NQC} = 1$ is replaced by $\Delta t_{\rm NQC} = 4$. The area in which the change is applied is given as

$$8 < q < 11 \text{ and } \chi_1 < -0.9, \tag{4.39}$$

$$11 < q < 19 \text{ and } \chi_1 < -0.8. \tag{4.40}$$

It is worth pointing out that despite this the lack of dependency on χ_2, the boundary still sufficiently prohibits the occurrence of the amplitude-pathology for most cases. To estimate the uncertainty this jump produces in the waveform the unfaithfulness is computed at the border between waveforms generated for identical parameters with $\Delta t_{\rm NQC} = 1$ and $\Delta t_{\rm NQC} = 4$. As it is found that $\bar{F}$ (see Fig. (4.9)) on average falls around 10^{-3}, it can be safely assumed that the error introduced through this modification is limited and will not create additional errors.

The reader should note though, that in some highly extreme cases (see Fig. 4.10) the feature still survives as the crossing through zero cannot be prohibited by this measure completely, yet this was taken as trade-off as the error introduced at the boundary is sufficiently low and the effect only occurs in sufficiently rare cases. Ultimately, to solve this problem the $(\hat{G}_S, \hat{G}_{S_*})$ need to be adapted to prevent this crossing of the frequency Ω through zero, yet this would require a new determination of c_3 and a repeat of the analysis of the model performance in the spinning sector, which due to the limited impact seems unwarranted at this stage and will be addressed in `TEOBiResumS_SM`.

Waveform robustness for large spin magnitudes: Lastly, it remains to be explored how the model performs for large spins outside the domain of calibration. In particular the waveform around merger is most strongly adapted to NR and thus might show potential issues. Several

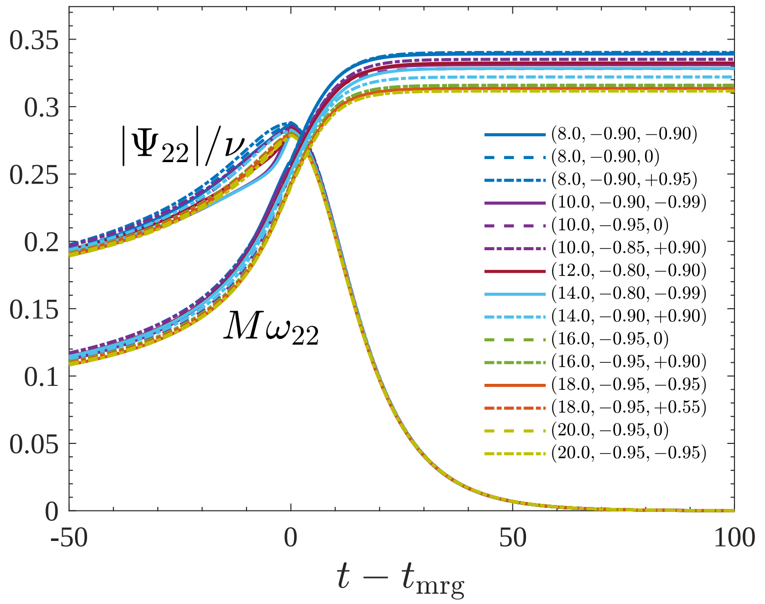

Figure 4.10: Due to the modified $\Delta t_{\rm NQC}$ given by eq. (4.39)-(4.40), it is important explore the consistency at peak between the fitted postmerger template and the analytical inspiral waveform. As can be seen largely the unphysical amplitude is gone for most waveforms. Only two quite extreme waveforms $(10, -0.9, -0.99)$ and $(14, -0.8, -0.99)$ show a small dip in the amplitude at merger. As these effects only occur in these very extreme cases and only mildly there, these are acceptable limits onto the model. And in fact it can be checked that these waveforms become stable and free of pathological features for `TEOBiResumS_SM`.

waveforms have been computed. Fig. 4.11 shows waveforms, listed in Tab. I of Ref. [53] and used in the calibration of `SEOBNRv4`, which have not been available in the calibration of `TEOBResumS`. To explore the robustness of `TEOBResumS` the parameter combinations have been evaluated and plotted focusing in on amplitude and frequency around merger. It is evident that both amplitude and frequency perform excellently and no pathological features can be detected. Fig. 4.10 and Fig. 4.12 systematically explore the large spin regions with χ_1 chosen either to be strongly anti-aligned (Fig. 4.10) or aligned (Fig. 4.12). Here only two highly extreme waveforms, $(10, -0.9, -0.99)$ and $(14, -0.8, -0.99)$, show a sign of the pathology discussed above. Yet these are both highly relativistic with $\chi_2 = -0.99$ for both, thus for now this is an acceptable boundary to robustness of the waveform. In future work this obviously has to be improved upon. On a final note it is important to point out that since $(8, +0.85, +0.85)$ already showed a quite troublesome unfaithfulness it is more than likely that this will be carried over by all waveforms plotted Fig. 4.12 with $8 \geq 8$. Still the absence of clear pathological features in the waveform is an achievement on it's own and suggests that the consistent choice of the NR calibration between postmerger and NQC should be kept in future updates as well.

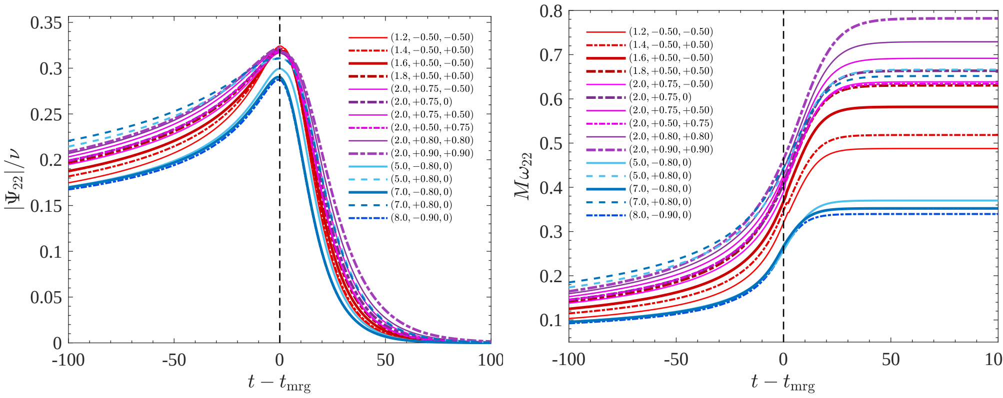

Figure 4.11: Tab. I of Bohé et al. [53] listed several waveforms used in the calibration of `SEOBNRv4` not available in the preparation of Paper I. As a potential sanity check outside the domain of calibration the parameter combinations are evaluated with `TEOBResumS` and the waveform is plotted on the level of both the amplitude (left) and frequency (right) focused in around merger. Demonstrating that that these waveforms indeed seem to behave qualitatively and quantitatively robust as the parameters are varied even outside the domain of calibration of both NQC and postmerger template.

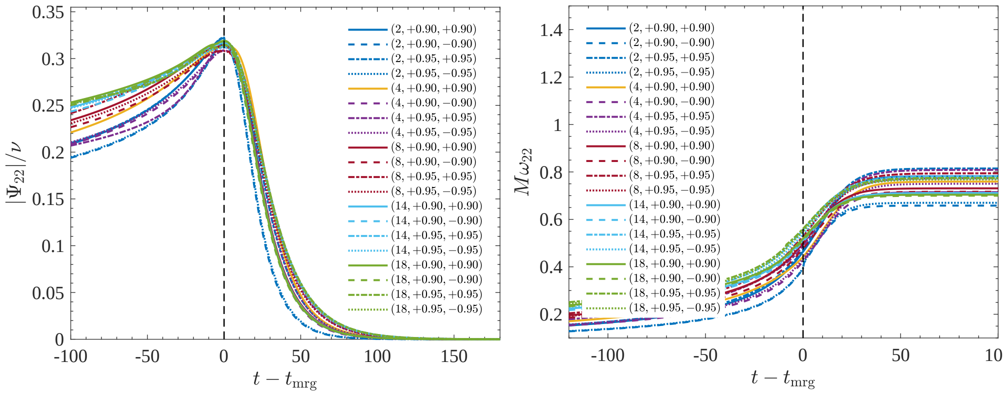

Figure 4.12: The fits of both NQC and postmerger, the peak in particular, have been done in similar fashion with the same variables for both amplitude and frequency quantities. Here several waveforms with high-spins and large range of mass-ratios are shown. Both the amplitude (left) and the frequency (right) are plotted focusing in around merger. The consistency enforced by the fit structure extrapolates exceptionally well leading to a highly consistent waveform throughout the parameter space.

Chapter 5

Subdominant modes: The non-spinning case

This chapter will now extend the discussion of Chapter 4 to include subdominant modes. The discussion will focus on the non-spinning Waveform model `TEOBiResumMultipoles`, both from the perspective of calibration and validation. Chapter 6 will extend this discussion to the spinning sector with `TEOBiResumS_SM`. `TEOBiResumMultipoles` has been introduced in Paper II, calibrated and validated by in total 19 `SXS` waveforms and 3 `BAM` waveforms, listed in Tab. F.14, lines #$526-547$[1].

5.1 Motivation: Subdominant modes

The necessity of including subdominant modes can be seen by a simple consideration. The fully calibrated waveform model `TEOBiResumMultipoles` is compared to `SXS:BBH:0303`, a non-spinning binary of mass ratio $q=10$, in Fig. 5.1. The waveform generated solely from the dominant quadrupolar mode is shown explicitly (dashed orange), next to the full multipolar waveform (dashed blue), both compared to NR. This comparison is done for three different inclination angles $\theta=0,\pi/3$ and $2\pi/3$ (corresponding to ι as used in other places of this thesis). For $\theta=0$ both agree very well with NR. For $\theta=\pi/3$ however the $(2,2)$ mode starts to departure from the NR waveform, and $\theta=2\pi/3$ it indeed almost vanishes. While the full multipolar waveform remains in good agreement with NR for all inclinations. This illustrates the effect of subdominant modes. As can be explored explicitly from eq. (2.4) – (2.5) the relative contributions of the multipoles do depend on the orientation of the observer relative to the source. And, thus, while in many cases the dominant mode is sufficient this is not always the case and it is necessary to incorporate subdominant modes into the waveform model.

5.2 Hamiltonian and waveform

5.2.1 Hamiltonian and the A-potential

The analytical structure of `TEOBiResumMultipoles` is identical to `TEOBResumS` as presented in Sec. 2.3.1 once $S_1=S_2=0$ is set. There are however two difference between the A-potential

---

[1] Within this chapter all unfaithfulness computations have been performed exclusively by Geraint Pratten.

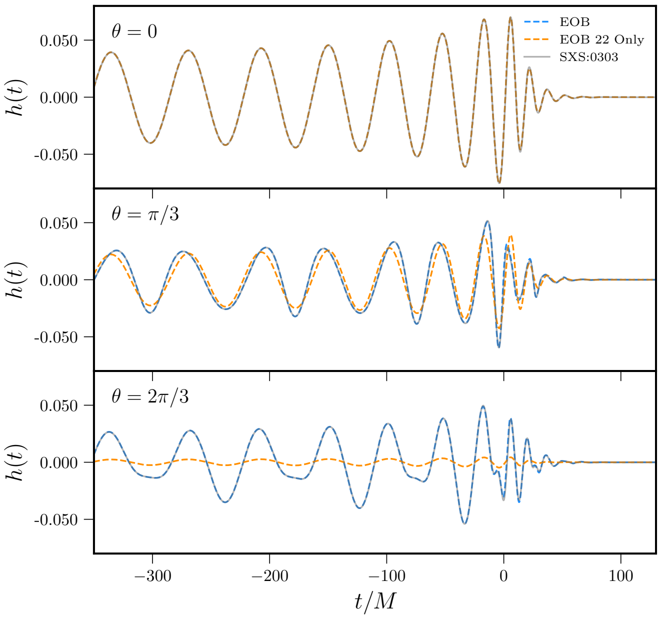

Figure 5.1: `TEOBiResumMultipoles` is compared to `SXS:BBH:0303`, a non-spinning binary of mass ratio $q = 10$, on the level of the pure $(2, 2)$ mode (dashed orange), and the full multipolar waveform (dashed blue). This comparison is done for three different inclination angles $\theta = 0, \pi/3$ and $2\pi/3$ (corresponding to ι as used in other places of this thesis). As for the former two it shows almost no effect which is used, even though the full multipolar waveform shows a better agreement with the NR all over. For the last inclination this is however not the case. The contribution of the $(2, 2)$ mode as good as vanishes and while multipolar waveform remains in good agreement with NR.

used for `TEOBResumS` and `TEOBiResumMultipoles` and thus we redefine eq. (4.1) as it was given in Paper II. The EOB radial potential A is now given as a function of the radius r. The A-potential is upgraded relative to `TEOBResumS` and taken from the full 4PN-accurate analytical term, completed by the 5PN logarithmic term [42, 48, 52, 72, 77], as

$$A^{\rm PN}_{\rm orb}(u) \;=\; 1 \;-\; 2u \;+\; 2\nu u^3 \;+\; \nu a_4 u^4 \;+\; \nu\left[a^c_5(\nu) + a^{\log}_5 \ln u\right] u^5 \;+\; \nu\left[a^c_6(\nu) + a^{\log}_6 \ln u\right] u^6, \quad (5.1)$$

here $u \equiv 1/r$ replaced the centrifugal radius and it's inverse, used in `TEOBResumS`. The 4PN and 5PN logarithmic coefficients are given as

$$a^{\log}_5 = \frac{64}{5}, \quad (5.2)$$

$$a^{\log}_6(\nu) = -\frac{7004}{105} - \frac{144}{5}\nu, \quad (5.3)$$

where the 4PN coefficient, $a^c_5(\nu)$, was computed in Ref. [48] and is given as

$$a^c_5(\nu) = a^{c0}_5 + \nu a^{c1}_5, \quad (5.4)$$

$$a^{c0}_5 = -\frac{4237}{60} + \frac{2275}{512}\pi^2 + \frac{256}{5}\ln 2 + \frac{128}{5}\gamma_E, \quad (5.5)$$

$$a^{c1}_5 = -\frac{221}{6} + \frac{41}{32}\pi^2, \quad (5.6)$$

with the Euler constant γ_E. The reader should note that this marks the another difference in the

A-potential. As stated above `TEOBResumS` utilizes, similar to Ref. [82], a_5^c fixed to its fiducial value $a_5^c = 23.5$ [32, 42, 48]. The coefficient $a_6^c(\nu)$ is chosen to be left flexible and to use it as a vessel for NR information. Before this coefficient is however fitted to NR, the PN-expanded radial potential $A(u)$ is resummed using a Padé approximate as

$$A(u;\nu;a_6^c) = P_5^1\left[A_{\rm orb}^{\rm PN}(u)\right]. \tag{5.7}$$

Due to the change of variable from u_c and r_c to u and r, it is important to restate the product of the A and B potential, $D \equiv A\,B$ which allows to recreate $B(r)$, taken at 3PN accuracy. The D potential is expanded as a P_3^0 approximate and reads

$$D(u) = \frac{1}{1 + 6\nu u^2 + 2(26-3\nu)\nu u^3}. \tag{5.8}$$

5.2.2 Resummed waveform and radiation reaction: two different multipolar EOB models

The discussion now turns to the updated resummation used in `TEOBiResumMultipoles`, which is the largest update in the analytical sector of the model relative to `TEOBResumS`. The standard EOB factorization was first introduced in [81] and have briefly reviewed in eq. (2.33) of Sec. 2.3.2. The new improved resummation starts at the residual amplitude correction factor $f_{\ell m}$ as

$$f_{\ell m} = \left[\rho_{\ell m}(x)\right]^{\ell}\;. \tag{5.9}$$

The individual $\rho_{\ell m}(x)$ are then factorized in an *orbital* and spin-dependent part as

$$\rho_{\ell m} = \rho_{\ell m}^{\rm orb}\hat{\rho}_{\ell m}^{\rm S} \tag{5.10}$$

where the superscript "orb" denotes *orbital* and the superscript "S" denotes *spin*, and all factors are properly resummed following Refs. [123, 129]. This improved resummation, while in the non-spinning case not yet as noticeable, greatly improved the performance of the `TEOB` model avatars. The interested reader is referred to Paper II and Paper III as well as Refs. [123, 129] for an in depth discussion and all necessary details of the improved resummation.

5.2.3 Newtonian prefactors in the waveform

With the NQC factor it is possible to capture several pieces of information that are not yet modeled within any given `TEOB` avatar, even if these are not modeled therein. However, there is a limit to what the NQC factor can correct as already seen on the `BAM` $(8,+0.85,+0.85)$ waveform in the previous chapter. During the testing and improvement of `TEOBiResumMultipoles` it was found that the Newtonian prefactor could be modified to improve the NQC performance.

The general form of the Newtonian prefactor of the circularized waveform is given as

$$h_{\ell m}^{(N,\epsilon)} = \nu c_{\ell+\epsilon}(\nu) n_{\ell m}^{(\epsilon)} x^{(\ell+\epsilon)/2} Y^{(\ell-\epsilon,-m)}(\pi/2,\varphi), \tag{5.11}$$

where $Y(\pi/2,\varphi)$ are the scalar spherical harmonics, $n_{\ell m}^{(\epsilon)}$ are parity-dependent constants given in eq. (5)-(6) of Ref. [81], while $c_{\ell+\epsilon}(\nu)$ represent the leading-order ν dependence. In the case of circularized evolution one finds the frequency parameters $x = v_\Omega^2$. However, following Ref. [73, 74] it was proven that the $(2,2)$ mode indeed performs actually better during the late inspiral and plunge if this constraint (often referred to within `TEOB` literature as Keppler's constraint) is relaxed to $x = v_\varphi^2 = (r_\omega \Omega)^2$ with $r_\omega \equiv r\psi^{1/3}$, where ψ is defined such that v_φ and r_ω satisfy Kepler's law $1 = \Omega^2 r_\omega^3$ during the approximately adiabatic phase of the inspiral. The standard procedure within `TEOB` is commonly to use x replaced by v_φ^2, as it is typically done for the radiation reaction within `TEOB`. As a consequence of this choice the amplitude of some multipoles are suppressed and comparatively small. This fact hinders the performance of the NQC factor that works best if it does not have to strongly correct the waveform. Further, one finds experimentally for the NQC factor that if the *bare* `TEOB` waveform is in fact larger then the NR amplitude, the performance of the NQC factor is usually most efficient.

Thus one way to increase the amplitude is to replace v_φ with v_Ω. However, instead of completely replacing them an individual choice was made multipole by multipole to effectively mimic missing analytical information and lead to a better agreement with the NR and an improved performance of the NQC correction factor. These choices are:

$$h_{22}^{(N,0)} = -8\sqrt{\frac{\pi}{5}}\nu\, v_\varphi^2 e^{-2\mathrm{i}\varphi}, \tag{5.12}$$

$$h_{21}^{(N,1)} = -\frac{8\mathrm{i}}{3}\sqrt{\frac{\pi}{5}}\nu\sqrt{1-4\nu}\, v_\varphi^3 e^{-\mathrm{i}\varphi}, \tag{5.13}$$

$$h_{33}^{(N,0)} = 3\mathrm{i}\sqrt{\frac{6\pi}{7}}\nu\sqrt{1-4\nu}\, v_\varphi v_\Omega^2 e^{-3\mathrm{i}\varphi}, \tag{5.14}$$

$$h_{32}^{(N,1)} = \frac{8}{3}\sqrt{\frac{\pi}{7}}\nu(1-3\nu)\, v_\varphi^2 v_\Omega^2 e^{-2\mathrm{i}\varphi}, \tag{5.15}$$

$$h_{31}^{(N,0)} = -\frac{\mathrm{i}}{3}\sqrt{\frac{2\pi}{35}}\nu\sqrt{1-4\nu} v_\Omega^3 e^{-\mathrm{i}\varphi}, \tag{5.16}$$

$$h_{44}^{(N,0)} = -\frac{64}{9}\sqrt{\frac{\pi}{7}}\nu(1-3\nu)\, v_\varphi^2 v_\Omega^2 e^{-4\mathrm{i}\varphi}, \tag{5.17}$$

$$h_{43}^{(N,1)} - \frac{9\mathrm{i}}{5}\sqrt{\frac{2\pi}{7}}\nu(2\nu-1)\sqrt{1-4\nu}\, v_\varphi^2 v_\Omega^3 e^{-3\mathrm{i}\varphi}, \tag{5.18}$$

$$h_{42}^{(N,0)} = \frac{8\sqrt{\pi}}{63}\nu(1-3\nu)\, v_\varphi v_\Omega^3 e^{-2\mathrm{i}\varphi}, \tag{5.19}$$

$$h_{41}^{(N,1)} = \frac{\mathrm{i}}{105}\sqrt{2\pi}\nu(2\nu-1)\sqrt{1-4\nu}\, v_\Omega^5 e^{-\mathrm{i}\varphi}, \tag{5.20}$$

$$h_{55}^{(N,0)} = \frac{125\mathrm{i}}{12}\sqrt{\frac{5\pi}{66}}\nu(2\nu-1)\sqrt{1-4\nu} v_\Omega^4 v_\varphi e^{-5\mathrm{i}\varphi}. \tag{5.21}$$

For all other multipoles the Newtonian prefactors in the `TEOB` waveform are obtained replacing $x = v_\varphi^2$ in Eq. (5.11) as is the common practice. The reader should note that this modification was not carried over into the waveform multipoles as they enter the radiation reaction. This is clearly an inconsistency between the waveform and the flux. However, an inner inconsistency between any two parts of the `TEOB` model in itself is not necessarily a problem, as the ultimate goal is to reproduce faithful waveforms. Consistency is however a powerful tool to improve the model and if too many inconsistencies are build in can potential increase the difficulty of improving the overall model. A further potential modification of the radiation reaction, aiming to increase its consistency with the waveform, was explored in Ref. [82]. Therein it was tested how incorporating the $(2,1)$ and $(3,3)$

Table 5.1: The values of a_6^c obtained through minimizing the EOB/NR dephasing at merger down to the order of the numerical error $\delta\phi^{\mathrm{NR}}_{\mathrm{mrg}}$. These values inform the fitting template given in eq. (5.22). The reader should note that the values of $\delta\phi^{\mathrm{NR}}_{\mathrm{mrg}}$ differ from those given in Tab. F.14 as the later are computed relative to the relaxation time, while the former have been evaluated setting the relaxation time to $200M$. As these values of $\delta\phi^{\mathrm{NR}}_{\mathrm{mrg}}$ have been used to inform the *first-guess* values of a_6^c it is best to state them here despite the difference.

ID	q	a_c^6	$\delta\phi^{\mathrm{NR}}_{\mathrm{mrg}}$ [rad]
SXS:BBH:0002	1.00	−42	−0.063
SXS:BBH:0007	1.50	−47	−0.0186
SXS:BBH:0169	2.00	−59	−0.0271
SXS:BBH:0259	2.50	−54	−0.0080
SXS:BBH:0030	3.00	−52	−0.0870
SXS:BBH:0297	6.50	−27	−0.053
SXS:BBH:0298	7.00	−26	−0.0775
SXS:BBH:0302	9.50	−17	+0.0206

NQC corrections in the radiation reaction would affect the model performance. Both modifications of the radiation reaction would likely come down to a redetermination of a_6^c, and not necessarily improve the model beyond that. Thus, for now this inconsistency is simply accepted to improve the model. Should the need arise to correct this inconsistency in the future it can be reimposed and explored without large effort.

5.3 Calibration of the *analytical flexibility*

5.3.1 The calibration of a_6^c

As both the waveform and the A-potential have been modified a new determination of a_6^c is in order[2]. To do so, 8 `SXS` waveforms with very small nominal errors are used, see Tab. 5.1. The first-guess values of a_6^c are determined in the manner already outlined in Sec. 4.2.3 and are listed in Tab. 5.1. The interpolating fit is obtained with the template of a rational function as

$$a_6^c = n_0 \frac{1 + n_1\nu + n_2\nu^2 + n_3\nu^3}{1 + d_1\nu}, \tag{5.22}$$

with the fitted parameters being given as

$$n_0 = \quad 5.9951, \tag{5.23}$$

$$n_1 = -34.4844, \tag{5.24}$$

$$n_2 = -79.2997, \tag{5.25}$$

$$n_3 = \quad 713.4451, \tag{5.26}$$

$$d_1 = -3.167. \tag{5.27}$$

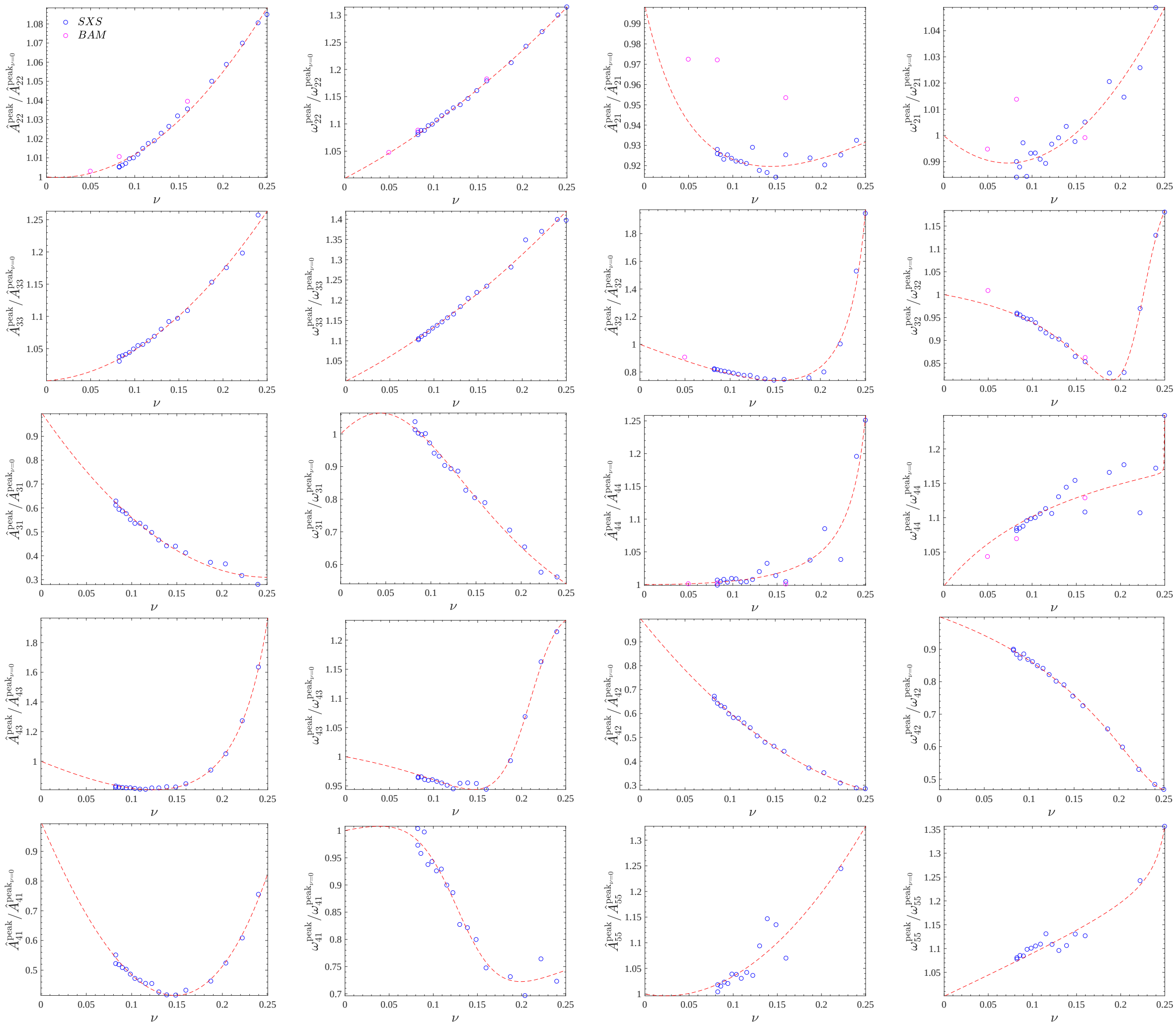

Figure 5.2: A comparison of the fits of $(\hat{A}^{\rm peak}_{\ell m}, \omega^{\rm peak}_{\ell m})$ versus `SXS` and `BAM` data for the multipoles $\ell \leq 4$, $1 \leq m \leq 4$, and $(\ell, m) = (5, 5)$. The reader should note that for the multipoles $(3, 3)$ and $(5, 5)$ the $\omega^{\rm peak}_{\ell m}$ at $q = 1$ was effectively determined by extrapolating $q = 1$ data with $\chi_1 \neq \chi_2$ down to $\tilde{a}_{12} = 0$, giving an effective estimate of the frequency at peak of the equal-mass limit. The addition of these points was needed ensure the proper limit of the frequency when equal-mass case is approached. The reader should further note that the amplitude plots contain an error in the description of the y-axis as they are normalized to $\hat{A}^0_{\ell m} c_{\ell+\epsilon}(\nu)$.

5.3.2 Fits: waveform peak frequency and amplitude.

The analytical fits of $(\hat{A}^{\rm peak}_{\ell m}, \omega^{\rm peak}_{\ell m})$ are build in a simple and straightforward manner, uniformly for all multipoles. First, leading-order ν behavior of the Newtonian prefactor given as

$$c_{\ell+\epsilon}(\nu) = X_2^{\ell+\epsilon-1} + (-)^{\ell+\epsilon} X_1^{\ell+\epsilon-1} \ , \tag{5.28}$$

is factored out for the amplitude. Second, the test-particle limit $(\hat{A}^0_{\ell m}, \omega^0_{\ell m})$, known with high accuracy (see Tab 3 of Ref. [90]), is factored out as well for all multipoles. Leaving the quantities

---

[2] This fit was performed by Alessandro Nagar.

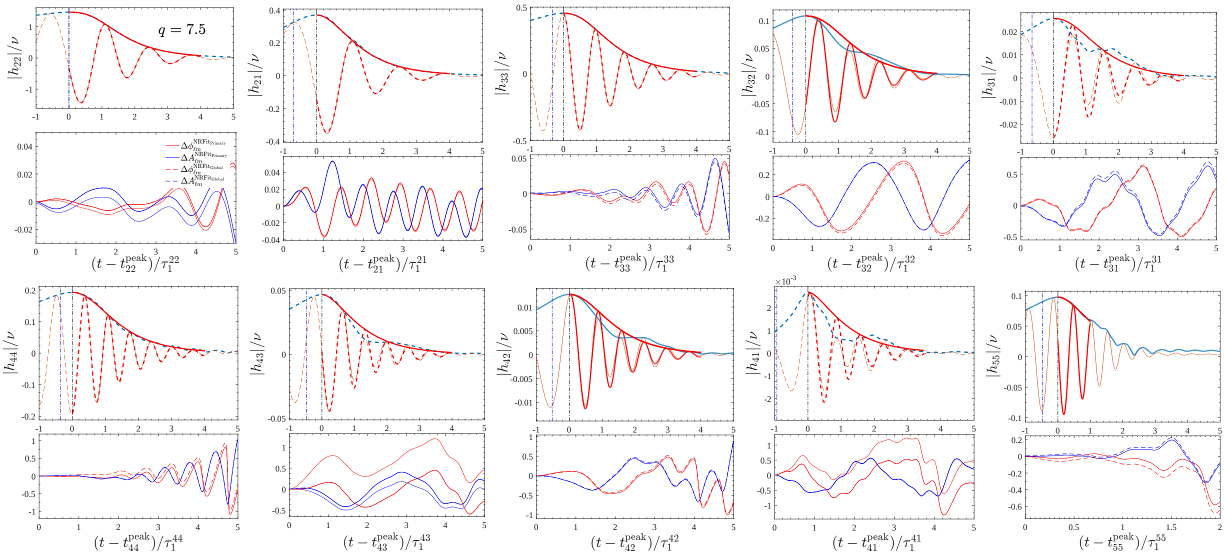

Figure 5.3: The performance of the primary and global postpeak fit over the multipoles $(\ell, m) = (2,2), (2,1), (3,3), (3,2), (3,1), (4,4), (4,3), (4,2), (4,1)$ and $(5,5)$ of `SXS:BBH:0299`, a mass ratio $q = 7.5$ waveform with high accuracy. For each mode the panel is divided into two subpanels, showing the direct waveform comparison (top) and the performance of both primary and global fit on the levels of phase and amplitude (bottom). In the top panel, the tick-red lines represent the fitted waveform template (amplitude is solid, while the real part is dashed) obtained from the primary fit of the eq. (2.46)-(2.47) to the NR data. This is contrasted by the real part of the NR waveform (thin, orange, dashed line) and the NR amplitude (dashed, blue). The black, vertical line marks $t_{\rm peak}^{\ell m}$, while the blue one corresponds to $t_{22}^{\rm peak}$. Each mode has a different time normalization given by the damping time of the fundamental QNM as units of $\tau_1^{\ell m} \equiv 1/\alpha_1^{\ell m}$ for the shifted time scale $t - t_{\ell m}^{\rm peak}$. The bottom subpanel shows the fit error for both primary and global fit on the level of phase and fractional amplitude. Comparing the two gives a general very good picture for this waveform.

to be fitted $(\hat{\hat{A}}_{\ell m}^{\rm peak}, \hat{\omega}_{\ell m}^{\rm peak})$ given by the factorization

$$\hat{A}_{\ell m}^{\rm peak} = c_{\ell+\epsilon}(\nu) \hat{A}_{\ell m}^{0} \hat{\hat{A}}_{\ell m}^{\rm peak}, \tag{5.29}$$

$$\omega_{\ell m}^{\rm peak} = \omega_{\ell m}^{0} \hat{\omega}_{\ell m}^{\rm peak}. \tag{5.30}$$

$(\hat{\hat{A}}_{\ell m}, \hat{\omega}_{\ell m})$ are plotted versus ν for all fitted multipoles in Fig. 5.2. Whenever possible the `BAM` data is shown as well. However, not all multipoles are well resolved in the `BAM` data and thus they had to be skipped for some. Lastly, $(\hat{\hat{A}}_{\ell m}, \hat{\omega}_{\ell m})$ are fitted with a general template of a rational function as

$$k_{\ell m} = \frac{1 + n_1^{k_{\ell m}} \nu + n_2^{k_{\ell m}} \nu^2}{1 + d_1^{k_{\ell m}} \nu + d_2^{k_{\ell m}} \nu^2}\ . \tag{5.31}$$

The fit coefficients are listed in Table C.1. All fits have been done with `fitnlm` of `MATLAB`. If `fitnlm` returned a sufficiently large p-value[3], i.e. $\gtrsim 0.3$, for a coefficient, it was set to zero manually and the fit was redone.

---

[3] The p-value of `fitnlm` indicates the probability of a specific coefficient to be zero as can be inferred from the data. In the following we simply refer to this quantity as the p-value.

5.3.3 Fits: postpeak waveform evolution

Similar as for the discussed in Sec. 4.2.7 and Sec. 2.3.4 the fit for $(c_3^{A_{\ell m}}, c_3^{\phi_{\ell m}}, c_4^{\phi_{\ell m}})$ is done following the same two-step procedure.

Primary and global fit: The $\ell = m = 2$ postpeak fits are using all 19 non-spinning datasets in the *calibration* set. These are the first 19 datasets in Tab. F.14. By contrast, only subsamples can be used for the subdominant modes, depending on the level of noise and unmodeled features present in the waveform. One such unmodeled feature is the existence of mode-mixing. Another feature is the beating between positive and negative QNMs [45]. While in principle it is possible to average over these effects in the waveform this is not always advisable as this leads to unrealistic and inconsistent parameters $(c_3^{A_{\ell m}}, c_3^{\phi_{\ell m}}, c_4^{\phi_{\ell m}})$ obtained for different waveforms. More precisely the following datasets are used for the individual multipoles (the numbering of Tab F.14 is shifted by 525, *i.e.* waveform #2 corresponds to $\#(525 + 2 = 527)$):$\{2 - 16, 18, 19\}$ for $(2, 1)$; $\{2 - 19\}$ for $(3, 3)$; $\{1 - 15, 17, 18\}$ for $(3, 2)$; $\{2 - 11, 13, 14, 17, 18\}$ for $(3, 1)$; $\{1 - 11, 13, 15 - 19\}$ for $(4, 4)$; $\{2 - 9, 13 - 19\}$ for $(4, 3)$; $\{1 - 8, 10 - 14, 17 - 18\}$ for $(4, 2)$ and $\{3, 6, 9 - 19\}$ for $(5, 5)$. For each (ℓ, m), the primary fit is performed over a consistently chosen time interval $\Delta\tau_{\ell m}$. For the $(2, 2)$ mode $\Delta\tau_{\ell m} = 4\tau_1^{\ell m} = 4/\alpha_1^{\ell m}$ was chosen. All multipoles (except $\ell = m = 5$) of the datasets $\{10 - 19\}$ (corresponding to $q \geq 6$) utilize $\Delta\tau_{\ell m} = 4\tau_1^{\ell m}$ as well. The datasets $\{1 - 9\}$(corresponding to $q \leq 5.5$) and the $\ell = m = 5$ mode all over, are fitted over $\Delta\tau_{\ell m} = \tau_1^{\ell m}$. This choice was driven by two factors: (i) data quality and (ii) presence of strong mode-mixing (see *e.g.* bottom, most-right panel of Fig. 5.3 as a demonstrative example of the data-quality issues in the $(5, 5)$ mode). Fig. 5.3 shows both primary and global fit illustrated on the data set `SXS:BBH:0299` of a $q = 7.5$ BBH waveform.

Mode-mixing: Mode-mixing best understood in the extreme-mass-ratio limit where it was studied in Ref. [45]. The origin of mode-mixing lies in the fact that during the postmerger-ringdown phase the natural basis of the GW signal shifts from the typical spin-weighted spherical harmonics to the spheroidal harmonic base of the final BH. This effect occurs for the $\ell \geq 3$ modes with $\ell \neq m$ as modes only receive mixed contributions from modes with smaller ℓ and equal m. Therefor the $(2, 1)$ mode is largely free from any mode-mixing, yet fraught with different challenges, while $(3, 2)$, $(3, 1)$, $(4, 3)$ and $(4, 2)$ all obtain mode-mixing contributions from different multipoles. The lack of modelization of this effect is reason for the larger scale oscillations in the fit error of phase and frequency for several of these modes. n conclusion, the postmerger template used here is a simple and effective average of the waveform to be fitted. It is still physically incomplete, yet is a solid approximation globally, as will be further explored below.

The fits of $(c_3^{A_{\ell m}}, c_3^{\phi_{\ell m}}, c_4^{\phi_{\ell m}})$ were obtained using the function `fitnlm` of `MATLAB`. As the functional form of the fitting template was chosen multipole by multipole, it was chosen to list the fits explicitly in Tab. C.2.

Inspecting the table, it can be seen that for the piece wise fits for $c_3^{\phi_{31}}$ and $c_3^{\phi_{41}}$ are discontinues in their derivatives with respect to ν at their juncture. A more complex fit was in fact needed to model the $(4, 2)$ phase coefficient $c_4^{\phi_{42}}$, with similar discontinuities in the derivative with respect to

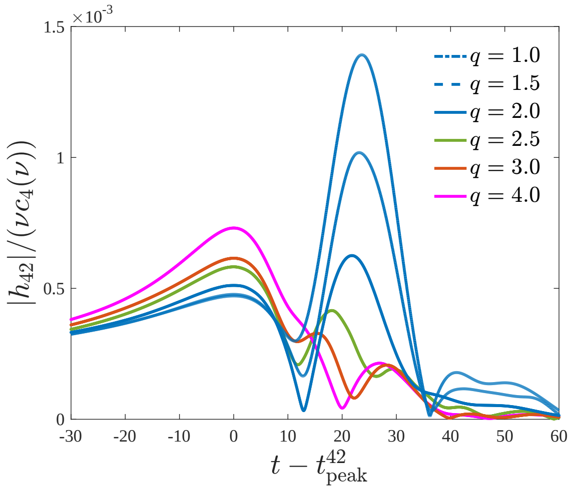

Figure 5.4: The NR data for $q \leq 4$ shows a peculiar double peak structure in the post-peak amplitude of the $(4, 2)$ mode. With a particularly large secondary peak.

ν was needed. $c_4^{\phi_{42}}$ was fitted with the piece-wise function

$$\begin{cases} \dfrac{132.56 - 1155.5\nu + 2516.8\nu^2}{1 - 3.8231\nu} & \text{if} \quad q \leq 2.5, \\ -554.18\nu + 120.23 & \text{if} \quad 2.5 < q < 3, \\ \dfrac{-0.58736 + 16.401\nu}{1 - 4.5202\nu} & \text{if} \quad q \geq 3. \end{cases} \tag{5.32}$$

The need of this complexity originates in the neglect to model mode-mixing in the postmerger. As can be seen in Fig. 5.4, the effect of mode-mixing is particularly strong for $1 \leq q \leq 2.5$ leading in fact to a double peak structure. And in fact the peak introduced by mode-mixing is larger for $1 \leq q \leq 2$. A model for which mode-mixing would be modeled accurately would like be able to reproduce the double structure, yet with the template used here the secondary peak is neglected and the model focuses in on capturing the first peak in an approximate fashion.

5.3.4 Fits: QNM parameters

The QNMs quantities $(\omega_1^{\ell m}, \alpha_1^{\ell m})$ and $\alpha_{21}^{\ell m} \equiv \alpha_2^{\ell m} - \alpha_1^{\ell m}$ are fitted for all multipoles considered, exploiting the accurate representation of in terms of χ_f already utilized in Sec. 4.2.6. The fitting template thus reads:

$$Y'_{\ell m}(\chi_f) = Y'_0 \, \frac{1 + b_1^{Y'}\chi_f + b_2^{Y'}\chi_f^2 + b_3^{Y'}\chi_f^3}{1 + c_1^{Y'}\chi_f + c_2^{Y'}\chi_f^2 + c_3^{Y'}\chi_f^3}. \tag{5.33}$$

The fit is following the same approach as laid out in Sec. 4.2.6. The coefficients of the fits above are collected in Table C.3. All fits were done with `fitnlm` of `MATLAB` and coefficients have been set to zero explicitly if the p-value was significant, similar as described in Sec. 5.3.2. Note that the fits of$(\omega_1^{22}, \alpha_1^{22}, \alpha_{21}^{22})$ have been updated as well as they contained parameters with large p-value, thus updating the fits of chapter 4, listed in Tab. B.3.

5.3.5 Fits: Peak-time-shift

The next step towards completing the NR calibration of the model is the determination fo the peak-time shift $\Delta t_{\ell m}$ relative to the $(2,2)$ mode as a function of ν. $\Delta t_{\ell m}$ is defined as

$$\Delta t^{\rm NR}_{\ell m} = t^{\rm peak}_{\ell m} - t^{\rm peak}_{22}. \tag{5.34}$$

The test-particle limit $\Delta t^{0}_{\ell m}$ (see Table 3 of Ref. [90]) is factored out as

$$\Delta t^{\rm NR}_{\ell m} = \Delta t^{0}_{\ell m} \hat{\Delta} t_{\ell m}. \tag{5.35}$$

$\hat{\Delta} t_{\ell m}$ is fitted against ν with the template

$$\hat{\Delta} t_{\ell m} = \frac{1 + n_1^{\Delta t_{\ell m}} \nu + n_2^{\Delta t_{\ell m}} \nu^2}{1 + d_1^{\Delta t_{\ell m}} \nu + d_2^{\Delta t_{\ell m}} \nu^2}. \tag{5.36}$$

The coefficients of the fits, together with the values of $\Delta t^{0}_{\ell m}$, are listed in Tab. C.4 explicitly. The fits have been done with `fitnlm` of `MATLAB`. As for the previous fits coefficients with a significant p-value are set to zero by hand.

5.3.6 Fits: NQC extraction point

The final piece to be fitted are the NQC extraction points $Y = \left\{ \hat{A}^{\rm NQC}_{\ell m}, \dot{\hat{A}}^{\rm NQC}_{\ell m}, \omega^{\rm NQC}_{\ell m}, \dot{\omega}^{\rm NQC}_{\ell m} \right\}$ Which are then used to determine the NQC correction parameters $(a_1^{\ell m}, a_2^{\ell m}, b_1^{\ell m}, b_2^{\ell m})$ entering the multipolar NQC correction factor given in eq. (2.34). Due to a special circumstance the calibration of the $(2,1)$ is postponed to be treated separately in Sec. 5.3.6 below due to the special behavior in the test-particle limit. The NQC extraction points are defined following the typical manner laid out in Sec. 2.3.2 and are fitted after the test-particle limit $Y^{0}_{\ell m}$ is factorized as

$$Y^{\rm NQC}_{\ell m} = Y^{0}_{\ell m} \, \hat{\hat{Y}}^{\rm NQC}_{\ell m}. \tag{5.37}$$

For frequency and derivatives the full ν dependence is encoded in $\hat{\hat{Y}}^{\rm NQC}_{\ell m}$, while the amplitude further exploited the leading order Newtonian dependence on ν and is fitted instead as $\hat{A}^{\rm NQC}_{\ell m}/|c_{\ell+\epsilon}(\nu)|$. The fits are listed explicitly in the Tab. C.5.

$(\ell, m) = (2,1)$ mode

Fig. 5.5 shows that the onset of oscillations in the frequency right in between both merger and NQC extraction time. This effect is due to beating of positive and negative frequency QNMs [45, 74, 130]. Thus, it can seen that the test-particle limit is currently unsuited for modeling the NQC extraction points as this effect is not yet captured in the model and in fact would lead to quantitatively wrong behavior of the derivatives. For this reasons the test-particle behavior is not factored out for the $(2,1)$ mode but rather fitted directly all over the available data. The $(2,1)$ fits are listed in the second row of Tab. C.5.

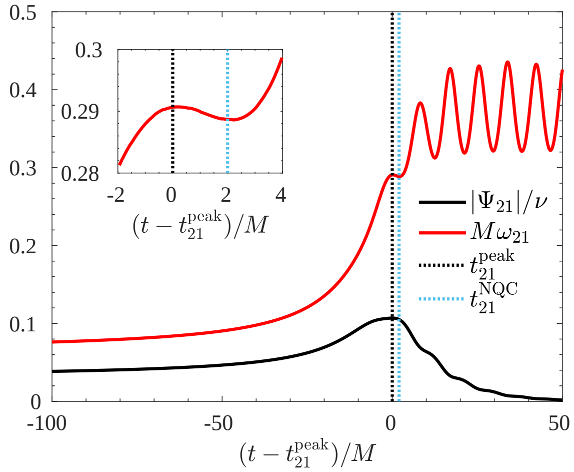

Figure 5.5: Amplitude $|\Psi_{21}|/\nu$ and frequency ω_{21} plotted in the test-particle limit around the peak of the mode. The waveform was generated by the code presented in Ref. [90]. As can be see zoomed in around the peak of the waveform, $t_{21}^{\rm NQC}$ lies beyond the onset of the beating between negative and positive QNMs [45, 74, 130] and thus is unsuited to be imposed onto the NQC fits due to the presence of unmodeled physical effects present.

5.4 Comparing `TEOBiResumMultipoles` and NR

So far in this chapter presented the individual building blocks that make up `TEOBiResumMultipoles`, based on the structure on the `TEOB` structure introduced in Sec. 2.3. As `TEOBiResumMultipoles` is now fully calibrated, it is time to focus on the validation of the model.

5.4.1 Unfaithfulness

Before starting into the discussion of the unfaithfulness it is important to point that in chapter 4 $\bar{F}$ was a simple function of a single parameter for two given waveforms to be compared: the total binary mass M. Now, as several multipoles are included it also depends on the angular orientation (ι, φ). Thus, $\bar{F}$ is plotted as a toned region between min-max curves of best and worst case orientation over the total mass M. With this setup in mind it is now useful to summarize the main results of the unfaithfulness computation presented in Paper II as[4]:

(i) The unfaithfulness computed for the dominant $(2, 2)$ mode is well below 10^{-3} for all 19 waveforms. As the $(2, 2)$ mode was already accurately reproduced all over the non-spinning catalog by `TEOBResumS` it is neglected here and the interested reader is referred to Fig. 13 of Paper II for a discussion of the $(2, 2)$ mode.

(ii) The unfaithfulness computation between `TEOBiResumMultipoles` and the $q = 10$ waveform, `SXS:BBH:`0303, is shown in Fig. 5.6 for a fixed total mass of $M = 100M_\odot$. The NR waveform is taken to include the multipoles $\{22, 21, 33, 44, 55\}$ and is varied over the entire sky orientation of the source binary. It demonstrates (a) that the $(2, \pm2)$ mode (right panel) is fully sufficient in the face-on or face-off case yet strongly degrades in the edge-on case where the contribution of the $(2, \pm2)$ mode is weakest; and (b) that `TEOBiResumMultipoles` reproduces

---

[4] As mentioned above, the computation of the unfaithfulness has been carried out by Geraint Pratten.

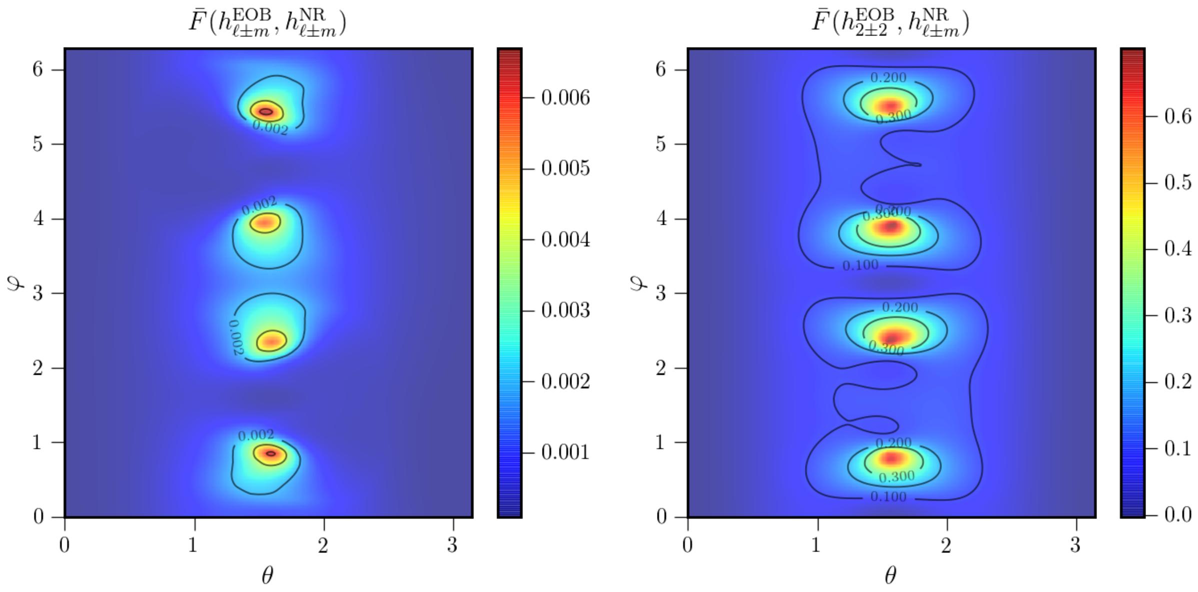

Figure 5.6: The full-sky unfaithfulness computed between `TEOBiResumMultipoles` and `SXS:BBH:0303`. The NR simulation represents a $q = 10$ waveform. The NR waveform is constructed from the multipoles $\{22, 21, 33, 44, 55\}$ and compared to `TEOBiResumMultipoles` over the same multipoles (left) and exclusively the $(2, \pm2)$ mode (right). The system mass $M = 100 M_\odot$ is held fixed throughout this computation. The reader should note that the color scales change by a factor of 100 from the left to the right plot. This signifies the much worse performance of the pure $(2, \pm2)$ mode when the edge-on case is approached, yet for the face-on and face-off case it performs reasonably well. Again as expected from general knowledge. Further it is remarkable how well the full multipolar model performs when compared to NR, staying below 7×10^{-3} in the worst case even.

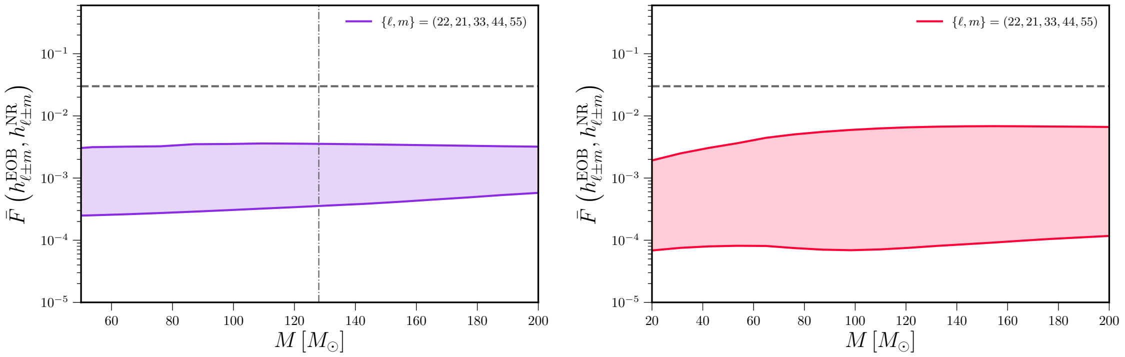

Figure 5.7: The minimum and maximum unfaithfulness region is computed between `TEOBiResumMultipoles` and the `BAM` $q = 18$ waveform [101] (left) and the `SXS:BBH:0166`, $q = 6$ waveform (right). The vertical dot-dashed line in the left panel shows the minimum mass for which the entire NR waveform is in band. The `TEOB`/NR performance for $q = 6$ is comparable to (though slightly better than) `SEOBNRv4HM`, for the same SXS dataset, as can be seen through direct comparison with Fig. 16 of Ref. [70].

$\{22, 21, 33, 44, 55\}$ very well for this system, reaching even in the worst case (edge-on) only slightly below $\bar{F} < 7 \times 10^{-3}$.

(iii) The single waveform comparison is continued for the multipole set $\{22, 21, 33, 44, 55\}$ against the `BAM` $q = 18$ and the `SXS:BBH:0166` $q = 6$ waveform (here showing a similar performance

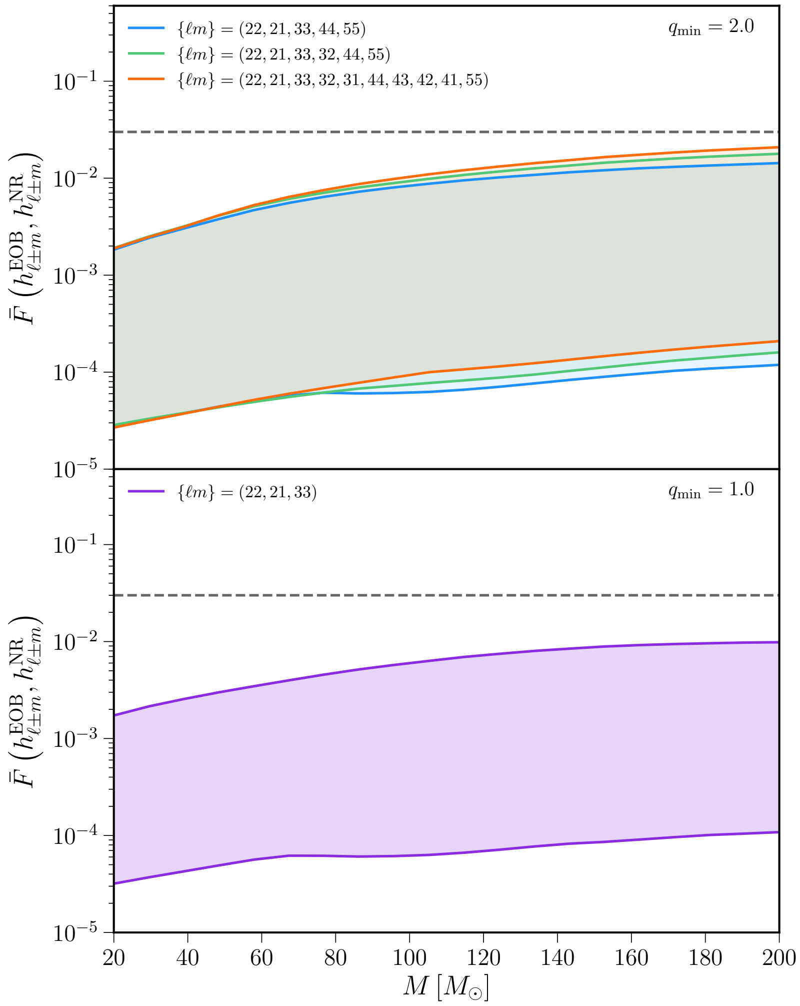

Figure 5.8: The minimum and maximum unfaithfulness varied over a grid of the angles (θ, φ) is shown, demonstrating clearly that the worst case performance is always below 3% for binaries with a total mass $M \lesssim 200 M_\odot$. The neglecting of mode-mixing in `TEOBiResumMultipoles` does not show a significant increase in the unfaithfulness as it seems. The analysis in the top-panel is restricted to $q \geq 2$ as the $(4, 4)$ mode shows several pathological features in the NR for $q < 2$. The best performance can be found when constraining the $\bar{F}$ computation to the modes $\{22, 21, 33, 44, 55\}$ (blue). A slight degrading occurs when the $(3, 2)$ mode (green) or all calibrated modes (orange) are added, yet it remains below 3% for all masses up to $200 M_\odot$. The bottom panel, constrains the mode selection to $\{22, 21, 33\}$, neglecting the $(4, 4)$ mode. This yields an excellent agreement between `TEOBiResumMultipoles` and NR for all mass-ratios down to $q = 1$.

as `SEOBNRv4HM` demonstrated in Fig. 16 of Ref. [70]). The comparison is shown in Fig 5.7. An excellent agreement is found for the entire mass-range, though the low-mass cutoff is increased to $50 M_\odot$ for $q = 18$ and to $20 M_\odot$ for $q = 6$. Notably, $q = 18$ only enters the observable band fully with a total mass of over $120 M_\odot$. In fact Fig. 5.8 shows that this excellent performance holds for all mass-ratios $q \geq 2$ and can be extended to include *all calibrated modes* without exceeding the maximum unfaithfulness.

(iv) Recalling the discussion of Sec. 3.5, the $(4, 4)$ mode shows evidence of pathological features in the region of $q < 2$ of the `SXS` catalog. Thus, an additional computation of the mismatch is presented in the bottom panel of Fig. 5.8 to perform an unfaithfulness computation constrained to the modes $\{22, 21, 33\}$ for all waveforms down to $q = 1$ and it is found that the performance

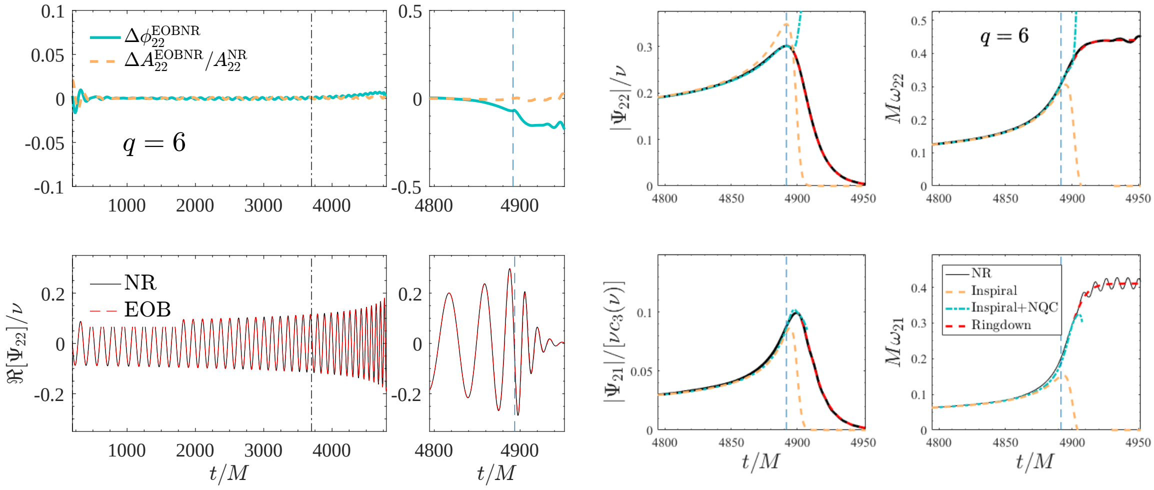

Figure 5.9: The time-domain comparison for the $q = 6$ `SXS` waveform (given by SXS:BBH:0166) compared `TEOBiResumMultipoles`. The upper left panel shows the full waveform comparison on the level of phase and relative amplitude difference, showing an excellent agreement and only a small dephasing accumulated at merger despite the alignment in the inspiral. The lower left panel shows the direct comparison for the real part of the waveform. The left hand side of this figure is complemented by the direct comparison of the $(2, 2)$ and $(2, 1)$ amplitude and frequency between `TEOBiResumMultipoles` and the NR. The four panels on the right hand side show: The NR waveform (black), the bare `TEOB` waveform prior to NQC and postmerger attachment (orange-dashed), the the `TEOB` with NQC corrections imposed (blue-dashed) and the full `TEOBiResumMultipoles` waveform, combined with the postpeak waveform (red-dashed). It is noteworthy that the waveform prior to the addition of the NQC is already in quite good agreement with NR up until merger. It is also possible to note that the $(2, 1)$ frequency exhibit oscillations in the late ringdown waveform. This is likely an effect of mode-mixing or potentially due to the excitation of negative frequency QNMs. In either case it is not captured at the moment by the postpeak-ringdown template.

of `TEOBiResumMultipoles` relative to the NR data is excellent over these modes as well.

In summary, `TEOBiResumMultipoles` performs with excellence when compared to several combinations of modes for $q \geq 2$, while for $q \geq 1$ the analysis has to be constrained to exclude the $(4, 4)$ mode but can still produce excellent results. Improved NR data will be necessary to explore the $q < 2$ performance of many subdominant modes, starting with the $(4, 4)$ mode.

5.4.2 Time-domain phasing

It is now established that `TEOBiResumMultipoles` faithfully represents the NR, non-spinning waveforms used here. Within this context it is worth it to perrform an explicit, in depth comparison in the time-domain for the $q = 6$ waveform, `SXS:BBH:0166`. With this comparison the following four points can be made: (i) The *bare* `TEOB` reproduces both amplitude and frequency reasonably well without any further need of NR calibration beyond the parameter a_6^c. (ii) The effect of the NQC is small, limited and thus efficient, as is the ideal case for a well build `TEOB` avatar. (iii) The transition between inspiral and postpeak waveform can be done smoothly for all modes if the NR information is taken into account properly. (iv) The description of the postpeak-ringdown waveform is reliable and robust, even though incomplete with respect to mode-mixing.

The time-domain comparison is shown over Fig. 5.9 – 5.12 and a summary plot is shown in Fig. 5.13. Studying these figures in depth the following conclusions and observations can be made:

(i) The $(2, 2)$ shows an excellent agreement with `TEOBiResumMultipoles` when aligned in the in-

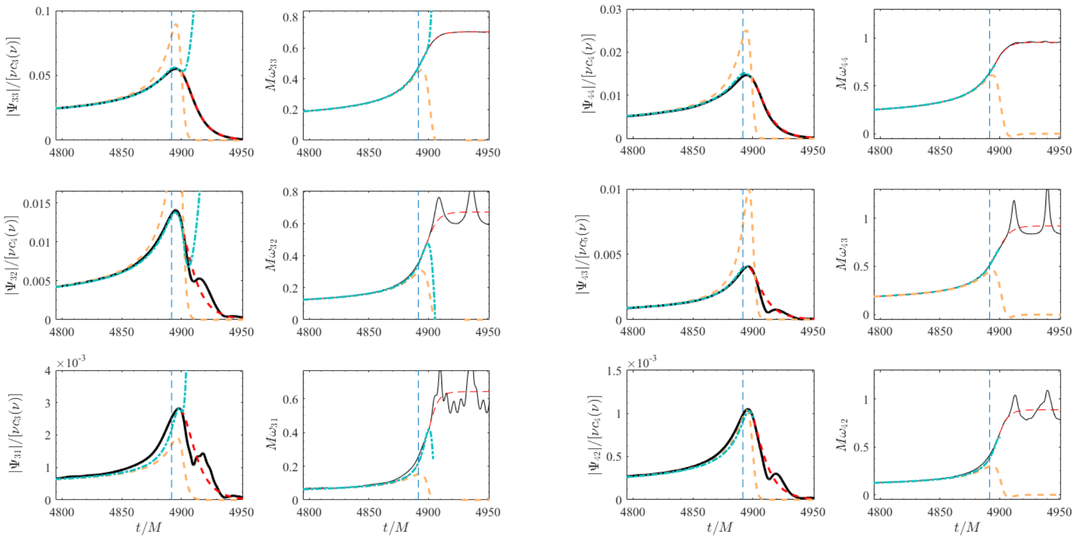

Figure 5.10: The continuation of Fig. 5.9, extending the comparison between `TEOBiResumMultipoles` and `SXS:BBH:0166`, $q = 6$ to the multipoles $\{33, 32, 31, 44, 43, 42\}$ mode, all calibrated to NR. Note that even though clear effects of mode-mixing are visible, and while not incorporated in the analytical ringdown description, still did not affect the overall unfaithfulness.

spiral, leading up to only a minimal dephasing, with all likely hood well within the uncertainty of the waveform, even though this cannot be estimated due to the lack of a second resolution.

(ii) The bare `TEOB` waveform reproduces the frequency across *all* multipoles accurately until around the merger. In itself this is already remarkable. Even though uncalibrated on any level this holds true for the $\{54, 53, 52, 66\}$ modes as well.

(iii) The $(2, 1)$ mode postpeak-ringdown waveform lacks in modelization of the oscillation excited in the late NR ringdown. Due to the shape of the oscillation this could potentially be the beating of positive and negative frequency QNMs, but it would also be possible that it is an effect due to mode-mixing. In either case this effect is currently not modeled in the postpeak waveform, even though it is averaged in a robust manner. For all further modes with $\ell \neq m$ clear signs of mode-mixing can be observed, yet the postpeak waveform averages the amplitude accurately.

(iv) Considering the summary plot Fig. 5.13, it appears `TEOBiResumMultipoles`, while certainly not perfectly, still robustly reproduces the waveforms `SXS:BBH:0166` of a $q = 6$ BBH system.

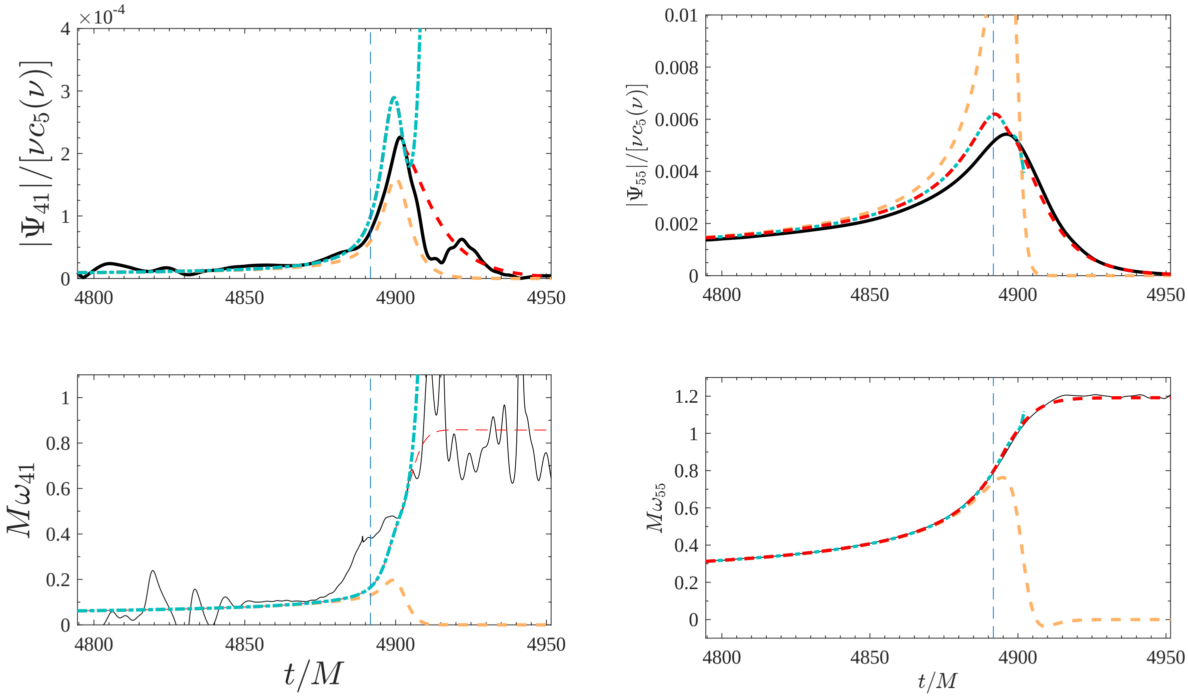

Figure 5.11: The continuation of Fig. 5.9 – 5.10, extending the comparison between `TEOBiResumMultipoles` and `SXS:BBH:0166`, $q = 6$ to the multipoles $\{41, 55\}$ mode, thus concluding all NR calibrated multipoles. Note that even though clear effects of mode-mixing are visible, and while not incorporated in the analytical ringdown description, still did not affect the overall unfaithfulness. Even though the $(4,1)$ mode shows heavy numerical noise in the frequency, it shows qualitative an agreement the three steps of evolution of NR calibration. The $(5,5)$ frequencies are in remarkably good agreement all over. For both modes, the NQC-corrected amplitude, close to merger tends to be larger compared to the NR one. While in the case of the $(5,5)$ mode it seems that NR is sufficiently resolved such that this disagreement is a potentially physically relevant one, this cannot be said for the $(4,1)$ mode as it is clearly dominated by noise preventing any statement, on the quality of the waveform comparison here, to be conclusive.

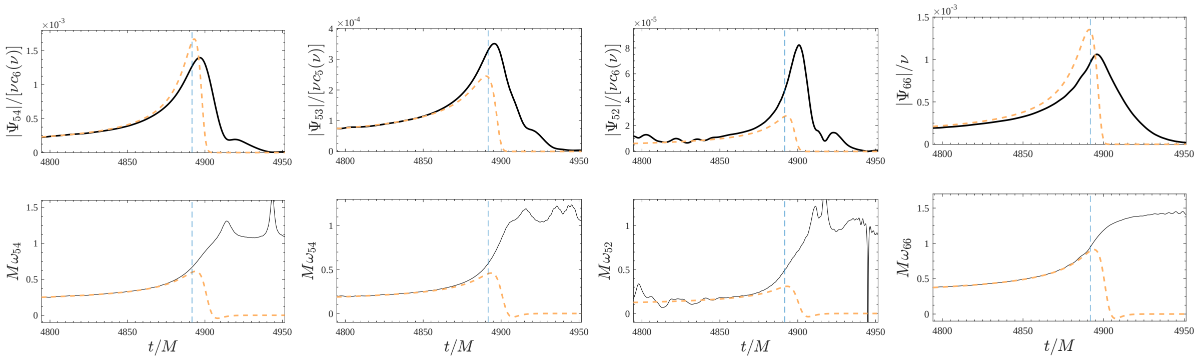

Figure 5.12: The conclusion of Fig. 5.9 – 5.11 comparing the mass ratio $q = 6$ waveform, `SXS:BBH:0166`, to `TEOBiResumMultipoles`. The multipoles $\{54, 53, 52, 66\}$ are added, uncalibrated and thus only the bare analytical waveform is given on the `TEOBiResumMultipoles` side. The vertical line in each panel marks the location of the $\ell = m = 2$ waveform peak, i.e. the merger. It is indeed remarkable that the bare frequency reproduces the NR one with a reasonably good agreement up until merger across al multipoles.

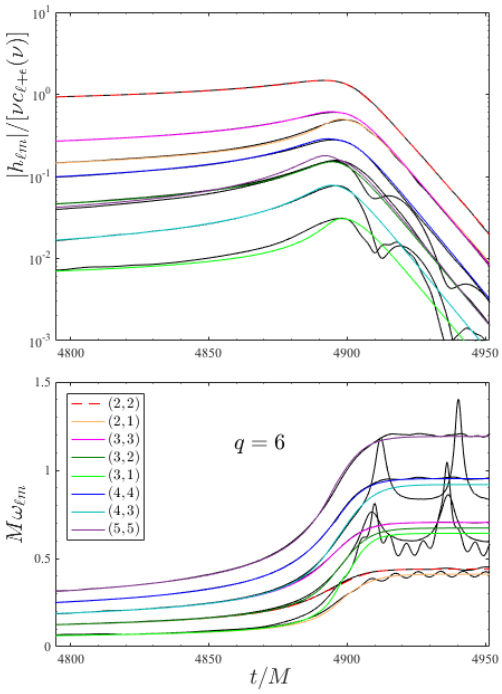

Figure 5.13: The full picture around merger for the mass-ratio $q = 6$, `SXS:BBH:0166` data set (black lines). `TEOBiResumMultipoles` is compared on the level of amplitudes $|h_{\ell m}(t)|/\left[\nu c_{\ell+\epsilon}(\nu)\right]$ (top panel) and frequencies $\omega_{\ell m}(t)$ (bottom panel) to the NR waveform.

Chapter 6

Subdominant modes: The spinning case

The discussion will now turn to `TEOBiResumS_SM`, the third avatar of the `TEOB` model introduced in Sec. 2.3. This chapter will be devoted to the extension of the multipoles of `TEOBiResumMultipoles` to the spinning case. After the improved NR calibration is presented, following Paper III, it is validated on the full NR catalog presented in chapter 3. The model will be evaluated in comparison to both the *calibration* set, that was used to inform the model, and the *validation* that, with some exceptions, was only used to test the performance of the model.

6.1 `TEOBiResumS_SM` Hamiltonian and waveform

The structure of `TEOBiResumS_SM` is take in the non-spinning sector to be that of `TEOBiResumMultipoles`, with respect to the A-potential and waveform. For further details on the concrete resummation and factorization of the waveform the reader is referred to Paper II and Paper III as well as Refs. [123, 129]. The gyro-gravitomagnetic ratios (G_S, G_{S_*}) are re-expressed as functions of $u = 1/r$ and r instead of u_c and $1/r_c$ as motivated by the discussion in Paper I and the robustness analysis of the waveform presented in Sec. 4.4. These changes require an improved calibration of the NNNLO spin-orbit parameter $c_3(\nu, \tilde{a}_1, \tilde{a}_2)$. And due to the updated availability of an improved $(8, +0.85, +0.85)$ waveform an updated calibration of the postmerger as well as the NQC of the $(2,2)$ mode is required.

6.2 Improved NR calibration of the multipolar ringdown waveform

It is now time to turn to the improved NR calibration of `TEOBiResumS_SM`. The updated NR calibration includes:

(i) An improved fit of c_3, to account for the changes in the Hamiltonian, the improved resummation of the waveform and the improved A-potential combined with the updated a_6^c introduced in the previous chapter.

(ii) Peak amplitude and frequency for the individual multipoles.

(iii) The peak-time-shifts $\Delta t_{\ell m}$ of the subdominant modes relative to the merger.

(iv) The fits of the NR NQC extraction points $\left(A^{\rm NQC}_{\ell m}, \omega^{\rm NQC}_{\ell m}, \dot{A}^{\rm NQC}_{\ell m}, \dot{\omega}^{\rm NQC}_{\ell m}\right)$.

(v) The phenomenological postpeak evolution parameters $(c_3^{A_{\ell m}}, c_3^{\phi_{\ell m}}, c_4^{\phi_{\ell m}})$.

However, the reader should note that in some situations the non-spinning fits of $(c_3^{A_{\ell m}}, c_3^{\phi_{\ell m}}, c_4^{\phi_{\ell m}})$ presented in Chap. 5 and Paper II are more stable and give overall a more robust representation of the postpeak waveform. In some situations it was found indeed that the peak and ringdown are sufficient to capture the spins dependence and thus the non-spinning evolution parameter were chosen right away.

The fits of the quasi-normal-mode frequencies and (inverse) damping times entering $\left(\omega_1^{\ell m}, \alpha_1^{\ell m}, \alpha_{21}^{\ell m}\right)$ are given in Paper II and discussed in Chap. 5. Due to their spin-dependence being captured by the fit of χ_f presented in Ref. [107] no further modification is necessary.

The NQC extraction points of the waveform are now extracted analytically from the postpeak template as will discussed below. For the $(4,4)$ mode, however, this procedure was not able to deliver an accurate time-derivative of the waveform amplitude, so that a dedicated fit is required. Due to the inclusion of the $(\ell, m) = (2,2)$ NQC in the radiation reaction it is here necessary as well to provide accurate fits for all 4 NQC quantities. Unless otherwise stated all fits are done using `fitnlm` of `matlab` and `NonLinearModelFit` of `MATHEMATICA`. All fits exclusively use the data taken from the `BAM` catalog, test-particle data and the *calibration set* of SXS waveforms listed in Appendix F and detailed in chapter 3. The exception is Δt_{21}, which is informed additionally by the *validation* set of `SXS` waveforms.

6.2.1 NR-informed EOB functions: $\mathbf{a_6^c}$ and $\mathbf{c_3}$

The fit of $a_6^c(\nu)$ is used as presented in eq. (5.22) of Chap. 5. The improved fit of c_3[1] is done in an identical manner to the method discussed in Sec. 4.2.3, however with an increased set of NR waveforms, listed in Tab. 6.1, consisting of 30 `SXS` and 2 `BAM` waveforms.

The data of Table 6.1 are fitted globally with a template simplified relative to the one used in Sec. 4.2.3. The template is given by

$$\begin{aligned} c_3(\tilde{a}_1, \tilde{a}_2, \nu) = {}& p_0 \frac{1 + n_1 \tilde{a}_0 + n_2 \tilde{a}_0^2 + n_3 \tilde{a}_0^3 + n_4 \tilde{a}_0^4}{1 + d_1 \tilde{a}_0} \\ & + p_1 \tilde{a}_0 \nu \sqrt{1 - 4\nu} + p_2 \left(\tilde{a}_1 - \tilde{a}_2\right) \nu^2, \end{aligned} \tag{6.1}$$

where the fitted parameters are given as

$$p_0 = 45.235903, \tag{6.2}$$

$$n_1 = -1.688708, \tag{6.3}$$

$$n_2 = 0.787959, \tag{6.4}$$

$$n_3 = -0.018080, \tag{6.5}$$

$$n_4 = -0.001906, \tag{6.6}$$

$$d_1 = -0.751479, \tag{6.7}$$

$$p_1 = 47.3756, \tag{6.8}$$

$$p_2 = -36.1964. \tag{6.9}$$

---

[1] This fit was performed by Alessandro Nagar.

Table 6.1: Binary configurations, first-guess values of c_3 used to inform the global interpolating fit given in eq. (6.1), and the corresponding $c_3^{\rm fit}$ values.

#	ID	(q, χ_1, χ_2)	$c_3^{\rm first\ guess}$	$c_3^{\rm fit}$
1	SXS:BBH:0156	$(1, -0.95, -0.95)$	88	87.87
2	SXS:BBH:0159	$(1, -0.90, -0.90)$	85.5	85.54
3	SXS:BBH:0154	$(1, -0.80, -0.80)$	81	80.90
4	SXS:BBH:0215	$(1, -0.60, -0.60)$	71.5	71.72
5	SXS:BBH:0150	$(1, +0.20, +0.20)$	38.0	36.92
6	SXS:BBH:0228	$(1, +0.60, +0.60)$	22.0	21.94
7	SXS:BBH:0230	$(1, +0.80, +0.80)$	15.5	16.25
8	SXS:BBH:0153	$(1, +0.85, +0.85)$	14.5	15.25
9	SXS:BBH:0160	$(1, +0.90, +0.90)$	14.9	14.53
10	SXS:BBH:0157	$(1, +0.95, +0.95)$	14.3	14.20
11	SXS:BBH:0177	$(1, +0.99, +0.99)$	14.2	14.32
12	SXS:BBH:0004	$(1, -0.50, 0)$	54.5	56.61
13	SXS:BBH:0231	$(1, +0.90, 0)$	27.0	26.18
14	SXS:BBH:0232	$(1, +0.90, +0.50)$	19.0	18.38
15	SXS:BBH:0005	$(1, +0.50, 0)$	34.3	34.34
16	SXS:BBH:0016	$(1.5, -0.50, 0)$	57.0	58.19
17	SXS:BBH:0255	$(2, +0.60, 0)$	29.0	29.75
18	SXS:BBH:0256	$(2, +0.60, +0.60)$	22.8	23.68
19	SXS:BBH:0257	$(2, +0.85, +0.85)$	15.7	17.73
20	SXS:BBH:0036	$(3, -0.50, 0)$	60.0	60.39
21	SXS:BBH:0267	$(3, -0.50, -0.50)$	69.5	65.28
22	SXS:BBH:0174	$(3, +0.50, 0)$	30.0	31.20
23	SXS:BBH:0286	$(3, +0.50, +0.50)$	26.0	27.28
24	SXS:BBH:0291	$(3, +0.60, +0.60)$	23.4	24.22
25	SXS:BBH:0293	$(3, +0.85, +0.85)$	16.2	18.48
26	SXS:BBH:0060	$(5, -0.50, 0)$	62.0	61.91
27	SXS:BBH:0110	$(5, +0.50, 0)$	31.0	29.97
28	SXS:BBH:1375	$(8, -0.90, 0)$	64.0	78.27
29	SXS:BBH:0064	$(8, -0.50, 0)$	57.0	63.23
30	SXS:BBH:0065	$(8, +0.50, 0)$	28.5	28.86
31	BAM	$(8, +0.80, 0)$	24.5	20.85
32	BAM	$(8, +0.85, +0.85)$	16.3	18.11

6.2.2 Modeling the peak of each multipole

The modelization of the peak and postpeak waveform multipole by multipole is done following precisely the same procedure adopted in the nonspinning case, but incorporating spin dependence (whenever possible) in all fits. In practice the spin-dependence is included as: (i) complete spin-dependence for what concerns peak quantities and postpeak fits in all $\ell = m$ modes up to $\ell = 5$; (ii) modes like $(2, 1)$, $(3, 2)$, $(4, 3)$ and $(4, 2)$ include spin dependence for peak frequency and amplitude, but they adopt the simpler nonspinning fits for the parameters entering the postpeak waveform description; (iii) the $(3, 1)$ and $(4, 1)$ mode only rely on nonspinning information. The values at the NQC determination points are either obtained with dedicated fits of the corresponding NR quantities, or directly from the postpeak behavior. It will be shown, this approach allows one to obtain a rather robust description of the ringdown waveform all over the parameter space. Firstly, it is useful to recall some symmetric combinations of the spin variables that will be useful later on

$$\hat{S} \equiv \frac{S_1 + S_2}{M^2} = \frac{1}{2}\left(\hat{a}_0 + X_{12}\tilde{a}_{12}\right), \tag{6.10}$$

$$\bar{S} \equiv \frac{S_1 - S_2}{M^2} = \frac{1}{2}\left(X_{12}\hat{a}_0 + \tilde{a}_{12}\right). \tag{6.11}$$

Motivated by the leading-order analytical behavior of each multipole, rescaled multipolar amplitudes $\hat{A}_{\ell m}$ which previously have only been rescaled by ν now are redefined as:

$$\hat{A}_{22} \equiv A_{22}/\left[\nu\left(1 - \hat{S}\omega_{22}\right)\right], \tag{6.12}$$

$$\hat{A}_{21} \equiv A_{21}/\nu, \tag{6.13}$$

$$\hat{A}_{33} \equiv A_{33}/\nu, \tag{6.14}$$

$$\hat{A}_{32} \equiv A_{32}/\left[\nu\left(1 - \hat{a}_0\left(\omega_{32}/2\right)^{1/3}\right)\right], \tag{6.15}$$

$$\hat{A}_{44} \equiv A_{44}/\left[\nu\left(1 - \frac{1}{2}\hat{S}\omega_{44}\right)\right], \tag{6.16}$$

$$\hat{A}_{43} \equiv A_{43}/\nu, \tag{6.17}$$

$$\hat{A}_{42} \equiv A_{42}/\left[\nu\left(1 - \hat{a}_0\left(\omega_{42}/2\right)^{1/3}\right)\right]. \tag{6.18}$$

Now each mode will be discussed individually.

$(\ell, m) = (2, 2)$ multipole

The first mode to discuss is by describing the template with which $\omega_{22}^{\rm mrg}$ and $\hat{A}_{22}^{\rm mrg}$ were fitted. The same structure is used both for the amplitude and frequency at merger. The template is here presented explicitly for $\omega_{22}^{\rm mrg}$, while the same for $\hat{A}_{22}^{\rm mrg}$ is obtained by suitably changing the coefficient labels. The frequency at merger $\omega_{22}^{\rm mrg}$ is factorized as

$$\omega_{22}^{\rm mrg} = \omega_{22}^{\rm mrg_0}\omega_{22}^{\rm orb}(\nu)\omega_{22}^{\hat{S}}(\hat{S}, X_{12}), \tag{6.19}$$

where $\omega_{22}^{\rm mrg_0}$ is the value of the merger frequency obtained from a nonspinning test-particle waveform (see e.g. Tab. 3 of [90]). The nonspinning ν-dependence is then introduced by fitting the nonspinning data with a template of the form

$$\omega_{22}^{\rm orb}(\nu) = 1 + a_1^{\omega}\nu + a_2^{\omega}\nu^2, \tag{6.20}$$

where the coefficients a_i^{ω} are determined using 19 non-spinning SXS waveforms with mass ratios $1 \leq m_1/m_2 \leq 10$. The spin dependence is introduced in two steps: first one accurately fits the spin-dependence of equal-mass data. Then, additional flexibility to incorporate the spinning, unequal-mass data is introduced. More precisely the equal-mass, spin-dependence is obtained with

$$\omega_{22}^{\hat{S}}(\hat{S}, X_{12} = 0) = \frac{1 + b_1^{\omega_{m_1=m_2}}\hat{S} + b_2^{\omega_{m_1=m_2}}\hat{S}^2}{1 + b_3^{\omega_{m_1=m_2}}\hat{S}}, \tag{6.21}$$

which is informed by 39 equal-mass, spin-aligned, SXS waveforms. The additional dependence on mass ratio is incorporated substituting into Eq. (6.21)

$$b_i^{\omega_{m_1=m_2}} \to \frac{b_i^{\omega_{m_1=m_2}} + c_{i1}^{\omega} X_{12}}{1 + c_{i2}^{\omega} X_{12}} \ , \tag{6.22}$$

with $i = \{1, 3\}$. where the additional coefficients c_{ij} are fitted using test-particle data, 77 additional SXS spinning waveforms and 14 additional NR waveforms from BAM. The coefficients are explicitly given in Table D.1.

$(\ell, m) = (2, 1)$ multipole

The procedure followed for the subdominant modes is similar to what is done for the $(2, 2)$. There are however some differences. First of all, the peak time shift $\Delta t_{\ell m}$ is also fitted to NR simulations. Second, based on the analytical behavior of the multipolar waveform, it was decided to use different factorizations and different variables to model each mode. For example, the $(2, 1)$ multipole (and every m-odd mode) vanishes because of symmetry in the equal-mass, equal-spin case. This motivated the choice of the following factorization for $\hat{A}_{21}^{\rm peak}$, which is written as

$$\hat{A}_{21}^{\rm peak} = \hat{A}_{21}^{\rm peak_0} X_{12} \hat{A}_{21}^{\rm orb}(\nu) + \hat{A}_{21}^{\rm Spin}\left(\bar{S}, \nu\right) . \tag{6.23}$$

where $\hat{A}_{21}^{\rm peak_0}$ is the peak amplitude in the test-particle limit. The factor $\hat{A}_{21}^{\rm orb}$ is informed by nonspinning waveforms and is fitted with the template

$$\hat{A}_{21}^{\rm orb}(\nu) = \frac{1 + a_1^{\hat{A}_{21}}\nu + a_2^{\hat{A}_{21}}\nu^2}{1 + a_3^{\hat{A}_{21}}\nu} \ . \tag{6.24}$$

The spin dependence is first captured in the test-particle limit with the function

$$\hat{A}_{21}^{\rm Spin}(\bar{S}, \nu = 0) = \frac{1 + b_1^{\hat{A}_{21}^0}\bar{S} + b_2^{\hat{A}_{21}^0}\bar{S}^2}{1 + b_3^{\hat{A}_{21}^0}\bar{S}} \ . \tag{6.25}$$

The ν-dependence is then modeled via the replacement

$$b_i^{\hat{A}_{21}^0} \to b_i^{\hat{A}_{21}^0} + c_{i1}^{\hat{A}_{21}}\nu + c_{i2}^{\hat{A}_{21}}\nu^2 \ , \tag{6.26}$$

with $i = \{1, 2, 3\}$.

The gravitational wave frequency ω_{21} is instead factorized as

$$\omega_{21}^{\rm peak} = \omega_{21}^{\rm peak_0}\omega_{21}^{\rm orb}(\nu)\omega_{21}^{\rm Spin}\left(\hat{S}, \nu\right) , \tag{6.27}$$

where the ν-dependence of the nonspinning part is modeled as

$$\omega_{21}^{\rm orb}(\nu) = 1 + a_1^{\omega_{21}}\nu + a_2^{\omega_{21}}\nu^2 \ . \tag{6.28}$$

The spin dependence is fitted first in the test-particle limit

$$\omega_{21}^{\rm Spin}\left(\hat{S},\nu=0\right) = 1 + b_1^{\omega_{21}^0}\hat{S} + b_2^{\omega_{21}^0}\hat{S}^2 \ , \tag{6.29}$$

and then extended to a general mass ratio via the replacement

$$b_i^{\omega_{21}^0} \to b_i^{\omega_{21}^0} + c_i^{\omega_{21}}\nu \ , \tag{6.30}$$

with $i=\{1,2\}$.

Finally, to represent analytically the time-delay Δt_{21} the following template was used

$$\Delta t_{21} = \Delta t_{21}^{\rm orb}(\nu)\Delta t_{21}^{\rm spin}\left(\bar{S},X_{12}\right) \ , \tag{6.31}$$

where the orbital behavior is factorized into two separate parts before fitting with

$$\begin{aligned}\Delta t_{21}^{\rm orb}(\nu) = &\left(\Delta t_{21}^0(1-4\nu) + \Delta t_{21}^{\nu=1/4}4\nu\right) \\ &\times\left(1 + a_1^{\Delta t_{21}}\nu\sqrt{1-4\nu}\right) \ .\end{aligned} \tag{6.32}$$

The factor $\Delta t_{21}^{\nu=1/4}$ is obtained by fitting a 2nd-order polynomial, in $\hat{a}_0$ to the equal-mass waveforms. Δt_{21}^0 is the test-particle value. The equal-mass spin behavior is fitted with

$$\Delta t_{21}^{\rm spin}\left(\bar{S},X_{12}=0\right) = 1 + b_1^{\Delta t_{21}^{\nu=1/4}}\hat{a}_0 + b_2^{\Delta t_{21}^{\nu=1/4}}\hat{a}_0^2 \ , \tag{6.33}$$

while the comparable mass case is extrapolated using

$$b_1^{\Delta t_{21}^{\nu=1/4}} \to \frac{b_1^{\Delta t_{21}^0} + c_{i1}^{\Delta t_{21}}X_{12}}{1 + c_{i2}^{\Delta t_{21}}X_{12}} \ , \tag{6.34}$$

with $i=\{1,2\}$. The outcome of the fit, with the explicit values of all coefficients, id found in Table D.2.

$(\ell,m)=(3,3)$ multipole

For this mode, the peak amplitude is written as the sum of two terms

$$\hat{A}_{33}^{\rm peak} = \hat{A}_{33}^{\rm peak_0}X_{12}\hat{A}_{33}^{\rm orb}(\nu) + \hat{A}_{33}^{\rm Spin}(\tilde{a}_{12},\nu) \ , \tag{6.35}$$

where $\hat{A}_{33}^{\rm peak_0}$ is the peak amplitude in the test particle limit. The orbital term is modeled as

$$\hat{A}_{33}^{\rm orb}(\nu) = \frac{1 + a_1^{\hat{A}_{33}}\nu + a_2^{\hat{A}_{33}}\nu^2}{1 + a_3^{\hat{A}_{33}}\nu} \ . \tag{6.36}$$

The spin dependence is first fitted in the test-particle limit using

$$\hat{A}_{33}^{\rm Spin}(\tilde{a}_{12},\nu=0) = \frac{b_1^{\hat{A}_{33}^0}\tilde{a}_{12}}{1 + b_2^{\hat{A}_{33}^0}\tilde{a}_{12}} \ , \tag{6.37}$$

and then extended to comparable masses via the replacements

$$b_1^{\hat{A}^0_{33}} \to \frac{b_1^{\hat{A}^0_{33}} + c_{11}^{\hat{A}_{33}}\nu}{1 + c_{12}^{\hat{A}_{33}}\nu + c_{13}^{\hat{A}_{33}}\nu^2} \ , \tag{6.38}$$

$$b_2^{\hat{A}^0_{33}} \to \frac{b_2^{\hat{A}^0_{33}} + c_{21}^{\hat{A}_{33}}\nu}{1 + c_{22}^{\hat{A}_{33}}\nu + c_{23}^{\hat{A}_{33}}\nu^2} \ . \tag{6.39}$$

The instantaneous frequency ω_{33} is factorized as

$$\omega_{33}^{\rm peak} = \omega_{33}^{{\rm peak}_0}\omega_{33}^{\rm orb}(\nu)\omega_{33}^{\rm Spin}\left(\hat{S},\nu\right) \ , \tag{6.40}$$

where

$$\omega_{33}^{\rm orb}(\nu) = 1 + a_1^{\omega_{33}}\nu + a_2^{\omega_{33}}\nu^2 \ . \tag{6.41}$$

The test-particle spin factor is given by

$$\omega_{33}^{\rm Spin}\left(\hat{S},\nu=0\right) = \frac{1 + b_1^{\omega^0_{33}}\hat{S} + b_2^{\omega^0_{33}}\hat{S}^2}{1 + b_3^{\omega^0_{33}}\hat{S}} \ , \tag{6.42}$$

while the general spin-dependence stems from the replacement

$$b_i^{\omega^0_{33}} \to \frac{b_i^{\omega^0_{33}} + c_{i1}^{\omega_{33}}\nu}{1 + c_{i2}^{\omega_{33}}\nu} \ , \tag{6.43}$$

with $i = \{1, 3\}$.

To describe Δt_{33} we start from the expression

$$\Delta t_{33} = \Delta t_{33}^0 \Delta t_{33}^{\rm orb}(\nu)\Delta t_{33}^{\rm spin}\left(\hat{S},\nu\right) \ , \tag{6.44}$$

with

$$\Delta t_{33}^{\rm orb}(\nu) = 1 + a_1^{\Delta t_{33}}\nu + a_2^{\Delta t_{33}}\nu^2 \ , \tag{6.45}$$

$$\Delta t_{33}^{\rm spin}\left(\hat{S},\nu=0\right) = \frac{1 + b_1^{\Delta t^0_{33}}\hat{S} + b_2^{\Delta t^0_{33}}\hat{S}^2}{1 + b_3^{\Delta t^0_{33}}\hat{S}} \ . \tag{6.46}$$

The spin-dependence is obtained from the replacement

$$b_1^{\Delta t^0_{33}} \to \frac{b_1^{\Delta t^0_{33}} + c_{i1}^{\Delta t_{33}}\nu}{1 + c_{i2}^{\Delta t_{33}}\nu} \ , \tag{6.47}$$

with $i = \{1, 2, 3\}$. The explicit values of the fit coefficients are listed in Table D.3.

$(\ell, m) = (3,2)$ multipole

The peak amplitude of the $(3,2)$ mode is fitted with a factorized template of the form

$$\hat{A}_{32}^{\rm peak} = \hat{A}_{32}^{\rm peak_0} \left(1-3\nu\right) \hat{A}_{32}^{\rm orb}\left(\nu\right) \hat{A}_{32}^{\rm Spin}\left(\bar{S},\nu\right) \ , \tag{6.48}$$

where $\hat{A}_{32}^{\rm peak_0}$ is the peak amplitude of the mode in the test-particle limit. The factor $\hat{A}_{32}^{\rm orb}$ is informed by non-spinning waveforms and is fitted with the template

$$\hat{A}_{32}^{\rm orb}(\nu) = \frac{1 + a_1^{\hat{A}_{32}}\nu + a_2^{\hat{A}_{32}}\nu^2}{1 + a_3^{\hat{A}_{32}}\nu} \ . \tag{6.49}$$

The spin dependence is first captured for the test-particle limit with the function

$$\hat{A}_{32}^{\rm Spin}(\bar{S},\nu=0) = \frac{1 + b_1^{\hat{A}_{32}^0}\tilde{a}_0}{1 + b_2^{\hat{A}_{32}^0}\tilde{a}_0} \ , \tag{6.50}$$

while the ν-dependence enters via the replacement

$$b_i^{\hat{A}_{32}^0} \to \frac{b_i^{\hat{A}_{32}^0} + c_{i1}^{\hat{A}_{32}}\nu + c_{i2}^{\hat{A}_{32}}\nu^2}{1 + c_{i3}^{\hat{A}_{32}}\nu + c_{i4}^{\hat{A}_{32}}\nu^2} \ , \tag{6.51}$$

with $i = \{1,2\}$.

The instantaneous frequency ω_{32} mode is factorized as

$$\omega_{32}^{\rm peak} = \omega_{32}^{\rm peak_0}\omega_{32}^{\rm orb}(\nu)\omega_{32}^{\rm Spin}\left(\tilde{a}_0,\nu\right) \ . \tag{6.52}$$

The orbital dependence is modeled as

$$\omega_{32}^{\rm orb}(\nu) = \frac{1 + a_1^{\omega_{32}}\nu + a_2^{\omega_{32}}\nu^2}{1 + a_3^{\omega_{32}}\nu + a_4^{\omega_{32}}\nu^2} \ . \tag{6.53}$$

The spin dependence is fitted first for the equal-mass case

$$\omega_{32}^{\rm Spin}\left(\tilde{a}_0,\nu=1/4\right) = \frac{1 + b_1^{\omega_{32}^{\nu=1/4}}\tilde{a}_0 + b_2^{\omega_{32}^{\nu=1/4}}\tilde{a}_0^2}{1 + b_3^{\omega_{32}^{\nu=1/4}}\tilde{a}_0} \ , \tag{6.54}$$

while the additional dependence on the mass ratio enters via the replacements

$$b_i^{\omega_{32}^0} \to \frac{b_i^{\omega_{32}^{\nu=1/4}} + c_{i1}^{\omega_{32}}X_{12} + c_{i2}^{\omega_{32}}X_{12}^2}{1 + c_{i3}^{\omega_{32}}X_{12}} \ , \tag{6.55}$$

with $i = \{1,2\}$. The coefficients of $\hat{A}_{32}^{\rm peak}$ and $\omega_{32}^{\rm peak}$ are explicitly listed in Table D.4.

Moving to Δt_{32}, it is given by

$$\Delta t_{32} = \Delta t_{32}^0 \Delta t_{32}^{\rm orb}(\nu) \Delta t_{32}^{\rm spin}\left(\hat{S},\nu\right) \ , \tag{6.56}$$

where the orbital behavior is fitted with

$$\Delta t_{32}^{\rm orb}(\nu) = \frac{1 + a_1^{\Delta t_{32}}\nu + a_2^{\Delta t_{32}}\nu^2}{1 + a_3^{\Delta t_{32}}\nu + a_4^{\Delta t_{32}}\nu^2} \ . \tag{6.57}$$

The spin behavior is more complicated than the corresponding term of other modes. This is separated into two sectors, as

$$\begin{aligned}\Delta t_{32}^{\rm spin}\left(\hat{S},\nu\right) &= \Delta t_{32}^{{\rm spin}_{\nu>1/5}}\left(\hat{S},\nu\right)\Theta\left(\nu-1/5\right)\\ &+ \Delta t_{32}^{{\rm spin}_{\nu\leq 1/5}}\left(\hat{S},\nu\right)\left[1-\Theta\left(\nu-1/5\right)\right] \ ,\end{aligned} \tag{6.58}$$

where Θ denotes the Heaviside step function. In the $\nu > 1/5$ regime the fit is first done to the equal-mass case

$$\Delta t_{32}^{{\rm spin}_{\nu>1/5}}\left(\hat{S},\nu=1/4\right) = \frac{1 + b_1^{\Delta t_{32}^{\nu=1/4}}\hat{S} + b_2^{\Delta t_{32}^{\nu=1/4}}\hat{S}^2}{1 + b_3^{\Delta t_{32}^{\nu=1/4}}\hat{S}} \ . \tag{6.59}$$

Then it is extrapolated following

$$b_i^{\Delta t_{32}^{\nu=1/4}} \to \frac{b_1^{\Delta t_{32}^{\nu=1/4}} + c_{i1}^{\Delta t_{32}}X_{12} + c_{i2}^{\Delta t_{32}}X_{12}^2 + c_{i3}^{\Delta t_{32}}X_{12}^3}{1 + c_{i4}^{\Delta t_{43}}X_{12} + c_{i5}^{\Delta t_{43}}X_{12}^2} \ , \tag{6.60}$$

with $i = \{1,2,3\}$.

In the $\nu \leq 1/5$ regime the fit is first done to the equal-mass case

$$\Delta t_{32}^{{\rm spin}_{\nu\leq 1/5}}\left(\hat{S},\nu=0\right) = \frac{1 + b_1^{\Delta t_{32}^0}\hat{S} + b_2^{\Delta t_{32}^0}\hat{S}^2}{1 + b_3^{\Delta t_{32}^0}\hat{S}} \ . \tag{6.61}$$

Then it is extrapolated following

$$b_i^{\Delta t_{32}^0} \to \frac{b_1^{\Delta t_{32}^0} + c_{i1}^{\Delta t_{32}}\nu + c_{i2}^{\Delta t_{32}}\nu^2 + c_{i3}^{\Delta t_{32}}\nu^3}{1 + c_{i4}^{\Delta t_{32}}\nu + c_{i5}^{\Delta t_{32}}\nu^2} \ , \tag{6.62}$$

with $i = \{1,2,3\}$. The coefficients appearing in Δt_{32} are shown in Table D.5.

$(\ell, m) = (4,4)$ multipole

The peak amplitude of the $(4,4)$ mode is fitted with

$$\hat{A}_{44}^{\rm peak} = \hat{A}_{44}^{{\rm peak}_0}\left(1-3\nu\right)\hat{A}_{44}^{\rm orb}\left(\nu\right)\hat{A}_{44}^{\rm Spin}\left(\hat{S},\nu\right) \ , \tag{6.63}$$

where $\hat{A}_{44}^{{\rm peak}_0}$ is the peak amplitude of the mode in the test-particle limit. The factor $\hat{A}_{44}^{\rm orb}$ is informed by non-spinning waveforms and is fitted with the template

$$\hat{A}_{44}^{\rm orb}(\nu) = \frac{1 + a_1^{\hat{A}_{44}}\nu + a_2^{\hat{A}_{44}}\nu^2}{1 + a_3^{\hat{A}_{44}}\nu} \ . \tag{6.64}$$

The spin dependence is first captured for the test-particle limit with the function

$$\hat{A}_{44}^{\rm Spin}(\hat{S},\nu=0)=\frac{1+b_1^{\hat{A}^0_{44}}\hat{S}+b_2^{\hat{A}^0_{44}}\hat{S}^2}{1+b_3^{\hat{A}^0_{44}}\hat{S}}\ , \tag{6.65}$$

and then extended in the comparable mass region of the parameter space through

$$b_i^{\hat{A}^0_{44}}\to\frac{b_i^{\hat{A}^0_{44}}+c_{i1}^{\hat{A}_{44}}\nu+c_{i2}^{\hat{A}_{44}}\nu^2}{1+c_{i3}^{\hat{A}_{44}}\nu+c_{i4}^{\hat{A}_{44}}\nu^2}\ ,\ \text{with } i=\{1,2,3\}\,. \tag{6.66}$$

The peak frequency ω_{44} is factorized as

$$\omega_{44}^{\rm peak}=\omega_{44}^{{\rm peak}_0}\omega_{44}^{\rm orb}(\nu)\omega_{44}^{\rm Spin}\left(\hat{S},\nu\right)\ . \tag{6.67}$$

The orbital dependence is modeled through

$$\omega_{44}^{\rm orb}(\nu)=\frac{1+a_1^{\omega_{44}}\nu+a_2^{\omega_{44}}\nu^2}{1+a_3^{\omega_{44}}\nu+a_4^{\omega_{44}}\nu^2}\ . \tag{6.68}$$

The spin dependence is fitted first for the test-particle limit as

$$\omega_{44}^{\rm Spin}\left(\hat{S},\nu=0\right)=\frac{1+b_1^{\omega^0_{44}}\hat{S}+b_2^{\omega^0_{44}}\hat{S}^2+b_3^{\omega^0_{44}}\hat{S}^3}{1+b_4^{\omega^0_{33}}\hat{S}}\ . \tag{6.69}$$

The spin dependence in the comparable mass region of the parameter space is modeled through

$$b_i^{\omega^0_{44}}\to\frac{b_i^{\omega^0_{44}}+c_{i1}^{\omega_{44}}\nu+c_{i2}^{\omega_{44}}\nu^2}{1+c_{i3}^{\omega_{44}}\nu+c_{i4}^{\omega_{44}}\nu^2}\ , \tag{6.70}$$

with $i=\{1,2,3,4\}$.

We fit Δt_{44} in a factorized form as

$$\Delta t_{44}=\Delta t_{44}^0\Delta t_{44}^{\rm orb}(\nu)\Delta t_{44}^{\rm spin}\left(\hat{S},X_{12}\right)\ . \tag{6.71}$$

The orbital behavior is fitted with

$$\Delta t_{44}^{\rm orb}(\nu)=\frac{1+a_1^{\Delta t_{44}}\nu+a_2^{\Delta t_{44}}\nu^2}{1+a_3^{\Delta t_{44}}\nu+a_4^{\Delta t_{44}}\nu^2}\ , \tag{6.72}$$

while the spinning one is first fitted to equal mass simulations as

$$\Delta t_{44}^{\rm spin}\left(\hat{S},X_{12}=0\right)=\frac{1+b_1^{\Delta t_{44}^{\nu=1/4}}\hat{S}}{1+b_2^{\Delta t_{44}^{\nu=1/4}}\hat{S}}\ . \tag{6.73}$$

The general ν-dependence enters via the replacement

$$b_i^{\Delta t_{44}^{\nu=1/4}}\to b_i^{\Delta t_{44}^{\nu=1/4}}+c_{i1}^{\Delta t_{44}}X_{12}+c_{i2}^{\Delta t_{44}}X_{12}^2\ , \tag{6.74}$$

with $i = \{1, 2\}$. The explicit values of the fit coefficients can be found in Table D.6.

$(\ell, m) = (4, 3)$ **multipole**

The peak amplitude of the $(4, 3)$ mode is fitted with

$$\hat{A}_{43}^{\text{peak}} = \hat{A}_{43}^{\text{peak}_0} X_{12} \left(1 - 2\nu\right) \hat{A}_{43}^{\text{orb}} \left(\nu\right) + \hat{A}_{43}^{\text{Spin}} \left(\tilde{a}_0, \nu\right) \ , \tag{6.75}$$

where $\hat{A}_{43}^{\text{peak}_0}$ is the peak amplitude of the mode in the test-particle limit. The factor $\hat{A}_{43}^{\text{orb}}$ is informed by non-spinning waveforms and is fitted with the template

$$\hat{A}_{43}^{\text{orb}}(\nu) = \frac{1 + a_1^{\hat{A}_{43}}\nu + a_2^{\hat{A}_{43}}\nu^2}{1 + a_3^{\hat{A}_{43}}\nu} \ . \tag{6.76}$$

The spin dependence is first captured for the test-particle limit with the function

$$\hat{A}_{43}^{\text{Spin}}(\tilde{a}_0, \nu = 0) = \frac{1 + b_1^{\hat{A}_{43}^0}\tilde{a}_0 + b_2^{\hat{A}_{43}^0}\tilde{a}_0^2}{1 + b_3^{\hat{A}_{43}^0}\tilde{a}_0} \ . \tag{6.77}$$

The spin dependence in the comparable mass region of the parameter space is modeled through

$$b_i^{\hat{A}_{43}^0} \to \frac{b_i^{\hat{A}_{43}^0} + c_{i1}^{\hat{A}_{43}}\nu}{1 + c_{i2}^{\hat{A}_{43}}\nu + c_{i3}^{\hat{A}_{43}}\nu^2} \ , \tag{6.78}$$

with $i = \{1, 2, 3\}$. For the equal mass case however a special fit is made to accurately capture the correct behavior, i.e.

$$\hat{A}_{43}^{\text{peak}}\left(\tilde{a}_{12}, \nu = \frac{1}{4}\right) = \frac{b_1^{\hat{A}_{43}^{\nu=1/4}}\tilde{a}_{12} + b_2^{\hat{A}_{43}^{\nu=1/4}}\tilde{a}_{12}^2}{1 + b_3^{\hat{A}_{43}^{\nu=1/4}}\tilde{a}_{12}} \ . \tag{6.79}$$

The instantaneous frequency at peak $\omega_{43}^{\text{peak}}$ is factorized as

$$\omega_{43}^{\text{peak}} = \omega_{43}^{\text{peak}_0}\omega_{43}^{\text{orb}}(\nu)\omega_{43}^{\text{Spin}}\left(\hat{S}, \nu\right) , \tag{6.80}$$

where the orbital factor is modeled as

$$\omega_{43}^{\text{orb}}(\nu) = \frac{1 + a_1^{\omega_{43}}\nu + a_2^{\omega_{43}}\nu^2}{1 + a_3^{\omega_{43}}\nu + a_4^{\omega_{43}}\nu^2} \ . \tag{6.81}$$

The spin dependence is fitted first for the test-particle case

$$\omega_{43}^{\text{Spin}}\left(\hat{S}, \nu = 0\right) = \frac{1 + b_1^{\omega_{43}^0}\hat{S} + b_2^{\omega_{43}^0}\hat{S}^2}{1 + b_3^{\omega_{43}^0}\hat{S}} \ , \tag{6.82}$$

and then extended to other regions of the parameter space with

$$b_i^{\omega_{43}^0} \to \frac{b_i^{\omega_{43}^0} + c_{i1}^{\omega_{43}}\nu + c_{i2}^{\omega_{43}}\nu^2}{1 + c_{i3}^{\omega_{43}}\nu} \ , \tag{6.83}$$

where $i = \{1, 2, 3\}$.

For what concerns Δt_{43}, it is represented as

$$\Delta t_{43} = \Delta t_{43}^{0} \Delta t_{43}^{\rm orb}(\nu) \Delta t_{43}^{\rm spin}\left(\hat{S}, \nu\right) \ , \tag{6.84}$$

with

$$\Delta t_{43}^{\rm orb}(\nu) = \frac{1 + a_1^{\Delta t_{43}} \nu + a_2^{\Delta t_{43}} \nu^2}{1 + a_3^{\Delta t_{43}} \nu + a_4^{\Delta t_{43}} \nu^2} \ , \tag{6.85}$$

$$\Delta t_{43}^{\rm spin}\left(\hat{S}, \nu = 0\right) = \frac{1 + b_1^{\Delta t_{43}^0} \hat{S} + b_2^{\Delta t_{43}^0} \hat{S}^2}{1 + b_3^{\Delta t_{43}^0} \hat{S}} \ . \tag{6.86}$$

We then incorporate the general ν-dependence via the replacement

$$b_i^{\Delta t_{43}^0} \to \frac{b_1^{\Delta t_{43}^0} + c_{i1}^{\Delta t_{43}} \nu + c_{i2}^{\Delta t_{43}} \nu^2}{1 + c_{i3}^{\Delta t_{43}} \nu + c_{i4}^{\Delta t_{43}} \nu^2} \ , \tag{6.87}$$

with $i = \{1, 2, 3\}$. The explicit values of the fit coefficients are listed in Table D.7.

$(\ell, m) = (4, 2)$ multipole

The peak amplitude of the $(4, 2)$ mode is fitted with a factorized template of the form

$$\hat{A}_{42}^{\rm peak} = \hat{A}_{42}^{\rm peak_0} \left(1 - 3\nu\right) \hat{A}_{42}^{\rm orb}\left(\nu\right) \hat{A}_{42}^{\rm Spin}\left(\hat{S}, \nu\right) \ , \tag{6.88}$$

where $\hat{A}_{42}^{\rm peak_0}$ is the peak amplitude of the mode in the test-particle limit. The factor $\hat{A}_{42}^{\rm orb}$ is informed by non-spinning waveforms and is fitted with the template

$$\hat{A}_{42}^{\rm orb}(\nu) = 1 + a_1^{\hat{A}_{42}} \nu + a_2^{\hat{A}_{42}} \nu^2 \ . \tag{6.89}$$

The spin dependence is first captured for the test-particle limit with the function

$$\hat{A}_{42}^{\rm Spin}(\hat{S}, \nu = 0) = \frac{1 + b_1^{\hat{A}_{42}^0} \hat{S} + b_2^{\hat{A}_{42}^0} \hat{S}^2}{1 + b_3^{\hat{A}_{42}^0} \hat{S} + b_4^{\hat{A}_{42}^0} \hat{S}^2} \ . \tag{6.90}$$

The general ν-dependence is then taken into account via the replacement

$$b_i^{\hat{A}_{42}^0} \to \frac{b_i^{\hat{A}_{42}^0} + c_{i1}^{\hat{A}_{42}} \nu}{1 + c_{i2}^{\hat{A}_{42}} \nu} \ , \tag{6.91}$$

with $i = \{1, 2, 3, 4\}$.

The instantaneous frequency $\omega_{42}^{\rm peak}$ is factorized as

$$\omega_{42}^{\rm peak} = \omega_{42}^{\rm peak_0} \omega_{42}^{\rm orb}(\nu) \omega_{42}^{\rm Spin}\left(\hat{S}, \nu\right) \tag{6.92}$$

The orbital dependence is modeled through

$$\omega_{42}^{\rm orb}(\nu) = \frac{1 + a_1^{\omega_{42}}\nu + a_2^{\omega_{42}}\nu^2}{1 + a_3^{\omega_{42}}\nu + a_4^{\omega_{42}}\nu^2} \ . \tag{6.93}$$

The spin dependence is fitted first for the test-mass case with

$$\omega_{42}^{\rm Spin}\left(\hat{S}, \nu = 0\right) = \frac{1 + b_1^{\omega_{42}^0}\hat{S} + b_2^{\omega_{42}^0}\hat{S}^2}{1 + b_3^{\omega_{42}^0}\hat{S} + b_4^{\omega_{42}^0}\hat{S}^2} \ , \tag{6.94}$$

and then the general ν-dependence is taken into account via the replacement

$$b_i^{\omega_{42}^0} \to \frac{b_i^{\omega_{42}^0} + c_{i1}^{\omega_{42}}\nu}{1 + c_{i2}^{\omega_{42}}\nu + c_{i3}^{\omega_{42}}\nu^2} \ , \tag{6.95}$$

with $i = \{1, 2, 3, 4\}$. The delay Δt_{42} is fitted as

$$\Delta t_{42} = \Delta t_{42}^0 \Delta t_{42}^{\rm orb}(\nu) \Delta t_{42}^{\rm spin}\left(\hat{S}, \nu\right) \ , \tag{6.96}$$

where

$$\Delta t_{42}^{\rm orb}(\nu) = \frac{1 + a_1^{\Delta t_{42}}\nu + a_2^{\Delta t_{42}}\nu^2}{1 + a_3^{\Delta t_{42}}\nu + a_4^{\Delta t_{42}}\nu^2} \ , \tag{6.97}$$

$$\Delta t_{42}^{\rm spin}\left(\hat{S}, \nu = 0\right) = \frac{1 + b_1^{\Delta t_{42}^0}\hat{S}}{1 + b_2^{\Delta t_{42}^0}\hat{S}} \ . \tag{6.98}$$

For $\nu < 6/25$ the spin factor is approximated by the test-particle fit. For the other regions, it is extrapolated using

$$b_i^{\Delta t_{42}^0} \to \frac{b_1^{\Delta t_{42}^0} + c_{i1}^{\Delta t_{42}}\nu}{1 + c_{i2}^{\Delta t_{42}}\nu} \ , \tag{6.99}$$

with $i = \{1, 2\}$. The explicit values of the coefficients of the fits are listed in Table D.8.

$(\ell, m) = (5, 5)$ **multipole**

For this multipole, the peak amplitude is written as the sum of two terms as

$$\hat{A}_{55}^{\rm peak} = \hat{A}_{55}^{\rm peak_0} X_{12}\left(1 - 2\nu\right) \hat{A}_{55}^{\rm orb}(\nu) + \hat{A}_{55}^{\rm Spin}(\tilde{a}_{12}, \nu) \ , \tag{6.100}$$

where $\hat{A}_{55}^{\rm peak_0}$ is the peak amplitude in the test particle limit. The non-spinning ν-dependence is modeled as

$$\hat{A}_{55}^{\rm orb}(\nu) = 1 + a_1^{\hat{A}_{55}}\nu + a_2^{\hat{A}_{55}}\nu^2 \ . \tag{6.101}$$

The spin dependence is first fitted to the test-particle limit using

$$\hat{A}_{55}^{\rm Spin}(\tilde{a}_{12},\nu=0)=\frac{b_1^{\hat{A}^0_{55}}\tilde{a}_{12}}{1+b_2^{\hat{A}^0_{55}}\tilde{a}_{12}}\ , \tag{6.102}$$

and then extrapolated to the comparable mass region through

$$b_1^{\hat{A}^0_{55}}\rightarrow\frac{b_1^{\hat{A}^0_{55}}}{1+c_{11}^{\hat{A}_{55}}\nu+c_{12}^{\hat{A}_{55}}\nu^2}\ , \tag{6.103}$$

$$b_2^{\hat{A}^0_{55}}\rightarrow\frac{b_2^{\hat{A}^0_{55}}}{1+c_{21}^{\hat{A}_{55}}\nu+c_{22}^{\hat{A}_{55}}\nu^2}\ . \tag{6.104}$$

The frequency of the $(5,5)$ mode is factorized as

$$\omega_{55}^{\rm peak}=\omega_{55}^{\rm peak_0}\omega_{55}^{\rm orb}(\nu)\omega_{55}^{\rm Spin}\left(\hat{S},\nu\right)\ , \tag{6.105}$$

where

$$\omega_{55}^{\rm orb}(\nu)=\frac{1+a_1^{\omega_{55}}\nu+a_2^{\omega_{55}}\nu^2}{1+a_3^{\omega_{55}}\nu}\ , \tag{6.106}$$

and the test-particle spin factor is given by

$$\omega_{55}^{\rm Spin}\left(\hat{S},\nu=0\right)=\frac{1+b_1^{\omega^0_{55}}\hat{S}}{1+b_2^{\omega^0_{55}}\hat{S}}\ . \tag{6.107}$$

The spin dependence in the general case is obtained by means of

$$b_i^{\omega^0_{55}}\rightarrow\frac{b_i^{\omega^0_{55}}+c_{i1}^{\omega_{55}}\nu}{1+c_{i2}^{\omega_{55}}\nu}\ , \tag{6.108}$$

with $i=\{1,2\}$. Note that, in this case, we do not incorporate spin-dependence in Δt_{55}, but only rely on the nonspinning fit of Ref. [133]. The coefficients of the fits if $\hat{A}_{55}^{\rm peak}$ and $\omega_{55}^{\rm peak}$ are listed in Table D.9

6.2.3 NR-fitting of the postpeak parameters

The discussion turns now to the fits of the postpeak evolution parameters $(c_3^{A_{\ell m}},c_3^{\phi_{\ell m}},c_4^{\phi_{\ell m}})$ for $(2,2)$, $(3,3)$, $(4,4)$, $(5,5)$. The fits that explicitly depend on the spins of the black holes are presented here. By contrast, the same parameters for the other multipoles $(2,1)$, $(3,2)$, $(3,1)$ $(4,3)$, $(4,2)$, are approximated by the spin-independent fits of Paper II. Even though the best fits obtained of $(c_3^{\phi_{33}},c_4^{\phi_{33}})$ and $(c_3^{\phi_{44}},c_4^{\phi_{44}})$, it is preferred not to use them as to improve the robustness of the model. Here too the fits of `TEOBiResumMultipoles` model are used to get a more robust behavior of ω_{33} and ω_{44} in all corners of the parameter space. This choice will be discussed further in Sec. 6.2.3.

The $(\ell, m) = (2,2)$ postpeak

The data of $(c_3^{A_{22}}, c_3^{\phi_{22}}, c_4^{\phi_{22}})$ were extracted from NR fitting the NR waveforms in the calibration set over an interval starting at the peak of length $4\tau_1^{22}$.

The fits are done in three steps, based on the model

$$\begin{aligned} Y(\nu;\, \hat{S}) = b_0^Y(\nu) + & b_1^Y\,(X_{12})\,\hat{S} + b_2^Y\,(X_{12})\,\hat{S}^2 \\ & + b_3^Y\,(X_{12})\,\hat{S}^3 + b_4^Y\,(X_{12})\,\hat{S}^4. \end{aligned} \tag{6.109}$$

In the first step $Y(\nu;\, \hat{S}=0)$ is fitted to the non-spinning data. In the second step $b_i^Y\,(X_{12}=0)$ are fitted to the equal mass data. In the third and final step the fits are extrapolated to the comparable mass case imposing the 1-D fits informed in the previous two steps. The coefficients of the fit are listed in Table D.10.

The $(\ell, m) = (3,3)$ postpeak

The data of $(c_3^{A_{33}}, c_3^{\phi_{33}}, c_4^{\phi_{33}})$ were extracted from NR fitting the NR waveforms in the calibration set over an interval starting at the peak of length $1\tau_1^{33}$. The interpolation is modeled with the template

$$Y(\nu;\, \hat{S}) = b_0^Y(\nu) + b_1^Y\,(X_{12})\,\hat{S}. \tag{6.110}$$

While for the case of $c_3^{A_{33}}$ the fit is done versus $\tilde{a}_{12}$. The fits are done in two hierarchical steps. (i) $b_0^Y(\nu)$ is fitted to the non-spinning data. (ii) $b_1^Y\,(X_{12})$ is fitted with a quadratic polynomial, while imposing the fit of $b_0^Y(\nu)$. The fits are given explicitly in Table D.11.

The $(\ell, m) = (4,4)$ postpeak

The data of $(c_3^{A_{44}}, c_3^{\phi_{44}}, c_4^{\phi_{44}})$ were extracted from NR fitting the NR waveforms in the calibration set over an interval starting at the peak of length $1\tau_1^{44}$. The interpolation of $(c_3^{\phi_{44}}, c_4^{\phi_{44}})$ is modeled with the template

$$Y(\nu;\, \hat{S}) = b_0^Y(\nu) + b_1^Y\,(X_{12})\,\hat{S} + b_2^Y\,(X_{12})\,\hat{S}^2 \tag{6.111}$$

in three steps, similar to the the $(2,2)$ mode. (i) $b_0^Y(\nu)$ is fitted to the non-spinning data. (ii) $b_i^Y\,(X_{12}=0)$ is fitted to the equal mass data. (iii) The full dependence of $b_i^Y\,(X_{12})$ on X_{12} is fitted while imposing the one-dimensional fits informed in the first two steps. $c_3^A{}_{44}$ is modeled with the template

$$c_3^{A_{44}}(\nu;\, \hat{S}) = b_0^{c_3^{A_{44}}}(\nu) + b_1^{c_3^{A_{44}}}\,\nu\hat{S} + b_2^{c_3^{A_{44}}}\,\nu\hat{S}^2. \tag{6.112}$$

The fit is is done in two steps. (i) $b_0^{c_3^{A_{44}}}(\nu)$ is fitted to the non-spinning data. (ii) The coefficients $b_i^{c_3^{A_{44}}}$ are informed using the spinning data, while imposing the non-spinning fit. The fits are given explicitly in Table D.12.

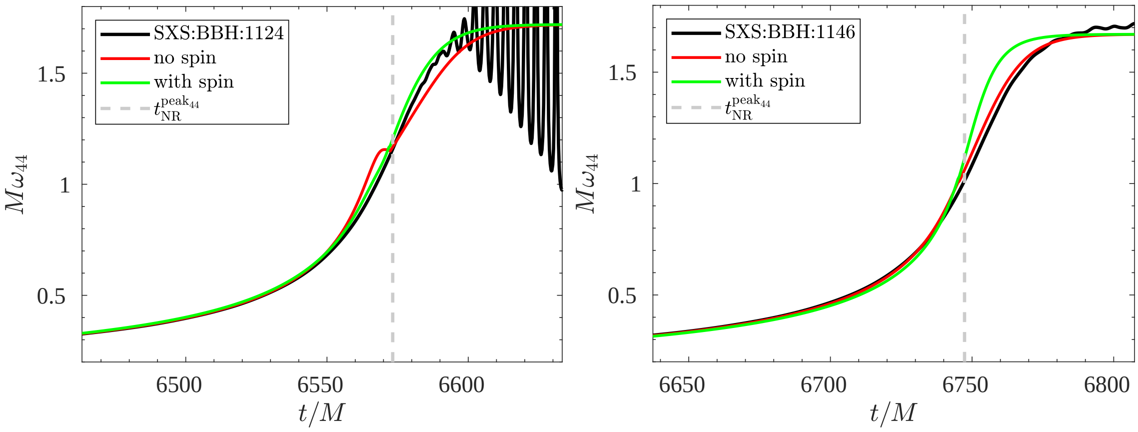

Figure 6.1: In this figure we compare the frequency $M\omega_{44}$ for the two NR waveforms (black) SXS:BBH:1124 $(1, 0.998, 0.998)$ (left panel) and SXS:BBH:1146 $(1.5, 0.95, 0.95)$ (right) with the corresponding EOB waveforms, once obtained using the fits of Ref. [133] (right panel) and once with the spin-dependent fits (green).

The $(\ell, m) = (5, 5)$ postpeak

The data of $(c_3^{A_{55}}, c_3^{\phi_{55}}, c_4^{\phi_{55}})$ were extracted fitting the NR waveforms in the calibration set over an interval of length τ_1^{55} starting at the peak. Their dependence on spin and mass ratio is modeled as

$$Y(\nu;\, \hat{S}) = b_0^Y(\nu) + b_1^Y\,(X_{12})\,\hat{S} + b_2^Y\,(X_{12})\,\hat{S}^2. \tag{6.113}$$

, For the case of $c_3^{A_{55}}$, we use the same functional form where however $\hat{S}$ is replaced by $\tilde{a}_{12}$. The fits are done in two hierarchical steps: (i) $b_0^Y(\nu)$ is fitted to the non-spinning data; (ii) $b_i^Y\,(X_{12})$ are fitted with a linear polynomial, while imposing the fit of $b_0^Y(\nu)$. The fits are given explicitly in Table D.13.

Motivating the choices for the $(3, 3)$ and $(4, 4)$ postmerger phases

As mentioned above, the spin dependence of $(c_3^{\phi_{33}}, c_4^{\phi_{33}})$ and $(c_3^{\phi_{44}}, c_4^{\phi_{44}})$ is neglected. This choice was made so to ensure a more robust behavior of the frequency at the beginning of the ringdown when the spins are positive and large. Inspecting the behavior of ω_{44} for two highly-spinning configurations illustrates this argument. Figure 6.1 shows EOB/NR comparisons with two EOB waveforms obtained with either the nonspinning fits (red online) or those with the full spin dependence (green). One sees that the spin-dependent fit performs rather well for `SXS:BBH:1124` $(1, 0.998, 0.998)$, consistently with the fact that we used `SXS:BBH:0178`, with parameters $(1, 0.9942, 0.9942)$, to inform the fit. By contrast, one sees that the same description applied to a different configuration, $(1.5, 0.95, 0.95)$, corresponding to `SXS:BBH:1146`, does not perform equally well, with a nonnegligible gap between the EOB and NR frequencies accumulating right after the peak. One finds, however, that removing the spin-dependence in $(c_3^{\phi_{44}}, c_4^{\phi_{44}})$ allows one to obtain a much closer EOB/NR consistency for `SXS:BBH:1146`. For the other case, moving to the nonspinning description slightly worsens the agreement, both before and after the waveform peak. On the basis of these results, and especially seen the rather good $\bar{F}$ behavior illustrated below in Fig. 6.8, it was decided to chose the simple option of removing the spin dependence in $(c_3^{\phi_{44}}, c_4^{\phi_{44}})$. The same rational also applies to the $(3, 3)$ mode. Clearly, in case of very high-spins, currents fits should be improved to some extent, increasing the calibration set so to incorporate more points in that corner of the parameter space. This will be investigated in future work.

6.2.4 Modeling the NQC extraction points

The discussion will now turn to the updated fits of the NQC extraction points defined as in Sec. 2.3.2.

The $(2, 2)$ NQC extraction point

For the $(2, 2)$ mode the NQC-point quantities $\left\{\hat{A}_{22}^{\rm NQC}, \dot{A}_{22}^{\rm NQC}, \omega_{22}^{\rm NQC}, \dot{\omega}_{22}^{\rm NQC}\right\}$ are fitted directly. The 3-piece hybrid fit, presented in [132] and Paper I is modified for $q > 4$. The fits of $\left\{\hat{A}_{22}^{\rm NQC}\omega_{22}^{\rm NQC}\right\}$ are done using the template discussed already for the peak. The reader should note however that the fit of $\omega_{22}^{\rm NQC}$ has additional flexibility. The replacement in (6.22) is also done for $i = 2$ for this case.

In the following the fitting of $\dot{A}_{22}^{\rm NQC}$ and $\dot{\omega}_{22}^{\rm NQC}$. Both rely on the same template thus it is only given for the former explicitly. To fit the time derivative of the amplitude at $t_{\rm NQC}$ it was proven useful to not fit it directly, but to fit $\dot{A}_{22}^{\rm NQC}/\nu\omega_{22}^{\rm NQC}$, starting with the following factorization

$$\frac{\dot{A}_{22}^{\rm NQC}}{\nu\omega_{22}^{\rm NQC}} = \left[\hat{\dot{A}}_{22}^{{\rm NQC}_{\rm orb}}(\nu) + \hat{\dot{A}}_{22}^{{\rm NQC}_{\rm Spin}}\left(X_{12}, \hat{S}\right)\right]. \tag{6.114}$$

The nonspinning contribution is fitted as

$$\hat{\dot{A}}_{22}^{{\rm NQC}_{\rm orb}}(\nu) = 1 + a_1^{\dot{A}_{22}^{\rm NQC}}\nu + a_2^{\dot{A}_{22}^{\rm NQC}}\nu^2. \tag{6.115}$$

The spin-dependence is represented as

$$\hat{\dot{A}}_{22}^{{\rm NQC}_{\rm Spin}}\left(X_{12}\hat{S}\right) = b_1^{\dot{A}_{22}^{{\rm NQC}_{m_1=m_2}}}\hat{S} + b_1^{\dot{A}_{22}^{{\rm NQC}_{m_1=m_2}}}\hat{S}^2\,. \tag{6.116}$$

The extrapolation to the $m_1 \neq m_2$ regime is done via the replacement

$$b_i^{\dot{A}_{22}^{{\rm NQC}_{m_1=m_2}}} \to b_i^{\dot{A}_{22}^{{\rm NQC}_{m_1=m_2}}} + c_i^{\dot{A}_{22}^{{\rm NQC}_{m_1=m_2}}} X_{12}\,, \tag{6.117}$$

with $i = \{1, 2\}$. All coefficients are listed explicitly in Table D.14.

Calculation of NQC quantities from the postpeak analytical waveform

The discussion will now focus on the computation of the NQC quantities $\left(A_{\ell m}^{\rm NQC}, \omega_{\ell m}^{\rm NQC}, \dot{A}_{\ell m}^{\rm NQC}, \dot{\omega}_{\ell m}^{\rm NQC}\right)$ from the NR-informed analytical description of the postpeak waveform, defined in Sec. 2.3.4. Although the formulas have to be intended valid multipole by multipole, in the following the (ℓ, m) indexes are dropped for clarity. The analytical expression for the amplitude and its time derivative read

$$A_h/\nu = e^{-\alpha_1 \frac{t-t_{\rm peak}}{M_{\rm BH}}}\left[c_1^A \tanh\left(c_2^A \frac{t-t_{\rm peak}}{M_{\rm BH}} + c_3^A\right) + c_4^A\right], \tag{6.118}$$

$$\dot{A}_h/\nu = \frac{c_1^A c_2^A e^{-\alpha_1 \frac{t-t_{\rm peak}}{M_{\rm BH}}} \operatorname{sech}^2\left(c_2^A \frac{t-t_{\rm peak}}{M_{\rm BH}} + c_3^A\right)}{M_{\rm BH}} - \frac{\alpha_1 e^{-\alpha_1 \frac{t-t_{\rm peak}}{M_{\rm BH}}}\left[c_1^A \tanh\left(c_2^A \frac{t-t_{\rm peak}}{M_{\rm BH}} + c_3^A\right) + c_4^A\right]}{M_{\rm BH}}, \tag{6.119}$$

while those for the phase and its derivatives read

$$\phi_h = -\,\omega_1 \frac{t-t_{\rm peak}}{M_{\rm BH}^2} - c_1^\phi \ln\left(\frac{1 + c_3^\phi e^{-c_2^\phi \frac{t-t_{\rm peak}}{M_{\rm BH}}} + c_4^\phi e^{-2c_2^\phi \frac{t-t_{\rm peak}}{M_{\rm BH}}}}{1 + c_3^\phi + c_4^\phi}\right), \tag{6.120}$$

$$\omega_h = -\,\dot{\phi}_h = \frac{\omega_1}{M_{\rm BH}^2} - \frac{c_1^\phi c_2^\phi}{M_{\rm BH}} \frac{c_3^\phi x(t) + 2c_4^\phi x^2(t)}{1 + c_3^\phi x(t) + c_4^\phi x^2(t)}, \tag{6.121}$$

$$\dot{\omega}_h = -\,\ddot{\phi}_h = \frac{c_1^\phi c_2^{\phi 2}}{M_{\rm BH}^2}\left[\frac{c_3^\phi x(t) + 4c_4^\phi x^2(t)}{1 + c_3^\phi x(t) + c_4^\phi x^2(t)} - \left(\frac{c_3^\phi x(t) + 2c_4^\phi x^2(t)}{1 + c_3^\phi x(t) + c_4^\phi x^2(t)}\right)^2\right], \tag{6.122}$$

where the quantity x is given as

$$x(t) = e^{-c_2^\phi \frac{t-t_{\rm peak}}{M_{\rm BH}}}. \tag{6.123}$$

The waveform quantities needed to compute the NQC correction to amplitude and phase are simply obtained by evaluating the above expressions at $t = t_{\ell m}^{\rm NQC} = t_{\ell m}^{\rm peak} + 2$ multipole by multipole.

The fitted derivative of the $(\ell, m) = (4,4)$ amplitude at the NQC extraction point

Unfortunately, the accuracy of the derivative obtained with the above template does not always have sufficient accuracy. This is due to insufficient flexibility of the fitting template, that will be modified in future work. To overcome this difficulty, an explicit fit of the amplitude time-derivative is given. The derivative of NQC amplitude is separated in two terms as

$$\dot{A}_{44}^{\rm NQC} = \nu \dot{A}_{44}^{\rm NQC_0} \hat{\dot{A}}_{44}^{\rm orb}(\nu) + \hat{\dot{A}}_{44}^{\rm Spin}(\hat{S}, \nu) , \tag{6.124}$$

where $\dot{A}_{44}^{\rm NQC_0}$ is the peak amplitude in the test particle limit. The non-spinning behavior is modeled with

$$\hat{\dot{A}}_{44}^{\rm orb}(\nu) = \frac{1 + a_1^{\dot{A}_{44}^{\rm NQC}} \nu + a_2^{\dot{A}_{44}^{\rm NQC}} \nu^2}{1 + a_3^{\dot{A}_{44}^{\rm NQC}} \nu + a_4^{\dot{A}_{44}^{\rm NQC}} \nu^2} . \tag{6.125}$$

The spin dependence is first fitted to the test-particle limit using

$$\hat{\dot{A}}_{44}^{\rm Spin}(\hat{S}, \nu = 0) = \frac{b_1^{\dot{A}_{44}^{\rm NQC}} \hat{S}}{1 + b_2^{\dot{A}_{44}^{\rm NQC}} \hat{S}} , \tag{6.126}$$

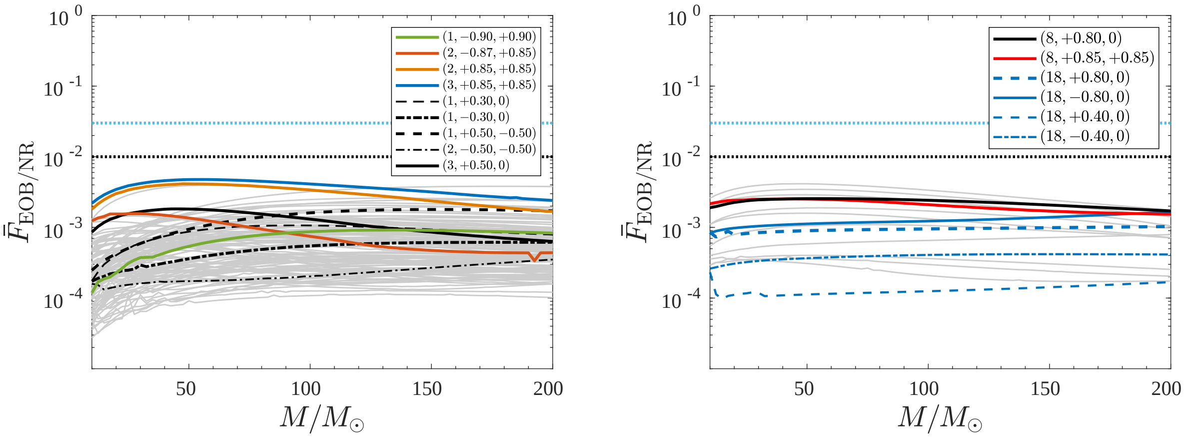

Figure 6.2: EOB/NR unfaithfulness for the $\ell = m = 2$ mode obtained from Eq. (A.12). Left panel: computation using SXS waveforms publicly released before February 3, 2019. Right panel: same computation done with BAM waveform data. As explained in Sec. 6.2.1, a subset of all this data (see Table 4.1) is used to inform the c_3 EOB function. Comparison with Figs. 1 and 3 of Ref. [135] allows one to appreciate the improvement with respect to the original implementation The reader should actually note that we changed from the, outdated, zero-detuned, high-power noise spectral density of Ref. [145] used in Ref. [135], to its most recent realization, Ref. [11]. of `TEOBResumS`. Comparison with Fig. 3.1 highlights that the $\bar{F}_{\rm EOB/NR}$ is either of the order of, or larger than the NR/NR uncertainties.

and then extrapolated to the comparable mass region through

$$b_1^{\dot{A}_{44}^{\rm NQC}} \to \frac{b_1^{\dot{A}_{44}^{\rm NQC}} + c_{11}^{\dot{A}_{44}^{\rm NQC}}\,\nu}{1 + c_{12}^{\dot{A}_{44}^{\rm NQC}}\,\nu}\,, \tag{6.127}$$

$$b_2^{\dot{A}_{44}^{\rm NQC}} \to \frac{b_2^{\dot{A}_{44}^{\rm NQC}} + c_{21}^{\dot{A}_{44}^{\rm NQC}}\,\nu}{1 + c_{22}^{\dot{A}_{44}^{\rm NQC}}\,\nu}\,. \tag{6.128}$$

The explicit coefficients of the fits are listed in Table D.15.

6.3 The $\ell = m = 2$ mode: EOB/NR unfaithfulness

The discussion now turns to the performance of the analytical waveform model in terms of unfaithfulness between `TEOBiResumS_SM` and the full NR *calibration* and *validation* sets plotted for the $\ell = m = 2$ mode, obtained computing Eq. (A.12) between `TEOBiResumS_SM` and NR waveforms, using the PSD presented in Ref. [11]. Further details are given in appendix A. Figure 6.2 shows the comparison with the *calibration* set already used to validate `TEOBResumS`. The global performance of the model is largely greatly improved with respect to `TEOBResumS` as discussed in Sec. 4.3. Remarkably, the model performs excellently also for large mass ratios and large spins, without any outlier above the 1% threshold, but even $\bar{F}^{\rm max}_{\rm EOB/NR} \lesssim 0.5\%$ all over, meeting the NR uncertainty level conservatively set in Sec. 3.3.1 for both `SXS` and `BAM` data.

The *validation* set of an additional 420 `SXS` waveforms is shown in Fig. 6.3. It is found that $\bar{F}^{\rm max}_{\rm EOB/NR}$ always remains *below* 0.85%, a value reached only by one dataset, $(1.5, +0.95, +0.95)$ `SXS:BBH:1146`, while for all others it stays at $\bar{F}^{\rm max}_{\rm EOB/NR} \lesssim 0.4\%$. This outlier is not surprising since the sets of NR waveforms used to inform c_3 do not cover the region of $1 < q < 2$ with

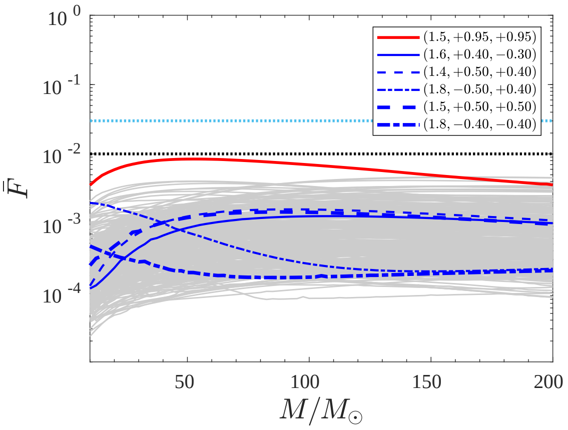

Figure 6.3: EOB/NR $\ell = m = 2$ unfaithfulness computation with SXS waveform data publicly released after February 3, 2019. None of these datasets was used to inform the model in the dynamical EOB functions (a_6^c, c_3), although several were used for the postmerger waveform part. It is remarkable that $\bar{F}^{\rm max}_{\rm EOB/NR}$ is always below 0.4% except for a single outlier, red online, that however never exceeds 0.85%. The plot includes five exceptionally long waveforms, each one developing more than 139 GW cycles before merger, SXS:BBH:1412, 1413, 1414, 1415 and 1416 (blue online).

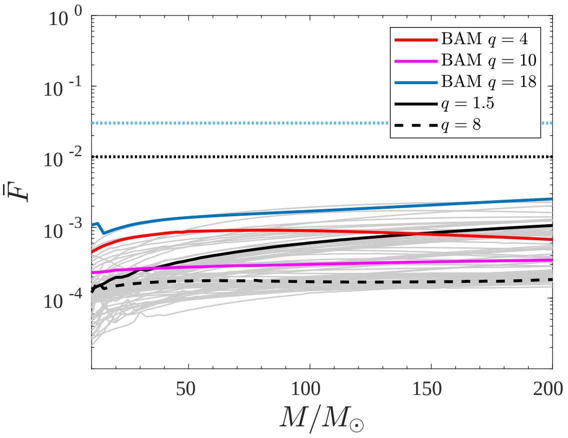

Figure 6.4: EOB/NR unfaithfulness for all available non-spinning datasets. The analytical waveforms are evaluated with $(\chi_1, \chi_2) = (0, 10^{-4})$, so as to probe the stability of the model and its robustness in this regime.

the exception of one single dataset with $(1.5, -0.5, 0)$. In this respect, to better understand the behavior of this outlier it was checked that the fit of c_3 yields for this parameter combination $c_3^{\rm fit}(1.5, +0.95, +0.95) = 15.96$ leading to an accumulated phase difference~ 4.7 rad at merger once the two waveforms are aligned during the inspiral. Interestingly, by *lowering* the value of c_3, and thus *increasing* the magnitude of the spin-orbit effective coupling and thus making the EOB waveform longer, one can easily reconcile it with the NR data. For convenience this result is illustrated in Fig. 6.6, that is obtained with $c_3 = 11.1$ (the two dash-dotted vertical lines indicate the alignment region). We also point the reader to Table F.8, where the NR uncertainty for this dataset is estimated to be $\bar{F}_{\rm NR/NR} = 0.0446\%$. On a different note, this suggests that the current model could be additionally, and easily, improved by also considering `SXS:BBH:1146` to inform $c_3^{\rm fit}$. Yet, this results highlights the robustness of our model: without any additional input from NR simulations to determine c_3, it is able to deliver rather accurate waveforms even in a region of the parameter

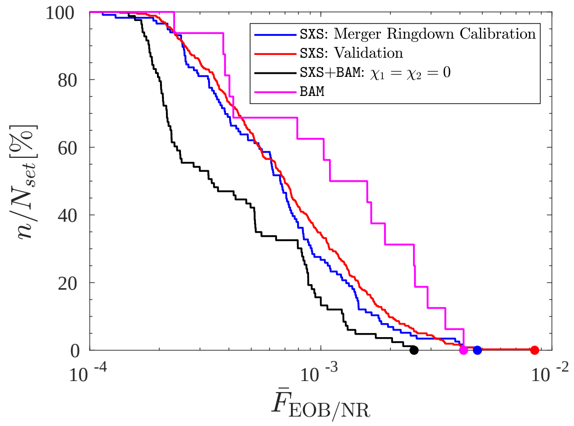

Figure 6.5: Global representation of $\bar{F}^{\rm max}_{\rm EOB/NR}$ all over the SXS (555) and BAM (19) NR simulations. The various SXS subsets, nonspinning (black online, 83 waveforms), merger-ringdown calibration (blue online, 116 spin-aligned waveforms) and validation (red online, 359 spin-aligned waveform) discussed in the text are represented separately. The plot shows the fraction (expressed in %) $n/N_{\rm set}$, where $N_{\rm set}$ is the total number of waveforms in a given NR-waveform set and n is the number of waveforms, in the same set, that, given a value $\bar{F}$, have $\bar{F}^{\rm max}_{\rm EOB/NR} \geq \bar{F}$. The colored marker highlight the largest values in each NR dataset. Note that this plot incorporates 420 new SXS waveforms that were not included in Fig. 6 of Paper I.

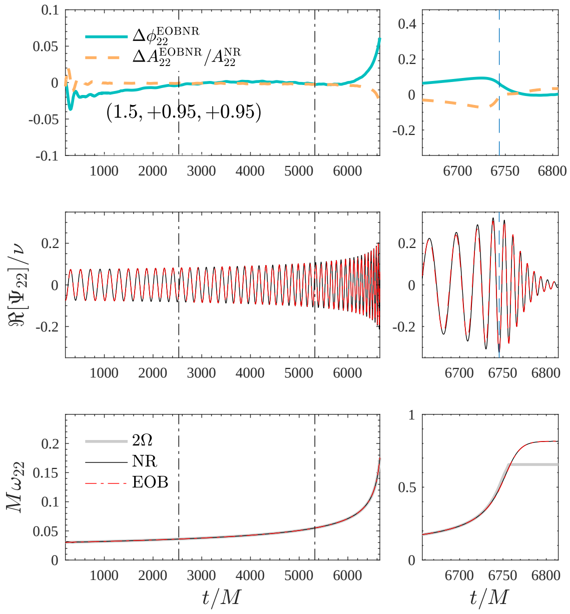

Figure 6.6: Improved EOB/NR phasing comparison for `SXS:BBH:1146` when the value of $c_3^{\rm fit} = 15.96$ used in Fig. 6.3 is lowered to $c_3 = 11.1$. Top panel: (relative) amplitude and phase differences. Middle panel: real part of the waveform. Bottom panel: gravitational frequencies. For convenience, also twice the EOB orbital frequency 2Ω is shown on the plot. The dash-dotted vertical lines indicate the alignment frequency region, while the dashed one the merger time. This comparison illustrates that `SXS:BBH:1146` is an outlier in Fig. 6.3 only because of the rather limited amount of NR waveforms used to inform $c_3^{\rm fit}$.

space previously not covered by NR data. The model performance is summarized in Fig. 6.5. For each dataset considered above, the figure exhibits the fraction of waveform whose $\bar{F}^{\rm max}_{\rm EOB/NR}$ is larger or equal a given value $\bar{F}$. Thanks to the additional analytical information incorporated and to the improved waveform resummation, `TEOBiResumS_SM` is currently the EOB model that exhibits the lowest EOB/NR unfaithfulness for the $\ell = m = 2$ mode.

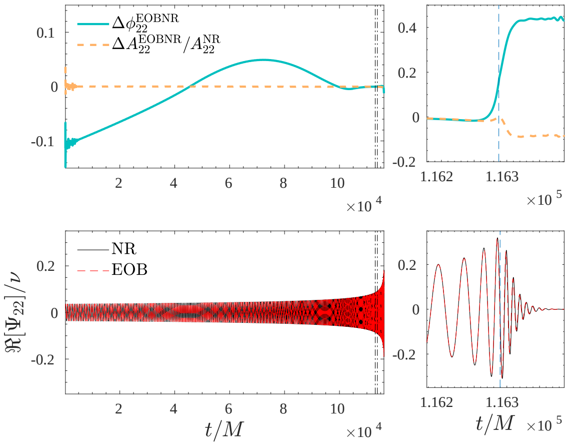

Figure 6.7: EOB/NR phasing comparison for SXS:BBH:1415, $(1.5, +0.50, +0.50)$. Note that it does not seem possible to flatten the phase difference up to $t/M \simeq 1 \times 10^5$. The vertical lines indicate the alignment frequency region $[M\omega_L, M\omega_R] = [0.038, 0.042]$.

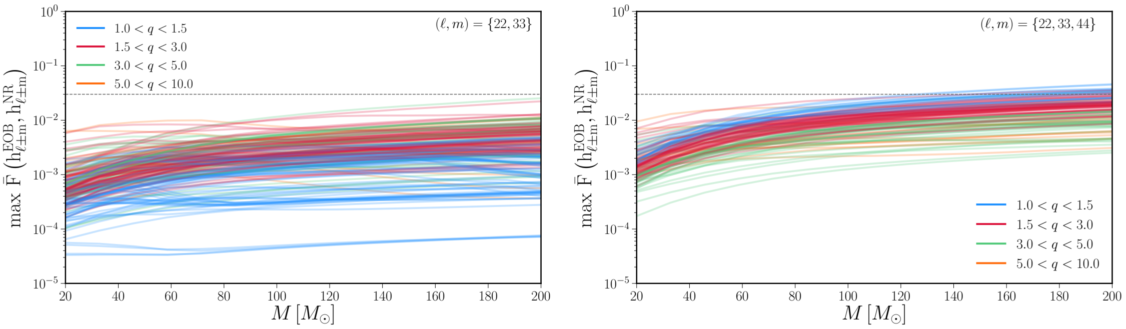

Figure 6.8: EOB/NR unfaithfulness computation putting together all $\ell = m$ modes up to $\ell = 4$. Plotted is the worst-case performance maximizing the unfaithfulness over the sky, Eq.(A.12). The worst-case mismatches arise from near edge-on configurations, when the power emitted in the $(2, 2)$ mode is minimized.

6.3.1 Long-inspiral Numerical Relativity waveforms

Now a brief comment is given on 5 exceptionally long NR waveforms contained in the *validation* set. To explore the possible impact of these waveforms they are compared to `TEOBiResumS_SM` in the time-domain. Fig. 6.7 shows this comparison for the particularly interesting case of `SXS:BBH:1415`. A waveform of a $(1.5, +0.50, +0.50)$ BBH system. Interestingly enough, the phase alignment fails for low frequency and it is required to consistently increase the frequency window until $[M\omega_L, M\omega_R] = [0.038, 0.042]$ is reach for which a stable alignment is finally successful. What is even more interesting is that it seems that drift exists in the phase of the NR waveform relative to the `TEOBiResumS_SM` waveform that a priori seems unphysical. as can be seen in the top-right panel of Fig. 3.1 the unfaithfulness for low frequency with respect to the second highest waveform is quite large. For now this is merely an interesting observation. It seems likely that the `TEOBiResumS_SM` in fact is more physical as it is primarily informed by analytical sources of information assumed to be more accurate at low frequencies, such as PN and GSF theory.

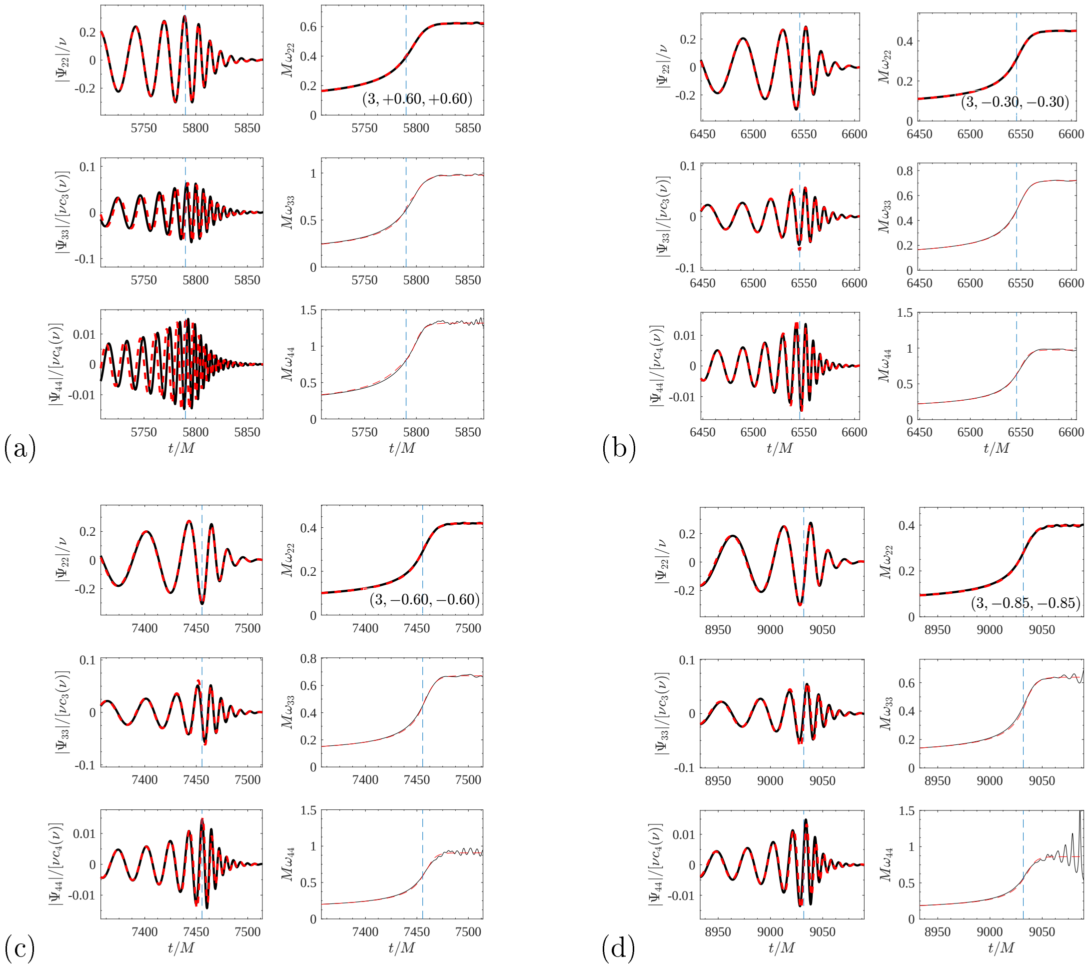

Figure 6.9: Behavior of (2, 2), (3, 3) and (4, 4) modes for a few, illustrative, spin-aligned configurations with $q = 3$: comparing NR (black) with EOB (red) waveform around the peak of the EOB (2, 2) mode (dashed blue vertical line). Each panel plots the real part (left columns) and the instantaneous frequency (right columns).

6.3.2 Nonspinning limit

AS an addendum to the excellent performance of `TEOBiResumMultipoles` in the non-spinning sector it is tested how `TEOBiResumS_SM` performance when the spins are low. To check the consistency with the non-spinning limit the unfaithfulness is computed between `TEOBiResumS_SM` and 89 non-spinning NR waveforms listed in Tab. F.14-F.15. Figure 6.4 shows $\bar{F}_{\rm EOB/NR}$ for the 89 `SXS` nonspinning waveforms with `TEOBiResumS_SM` evaluated at $(\chi_1, \chi_2) = (0, 10^{-4})$. Only two waveforms show a large $\bar{F}_{\rm NR/NR}$ value: `SXS:BBH:0093` ($q = 1.5$) and `SXS:BBH:0063` ($q = 8$), though both remain below 8×10^{-4}. Consistently with Paper II, $\bar{F}_{\rm EOB/NR}$ shows a very well behaved unfaithfulness all over. The largest unfaithfulness is reached by the `BAM`, $q = 18$ waveform at $\max(\bar{F}_{\rm EOB/NR}) = 0.2533\%$.

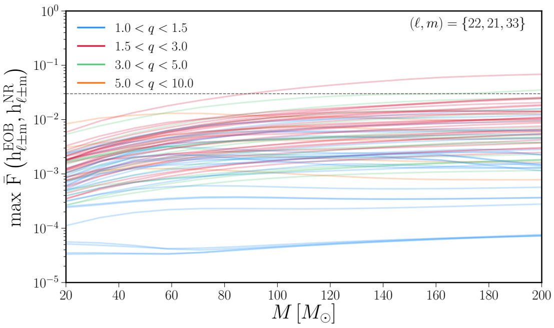

Figure 6.10: EOB/NR unfaithfulness, maximized over the direction from the sky, when including $(2, 2)$, $(2, 1)$ and $(3, 3)$ modes. Here we only consider a subset of the SXS waveforms with $\chi_i > -0.4$, where the $(2, 1)$ EOB waveform mode does not present pathologies. The worst case configuration is `SXS:BBH:0239`, a binary of mass ratio and spins $(2.0, -0.37, +0.85)$.

6.4 Higher multipolar modes

6.4.1 Multipoles $(2, 2)$, $(3, 3)$ and $(4, 4)$

It is now time to move the discussion onto the validation of the subdominant modes[2]. The quality of the waveform model is illustrated with four $q = 3$ configurations, with equal spins, both aligned or anti-aligned to the orbital angular momentum. More precisely, $(3, -0.85, -0.85)$, $(3, -0.60, -0.60)$, $(3. -0.30, -0.30)$ and $(3, +0.60, +0.60)$ are used. This behavior can be considered fully representative over the entire `SXS` catalog. Figure 6.9 illustrates the behavior of the $(2, 2)$, $(3, 3)$ and $(4, 4)$ mode. For each multipole, the real part of the `TEOBiResumS_SM` and NR waveform are shown together with the instantaneous GW frequency $\omega_{\ell m}$. The `TEOBiResumS_SM` waveform is aligned to the NR around merger, so to focus in on the excellent agreement between the waveforms around merger. The EOB/NR agreement is rather good either for spins both anti-aligned or aligned with the orbital angular momentum. It is however prudent to point out that when the spins are large and aligned there is an increasing dephasing accumulating between the EOB and NR $(4, 4)$ mode. This can be seen in Fig. 6.9 (a). As it was the case for the $\ell = m = 2$ mode discussed above, a global understanding of the actual performance of the model requires the computation of the EOB/NR unfaithfulness. While in the previous chapter the range from best to worst case of the unfaithfulness was computed here only the worst case is considered. In Fig. 6.8, this is shown explicitly for the $\ell = m$ modes up to $\ell = 4$, finding excellent agreement up to $\sim 120 M_\odot$ above which the model performance degrades slightly and moves above 3%. As one would expect the worst case scenario is always the edge-on case for which the excellent $(2, 2)$ mode is most suppressed. Further the worst mismatches occur for mass ratios $1 \leq q \leq 1.5$ and equal-spin configurations. These are in particular the cases for which the $m =$ odd modes are suppressed. For these binaries, the degraded performance can be seen to correlate with the $(4, 4)$ mode, both the `TEOBiResumS_SM` and on the NR side, increasingly failing to be physically accurate.

6.4.2 Other subdominant multipoles

It is now useful to only summarize the thorough analysis of the $(2,1)$, $(3,2)$, $(3,1)$, $(4,3)$, $(4,2)$ and $(5,5)$ modes[3].

(i) When the peak of a given subdominant mode $h_{\ell m}$ is significantly delayed ($\sim 7-8M$) with respect to the peak of the dominant h_{22} mode, which can happen for most $m \neq \ell$ modes, in particular for $(2,1)$, $(4,3)$ or $(3,1)$, a crossing of the Ω into the negative prevents the correct determination of the NQC.

(ii) The postmerger reproduces a robust waveform all over the parameter space even though it does not model effects of mode-mixing or the beating between positive and negative QNMs.

(iii) Fig. 6.10, shows the mismatch for the $\{22, 21, 33\}$ modes already showing a strong outlier for waveforms with $\chi_i > -0.4$. The unfaithfulness only exceeds the maximal bound of 3% for two waveforms. And this case only slightly.

(iv) For a few select waveforms with mild spins an explicit comparison between `TEOBiResumS_SM` is shown for all modes, indicating that the NR calibration works sufficiently well for mild spins, as for larger spins the analytical model underlying is not sufficient to perform an analysis.

6.4.3 Peculiar behavior of $\mathbf{m = 1}$ waveform amplitudes for $\mathbf{1 \leq q \leq 2}$.

It is finally interesting to point out an interesting aspect captured in the `TEOBiResumS_SM`multipolar waveform. Ref. [70] pointed out that a peculiar feature, a minimum, appeared in the late inspiral waveform for the $(2,1)$ mode of several waveforms with approximately equal mass and oppositely aligned spins. Paper III further explored this topic going into several details that while very interesting but it is chosen to only remark upon it briefly by a single example. As can be seen in Fig. 6.11 – 6.13, `SXS:BBH:1466` is one such data set containing a minimum. And in fact this is reproduced with high accuracy by the bare `TEOBiResumS_SM`, without NQC corrections. Further the full model accurately reproduces the waveform with the peculiar $(2,1)$ mode included on the level of unfaithfulness. Paper III manages to go deeper and actually predict the minimum for several further waveforms and find waveforms overlooked in Ref. [70]. The interested reader is directed to the discussion in Paper III.

6.5 Fitting the NQC parameters

We will briefly review the NQC parameters for clarity. Each multipole (ℓ, m) is modified by 4 NQC parameters $(a_1^{\ell m}, a_2^{\ell m}, b_1^{\ell m}, b_2^{\ell m})$. $(a_1^{\ell m}, a_2^{\ell m})$ determine the NQC correct of the amplitude and $(b_1^{\ell m}, b_2^{\ell m})$ determine NQC correction to the phase and frequency of the multipole (ℓ, m). The parameters (a_1^{22}, a_2^{22}) hold a special place among them. They are the only parameters that also enter the radiation reaction of the waveform. Thus, allowing to iterate on them. The first evaluation of the model is started with $(a_1^{22}, a_2^{22}) = (0,0)$. Once the waveform is generated $(a_1^{\ell m}, a_2^{\ell m}, b_1^{\ell m}, b_2^{\ell m})$ are generated by solving a set of 4 coupled equations by imposing NR-informed fits of Amplitude,

---

[2] The unfaithfulness computations of the subdominant modes was performed by Geraint Pratten.

[3] As this analysis was performed by Alessandro Nagar and Geraint Pratten and does not utilize additional methods not yet employed in this thesis, it is only referenced here.

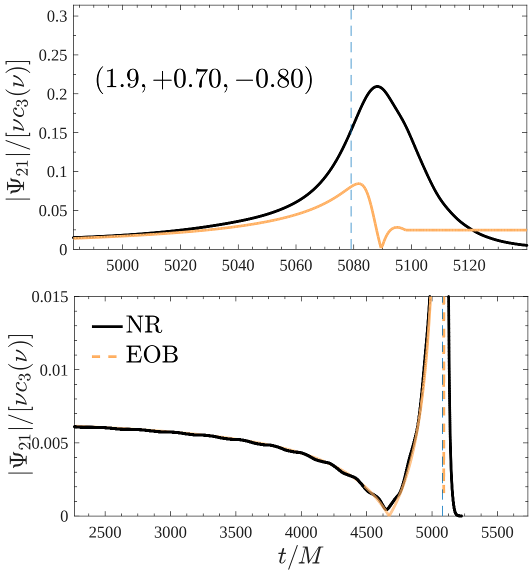

Figure 6.11: Mode $(2,1)$: comparison between the EOB amplitude (orange) and the corresponding NR one from dataset `SXS:BBH:1466`. The purely analytical EOB waveform multipole can accurately predict the location of the minimum (that analytically is a zero of the modulus) consistently with the one found in the NR data. The excellent agreement shown is obtained *naturally*, without the need of calibrating any additional parameter entering the waveform amplitude. The dashed vertical line corresponds to merger time, i.e. the peak of the $\ell = m = 2$ waveform. The cusp in the analytical amplitude occurs because of a zero in $\hat{f}^{\rm S}_{21}$ as illustrated in Fig. 6.12.

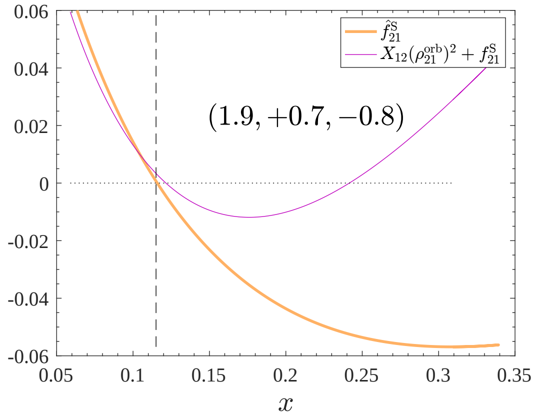

Figure 6.12: Complementing Fig. 6.11: the behavior of the resummed versus non-resummed amplitude versus $x = \Omega^{2/3}$.

Frequency and their first derivatives. The resulting values of (a_1^{22}, a_2^{22}) are then used as input in the radiation reaction. This process is repeated until a convergence is found. Hereafter and prior to this section, we refer to (a_1^{22}, a_2^{22}) as (a_1, a_2).

(a_1, a_2) has been generated for a large number of waveforms up to a total mass-ratio of $q = 30$ with $\chi = \chi_1 = \chi_2$. The NR informed fits are structured in 4 different regions:

1. $\chi_1 = \chi_2 = 0$,
2. Spinning, equal-mass sector with $\nu > 0.2485$,
3. $0.2485 \geq \nu > 0.16$, spinning sector,

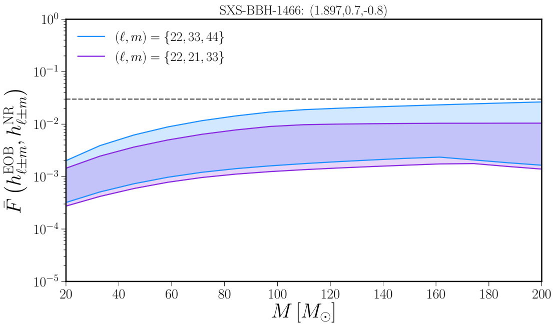

Figure 6.13: The minimum and maximum EOB/NR unfaithfulness for `SXS:BBH:1466` over the whole sky. The blue curve uses the $(2,2),(3,3)$ and $(4,4)$ modes. The purple curve uses the $(2,2),(2,1)$ and $(3,3)$ modes. Worst case mismatches occur near edge on configurations with the unfaithfulness being below 3% up to $200 M_\odot$.

4. $0.16 \geq \nu$, spinning sector.

The fits of (a_1, a_2) are structured accordingly due to the slightly different values of (a_1, a_2) at the border. The mismatch at the border due to the jump is not significantly large. For large negative spins no bad behavior shows up, but a choice was made for the robustness of the model to to hard fix $\Delta t_{\rm NQC} = 4$ instead of the large negative spins and large mass ratios, see Ref. [135] for further details. This choice creates a small jump thus this region is merely extrapolated from the rest. This works particularly well since (a_1, a_2) are very stable for large negative spins and large mass-ratios.

For large positive spins (a_1, a_2) diverge for increasing iteration. This shows up as $q = 30$ the maximum spin is $\chi = 0.6$. While for $q = 18$ and below spins up to $\chi = 0.85$ are used. The fits are presented in Appendix E.

We will now evaluate these fits. We compute the `TEOBiResumS_SM` with NR, using the fits of (a_1, a_2)without iteration. Two major differences exist. Firstly, the validation is done using also the PA approach. Secondly, the results presented so far have been obtained with the `MATLAB` version of the code. These results have been redone with the c code and the fits presented in Appendix E. These give a comparative estimate of the validity relative to the fully iterated code but can also serve standalone. The results are summarized in Fig. 6.14. The $\bar{F}$ computation results are good. Globally below 1%, although slightly worse than the fully iterated `MATLAB` code which is to be expected.

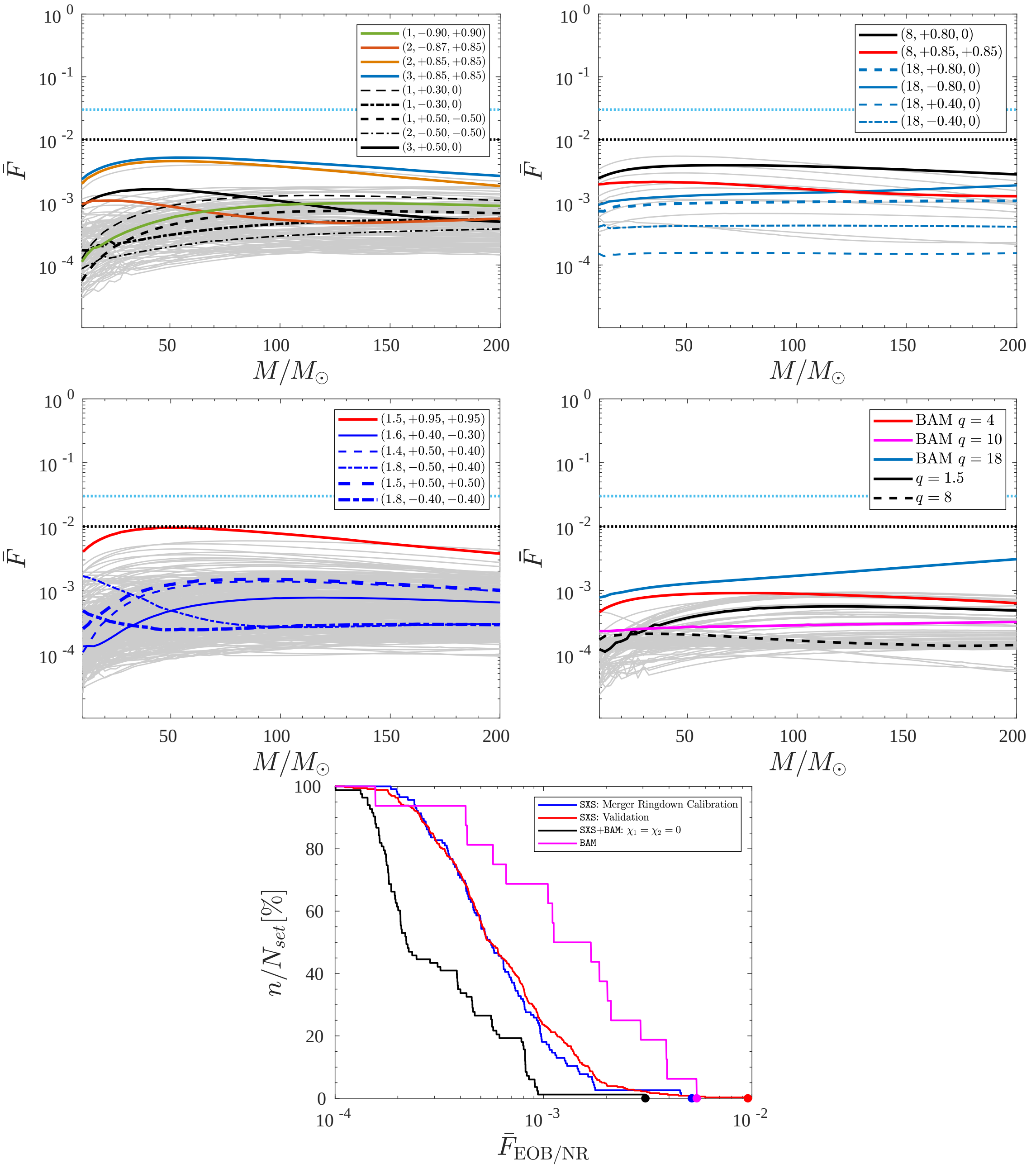

Figure 6.14: EOB/NR unfaithfulness for the $\ell = m = 2$ mode obtained by comparing the full catalog of NR waveforms presented in Paper I with `TEOBResumS`. Two differences exist between this work and Paper I. (i) `TEOBResumS` was evaluated with the Post-Adiabatic approximation. (ii) `TEOBResumS` was not iterated until convergence but instead used the fits presented above and a single iteration. This was much faster relative to the lengthy computation of waveforms with the `MATLAB` version. Top-left shows the *calibration set*, Top-right shows the `BAM` data. Center-left shows the full, spin-dependent *Validation set* and Center-right shows the non-spinning set. The bottom figure shows the accumulation plot $n/N(\bar{F})$. Where $n/N(\bar{F})$ defined for any value of $\bar{F}$ as the fraction of waveforms with a larger value of $max\left(\bar{F}\right)$.

Chapter 7

Peak-frequency

The advent of Gravitational Wave Astronomy (GWA), brought forward by the the LIGO and Virgo Collaborations [13, 30], has opened several avenues to test GR in the strong-field regime through CBC events. GW150914 [13] and several following detections [14, 18, 20] have provided to date the best dynamical constraints on GR [14, 16, 20]. GW150914 in particular has provided excellent opportunities for such tests [16], in large due to its mass and luminosity. As a matter of fact it allowed to show the existence of the fundamental QNM of the presumed remnant BH, visible during the end stages of the BBH waveform observed [16].

GR predicts that GWs have two independent polarizations namely $(h_+, h_\times)$ detectable as roughly sketched out in chapter 2. The observed frequency is obtained from the complex GW strain $h = h_+ - ih_\times$ as

$$f(t) = \frac{1}{2\pi}\frac{d}{dt}(\arg(h)) \ . \tag{7.1}$$

In particular, the peak of the GW amplitude, taken as the peak of $\left(h_+^2 + h_\times^2\right)^{1/2}$, correlates to the most turbulent period observed, which in the case of a BBH system corresponds to the merger. Thus, the frequency at peak f^{peak} is directly connected to the strong-field dynamics of merging BBH systems when curvature, velocity and acceleration of and around the BHs are maximal. To study f^{peak} of BBH systems requires full NR simulations, stable, accurate and precise throughout the merging of the two BHs. As NR simulations are computationally very costly it would be better to fit the frequency. Indeed several fits of the multipolar (ℓ, m) peak frequency do exist [53, 70, 93–95, 134, 135]. Two aspects have to be considered when using these fits to estimate f^{peak}: (i) All of them focus on the peak frequencies for the individual $h_{\ell m}$, not on the peak of $\left(h_+^2 + h_\times^2\right)^{1/2}$. As the peaks of the individual multipoles are often shifted with respect to each as has been discussed in detail in the previous chapters, it is easy to see that likely only a full reconstruction of h would allow to determine the peak frequency of h. (ii) As elaborated in chapter 2 GW observatories show a bias towards the detection of spin-aligned binaries, thus the dominant number of fits focuses on the spin-aligned (nonprecessing) case.

Paper IV presented a potential test of GR focused around f^{peak}. The aforementioned prediction of GR is compared to an agnostic, unmodeled reconstruction of the polarizations $(h_+, h_\times)$[1]. This

---

[1] This can be extended to more generic polarization, see [102]

allows to statistically test GR in the strong-field regime, similar to the test suggested in Ref. [95]. This test is build up along three steps:

(i) $f^{\rm peak}$ has be reconstructed as predicted by GR.

(ii) The BayesWave method [69, 124] is used to reconstruct $(h_+, h_\times)$ and obtain $f^{\rm peak}$ for GW150914 in a model-independent way[2].

(iii) The reconstructed distributions of $f^{\rm peak}$ are compared directly[3].

GR peak frequency As GW150914 did not show any evidence of subdominant modes, it will suffice to consider a GW model capable of reproducing the $(\ell, m) = \{(2,2),(2,-2)\}$ modes [29]. Recall that for spin-aligned binaries multipoles of opposite m are related as $h_{\ell,-m} = (-1)^\ell h^*_{\ell m}$, thus the complex GW strain is given as

$$h_+ - ih_\times = {}_{-2}Y_{22}(\iota,\phi)h_{22} + {}_{-2}Y_{2-2}(\iota,\phi)h^*_{22}\ . \tag{7.2}$$

Further, as the posterior distribution of the inclination angle strongly favors the *face-off* (with the angular momentum anti-aligned to the line of sight) [17] it is reasonable to simplify the computation by imposing the *face-off* orientation exactly. In the face-off case, multipolar factors reduce to ${}_{-2}Y_{22}(\pi,\phi) = 0$, and ${}_{-2}Y_{2-2}(\pi,\phi) = \sqrt{\frac{5}{4\pi}}e^{-2i\phi} \equiv \kappa\, e^{-2i\phi}$, inserted into eq. (7.2) this yields

$$h_+ - ih_\times = A_{22}(t)e^{i\varphi_{22}(t)}\,\kappa\, e^{-2i\phi}, \tag{7.3}$$

reproducing the frequency as

$$f(t) = \frac{1}{2\pi}\frac{d(\arg(h_+ - ih_\times))}{dt} = \frac{\dot\varphi_{22}(t)}{2\pi} = f_{22}(t)\,, \tag{7.4}$$

connecting f directly to f_{22}. Considering further that, in the face-off approximation, the amplitude is given as

$$|h_+ - ih_\times| = A_{22}(t)\,\kappa\,, \tag{7.5}$$

thus further, implying that both the peak of $|h|$ and the peak of the $(\ell,m) = (2,2)$ mode coincide. While it is fortunate that these simplifications appear for GW150914 they do not hold generally and a full reconstruction of h is necessary. To access the error the NR simulation and released posterior samples for GW150914 are combined [6, 14, 17]. Explicit reconstruction of h showed that the face-off approximation indeed is a good, introducing no large errors.

The GR prediction for $f^{\rm peak}$ is given as

$$f^{\rm peak}_{\rm GR} = \frac{M\omega^{\rm mrg}_{22}\left(\nu, X_{12}, \hat S\right)}{2\pi M}, \tag{7.6}$$

with $M\omega^{\rm mrg}_{22}$ defined in eq. (6.19) – (6.22) and evaluated with the coefficients of Tab. D.1. Note that the total mass is here restored twice explicitly. Even though largely omitted to be pointed out explicitly to simplify notation, $M\omega^{\rm mrg}_{22}$ is fitted, not $\omega^{\rm mrg}_{22}$. Thus, the total mass needs to be restored

---

[2] This analysis was carried out by Ka Wa Tsang.

[3] This analysis was carried out by Gregorio Carullo.

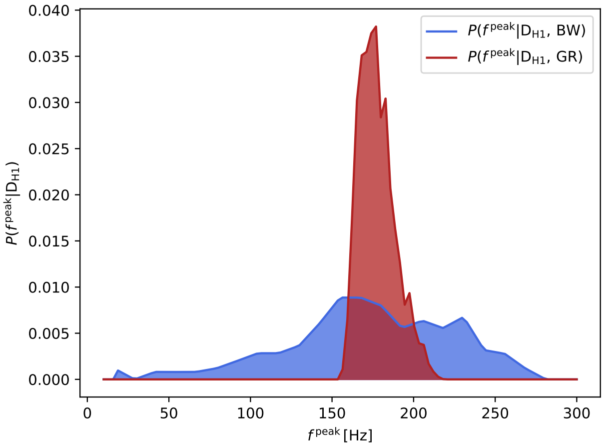

Figure 7.1: direct comparison of the peak frequency prediction of GR (red) and by the unmodelled `BayesWave` reconstruction (blue) using Hanford data.

in the denominator as well. The distribution of $f_{\mathrm{GR}}^{\mathrm{peak}}$ is then obtained by evaluating the analytical expression explicitly over a given posterior distribution, obtained from a full Bayesian parameter estimation analysis (with the waveform model IMRPhenomPv2 [101]) of GW150914. In this case the publicly released samples have been used [6, 14, 17]. f^{peak} as predicted by GR, is now shown in Figure 7.1

It is now useful to depart from the case of the face-off approximation used for GW150914. Thus, two methods are briefly mentioned that allow to faithfully represent the dependence on (ι, ϕ):

(i) The peak frequency can be reconstructed directly using an NR-surrogate model [50, 149] or a Waveform model containing higher mode contributions, such as `TEOBiResumS_SM` or Refs. [70, 101, 114, 122]. Either method allows to fully reconstruct h and thus directly access the peak of $|h|$ directly.

(ii) the peak frequency could be fitted directly to NR data, as many NR codes provide information for such a fit [7, 49, 57, 59, 67, 68, 89, 90, 98, 101, 116, 118, 126, 142]. It might even be possible to exploit quasi-universal structures, yet unlikely as the general case has a strong dependency on several parameters in the general case of a BBH merger $(q, \vec{\chi}_1, \vec{\chi}_2, \iota, \phi, \varepsilon)$, making this even constrained to the spin-aligned, non-eccentric case an exceptionally challenging task.

Unmodeled peak frequency To obtain a model-independent reconstruction of the peak frequency the `BayesWave` algorithm is employed on GW150914, building a distribution of reconstructed waveforms.

`BayesWave` ([69, 124]) is a morphology-independent search algorithm. It utilizes Bayesian evidences to distinguish a potential signal from either a potential glitch or noise, while reconstructing the waveform. The h_+ polarization is modeled by a decomposition into a sum of Morlet-Gabor wavelets, which form a complete functional basis thus allowing the decomposition of arbitrary GW signals. $h_\times$ is then built with ϵ an ellipticity parameter as $h_\times = \epsilon h_+ e^{i\pi/2}$. From this distribution both h and f_{peak} can be reconstructed. The result of this computation is shown in Fig. 7.1

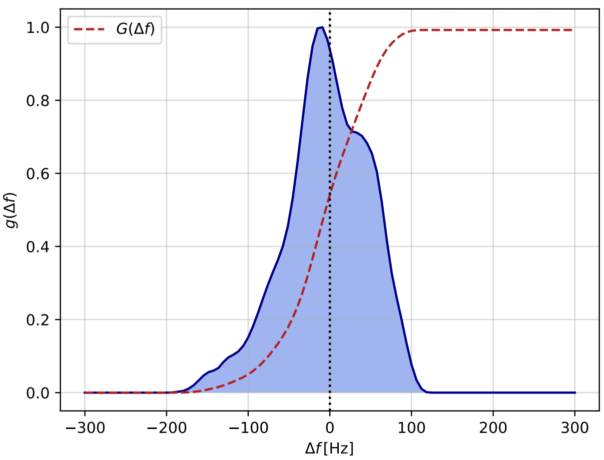

Figure 7.2: The cumulative distribution $G(\Delta f)$ is plotted as function of Δf, using the Hanford data (red), is plotted above the difference distribution (blue). The difference distribution is obtained from the distributions shown in Fig. 7.1 between the GR prediction and the unmodeled reconstruction.

Null-hypothesis test The distribution of the peak frequency obtained from GR and the `BayesWave` algorithm are combined as

$$\Delta f \equiv f^{\text{peak}}_{\text{rec}} - f^{\text{peak}}_{\text{GR}} . \tag{7.7}$$

The posteriors $p(f^{\text{peak}}|\text{D}\,,\text{GR}) \equiv q(f^{\text{peak}})$ and $p(f^{\text{peak}}|\text{D}\,,\text{BW}) \equiv r(f^{peak})$ are defined. his allows to compute the posterior distribution for Δf as

$$g(\Delta f) = \int r(f^{\text{peak}}_{rec})\, q(f^{\text{peak}}_{rec} - \Delta f) df^{\text{peak}}_{rec} \ . \tag{7.8}$$

The *null* hypothesis of this analysis is that GR is the correct theory of nature. In such a scenario it is evident that both the modeled and unmodeled reconstruction should be consistent giving a distribution of $g(\Delta f)$ centered around zero. In other words, Δf is a quantitative indicator of the agreement or disagreement between GR and the observed signal. It is therefor useful to compute the cumulative distribution $G(\Delta f) = \int_{-\infty}^{\Delta f} g(x)dx$ and computed the p-value $p \equiv \min\left[1 - \text{G}(0), \text{G}(0)\right]$ through it. This computation applied to the Hanford strain is shown in Fig. 7.2, yielding a p-value $p = 0.48$. As the strain observed at Livingston yields $p = 0.46$. Thus, no significant deviation from the null hypothesis prediction $p = 0.5$ is present and therefor no violation of GR is observed.

Summary This test of GR exploited the correlation between the merger phase of a BBH system with the peak of complex GW strain h. The peak frequency is reconstructed through two independent methods. First, the peak frequency is reconstructed with a GR waveform model. The model is used to perform a fully Bayesian parameter estimation run. The obtained posterior distribution is then used to reconstruct the peak-frequency as predicted by the waveform model, thus, imposing consistency between the peak and the full IMR waveform as predicted by GR. If GR is a true theory of nature describing gravity this would be perfectly consistent with the model-independent reconstruction through the `BayesWave` algorithm applied to the data.

As mentioned already above the face-off approximation does not hold for a general Binary complicating the form of h to be reconstructed. Given a reliable multipolar model such as an NR-surrogate model [50, 149] or a Waveform model containing higher mode contributions, such as

`TEOBiResumS_SM` or Refs. [70, 101, 114, 122] ,the reconstruction of h, even though not trivial, is straightforward.

The unmodeled reconstruction of $f_{\rm rec}^{\rm peak}$ through the `BayesWave` algorithm is however highly sensitive to the noise of the detector. With GW150914 this is clearly the limiting factor of this analysis, as can be seen from the shape of the distribution in Fig. 7.1. It might be interesting to repeat this analysis with signals observed at improved detector quality. Further the null-hypothesis test can be hardened by combining the p-values of several different GW events observed. Yet these considerations are left to future work.

Chapter 8

Discussion and Conclusion

This thesis presents an introduction to the NR driven completion and validation of waveform models on the example of the `TEOB` infrastructure. In total three avatars of the model have been discussed all focusing on spin-aligned, non-eccentric BBH systems. The model was calibrated and validated with a catalog of 555 `SXS` and 19 `BAM` waveforms, completed by a set of test-particle waveforms.

The analysis of the NR catalog Within this thesis the NR was separated into two catalogs. The *calibration* and *validation* set. The *calibration* set contains 135 `SXS`, 19`BAM` waveforms and is completed by a set waveforms generated by a test-particle falling into a Kerr BH. Of those 19 `SXS`, 3 `BAM` and 1 test-particle waveform were non-spinning. With this data both `TEOBResumS` and `TEOBiResumMultipoles` have been calibrated and validated. In the context of Paper III, it was discussed that a total of 110 `SXS` waveforms in this set had been given with a next-to-highest resolution. For each of these waveforms $\bar{F}_{\rm NR/NR}$ was computed for h_{22} between the two highest levels. Showing that the large majority of waveforms did not reach $\bar{F}_{\rm NR/NR} \sim 10^{-4}$. To remain on the strongly conservative side the uncertainty was estimated to be at $\sim 0.5\%$. All data sets are given in Tab. F.1 – F.4 and Tab. F.14.

The *Validation* set consists of an additional 420 `SXS` waveforms, expanding and refining the parameter space covered by the `SXS` data. These waveforms are listed explicitly in Tab. F.5 – F.15. Of these 382 have are given with an additional resolution, which was used to evaluate $\bar{F}_{\rm NR/NR}$ for h_{22}, finding a similar situation as for the *calibration* set. Most waveforms have an unfaithfulness of $\sim 10^{-4}$. Thus, the uncertainty of the unfaithfulness is estimated to be $\sim 0.5\%$, to remain on the conservative side.

This analysis forms the basis of using this NR catalog for calibration and validation of the three `TEOB` avatars discussed in this thesis. However, while this analysis reached it's goal to get a measure of uncertainty for h_{22} further improvement is possible. Two routs can be pursued to potentially improve this catalog in future works. (i) The analysis of the h_{22} unfaithfulness between the two highest levels of any given NR waveform should be extended to the subdominant modes. In particular the analysis of h_{44} for nearly-equal-mass waveforms will be insightful and useful as currently the $(4,4)$ mode does show disagreements between NR and the multipolar `TEOB` avatars. Any error analysis in this area would shed additional insight onto whether or not the disagreement warrants an improvement of the calibration or analytical baseline information included in `TEOBiResumMultipoles` and `TEOBiResumS_SM`. (ii) In this thesis only 19 `BAM` waveforms are used together with 555 `SXS` waveforms.

While the parameter spaces do overlap, they are not fully covering each other. Therefor it would be advisable to include a third or potentially fourth set of waveforms from different catalogs[1]. This code should be chosen such that the maximum region of the parameter space is covered by at least two different codes. While it is unlikely that this extension will have any effect on the calibration or validation of h_{22}, the same cannot be said for the subdominant modes. For many waveforms these are very noisy and difficult to analyze. Given any problematic NR waveform, if two versions generated by independent codes exist, it would be possible to tune the waveform model to minimize the the unfaithfulness with respect to both waveforms. Thus, avoiding the danger of over-fitting of parameters, as it is unlikely that both NR waveforms deviate in a similar manner from GR. (iii) The validation and calibration can be attempted based on an NR surrogate model (see *e.g.* Ref. [150]). It is reasonable to assume that the surrogate model will have filtered a significant aspect of the noise and thus might give a more reliable picture, in particular in areas in which only a few NR waveforms of high quality are available.

The dominant $(2,2)$ mode In total 3 different fully calibrated models of h_{22} are discussed in this thesis. First, `TEOBResumS` was presented in Paper I and while several aspects have been improved, some were taken over from its predecessors presented in Refs. [76, 132]. The full calibration of the model based on the *calibration* of 135 `SXS` and 19 `BAM` waveforms is presented and discussed. $\max(\bar{F}) \lesssim 2.5 \times 10^{-3}$ over the full set of `SXS` waveforms is achieved with one exception: $(3, +0.85, +0.85)$ where $\max(\bar{F}) \lesssim 7.1 \times 10^{-3}$. As was shown, a more flexible fit of c_3, in particular if c_3 is fitted with explicit *quadratic* dependence on the individual spin variables, it is possible to achieve $\max(\bar{F}) \lesssim 2.5 \times 10^{-3}$ *all over* the SXS waveform catalog. For the `BAM` waveforms, $\bar{F}$ is well below the 1% level with again a single exception of $(8, +0.85, +0.85)$, reaching 5.2%. This problem was shown to be caused by a discrepancy in the strength of the EOB-predicted spin-orbit interaction. Exploring this through modification of c_3 showed that the spin-orbit interaction is too small (i.e., leading to an earlier transition from inspiral to plunge as compared to NR) within this sector of the parameter space. This issue can in principle be fixed by a modified value of c_3. However, even if the value of c_3 is modified, it was still not possible to iterate on the NQC for this waveform, indicating that the NR calibration is at it's limit. While NR calibration can account for a significant improvement in the waveform performance, it has limits to how far it can be done robustly. Therefor the choice was made to postpone the solving of this issue until the resummation of the waveform was improved with the methods presented in Refs. [123, 129] that, as was shown in Paper III and chapter 6, indeed solve these problems and are thus no longer there for `TEOBiResumS_SM`.

The study of the BBH sector of `TEOBResumS` was concluded with an analysis outside of the domain of calibration and validation. A trick in the NR calibration was applied. Both NQC and peak amplitude and frequency were fitted very similar templates to the same data. Thus leading to similar extrapolation behavior making the waveform peak very robust even in domains where no NR data is available. This was explored in detail for large mass-ratios ($q \leq 20$) and high-spins ($\chi_1 = \chi_2 = \pm 0.95$). Especially, the robust nature of the peak, while not guaranteeing low $\bar{F}$, it does prevent pathological behavior that would increase $\bar{F}$ by a few percent.

Within `TEOBiResumMultipoles`, presented in Paper II and chapter 5, h_{22} was improved relative

---

[1] Some examples of such catalogs based on individual codes are NINJA [31, 37], NRAR [99], Georgia Tech [105] and RIT [96, 97].

to `TEOBResumS`. The analytical information and the NR calibration of the A-potential have been updated. An improved resummation of the waveform has been implemented [123, 129]. As the performance of `TEOBResumS` was however already sufficient from the point of both calibration and validation in the non-spinning sector it only remained to verify that `TEOBiResumMultipoles` did indeed perform similarly well. This is especially important looking to the subdominant modes. As mentioned already in Sec. 2.3, the $(2,2)$ mode holds a special place as it is the only mode for which the NQC corrections enter the radiation reaction. Thus, within `TEOB` it will always be important to check the $(2,2)$ mode independently to ensure that no pathological features enter through the NQC into the radiation reaction. The discussion of `TEOBiResumMultipoles` will be continued below with respect to the extension to the subdominant modes in the non-spinning sector.

The extension of `TEOBiResumMultipoles` to the spinning sector is `TEOBiResumS_SM`, introduced in Paper III and chapter 6. Almost all pieces of the analytical information in `TEOBiResumS_SM` were changed relative to `TEOBResumS`. It is useful to summarize the changes. The non-spinning sector is given by `TEOBiResumMultipoles`. The updated A-potential of `TEOBiResumMultipoles` is kept as well together with the improved calibration of the effective PN parameter $a_6^c(\nu)$. Additionally, the waveform resummation is greatly improved relative to `TEOBResumS`. Due to the changes in waveform and A-potential it is also become necessary to redetermine the effective PN parameter $c_3(\nu, S_1, S_2)$. Finally, the fits of the NQC are improved for $q \geq 4$, as well as for the over all *merger-ringdown* templates. Once calibrated, `TEOBiResumS_SM` was validated through the computation of $\bar{F}_{\rm EOB/NR}$ for the $(2,2)$ mode. All over 19 `BAM` and 555 `SXS` waveforms, including the *calibration* set, $\bar{F}_{\rm EOB/NR}$ for the $(2,2)$ mode is always below 0.5%. A single outlier is found for $(1.5, +0.95, +0.95)$, for which $max\left[\bar{F}_{\rm EOB/NR}\right] \approx 0.85\%$. This is evidently a significant improvement relative to the performance of `TEOBResumS`, which struggled immensely with $(8, +0.85, +0.85)$, comparing this to $\bar{F}_{\rm EOB/NR} \sim 10^{-3}$ for `TEOBiResumS_SM` is quite an impressive improvement. This jump in performance highlights that NR calibration has to be done with care. While it might be in principle possible to solve a problem through increasing the impact of the NR calibration, it might be recommendable to instead improve the analytical information baseline of the model.

While most results of `TEOBiResumS_SM` are obtained with the `MATLAB` implementation of the code, a stand-alone C-implementation of the model is available at Ref. [12]. Further, due to the improved waveform resummation of `TEOBiResumS_SM` it was possible to fit the NQC parameters (a_1^{22}, a_2^{22}) of the $(2,2)$. With this fit it is possible to skip the iteration process to improve the NQC accuracy and obtain a good agreement between `TEOBiResumS_SM` and NR globally of $\bar{F}_{\rm EOB/NR} < 1\%$. After the exclusion of $(1.5, +0.95, +0.95)$, the global maximum is around $\sim 0.6\%$. Thus even though the goal set by the NR uncertainty is missed, it is not missed by much, while the performance demand of GWA is still met. The importance of this result can easily be seen once one considers that the evaluation time of the C-implementation of `TEOBiResumS_SM` is dominated by the integration of the `TEOB` Hamiltonian equations of motion. As each iteration requires a full integration, it is easy to see that the computation time goes linearly with the number of iterations necessary. Thus this is a major step towards meeting the $\sim 0.1ms$ evaluation time goal for `TEOBResumS`.

Subdominant modes: The non-spinning case In chapter 5 and Paper II, `TEOBiResumMultipoles` was introduced and discussed. As mentioned above, several improvements have been made relative to `TEOBResumS`, in the A-potential and the resummed waveform[2]. The multipoles $(\ell, m) = (2,1), (3,3), (3,2), (3,1), (4,4), (4,3), (4,2), (4,1)$ and $(5,5)$ are fully calibrated to NR. All additional multipoles $\ell \leq 8$ are given by their pure analytical, `TEOB`-factorized and resummed expression, falling smoothly to 0 around the merger. The agreement between $\omega_{\ell m}$ on both NR and `TEOB` side is excellent up to the merger point. The major findings presented in chapter 5 are:

(i) Each multipole $h_{\ell m}$ of $(\ell, m) = (2,1), (3,3), (3,2), (3,1), (4,4), (4,3), (4,2), (4,1)$ and $(5,5)$ is fully calibrated to NR following the model as introduced in Sec.2.3. This includes a fully calibrated *merger-ringdown* template, the peak-time shit $\Delta t^{\rm NR}_{\ell m}$ and the NQC extraction points $\left\{\hat{A}^{\rm NQC}_{\ell m}, \dot{\hat{A}}^{\rm NQC}_{\ell m}, \omega^{\rm NQC}_{\ell m}, \dot{\omega}^{\rm NQC}_{\ell m}\right\}$. Especially the NQC are important for the final evolution of the subdominant modes, starting at $\sim 50M$ before the peak. It is worth pointing out that it is quite surprising that such a simple setup is very efficient in completing the waveform until the peak of the waveform. Important to note is that strong performance of the NQC was enabled by modifying the Newtonian (multipolar) prefactors in the waveform, while leaving it untouched in the radiation reaction, as discussed in Sec. 5.2.3. In particular the $m = 1$ multipoles are improved by this modification of the Newtonian (multipolar) prefactors, for these multipoles the derivatives of the radial momentum become especially important close to the peak of the multipole.

(ii) $\bar{F}_{\rm EOB/NR}$ evaluated between `TEOBiResumMultipoles` and the non-spinning sector of the *calibration* set was investigated thoroughly. For the inclusion of all modes the soft criteria of $< 3\%$ was met for almost all binaries with a total mass $50M_\odot \leq M \leq 200M_\odot$. In the parameter space sector $1 \lesssim q \lesssim 2$, for large total masses, this is however not the case. However, it stands to reason that this uncertainty in the model is likely due to pathological features in h_{44} of the NR waveform, amplified due to *e.g.* the waveform extrapolation. In contrast for a total mass of $100M_\odot$ or less, $\bar{F}_{\rm EOB/NR} < 1\%$ is generally met for all systems.

Subdominant modes: The spinning case `TEOBiResumS_SM` is the latest spin-aligned, non-eccentric BBH waveform model discussed in this thesis and is introduced in Paper III and chapter 6. Several modes, beyond the $(2,2)$ mode, for which `TEOBiResumMultipoles` was already defined, are extended in `TEOBiResumS_SM` to include spin dependence. Concretely, these are the $(\ell, m) = (2,1), (3,3), (3,2), (3,1), (4,4), (4,3), (4,2)$ and $(5,5)$. The best performance in the extension to the spinning domain is found for the $\ell = m$ modes up to $\ell = 5$. The remaining waveforms, in particular the $(2,1)$ mode can become problematic for spins $\chi_{1,2} \lesssim -0.5$. Several aspects of the `TEOBiResumS_SM` model are improved relative to `TEOBResumS`, as already mentioned above. Further all modes are NR completed with NQC and *merger-ringdown* template waveform attached at $t^{\rm EOB}_{{\rm NQC}_{\ell m}}$.

The results presented for the extension to the subdominant modes can be summarized as:

(i) The NR informed fits for many quantities already used in `TEOBiResumMultipoles` are extended to include spin. The inclusion of spin is done through factoring out orbital dependence and potentially also of leading order spin dependence. A spin parameter is chosen, exploiting quasi-universal or approximately quasi-universal structures, to effectively reduce the dimensionality

---

[2] For a general discussion of the analytical improvements in detail the reader is referred to Paper II and references therein, as the focus of this thesis is on the NR completion of `TEOB` model avatars.

of total fit to two: (i) ν or alternatively X_{12} or X_{12}^2, (ii) a spin parameter, most commonly chosen to be $\hat{S}$. With the exception of the effective *merger-ringdown* evolution parameters, all fits utilize the test-particle data to improve the extrapolation to higher mass-ratios.

The NR calibration and performance of the multipole as a whole is commonly most robust and reliable for $\ell = m$ modes, up to $\ell = m = 5$. The unfaithfulness of $m = \ell$ modes up to $\ell = 4$ is well below 3% for BBH system masses $M = 120M_\odot$. Due to disagreements between `TEOB` and NR waveform for the $(4,4)$ mode this limit is somewhat exceeded for larger masses. It is however not yet clear if this disagreement is entirely due to inaccurate modeling on the waveform model side, or insufficiently resolved, possibly pathological waveforms on the NR side[3]. Similarly, when the $(2,1)$ mode is included the unfaithfulness performs reasonable well $\bar{F} \lesssim 3\%$. However, for systems with large, anti-aligned spins relative to the orbital angular momentum, such as *e.g.* $(3, -0.85, -0.85)$, the situation is more challenging. As between the peak of the $(2,2)$ and $(2,1)$ mode the `TEOB` dynamics, as implemented in `TEOBiResumS_SM`, become unreliable in those conditions.

(ii) One of the major results of Paper III, which is only summarized here, is the increased difficulty that arises when the peak of a given subdominant mode $h_{\ell m}$ is significantly delayed ($\sim 7{-}8M$) with respect to the peak of the dominant h_{22} mode. This can happen for $m \neq \ell$, in particular for $(2,1)$, $(4,3)$ or $(3,1)$. One method to solve this is could be found in the extension of the *merger-ringdown* template into the late inspiral, as was done in Ref. [70]. The problem with such an approach is that it has a high potential to miss subtle physical structures in the waveform. One example is the zero in the waveform close to the peak of the $(2,1)$ mode for $(2, +0.60, -0.60)$. Thus, it is reasonable to instead focus on improving the dynamics and aiming at building an improved dynamical structure which is more stable after the peak of the $(2,2)$ mode.

$m = 1$ waveform minimum in the inspiral In Ref. [70] it was discovered that the $(2,1)$ mode for nearly-equal-mass waveforms with oppositely aligned spins can potentially show can contain a minimum or even a zero in the late-inspiral amplitude. This effect was loosely reproduced with the PN waveform in which the leading order spin-orbit correction cancels with the dominant orbital contribution. While the phenomena was pointed out it remains not included into the waveform model discussed therein `SEOBNRv4`$_{\texttt{HM}}$.

In chapter 6 touched upon this feature briefly, while Paper III discussed it more thoroughly, this topic was picked up in the context of `TEOBiResumS_SM`. The minimum, when it was sufficiently before the merger shows an excellent agreement with the factorized and resummed `TEOB` waveform developed in Ref. [123, 129], as was demonstrated. Starting from the analytical description of the $(2,1)$ mode it was in principle possible for any $m =$ odd multipole to develop a zero in the inspiral. Thus, the SXS catalog was investigated and an additional SXS waveform was found with a similar phenomenology. However, this waveform showed this behavior in the $(3,1)$ mode, which was very well modeled by the `TEOB` waveform even without NR calibration. Thus, even though this phenomenon was not intentionally targeted, the behavior could be recovered accurately, likely due to the robust resummation and factorization of the waveform.

---

[3] A possible solution is to extend the discussion through the inclusion of an additional NR waveform catalog as discussed above.

Future improvement of the `TEOB` model There are a three ways to include new physical phenomena into `TEOB`. (i) The basic infrastructure can be changed. Especially, when extending the model, to *e.g.* eccentricity [66] or precessing spins [33], an improvement of the `TEOB` infrastructure becomes necessary. (ii) The analytical information contained in the A-potential, the gyro-gravitomagnetic ratios (G_S, G_{S_*}) and the analytical waveform could be improved. (iii) The *merger-ringdown* templates can be improved in several ways:

(i) Ref. [66] presented a minimally modified version of `TEOBiResumS_SM` capable to include mild eccentricity. Following this work it would be interesting to investigate if it would be possible to modify the model independent sector of the *analytical flexibility* to include a dependency on eccentricity. As has been shown in Ref. [66] the approximation of no eccentricity in the *merger-ringdown* template is sufficiently accurate for mild eccentricity.

(ii) The inspiral model `TEOBResumSP`, allowing for generic, precessing spins was introduced in Ref. [33]. Improving *merger-ringdown* and NQC to include the dependence on generic spins.

(iii) Currently, all modes are modeled neglecting mode-mixing, which occurs because the $s = -2$ spin-weighted spherical harmonics are not an eigen basis of the radiation emitted in the final state and need to be replaced by spheroidal harmonics. Including this would greatly improve the robustness *merger-ringdown* phase. Examples of such improvements can be found in Ref. [113, 114].

(iv) Currently, model does not account for the beating between positive and negative frequency quasi-normal-modes [45]. An example of this effect can be observed for `BBH:1375` in Fig. 4.7. This can be incorporated following the method of Ref. [45].

(v) The model is calibrated up to mass-ratios $q = 20$ and robust up to $q = 30$. Extending the fits of the merger and postpeak evolution parameters up to the test-particle limit would complete the coverage of the aligned-spin parameter space The amplitude template of the merger needs to be modified to account for the test-particle behavior.

Future non-standard applications of the `TEOB` avatars Two possible future projects could be the following:

(i) The very short BBH event GW170729 was announced in Ref. [23]. It was visible during its late inspiral, merger and ringdown. It showed clear evidence of high spins, non-vanishing mass difference and the presence of subdominant multipoles. It would be interesting to use the merger-ringdown template developed in Paper III to explore a direct time-domain analysis of GW170729. The method of such an analysis has been explored for a previous version of the model on NR-injection samples in Ref. [83]. An analysis of the system has been presented in Ref. [65].

(ii) In chapter 7 a consistency test of GR was introduced utilizing the fortunate *face-off* orientation of GW150914 to perform a strongly simplified analysis. In the *face-off*/*face-on* case of a nearly-equal-mass waveform the signal is dominated by h_{22} or $h_{2,-2}$ and the error due to the exclusion of all subdominant multipoles is shown to be limited. In general this is not the case. Thus a full multipolar waveform model is required to reconstruct the peak as determined by an analysis of the signal. It would be interesting to see if this method can be applied to similar situations.

Acknowledgements

I thank Alessandro Nagar for his supervision of my thesis work and the opportunity to work, collaborate and learn from him. I thank Nicolao Fornengo for his support during the preparation of this thesis. I thank the physics department of the Università degli studi di Torino as well as the INFN sezione di Torino for the support I received, allowing me to visit several workshops and conferences. I am grateful to the Ministero dell'Istruzione, dell'Università e della Ricerca for the scholarship I received for the duration of my PhD. I thank IHES and Thibault Damour for their hospitality on multiple occasions during the developments of this research. I thank Mark Hannam and Sascha Husa for kindly providing the `BAM` waveforms used in this thesis. I am grateful to Walter del Pozzo for discussion and his valuable advice. I thank Piero Rettgno for his friendship and support.

Above all, I am grateful to my brother Sven and my family for their support during many difficult times.

Gunnar Markus Riemenschneider, Turin, May 2021

Appendix A

Unfaithfulness and FFT computation

This appendix is dedicated to introduce the FFT and unfaithfulness computation. Given a waveform h we will refer to its Fast Fourier Transform (FFT) by $\tilde{h}$. Prior to the FFT computation the waveform needs to be tapered as

$$h \rightarrow \begin{cases} 0 & , \, for \quad t \leq t_0 \\ h \cdot h_{\text{taper}} & , \, for \quad t > t_0 . \end{cases} \tag{A.1}$$

The time t_0 for NR waveforms is chosen just after the passing of the initial-state radiation. As EOB waveforms can typically be much longer the value of t_0 for the EOB waveform is chosen such that the initial frequency for both NR and EOB waveform agree. h_{taper} is given by a Schwartz-function

$$h_{\text{taper}} = \frac{1}{1 + e^{\alpha \cdot Z \cdot T_{\text{cyc}}}} \, , \tag{A.2}$$

$$with \; Z = \frac{1}{(t - t_0)} + \frac{1}{(t - t_0) - n_{\text{cyc}} \cdot T_{\text{cyc}}} \, . \tag{A.3}$$

Practice has shown that the following parameters give stable results

$$T_{\text{cyc}} = \frac{2\pi}{f_{GW}\,(t = t_0)} \, , \quad n_{\text{cyc}} = \; 1, \quad \alpha = 1 \, , \tag{A.4}$$

with $f_{GW}\,(t = t_0)$ being the GW frequency at $t = t_0$[1]. The FFT is computed with the `MATLAB` function `fft`.

In this work we will primarily use the noise Power Spectral Density (PSD) of advanced LIGO. The results presented in Papers I and II were computed using the anticipated sensitivity curve of Advanced LIGO more specifically the zero-detuned, high-power PSD [8]. In Paper III the results have been computed with the updated PSD presented in [11]. While Advanced Virgo and LIGO show a very different profiles in terms of performance and technology applied, from the point of view of waveform model development they are sufficiently similar.

To compare EOB waveform models with NR to access their standards of performance for third generation gravitational it is recommended to use the results published in [147]. The PSD curves can be found, prepared in `".txt"` and `".mat"` format, at [1]. The curve model `ET_D` is recommended.

---

[1] In practice it can happen that the numerical evaluation of h_{taper} is singular at $t = t_0$ but this singularity can be circumvented by manually imposing $h_{\text{taper}}\,(t = t_0) = 0$.

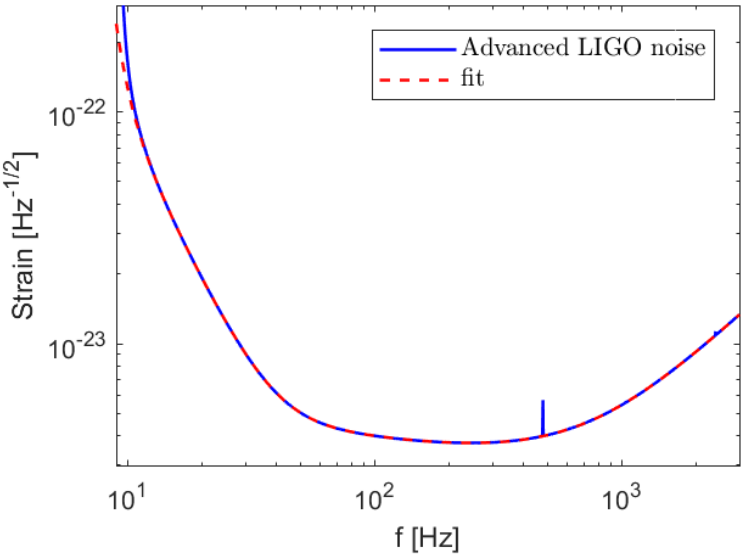

Figure A.1: A direct comparison of the noise spectrum and the fit shown in equations (A.5) – (A.11).

While the any code could handle raw PSDs as published some post-processing is advised. In particular the individual peaks in the PSD have to be smoothed out. The anticipated PSD $S_n^{\text{anticipated}}(f)$ was fitted and a direct comparison between the strains is shown in Fig. A.1.

$$\begin{aligned}
S_n^{\text{anticipated}}(f)_{\text{fit}} &= \frac{1.23693\times 10^{-45}}{f} \times S_n^{\star}\left(\frac{f}{56.56}\right) && \text{(A.5)}\\
S_n^{\star}(x) &= 0.41473797 + 0.0927076\log(x) + 0.44943703x && \text{(A.6)}\\
&+ 0.0034297409x\log(x) - 6.5736784\times 10^{-5}x^2 + 0.0026988759x^3 && \text{(A.7)}\\
&+ e^{S_n^{exp}(x)} && \text{(A.8)}\\
S_n^{exp}(x) &= -2.0158256 - 4.1577911\log(x) - 1.0904057\log^2(x) && \text{(A.9)}\\
&- 0.75793805\log^3(x) - 0.34979753\log^4(x) - 0.098312294\log^5(x) && \text{(A.10)}\\
&+ 3.3732744\times 10^{-6}x^{-7}. && \text{(A.11)}
\end{aligned}$$

Spikes in the updated Advanced LIGO noise PSD were removed by hand and the cuts have been smoothed out using the `MATLAB` function `spline`. The noise PSD of the Einstein Telescope can be prepared similar in the same way.

For two waveforms (h_I, h_J), the unfaithfulness is a function of the total mass M of the binary and is defined as

$$\bar{F}_{IJ}(M) \equiv 1 - F_{IJ} = 1 - \max_{t_0,\phi_0} \frac{\langle h_I, h_J\rangle}{||h_I||||h_J||}, \tag{A.12}$$

where (t_0, ϕ_0) are the initial time and phase, $||h|| \equiv \sqrt{\langle h, h\rangle}$, and the inner product between two waveforms is defined as $\langle h_I, h_J\rangle \equiv 4\Re \int_{f_{\text{min}}^{\text{NR}}(M)}^{\infty} \tilde{h}_I(f)\tilde{h}_J^*(f)/S_n(f)\, df$, where $\tilde{h}(f)$ denotes the Fourier transform of $h(t)$, $S_n(f)$ is one of the PSDs discussed above, $f_{\text{min}}^{\text{NR}}(M) = \hat{f}_{\text{min}}^{\text{NR}}/M$ is the initial frequency of the NR waveform at highest resolution after the transition of initial-state radiation.

In chapter 5 and chapter 6 the unfaithfulness is additionally varied over the orientation of the source given by the angles (ι, φ). Sec. 5.4.1 will introduce the reader onto the difference this generates on practical examples there presented.

Appendix B

`TEOBResumS` $\ell = m = 2$ mode, additional fit information

This appendix shows some additional information complimentary to the fits presented in Chapter 4.

B.1 NQC hybrid fit of the $\ell = m = 2$ mode

In previous works several excellent fits of the NQC extraction points $\left\{\hat{A}_{22}^{\rm NQC}, \dot{\hat{A}}_{22}^{\rm NQC}, \omega_{22}^{\rm NQC}, \dot{\omega}_{22}^{\rm NQC}\right\}$ have been obtained [76, 131, 132]. In both Paper I and Paper III these fits have been used to model the NQC extraction points for the cases $q = 1$, see eq. (B.1), and $1 < q < 4$, see eq. (B.2).

$$\hat{A}_{22}^{\rm NQC} = 0.00178195\hat{a}_0^4 + 0.00435589\hat{a}_0^3 + 0.00344489\hat{a}_0^2 - 0.00076165\hat{a}_0 + 0.31973334, \tag{B.1a}$$

$$\dot{\hat{A}}_{22}^{\rm NQC} = 0.00000927\hat{a}_0^4 - 0.00024550\hat{a}_0^3 + 0.00012469\hat{a}_0^2 + 0.00123845\hat{a}_0 - 0.00195014, \tag{B.1b}$$

$$\omega_{22}^{\rm NQC} = 0.00603482\hat{a}_0^4 + 0.01604555\hat{a}_0^3 + 0.02290799\hat{a}_0^2 + 0.07084587\hat{a}_0 + 0.38321834, \tag{B.1c}$$

$$\dot{\omega}_{22}^{\rm NQC} = 0.00024066\hat{a}_0^4 + 0.00038123\hat{a}_0^3 - 0.00049714\hat{a}_0^2 + 0.00041219\hat{a}_0 + 0.01190548. \tag{B.1d}$$

$$\begin{aligned}
\hat{A}_{22}^{\rm NQC} = {} & (0.04680896\nu - 0.00632114)\,\hat{a}_0^3 + (0.06586192\nu - 0.01180039)\,\hat{a}_0^2 \\
& - (0.11617413\nu - 0.02704959)\,\hat{a}_0 + (0.15597465\nu + 0.28034978)\,, \qquad \text{(B.2a)} \\
\dot{\hat{A}}_{22}^{\rm NQC} = {} & -(0.0013082\nu - 0.00006202)\,\hat{a}_0^3 + (0.0019986\nu - 0.00027474)\,\hat{a}_0^2 \\
& + (0.00218838\nu + 0.00071540)\,\hat{a}_0 - (0.00362779\nu + 0.00105397)\,, \qquad \text{(B.2b)} \\
\omega_{22}^{\rm NQC} = {} & \frac{0.46908067\nu + 0.27022141}{1 + (0.64131115\nu - 0.37878384)\,\hat{a}_0}, \qquad \text{(B.2c)} \\
\dot{\omega}_{22}^{\rm NQC} = {} & (0.00061175\nu + 0.00074001)\,\hat{a}_0 + (0.02504442\nu + 0.00548217)\,. \qquad \text{(B.2d)}
\end{aligned}$$

$$\tag{B.3}$$

Table B.1: Coefficients of the NQC extraction points defined in Eqs. (4.25)-(4.36). As top-left, top-right, bottom-left to bottom-right the columns show $\left\{\hat{A}_{22}^{\rm NQC}, \dot{\hat{A}}_{22}^{\rm NQC}, \omega_{22}^{\rm NQC}, \dot{\omega}_{22}^{\rm NQC}\right\}$.

$\hat{A}_{22}^{\rm NQC}$		$\dot{A}_{22}^{\rm NQC}/\nu$	
$c_0^{\hat{A}^{\rm NQC}_{\rm orb}}$ =	0.294888	$N_0^{\dot{A}^{\rm NQC}_{\rm orb}}$ =	−0.00421428
$c_1^{\hat{A}^{\rm NQC}_{\rm orb}}$ =	−0.0427442	$N_1^{\dot{A}^{\rm NQC}_{\rm orb}}$ =	−0.0847947
$c_2^{\hat{A}^{\rm NQC}_{\rm orb}}$ =	0.816756	$D_1^{\dot{A}^{\rm NQC}_{\rm orb}}$ =	16.1559
$c_3^{\hat{A}^{\rm NQC}_{\rm orb}}$ =	−0.986204		
$n_{1/4}^{\hat{A}^{\rm NQC}_{\rm spin}}$ =	−0.275052	$n_{1/4}^{\dot{A}^{\rm NQC}_{\rm spin}}$ =	0.00374616
$d_{1/4}^{\hat{A}^{\rm NQC}_{\rm spin}}$ =	−0.469378	$d_{1/4}^{\dot{A}^{\rm NQC}_{\rm spin}}$ =	0.0636083
$n_1^{\hat{A}^{\rm NQC}_{\rm spin}}$ =	0.143066	$n_1^{\dot{A}^{\rm NQC}_{\rm spin}}$ =	0.00129393
$n_2^{\hat{A}^{\rm NQC}_{\rm spin}}$ =	−0.0425947	$n_2^{\dot{A}^{\rm NQC}_{\rm spin}}$ =	−0.00239069
$d_1^{\hat{A}^{\rm NQC}_{\rm spin}}$ =	0.176955	$d_1^{\dot{A}^{\rm NQC}_{\rm spin}}$ =	−0.0534209
$d_2^{\hat{A}^{\rm NQC}_{\rm spin}}$ =	−0.111902	$d_2^{\dot{A}^{\rm NQC}_{\rm spin}}$ =	−0.186101
$\omega_{22}^{\rm NQC}$		$\dot{\omega}_{22}^{\rm NQC}$	
$c_0^{\omega^{\rm NQC}_{\rm orb}}$ =	0.286399	$N_0^{\dot{\omega}^{\rm NQC}_{\rm orb}}$ =	0.00649349
$c_1^{\omega^{\rm NQC}_{\rm orb}}$ =	0.251240	$N_1^{\dot{\omega}^{\rm NQC}_{\rm orb}}$ =	0.00452138
$c_2^{\omega^{\rm NQC}_{\rm orb}}$ =	0.542717	$D_1^{\dot{\omega}^{\rm NQC}_{\rm orb}}$ =	−1.44664
$n_{1/4}^{\omega^{\rm NQC}_{\rm spin}}$ =	−0.292192	$a_{1/4}^{\dot{\omega}^{\rm NQC}_{\rm spin}}$ =	0.1209112
$d_{1/4}^{\omega^{\rm NQC}_{\rm spin}}$ =	−0.686036	$b_{1/4}^{\dot{\omega}^{\rm NQC}_{\rm spin}}$ =	−0.1198332
$n_1^{\omega^{\rm NQC}_{\rm spin}}$ =	0.1996112	$a_1^{\dot{\omega}^{\rm NQC}_{\rm spin}}$ =	0.142343
$n_2^{\omega^{\rm NQC}_{\rm spin}}$ =	−0.236196	$a_2^{\dot{\omega}^{\rm NQC}_{\rm spin}}$ =	−0.1001772
$d_1^{\omega^{\rm NQC}_{\rm spin}}$ =	0.1843102	$b_1^{\dot{\omega}^{\rm NQC}_{\rm spin}}$ =	0.1844956
$d_2^{\omega^{\rm NQC}_{\rm spin}}$ =	−0.148057	$b_2^{\dot{\omega}^{\rm NQC}_{\rm spin}}$ =	−0.0612272

Table B.2: The left column shows the coefficients of the waveform amplitude at merger, defined in Eq. (4.15) – (4.20). The right column shows the coefficients of the waveform frequency at merger, defined in Eq. (4.23) – (4.24), relying on (4.19) – (4.20).

$c_0^{\hat{A}^{\rm mrg}_{\rm orb}}$	$=$	1.43842	$c_0^{\omega^{\rm mrg}_{\rm orb}}$	$=$	0.273813
$c_1^{\hat{A}^{\rm mrg}_{\rm orb}}$	$=$	0.100709	$c_1^{\omega^{\rm mrg}_{\rm orb}}$	$=$	0.223977
$c_2^{\hat{A}^{\rm mrg}_{\rm orb}}$	$=$	1.82657	$c_2^{\omega^{\rm mrg}_{\rm orb}}$	$=$	0.481959
$n_{\nu=1/4}^{\hat{A}^{\rm mrg}_{\rm spin}}$	$=$	-0.293524	$n_{\nu=1/4}^{\omega^{\rm mrg}_{\rm spin}}$	$=$	-0.283200
$d_{\nu=1/4}^{\hat{A}^{\rm mrg}_{\rm spin}}$	$=$	-0.472871	$d_{\nu=1/4}^{\omega^{\rm mrg}_{\rm spin}}$	$=$	-0.696960
$n_1^{\hat{A}^{\rm mrg}_{\rm spin}}$	$=$	0.176126	$n_1^{\omega^{\rm mrg}_{\rm spin}}$	$=$	0.1714956
$n_2^{\hat{A}^{\rm mrg}_{\rm spin}}$	$=$	-0.0820894	$n_2^{\omega^{\rm mrg}_{\rm spin}}$	$=$	-0.24547
$d_1^{\hat{A}^{\rm mrg}_{\rm spin}}$	$=$	0.20491	$d_1^{\omega^{\rm mrg}_{\rm spin}}$	$=$	0.1653028
$d_2^{\hat{A}^{\rm mrg}_{\rm spin}}$	$=$	-0.150239	$d_2^{\omega^{\rm mrg}_{\rm spin}}$	$=$	-0.1520046

Table B.3: Coefficients of the fits of the fundamental QNM frequency and inverse damping time of the final remnant (ω_1, α_1) as well as the difference $\alpha_{21} = \alpha_2 - \alpha_1$ of the inverse damping times of the first two modes. See Eq. (4.37) for definitions.

	$Y = \omega_1^{22}$	$Y = \alpha_1^{22}$	$Y = \alpha_{21}^{22}$
Y_0	0.373672	0.0889623	0.184953
b_1^Y	-1.74085	-1.82261	-1.41681
b_2^Y	0.808214	0.701584	-0.0593166
b_3^Y	-0.0598838	0.121126	0.476420
c_1^Y	-2.07641	-1.80020	-1.35955
c_2^Y	1.31524	0.720117	-0.0763529
c_3^Y	-0.235896	0.0811633	0.438558

Table B.4: The fitted coefficients of $\left\{c_3^A, c_3^\phi, c_4^\phi\right\}$ as defined in Eq. (4.38).

$Y = c_3^\phi$				$Y = c_4^\phi$			
$b_0^{c_3^\phi}(\nu)$	$=$	3.88838	$+0.455847\nu$	$b_0^{c_4^\phi}(\nu)$	$=$	1.49969	$+2.08223\nu$
$b_1^{c_3^\phi}(X_{12})$	$=$	5.11992	$-0.924642X_{12}$	$b_1^{c_4^\phi}(X_{12})$	$=$	8.26248	$-0.899952X_{12}$
$b_2^{c_3^\phi}(X_{12})$	$=$	10.29692	$-3.618048X_{12}$	$b_2^{c_4^\phi}(X_{12})$	$=$	14.27808	$-3.923652X_{12}$
$b_3^{c_3^\phi}(X_{12})$	$=$	-4.041224	$+3.501976X_{12}$	$b_3^{c_4^\phi}(X_{12})$	$=$	0	
$b_4^{c_3^\phi}(X_{12})$	$=$	-32.92144	$+29.24000X_{12}$	$b_4^{c_4^\phi}(X_{12})$	$=$	0	

$Y = c_3^A$			
$b_0^{c_3^A}(\nu)$	$=$	-0.561584	$+0.829868\nu$
$b_1^{c_3^A}(X_{12})$	$=$	-0.199494	$+0.0169543X_{12}$
$b_2^{c_3^A}(X_{12})$	$=$	0.0227344	$-0.0799343X_{12}$
$b_3^{c_3^A}(X_{12})$	$=$	0.0907477	$-0.115928X_{12}$
$b_4^{c_3^A}(X_{12})$	$=$	0	

Appendix C

`TEOBiResumMultipoles`, additional fit information

Table C.1: Parameters for the fit of the peak amplitude and frequency of all multipoles up to $\ell = m = 5$. From left to right, the columns report: the multipolar indices; the values of the amplitude and frequency in the test-particle limit, $(\hat{A}^0_{\ell m}, \omega^0_{\ell m})$; the amplitude fit coefficients $(n_i^{A_{\ell m}}, d_i^{A_{\ell m}})$ and the frequency fit coefficients $(n_i^{\omega_{\ell m}}, d_i^{\omega_{\ell m}})$ for the functions $(\hat{\hat{A}}_{\ell m}, \hat{\omega}_{\ell m})$ defined in Eqs. (5.29)-(5.30) and fitted using the rational function template of Eq. (5.31). Note that since all $d_2^{A_{\ell m}}$ values are found to be equal to zero we do not explicitly report them in the table.

ℓ	m	$\hat{A}^0_{\ell m}$	$n_1^{A_{\ell m}}$	$n_2^{A_{\ell m}}$	$d_1^{A_{\ell m}}$
2	2	0.295896	-0.041285	1.5971	...
	1	0.106935	9.0912	3.9331	11.108
3	3	0.051670	0.098379	3.8179	...
	2	0.018168	-6.142	11.372	-3.6448
	1	0.005694	-5.49	10.915	...
4	4	0.014579	-3.6757	0.32156	-3.6784
	3	0.004962	-5.7791	12.589	-3.3039
	2	0.001656	-4.7096	7.3253	...
	1	0.000487	-8.4449	26.825	-1.2565
5	5	0.005227	-0.29628	6.4207	...

ℓ	m	$\omega^0_{\ell m}$	$n_1^{\omega_{\ell m}}$	$n_2^{\omega_{\ell m}}$	$d_1^{\omega_{\ell m}}$	$d_2^{\omega_{\ell m}}$
2	2	0.273356	0.84074	1.6976	...	...
	1	0.290672	-0.060432	1.9995	0.23248	...
3	3	0.454622	1.1054	2.2957	...	...
	2	0.451817	-9.0214	21.078	-8.6636	19.493
	1	0.411755	...	7.5362	-2.7555	38.572
4	4	0.635415	3.2876	-29.122	1.696	-22.761
	3	0.636870	-9.0124	22.011	-8.732	20.518
	2	0.626030	-7.0558	12.738	-6.0595	9.3389
	1	0.552201	-10.876	37.904	-11.194	42.77
5	5	0.818117	-2.8918	-3.2012	-3.773	...

Table C.2: Fits of the postpeak functions $(c_3^{A_{\ell m}}, c_3^{\phi_{\ell m}}, c_4^{\phi_{\ell m}})$ entering Eqs. (2.46)-(2.47). Note the rather special functional form needed for $c_3^{A_{32}}$ and $c_3^{A_{44}}$, that is necessary to properly account for nearly equal-mass data. In addition, the fits of some multipoles are discontinuous, the interface between the branches being at mass ratios $q = 2.5$ or $q = 10$. Such mass ratios correspond to the values $\nu = 10/49$ and $\nu = 10/121$ that appear in the argument of the θ functions.

ℓ	m	$c_3^{A_{\ell m}}$
2	2	$-0.56187 + 0.75497\nu$
	1	$\frac{0.23882-2.2982\nu+5.7022\nu^2}{1-7.7463\nu+27.266\nu^2}$
3	3	$-0.39337 + 0.93118\nu$
	2	$\frac{0.1877-3.0017\nu+19.501\nu^2}{1-1.8199\nu} - e^{-703.67(\nu-2/9)^2}$
	1	$\frac{3.5042-55.171\nu+217\nu^2}{1-15.749\nu+605.17\nu^3}$
4	4	$-0.25808 + 0.84605\nu + 1.2376e^{-6054.7(\nu-10/49)^2}$
	3	$\frac{-0.02833+2.8738\nu-31.503\nu^2+93.513\nu^3}{1-10.051\nu+156.14\nu^3}$
	2	$\frac{0.27143-2.2629\nu+4.6249\nu^2}{1-7.6762\nu+15.117\nu^2}$
	1	$11.47 + 10.936\nu$
5	5	$\frac{-0.19751+3.607\nu-14.898\nu^2}{1-20.046\nu+108.42\nu^2}$

ℓ	m	$c_3^{\phi_{\ell m}}$	$c_4^{\phi_{\ell m}}$
2	2	$\frac{4.4414-63.107\nu+296.64\nu^2}{1-13.299\nu+69.129\nu^2}$	$\frac{7.1508-109.47\nu}{1+556.34\nu+287.42\nu^2}$
	1	$\frac{2.6269-37.677\nu+181.61\nu^2}{1-16.082\nu+89.836\nu^2}$	$\frac{4.355-53.763\nu+188.06\nu^2}{1-18.427\nu+147.16\nu^2}$
3	3	$3.1017 - 6.5849\nu$	$\frac{3.4521-24.153\nu+53.029\nu^2}{1+3.1413\nu}$
	2	$\frac{0.90944-1.8924\nu+3.6848\nu^2}{1-8.9739\nu+21.024\nu^2}$	$\frac{2.3038-50.79\nu+334.41\nu^2}{1-18.326\nu+99.54\nu^2}$
	1	$\frac{-6.1719+29.617\nu+254.24\nu^2}{1-1.5435\nu}\theta\left(\nu - \frac{10}{121}\right)$	$3.6485 + 5.4536\nu$ $-2.2784\ \theta\left(\frac{10}{121} - \nu\right)$
4	4	$\frac{2.3328-9.4841\nu+19.719\nu^2}{1-2.904\nu}$	$0.94564 + 3.2761\nu$
	3	$\frac{2.284-23.817\nu+70.952\nu^2}{1-10.909\nu+30.723\nu^2}$	$\frac{2.4966-6.2043\nu}{1-252.47\nu^4}$
	2	$\frac{2.2065-17.629\nu+65.372\nu^2}{1-4.7744\nu+3.1876\nu^2}$	Eq. (5.32)
	1	$(-6.0286 + 46.632\nu)\theta\left(\nu - \frac{10}{121}\right)$ $-2.1747\ \theta\left(\frac{10}{121} - \nu\right)$	$1.6629 + 11.497\nu$
5	5	$0.83326 + 10.945\nu$	$\frac{0.45082-9.5961\nu+52.88\nu^2}{1-19.808\nu+99.078\nu^2}$

Table C.3: Parameters of the fitting function given by Eq. (5.33) used to fit the QNM parameters entering the phenomenological description of the postmerger waveform. We list here the fundamental QNM frequency $\omega_1^{\ell m}$ and (inverse) damping time $\alpha_1^{\ell m}$ as well as the difference $\alpha_{21}^{\ell m} = \alpha_2^{\ell m} - \alpha_1^{\ell m}$.

Y'	ℓ	m	Y'_0	$b_1^{Y'}$	$b_2^{Y'}$	$b_3^{Y'}$	$c_1^{Y'}$	$c_2^{Y'}$	$c_3^{Y'}$
$\omega_1^{\ell m}$	2	2	0.373672	−1.5367	0.5503	...	−1.8700	0.9848	−0.10943
		1	0.373672	−0.79546	−0.1908	0.11460	−0.96337	−0.1495	0.19522
	3	3	0.599443	−1.84922	0.9294	−0.07613	−2.18719	1.4903	−0.3014
		2	0.599443	−0.251	−0.891	0.2706	−0.475	−0.911	+0.4609
		1	0.599443	−0.70941	−0.16975	0.08559	−0.82174	−0.16792	0.14524
	4	4	0.809178	−1.83156	0.9016	−0.06579	−2.17745	1.4753	−0.2961
		3	0.809178	−1.8397	0.9616	−0.11339	−2.0979	1.3701	−0.2675
		2	0.0941640	−1.44152	0.0542	0.39020	−1.43312	0.1167	0.32253
		1	0.0941640	1.1018882	−0.88643	−0.78266	1.1065495	−0.80961	−0.68905
	5	5	1.012295	−1.5659	0.5783	...	−1.9149	1.0668	−0.14663
$\alpha_1^{\ell m}$	2	2	0.08896	−1.90036	0.86200	0.0384893	−1.87933	0.88062	...
		1	0.0889623	−1.31253	−0.21033	0.52502	−1.30041	−0.1566	0.46204
	3	3	0.0927030	−1.8310	0.7568	0.0745	−1.8098	0.7926	0.0196
		2	0.0927030	−1.58277	0.2783	0.30503	−1.56797	0.3290	0.24155
		1	0.0927030	−1.2345	−0.30447	0.5446	−1.2263	−0.24223	0.47738
	4	4	0.0941640	−1.8662	0.8248	0.0417	−1.8514	0.8736	−0.0198
		3	0.0941640	−1.7177	0.5320	0.1860	−1.7065	0.5876	0.120939
		2	0.190170	−1.38840	...	0.39333	−1.37584	0.0600017	0.32632
		1	0.190170	1.0590157	−0.8650630	−0.75222	1.0654880	−0.7830051	−0.65814
	5	5	0.0948705	−1.8845	0.8585	0.0263	−1.8740	0.9147	−0.0384
$\alpha_{21}^{\ell m}$	2	2	0.184953	−1.89397	0.88126	0.0130256	−1.83901	0.84162	...
		1	0.184952	−1.1329	−0.3520	0.4924	−1.10334	−0.3037	0.4262
	3	3	0.188595	−1.8011	0.7046	0.0968	−1.7653	0.7176	0.0504
		2	0.188595	−1.5212	0.1563	0.3652	−1.4968	0.1968	0.3021
		1	0.188595	−1.035	−0.3816	0.4486	−1.023	−0.3170	0.3898
	4	4	0.190170	−1.8546	0.8041	0.0507	−1.8315	0.8391	−0.0051
		3	0.190170	−1.6860	0.4724	0.2139	−1.6684	0.5198	0.1508
		2	0.809178	−0.6644	−0.3357	0.1425	−0.8366	−0.2921	0.2254
		1	0.809178	−0.68647	−0.1852590	0.0934997	−0.77272	−0.1986852	0.1485093
	5	5	0.190947	−1.8780	0.8467	0.0315	−1.8619	0.8936	−0.0293

Table C.4: The fit parameters to analytically represent the time lag between the peak of the (ℓ, m) waveform multipole and the peak of the $(2, 2)$ mode, Eq. (5.34). The coefficients refer to the functional form of Eqs. (5.35)-(5.36).

ℓ	m	$\Delta t_{\ell m}^0$	$n_1^{\Delta t_{\ell m}}$	$n_2^{\Delta t_{\ell m}}$	$d_1^{\Delta t_{\ell m}}$	$d_2^{\Delta t_{\ell m}}$
2	1	11.7900	−3.764	6.9051	...	...
3	3	3.49238	−0.11298	5.0056	...	...
3	2	9.22687	−11.398	33.244	−8.1976	19.537
3	1	12.9338	...	−25.615	0.88803	16.292
4	4	5.28280	−8.4686	18.006	−6.7964	11.368
4	3	9.59669	−11.345	38.813	−7.5049	22.399
4	2	11.9225	−3.8284	−12.399	...	...
4	1	13.1116	−9.6225	38.451	−7.7998	32.405
5	5	6.561811	−12.198	40.327	−11.501	39.431

Table C.5: The fits of the NQC functioning points $\{\hat{A}^{\rm NQC}_{\ell m}, \dot{\hat{A}}^{\rm NQC}_{\ell m}/\nu, \omega^{\rm NQC}_{\ell m}, \dot{\omega}^{\rm NQC}_{\ell m}\}$. The fits are given explicitly. The fits are done after the factorization defined in eq. (5.37). For all multipoles the factorization of the test-particle limit $Y^0_{\ell m}$ is highlighted explicitly in the third and fifth column of the table. The exception to this is the $(2,1)$ mode for which the test-particle behavior has not been factorized (see Sec. 5.3.6). $\hat{\hat{Y}}^{\rm NQC}_{\ell m}$ is fitted for all multipoles with at most quadratic polynomials or rational functions in ν.

		$\hat{A}^{\rm NQC}_{\ell m}/\lvert c_{\ell+\epsilon}(\nu)\rvert$		$\omega^{\rm NQC}_{\ell m}$	
2	2	0.294773	$\left(1-0.051898\nu+1.5886\nu^2\right)$	0.285588	$\left(1+0.92487\nu+1.7206\nu^2\right)$
2	1	$0.097671-0.0014424\nu$		$0.29622+0.048182\nu+0.37472\nu^2$	
3	3	0.0512928	$\left(1+0.09537\nu+3.7217\nu^2\right)$	0.476647	$\left(1+1.1008\nu+2.84\nu^2\right)$
3	2	0.0178914	$\left(\frac{1-6.1472\nu+11.435\nu^2}{1-3.6362\nu}\right)$	0.482635	$\left(\frac{1-9.1403\nu+21.399\nu^2}{1-8.8647\nu+20.185\nu^2}\right)$
3	1	0.00520201	$\left(1-4.9441\nu+8.9339\nu^2\right)$	0.485186	$\left(1-0.4421\nu-6.8184\nu^2\right)$
4	4	0.0144330	$\left(\frac{1-3.7335\nu-0.2895\nu^2}{1-3.7298\nu}\right)$	0.665507	$(1+0.95802\nu)$
4	3	0.00487784	$\left(\frac{1-5.7951\nu+12.833\nu^2}{1-3.2681\nu}\right)$	0.673274	$\left(\frac{1-9.2007\nu+22.161\nu^2}{1-9.026\nu+21.238\nu^2}\right)$
4	2	0.00161809	$\left(1-4.6975\nu+7.3437\nu^2\right)$	0.663076	$\left(1-0.086381\nu-8.5978\nu^2\right)$
4	1	0.00043987	$\left(\frac{1-8.4975\nu+27.31\nu^2}{1-1.2002\nu}\right)$	0.735051	$\left(\frac{1-8.3628\nu+20.529\nu^2}{1-7.4883\nu+18.695\nu^2}\right)$
5	5	0.00516272	$\left(1-0.38892\nu+6.7413\nu^2\right)$	0.855016	$\left(\frac{1-2.8461\nu-3.7163\nu^2}{1-3.8378\nu}\right)$

		$\dot{\hat{A}}^{\rm NQC}_{\ell m}/\nu$		$\dot{\omega}^{\rm NQC}_{\ell m}$	
2	2	-0.00119366	$\left(1+3.0125\nu-2.1792\nu^2\right)$	0.00628027	$\left(1+2.5374\nu+3.9341\nu^2\right)$
2	1	$(-0.0011119+0.0042824\nu)\,/\,(1-3.0565\nu)$		$0.0020157+0.049725\nu$	
3	3	-0.00039568	$\left(1+1.0985\nu-13.458\nu^2\right)$	0.0110394	$\left(1+2.1358\nu+4.1544\nu^2\right)$
3	2	-0.00026840	$\left(\frac{1-8.4869\nu+18.736\nu^2}{1-5.7457\nu+7.9581\nu^2}\right)$	0.0141756	$\left(\frac{1-10.831\nu+37.969\nu^2}{1-12.954\nu+51.155\nu^2}\right)$
3	1	-0.00043382	$\left(\frac{1-9.0479\nu+23.054\nu^2}{1+88.626\nu^2}\right)$	0.0673118	$\left(\frac{1+13.318\nu}{1+70.552\nu}\right)$
4	4	-0.00015129	$\left(1-2.206\nu+2.0191\nu^2\right)$	0.0147878	$\left(\frac{1-3.4516\nu+4.8703\nu^2}{1-5.7616\nu+11.286\nu^2}\right)$
4	3	-0.00008468	$\left(1-4.1848\nu+4.2192\nu^2\right)$	0.0172836	$\left(\frac{1-19.234\nu+105.04\nu^2}{1-19.837\nu+107.76\nu^2}\right)$
4	2	-0.00004223	$\left(\frac{1-5.1172\nu+5.4408\nu^2}{+6.1593\nu}\right)$	0.0213781	$\left(\frac{1-6.2629\nu+10.1\nu^2}{1-8.4232\nu+21.204\nu^2}\right)$
4	1	-0.00001827	$\left(1-2.8242\nu-3.1871\nu^2\right)$	0.0739078	$\left(1+0.99186\nu-19.435\nu^2\right)$
5	5	-0.00006580	$(1-1.8592\nu)$	0.0178326	$(1+2.4606\nu)$

Appendix D

`TEOBiResumS_SM`, additional fit information

Table D.1: Explicit coefficients and their errors for the merger frequency and amplitude fits of the $(2,2)$ mode. The analytic template of the fit is defined in Eqs. (6.19) – (6.22).

$\omega_{22}^{\rm mrg_0}$	$=$	0.273356		$\hat{A}_{22}^{\rm mrg=0}$	$=$	1.44959	
a_1^{ω}	$=$	0.84074	± 0.014341	$a_1^{\hat{A}}$	$=$	-0.041285	± 0.0078878
a_2^{ω}	$=$	1.6976	± 0.075488	$a_2^{\hat{A}}$	$=$	1.5971	± 0.041521
$b_1^{\omega_{m_1=m_2}}$	$=$	-0.42311	± 0.088583	$b_1^{\hat{A}_{m_1=m_2}}$	$=$	-0.74124	± 0.016178
$b_2^{\omega_{m_1=m_2}}$	$=$	-0.066699	± 0.042978	$b_2^{\hat{A}_{m_1=m_2}}$	$=$	-0.088705	± 0.0081611
$b_3^{\omega_{m_1=m_2}}$	$=$	-0.83053	± 0.084516	$b_3^{\hat{A}_{m_1=m_2}}$	$=$	-1.0939	± 0.015318
c_{11}^{ω}	$=$	0.15873	± 0.1103	$c_{11}^{\hat{A}}$	$=$	0.44467	± 0.037352
c_{12}^{ω}	$=$	-0.43361	± 0.2393	$c_{12}^{\hat{A}}$	$=$	-0.32543	± 0.081211
c_{21}^{ω}	$=$	0.60589	± 0.076215	$c_{31}^{\hat{A}}$	$=$	0.45828	± 0.066062
c_{22}^{ω}	$=$	-0.71383	± 0.096828	$c_{32}^{\hat{A}}$	$=$	-0.21245	± 0.080254

Table D.2: Explicit coefficients of the fits of $\hat{A}_{21}^{\rm peak}$, $\omega_{21}^{\rm peak}$ and Δt_{21}.

$\hat{A}_{21}^{\rm peak_0}$	=	0.523878	$\omega_{21}^{\rm peak_0}$	=	0.290643	Δt_{21}^{0}	=	11.75925
$a_1^{\hat{A}_{21}}$	=	3.33622	$a_1^{\omega_{21}}$	=	−0.563075	$\Delta t_{21}^{\nu=1/4}$	=	6.6264
$a_2^{\hat{A}_{21}}$	=	3.47085	$a_2^{\omega_{21}}$	=	3.28677	$a_1^{\Delta t_{21}}$	=	−2.0728
$a_3^{\hat{A}_{21}}$	=	4.76236						
$b_1^{\hat{A}_{21}^0}$	=	−0.428186	$b_1^{\omega_{21}^0}$	=	0.179639	$b_1^{\Delta t_{21}^0}$	=	0.0472289
$b_2^{\hat{A}_{21}^0}$	=	−0.335659	$b_2^{\omega_{21}^0}$	=	−0.302122	$b_2^{\Delta t_{21}^0}$	=	0.115583
$b_3^{\hat{A}_{21}^0}$	=	0.828923						
$c_{11}^{\hat{A}_{21}}$	=	0.891139	$c_1^{\omega_{21}}$	=	−1.20684	$c_{11}^{\Delta t_{21}}$	=	−1976.13
$c_{12}^{\hat{A}_{21}}$	=	−5.191702	$c_2^{\omega_{21}}$	=	0.425645	$c_{12}^{\Delta t_{21}}$	=	3719.88
$c_{21}^{\hat{A}_{21}}$	=	3.480139				$c_{21}^{\Delta t_{21}}$	=	−2545.41
$c_{22}^{\hat{A}_{21}}$	=	10.237782				$c_{22}^{\Delta t_{21}}$	=	5277.62
$c_{31}^{\hat{A}_{21}}$	=	−13.867475						
$c_{32}^{\hat{A}_{21}}$	=	10.525510						

Table D.3: Explicit coefficients of the fits of $\hat{A}_{33}^{\rm peak}$, $\omega_{33}^{\rm peak}$ and Δt_{33}.

$\hat{A}_{33}^{\rm peak_0}$	=	0.566017	$\omega_{33}^{\rm peak_0}$	=	0.454128	Δt_{33}^{0}	=	3.42593
$a_1^{\hat{A}_{33}}$	=	−0.22523	$a_1^{\omega_{33}}$	=	1.08224	$a_1^{\Delta t_{33}}$	=	0.183349
$a_2^{\hat{A}_{33}}$	=	3.0569	$a_2^{\omega_{33}}$	=	2.59333	$a_2^{\Delta t_{33}}$	=	4.22361
$a_3^{\hat{A}_{33}}$	=	−0.396851						
$b_1^{\hat{A}_{33}^0}$	=	0.100069	$b_1^{\omega_{33}^0}$	=	−0.406161	$b_1^{\Delta t_{33}^0}$	=	−0.49791
$b_2^{\hat{A}_{33}^0}$	=	−0.455859	$b_2^{\omega_{33}^0}$	=	−0.0647944	$b_2^{\Delta t_{33}^0}$	=	−0.18754
			$b_3^{\omega_{33}^0}$	=	−0.748126	$b_3^{\Delta t_{33}^0}$	=	−1.07291
$c_{11}^{\hat{A}_{33}}$	=	−0.401156	$c_{11}^{\omega_{33}}$	=	0.85777	$c_{11}^{\Delta t_{33}}$	=	−1.9478
$c_{12}^{\hat{A}_{33}}$	=	−0.141551	$c_{12}^{\omega_{33}}$	=	−0.70066	$c_{12}^{\Delta t_{33}}$	=	13.9828
$c_{13}^{\hat{A}_{33}}$	=	−15.4949	$c_{31}^{\omega_{33}}$	=	2.97025	$c_{21}^{\Delta t_{33}}$	=	1.25084
$c_{21}^{\hat{A}_{33}}$	=	1.84962	$c_{32}^{\omega_{33}}$	=	−3.96242	$c_{22}^{\Delta t_{33}}$	=	−3.41811
$c_{22}^{\hat{A}_{33}}$	=	−2.03512				$c_{31}^{\Delta t_{33}}$	=	−1043.15
$c_{23}^{\hat{A}_{33}}$	=	−4.92334				$c_{32}^{\Delta t_{33}}$	=	1033.85

Table D.4: Explicit coefficients of the fits of $\hat{A}_{32}^{\rm peak}$ and $\omega_{32}^{\rm peak}$.

$\hat{A}_{32}^{\rm peak_0}$	$=$	0.199019	$\omega_{32}^{\rm peak_0}$	$=$	0.451607
$a_1^{\hat{A}_{32}}$	$=$	-6.06831	$a_1^{\omega_{32}}$	$=$	-9.13525
$a_2^{\hat{A}_{32}}$	$=$	10.7505	$a_2^{\omega_{32}}$	$=$	21.488
$a_3^{\hat{A}_{32}}$	$=$	-3.68883	$a_3^{\omega_{32}}$	$=$	-8.81384
			$a_4^{\omega_{32}}$	$=$	20.0595
$b_1^{\hat{A}^0_{32}}$	$=$	-0.258378	$b_1^{\omega_{32}^{\nu=1/4}}$	$=$	-0.458126
$b_2^{\hat{A}^0_{32}}$	$=$	0.679163	$b_2^{\omega_{32}^{\nu=1/4}}$	$=$	0.0474616
			$b_3^{\omega_{32}^{\nu=1/4}}$	$=$	-0.486049
$c_{11}^{\hat{A}_{32}}$	$=$	4.36263	$c_{11}^{\omega_{32}}$	$=$	3.25319
$c_{12}^{\hat{A}_{32}}$	$=$	-12.5897	$c_{12}^{\omega_{32}}$	$=$	0.535555
$c_{13}^{\hat{A}_{32}}$	$=$	-7.73233	$c_{13}^{\omega_{32}}$	$=$	-8.07905
$c_{14}^{\hat{A}_{32}}$	$=$	16.2082	$c_{21}^{\omega_{32}}$	$=$	1.00066
$c_{21}^{\hat{A}_{32}}$	$=$	3.04724	$c_{22}^{\omega_{32}}$	$=$	-1.1333
$c_{22}^{\hat{A}_{32}}$	$=$	46.5711	$c_{23}^{\omega_{32}}$	$=$	0.601572
$c_{23}^{\hat{A}_{32}}$	$=$	2.10475			
$c_{24}^{\hat{A}_{32}}$	$=$	56.9136			

Table D.5: Explicit coefficients of Δt_{32}.

Δt_{32}^0	$=$	9.16665	$c_{11}^{\Delta t_{32}^{\nu}}$	$=$	-0.037634	$c_{11}^{\Delta t_{32}^{X_{12}}}$	$=$	2.497188
$a_1^{\Delta t_{32}}$	$=$	-11.3497	$c_{12}^{\Delta t_{32}^{\nu}}$	$=$	12.456704	$c_{12}^{\Delta t_{32}^{X_{12}}}$	$=$	-7.532596
$a_2^{\Delta t_{32}}$	$=$	32.9144	$c_{13}^{\Delta t_{32}^{\nu}}$	$=$	2.670868	$c_{13}^{\Delta t_{32}^{X_{12}}}$	$=$	4.645986
$a_3^{\Delta t_{32}}$	$=$	-8.36579	$c_{14}^{\Delta t_{32}^{\nu}}$	$=$	-12.255859	$c_{14}^{\Delta t_{32}^{X_{12}}}$	$=$	-3.652524
$a_4^{\Delta t_{32}}$	$=$	20.1017	$c_{15}^{\Delta t_{32}^{\nu}}$	$=$	37.843505	$c_{15}^{\Delta t_{32}^{X_{12}}}$	$=$	3.398687
$b_1^{\Delta t^0_{32}}$	$=$	-0.34161	$c_{21}^{\Delta t_{32}^{\nu}}$	$=$	-25.058475	$c_{21}^{\Delta t_{32}^{X_{12}}}$	$=$	7.054185
$b_2^{\Delta t^0_{32}}$	$=$	-0.46107	$c_{22}^{\Delta t_{32}^{\nu}}$	$=$	449.470722	$c_{22}^{\Delta t_{32}^{X_{12}}}$	$=$	-12.260185
$b_3^{\Delta t^0_{32}}$	$=$	0.34744	$c_{23}^{\Delta t_{32}^{\nu}}$	$=$	-1413.508735	$c_{23}^{\Delta t_{32}^{X_{12}}}$	$=$	5.724802
$b_1^{\Delta t_{32}^{\nu=1/4}}$	$=$	0.15477	$c_{24}^{\Delta t_{32}^{\nu}}$	$=$	-11.852596	$c_{24}^{\Delta t_{32}^{X_{12}}}$	$=$	-3.242611
$b_2^{\Delta t_{32}^{\nu=1/4}}$	$=$	-0.755639	$c_{25}^{\Delta t_{32}^{\nu}}$	$=$	41.348059	$c_{25}^{\Delta t_{32}^{X_{12}}}$	$=$	2.714232
$b_3^{\Delta t_{32}^{\nu=1/4}}$	$=$	0.21816	$c_{31}^{\Delta t_{32}^{\nu}}$	$=$	-5.650710	$c_{31}^{\Delta t_{32}^{X_{12}}}$	$=$	2.614565
			$c_{32}^{\Delta t_{32}^{\nu}}$	$=$	-9.567484	$c_{32}^{\Delta t_{32}^{X_{12}}}$	$=$	-9.507583
			$c_{33}^{\Delta t_{32}^{\nu}}$	$=$	173.182999	$c_{33}^{\Delta t_{32}^{X_{12}}}$	$=$	7.321586
			$c_{34}^{\Delta t_{32}^{\nu}}$	$=$	-10.938605	$c_{34}^{\Delta t_{32}^{X_{12}}}$	$=$	-3.937568
			$c_{35}^{\Delta t_{32}^{\nu}}$	$=$	35.670656	$c_{35}^{\Delta t_{32}^{X_{12}}}$	$=$	4.584970

Table D.6: Explicit coefficients of the fits of $\hat{A}_{44}^{\rm peak}$, $\omega_{44}^{\rm peak}$ and Δt_{44}.

$\hat{A}_{44}^{\rm peak_0}$	$=$	0.276618	$\omega_{44}^{\rm peak_0}$	$=$	0.635659	Δt_{44}^{0}	$=$	5.27778
$a_1^{\hat{A}_{44}}$	$=$	-3.7082	$a_1^{\omega_{44}}$	$=$	-0.964614	$a_1^{\Delta t_{44}}$	$=$	-8.35574
$a_2^{\hat{A}_{44}}$	$=$	0.280906	$a_2^{\omega_{44}}$	$=$	-11.1828	$a_2^{\Delta t_{44}}$	$=$	17.5288
$a_3^{\hat{A}_{44}}$	$=$	-3.71276	$a_3^{\omega_{44}}$	$=$	-2.08471	$a_3^{\Delta t_{44}}$	$=$	-6.50259
			$a_4^{\omega_{44}}$	$=$	-6.89287	$a_4^{\Delta t_{44}}$	$=$	10.1575
$b_1^{\hat{A}^0_{44}}$	$=$	-0.316647	$b_1^{\omega^0_{44}}$	$=$	-0.445192	$b_1^{\Delta t^{\nu=1/4}_{44}}$	$=$	0.00159701
$b_2^{\hat{A}^0_{44}}$	$=$	-0.062423	$b_2^{\omega^0_{44}}$	$=$	-0.0985658	$b_2^{\Delta t^{\nu=1/4}_{44}}$	$=$	-1.14134
$b_3^{\hat{A}^0_{44}}$	$=$	-0.852876	$b_3^{\omega^0_{44}}$	$=$	-0.0307812			
			$b_4^{\omega^0_{44}}$	$=$	-0.801552			
$c_{11}^{\hat{A}_{44}}$	$=$	1.2436	$c_{11}^{\omega_{44}}$	$=$	-0.92902	$c_{11}^{\Delta t_4}$	$=$	-2.28656
$c_{12}^{\hat{A}_{44}}$	$=$	-1.60555	$c_{12}^{\omega_{44}}$	$=$	10.86310	$c_{12}^{\Delta t_{44}}$	$=$	1.66532
$c_{13}^{\hat{A}_{44}}$	$=$	-4.05685	$c_{13}^{\omega_{44}}$	$=$	-4.44930	$c_{21}^{\Delta t_{44}}$	$=$	-0.589331
$c_{14}^{\hat{A}_{44}}$	$=$	1.59143	$c_{14}^{\omega_{44}}$	$=$	3.01808	$c_{22}^{\Delta t_{44}}$	$=$	0.708784
$c_{21}^{\hat{A}_{44}}$	$=$	0.837418	$c_{22}^{\omega_{44}}$	$=$	1.62523			
$c_{22}^{\hat{A}_{44}}$	$=$	-2.93528	$c_{23}^{\omega_{44}}$	$=$	-7.70486			
$c_{23}^{\hat{A}_{44}}$	$=$	-11.5591	$c_{23}^{\omega_{44}}$	$=$	15.06517			
$c_{24}^{\hat{A}_{44}}$	$=$	34.1863	$c_{41}^{\omega_{44}}$	$=$	0.93790			
$c_{31}^{\hat{A}_{44}}$	$=$	0.950035	$c_{42}^{\omega_{44}}$	$=$	8.36038			
$c_{32}^{\hat{A}_{44}}$	$=$	7.95168	$c_{43}^{\omega_{44}}$	$=$	-4.85774			
$c_{33}^{\hat{A}_{44}}$	$=$	-1.26899	$c_{44}^{\omega_{44}}$	$=$	4.80446			
$c_{34}^{\hat{A}_{44}}$	$=$	-9.72147						

Table D.7: Explicit coefficients of the fits of $\hat{A}_{43}^{\rm peak}$, $\omega_{43}^{\rm peak}$ and Δt_{43}.

$\hat{A}_{43}^{\rm peak_0}$	=	0.0941570	$\omega_{43}^{\rm peak_0}$	=	0.636130	Δt_{43}^{0}	=	9.53705
$a_1^{\hat{A}_{43}}$	=	-5.74386	$a_1^{\omega_{43}}$	=	-9.02463	$a_1^{\Delta t_{43}}$	=	-11.2377
$a_2^{\hat{A}_{43}}$	=	12.6016	$a_2^{\omega_{43}}$	=	21.9802	$a_2^{\Delta t_{43}}$	=	38.3177
$a_3^{\hat{A}_{43}}$	=	-3.27435	$a_3^{\omega_{43}}$	=	-8.75892	$a_3^{\Delta t_{43}}$	=	-7.29734
$a_4^{\omega_{43}}$	=	20.5624				$a_4^{\Delta t_{43}}$	=	21.4267
$b_1^{\hat{A}^0_{43}}$	=	-0.02132252	$b_1^{\omega^0_{43}}$	=	-0.973324	$b_1^{\Delta t^0_{43}}$	=	-1.371832
$b_2^{\hat{A}^0_{43}}$	=	0.02592749	$b_2^{\omega^0_{43}}$	=	-0.109921	$b_2^{\Delta t^0_{43}}$	=	0.362375
$b_3^{\hat{A}^0_{43}}$	=	-0.826977	$b_3^{\omega^0_{43}}$	=	-1.08036	$b_3^{\Delta t^0_{43}}$	=	-1.0808402
$b_1^{\hat{A}^{\nu=1/4}_{43}}$	=	-0.00471163						
$b_2^{\hat{A}^{\nu=1/4}_{43}}$	=	0.0291409						
$b_3^{\hat{A}^{\nu=1/4}_{43}}$	=	-0.351031						
$c_{11}^{\hat{A}_{43}}$	=	0.249099	$c_{11}^{\omega_{43}}$	=	11.5224	$c_{11}^{\Delta t_{43}}$	=	3.215984
$c_{12}^{\hat{A}_{43}}$	=	-7.345984	$c_{12}^{\omega_{43}}$	=	-26.8421	$c_{12}^{\Delta t_{43}}$	=	42.133767
$c_{13}^{\hat{A}_{43}}$	=	108.923746	$c_{13}^{\omega_{43}}$	=	-2.84285	$c_{13}^{\Delta t_{43}}$	=	-9.440398
$c_{21}^{\hat{A}_{43}}$	=	-0.104206	$c_{21}^{\omega_{43}}$	=	3.51943	$c_{14}^{\Delta t_{43}}$	=	35.160776
$c_{22}^{\hat{A}_{43}}$	=	7.073534	$c_{22}^{\omega_{43}}$	=	-12.1688	$c_{21}^{\Delta t_{43}}$	=	1.133942
$c_{23}^{\hat{A}_{43}}$	=	-44.374738	$c_{23}^{\omega_{43}}$	=	-3.96385	$c_{22}^{\Delta t_{43}}$	=	-10.356311
$c_{31}^{\hat{A}_{43}}$	=	3.545134	$c_{31}^{\omega_{43}}$	=	5.53433	$c_{23}^{\Delta t_{43}}$	=	-6.701429
$c_{32}^{\hat{A}_{43}}$	=	1.341375	$c_{32}^{\omega_{43}}$	=	3.73988	$c_{24}^{\Delta t_{43}}$	=	10.726960
$c_{33}^{\hat{A}_{43}}$	=	-19.552083	$c_{33}^{\omega_{43}}$	=	4.219	$c_{31}^{\Delta t_{43}}$	=	-6.036207
						$c_{32}^{\Delta t_{43}}$	=	67.730599
						$c_{33}^{\Delta t_{43}}$	=	-3.082275
						$c_{34}^{\Delta t_{43}}$	=	11.547917

Table D.8: Explicit coefficients of the fits of $\hat{A}_{42}^{\rm peak}$, $\omega_{42}^{\rm peak}$ and Δt_{42}.

$\hat{A}_{42}^{\rm peak_0}$	$=$	0.0314364	$\omega_{42}^{\rm peak_0}$	$=$	0.617533	Δt_{42}^0	$=$	11.66665
$a_1^{\hat{A}_{42}}$	$=$	-4.56243	$a_1^{\omega_{42}}$	$=$	-7.44121	$a_1^{\Delta t_{42}}$	$=$	-9.844617
$a_2^{\hat{A}_{42}}$	$=$	6.4522	$a_2^{\omega_{42}}$	$=$	14.233	$a_2^{\Delta t_{42}}$	$=$	23.32294
			$a_3^{\omega_{42}}$	$=$	-6.61754	$a_3^{\Delta t_{42}}$	$=$	-5.760481
			$a_4^{\omega_{42}}$	$=$	11.4329	$a_4^{\Delta t_{42}}$	$=$	7.121793
$b_1^{\hat{A}_{42}^0}$	$=$	-1.63682	$b_1^{\omega_{42}^0}$	$=$	-2.37589	$b_1^{\Delta t_{42}^0}$	$=$	-1.3002045
$b_2^{\hat{A}_{42}^0}$	$=$	0.854459	$b_2^{\omega_{42}^0}$	$=$	1.97249	$b_2^{\Delta t_{42}^0}$	$=$	-0.9494348
$b_3^{\hat{A}_{42}^0}$	$=$	0.120537	$b_3^{\omega_{42}^0}$	$=$	-2.36107			
$b_4^{\hat{A}_{42}^0}$	$=$	-0.399718	$b_4^{\omega_{42}^0}$	$=$	2.16383			
$c_{11}^{\hat{A}_{42}}$	$=$	6.53943	$c_{11}^{\omega_{42}}$	$=$	10.1045	$c_{11}^{\Delta t_{42}}$	$=$	24.604717
$c_{12}^{\hat{A}_{42}}$	$=$	-4.00073	$c_{12}^{\omega_{42}}$	$=$	-6.94127	$c_{12}^{\Delta t_{42}}$	$=$	-0.808279
$c_{21}^{\hat{A}_{42}}$	$=$	-0.638688	$c_{13}^{\omega_{42}}$	$=$	12.1857	$c_{21}^{\Delta t_{42}}$	$=$	62.471781
$c_{22}^{\hat{A}_{42}}$	$=$	-3.94066	$c_{21}^{\omega_{42}}$	$=$	-1.62866	$c_{22}^{\Delta t_{42}}$	$=$	48.340961
$c_{31}^{\hat{A}_{42}}$	$=$	-0.482148	$c_{22}^{\omega_{42}}$	$=$	-2.6756			
$c_{32}^{\hat{A}_{42}}$	$=$	$7.668 \times 10^{-9} - 4$	$c_{23}^{\omega_{42}}$	$=$	-4.7536			
$c_{41}^{\hat{A}_{42}}$	$=$	1.25617	$c_{31}^{\omega_{42}}$	$=$	10.071			
$c_{42}^{\hat{A}_{42}}$	$=$	-4.04848	$c_{32}^{\omega_{42}}$	$=$	-6.7299			
			$c_{33}^{\omega_{43}}$	$=$	12.0377			
			$c_{41}^{\omega_{42}}$	$=$	-8.56139			
			$c_{42}^{\omega_{42}}$	$=$	-5.27136			
			$c_{43}^{\omega_{43}}$	$=$	5.10653			

Table D.9: Explicit coefficients of the fits of $\hat{A}_{55}^{\rm peak}$ and $\omega_{55}^{\rm peak}$

$\hat{A}_{55}^{\rm peak_0}$	$=$	0.00522697	$\omega_{55}^{\rm peak_0}$	$=$	0.818117
$a_1^{\hat{A}_{55}}$	$=$	-0.29628	$a_1^{\omega_{55}}$	$=$	-2.8918
$a_2^{\hat{A}_{55}}$	$=$	6.4207	$a_2^{\omega_{55}}$	$=$	-3.2012
			$a_3^{\omega_{55}}$	$=$	-3.773
$b_1^{\hat{A}_{55}^0}$	$=$	0.04360530	$b_1^{\omega_{55}^0}$	$=$	-0.332703
$b_2^{\hat{A}_{55}^0}$	$=$	-0.5769451	$b_2^{\omega_{55}^0}$	$=$	-0.675738
$c_{11}^{\hat{A}_{55}}$	$=$	5.720690	$c_{11}^{\omega_{55}}$	$=$	1.487294
$c_{12}^{\hat{A}_{55}}$	$=$	44.868515	$c_{12}^{\omega_{55}}$	$=$	-2.058537
$c_{21}^{\hat{A}_{55}}$	$=$	12.777090	$c_{21}^{\omega_{55}}$	$=$	1.454248
$c_{22}^{\hat{A}_{55}}$	$=$	-42.548247	$c_{22}^{\omega_{55}}$	$=$	-1.301284

Table D.10: The fitted coefficients of $(c_3^{A_{22}}, c_3^{\phi_{22}}, c_4^{\phi_{22}})$ as defined in Eq. (6.109).

Y	$= c_3^{A_{22}}$
$b_0^{c_3^A}(\nu)$	$= -0.5585 + 0.81196\nu$
$b_1^{c_3^A}(X_{12})$	$= -0.398576 + 0.1659421 X_{12}$
$b_2^{c_3^A}(X_{12})$	$= 0.099805 - 0.2560047 X_{12}$
$b_3^{c_3^A}(X_{12})$	$= 0.72125 - 0.9418946 X_{12}$
$b_4^{c_3^A}(X_{12})$	$= 0$

$Y = c_3^{\phi_{22}}$	$Y = c_4^{\phi_{22}}$
$b_0^{c_3^\phi}(\nu) = 3.8436 + 0.71565\nu$	$b_0^{c_4^\phi}(\nu) = 1.4736 + 2.2337\nu$
$b_1^{c_3^\phi}(X_{12}) = 5.12794 - 1.323643 X_{12}$	$b_1^{c_4^\phi}(X_{12}) = 8.26539 + 0.779683 X_{12}$
$b_2^{c_3^\phi}(X_{12}) = 9.9136 - 3.555007 X_{12}$	$b_2^{c_4^\phi}(X_{12}) = 14.2053 - 0.069638 X_{12}$
$b_3^{c_3^\phi}(X_{12}) = -4.1075 + 7.011267 X_{12}$	$b_3^{c_4^\phi}(X_{12}) = 0$
$b_4^{c_3^\phi}(X_{12}) = -31.5562 + 32.737824 X_{12}$	$b_4^{c_4^\phi}(X_{12}) = 0$

Table D.11: The explicit fits of $(c_3^{A_{33}}, c_3^{\phi_{33}}, c_4^{\phi_{33}})$. The reader should note that the fits of $(c_3^{\phi_{33}}, c_4^{\phi_{33}})$ are not used for any of the results given in the main text. Instead the corresponding fits of Ref. [133] are used. See Appendix 6.2.3 for a brief discussion.

$$\begin{aligned}
c_3^{A_{33}}(\nu, X_{12}, \tilde{a}_{12}) &= -0.5585 + 0.81196\nu + (-0.3502608 + 1.587606 X_{12} - 1.555325 X_{12}^2)\tilde{a}_{12} \\
c_3^{\phi_{33}}\left(\nu, X_{12}, \hat{S}\right) &= 3.0611 - 6.1597\nu + (-0.634377 + 5.983525 X_{12} - 5.8819 X_{12}^2)\hat{S} \\
c_4^{\phi_{33}}\left(\nu, X_{12}, \hat{S}\right) &= 1.789 - 5.6684\nu + (-3.877528 + 12.0433 X_{12} - 6.524665 X_{12}^2)\hat{S}
\end{aligned}$$

Table D.12: The explicit fits of $(c_3^{A_{44}}, c_3^{\phi_{44}}, c_4^{\phi_{44}})$. The reader should note that the fits of $(c_3^{\phi_{44}}, c_4^{\phi_{44}})$ are not used for any of the results given in the main text. Instead the corresponding fits of Paper II are used. See Sec. 6.2.3 for a brief discussion.

$$\begin{aligned}
c_3^{A_{44}}\left(\nu, \hat{S}\right) &= -0.41591 + 3.2099\nu - 9.614738\nu\,\hat{S} + 122.461125\nu\,\hat{S}^2 \\
c_3^{\phi_{44}}\left(\nu, X_{12}, \hat{S}\right) &= \frac{3.6662 - 30.072\nu + 76.371\nu^2}{1 - 3.5522\nu} + (-4.9184 + 7.911653 X_{12})\,\hat{S} \\
&\quad + (-15.6772 + 21.181688 X_{12})\,\hat{S}^2 \\
c_4^{\phi_{44}}\left(\nu, X_{12}, \hat{S}\right) &= 0.21595 + 23.216\nu + (-3.4207 + 11.746452 X_{12})\,\hat{S} \\
&\quad + (-15.5383 + 34.922883 X_{12})\,\hat{S}^2
\end{aligned}$$

Table D.13: The explicit fits of $(c_3^{A_{55}}, c_3^{\phi_{55}}, c_4^{\phi_{55}})$.

$$
\begin{aligned}
c_3^{A_{55}}\left(\nu, X_{12}, \tilde{a}_{12}\right) &= -7.063079 + 65.464944\nu + \left(-2.055335 - 0.585373 X_{12}\right)\tilde{a}_{12} \\
&\quad + \left(-12.631409 + 19.271346 X_{12}\right)\tilde{a}_{12}^2 \\
c_3^{\phi_{55}}\left(\nu, X_{12}, \hat{S}\right) &= -1.510167 + 30.569461\nu + \left(-2.687133 + 4.873750 X_{12}\right)\hat{S} \\
&\quad + \left(-14.629684 + 19.696954 X_{12}\right)\hat{S}^2 \\
c_4^{\phi_{55}}\left(\nu, X_{12}, \hat{S}\right) &= -1.383721 + 56.871881\nu + \left(+7.198729 - 3.870998 X_{12}\right)\hat{S} \\
&\quad + \left(-25.992190 + 36.882645 X_{12}\right)\hat{S}^2
\end{aligned}
$$

Table D.14: Coefficients of the $(2,2)$ quantities needed to calculate the NQC extraction point. From left to right the columns show $\left\{\hat{A}_{22}^{\rm NQC},\dot{A}_{22}^{\rm NQC},\omega_{22}^{\rm NQC},\dot{\omega}_{22}^{\rm NQC}\right\}$.

$\hat{A}_{22}^{\rm NQC}$			$\dot{A}_{22}^{\rm NQC}$		
$\hat{A}_{22}^{\rm NQC_0}$	=	0.294773	$\dot{A}_{22}^{\rm NQC_0}/\nu$	=	−0.000243654
$a_1^{\hat{A}_{22}^{\rm NQC}}$	=	−0.052697	$a_1^{\dot{A}_{22}^{\rm NQC}}$	=	2.86637
$a_2^{\hat{A}_{22}^{\rm NQC}}$	=	1.6088	$a_2^{\dot{A}_{22}^{\rm NQC}}$	=	−1.3667
$b_1^{\hat{A}_{22}^{\rm NQC_{m_1=m_2}}}$	=	−0.705226	$b_1^{\dot{A}_{22}^{\rm NQC_{m_1=m_2}}}$	=	0.02679530
$b_2^{\hat{A}_{22}^{\rm NQC_{m_1=m_2}}}$	=	−0.0953944	$b_2^{\dot{A}_{22}^{\rm NQC_{m_1=m_2}}}$	=	−0.0064409
$b_3^{\hat{A}_{22}^{\rm NQC_{m_1=m_2}}}$	=	−1.087280			
$c_{11}^{\hat{A}_{22}^{\rm NQC}}$	=	0.009335	$c_1^{\dot{A}_{22}^{\rm NQC}}$	=	−0.015395218
$c_{12}^{\hat{A}_{22}^{\rm NQC}}$	=	0.582869	$c_2^{\dot{A}_{22}^{\rm NQC}}$	=	0.008732589
$c_{31}^{\hat{A}_{22}^{\rm NQC}}$	=	−0.140747			
$c_{32}^{\hat{A}_{22}^{\rm NQC}}$	=	0.505807			

$\omega_{22}^{\rm NQC}$			$\dot{\omega}_{22}^{\rm NQC}$		
$\omega_{22}^{\rm NQC_0}$	=	0.285588	$\dot{\omega}_{22}^{\rm NQC_0}$	=	0.00628027
$a_1^{\omega_{22}^{\rm NQC}}$	=	0.91704	$a_1^{\dot{\omega}_{22}^{\rm NQC}}$	=	2.4351
$a_2^{\omega_{22}^{\rm NQC}}$	=	1.7912	$a_2^{\dot{\omega}_{22}^{\rm NQC}}$	=	4.4928
$b_1^{\omega_{22}^{\rm NQC_{m_1=m_2}}}$	=	−0.46550	$b_1^{\dot{\omega}_{22}^{\rm NQC_{m_1=m_2}}}$	=	0.001425242
$b_2^{\omega_{22}^{\rm NQC_{m_1=m_2}}}$	=	−0.078787	$b_2^{\dot{\omega}_{22}^{\rm NQC_{m_1=m_2}}}$	=	−0.00096073
$b_3^{\omega_{22}^{\rm NQC_{m_1=m_2}}}$	=	−0.852284			
$c_{11}^{\omega_{22}^{\rm NQC}}$	=	−0.338008	$c_1^{\dot{\omega}_{22}^{\rm NQC}}$	=	−0.000063766
$c_{12}^{\omega_{22}^{\rm NQC}}$	=	1.077812	$c_2^{\dot{\omega}_{22}^{\rm NQC}}$	=	0.000513197
$c_{21}^{\omega_{22}^{\rm NQC}}$	=	0.0555533			
$c_{22}^{\omega_{22}^{\rm NQC}}$	=	−0.312861			
$c_{31}^{\omega_{22}^{\rm NQC}}$	=	0.289185			
$c_{32}^{\omega_{22}^{\rm NQC}}$	=	−0.195838			

Table D.15: Explicit coefficients of the fit of $\dot{\hat{A}}_{44}^{\mathrm{NQC}}$.

$\dot{\hat{A}}_{44}^{\mathrm{NQC}_0} = -1.52614 \times 10^{-4}$

$a_1^{\dot{\hat{A}}_{44}^{\mathrm{NQC}}} = -7.63783$

$a_2^{\dot{\hat{A}}_{44}^{\mathrm{NQC}}} = 15.8089$

$a_3^{\dot{\hat{A}}_{44}^{\mathrm{NQC}}} = -5.88951$

$a_4^{\dot{\hat{A}}_{44}^{\mathrm{NQC}}} = 11.1555$

$b_1^{\dot{\hat{A}}_{44}^{\mathrm{NQC}}} = 3.76236 \times 10^{-5}$

$b_2^{\dot{\hat{A}}_{44}^{\mathrm{NQC}}} = -0.819379$

$c_{11}^{\dot{\hat{A}}_{44}^{\mathrm{NQC}}} = -6.45958 \times 10^{-6}$

$c_{12}^{\dot{\hat{A}}_{44}^{\mathrm{NQC}}} = -2.35613$

$c_{21}^{\dot{\hat{A}}_{44}^{\mathrm{NQC}}} = -298.678$

$c_{22}^{\dot{\hat{A}}_{44}^{\mathrm{NQC}}} = -1063.08$

Appendix E

Fits of (a_1, a_2) for `TEOBiResumS_SM`

All fits have been performed with `fitnlm` of `MATLAB`.

E.1 Non-spinning sector

a_1 in non-spinning sector is fitted against $X_{12}^2 = (1-4\nu)^2$ with the template

$$\begin{aligned} a_1 &= \frac{a_1^{q=1}}{1 + b_1^{a_1} X_{12}^2 + b_2^{a_1} X_{12}^4} \\ with \\ a_1^{q=1} &= 0.070974 \\ b_1^{a_1} &= 0.786350 \\ b_2^{a_1} &= -9.085105\ . \end{aligned} \tag{E.1}$$

$a_1^{q=1}$ is extracted from $q=1$.

a_2 in non-spinning sector is against $X_{12} = \sqrt{1-4\nu}$ with the template

$$a_2 = a_2^{q=1} \frac{1 + b_1^{a_2} X_{12} + b_2^{a_2} X_{12}^2}{1 + b_3^{a_2} X_{12}} \tag{E.2}$$

with

$$\begin{aligned} a_2^{q=1} &= 1.315133 \\ b_1^{a_2} &= -0.324849 \\ b_2^{a_2} &= -0.304506 \\ b_3^{a_2} &= -0.371614\ . \end{aligned}$$

$a_2^{q=1}$ is extracted from $q=1$.

Equal mass sector, $\nu > 0.2485$

a_1 in the equal mass case was fitted with the template:

$$a_1 = c_0^{a_1} \frac{1 + c_1^{a_1}\hat{S} + c_2^{a_1}\hat{S}^2 + c_3^{a_1}\hat{S}^3 + c_4^{a_1}\hat{S}^4}{1 + c_5^{a_1}\hat{S} + c_6^{a_1}\hat{S}^2 + c_7^{a_1}\hat{S}^3} \ . \tag{E.3}$$

with the fitted coefficients:

$$\begin{aligned} c_0^{a_1} &= \ \ 0.121187 & c_1^{a_1} &= \ \ -5.950663 \\ c_2^{a_1} &= \ \ 9.420324 & c_3^{a_1} &= -10.601339 \\ c_4^{a_1} &= 17.641549 & c_5^{a_1} &= \ \ -5.684777 \\ c_6^{a_1} &= 10.910451 & c_7^{a_1} &= \ \ -6.867377 \ . \end{aligned}$$

a_2 was fitted to the same template. The fitted coefficients are:

$$\begin{aligned} c_0^{a_2} &= \ \ 1.331703 & c_1^{a_2} &= -4.237724 \\ c_2^{a_2} &= \ \ 1.786023 & c_3^{a_2} &= \ \ 10.546205 \\ c_4^{a_2} &= -9.698233 & c_5^{a_2} &= -6.225823 \\ c_6^{a_2} &= \ \ 13.209381 & c_7^{a_2} &= -9.402513 \ . \end{aligned}$$

E.2 $1 < q < 4$ sector

In this sector the fit of a_1 differs in two ways from the previous. (i) The fit is factorized in a spinning part a_1^S and a non-spinning part a_1^0, and (ii) it is fitted against the spin variable $\hat{S}_n = \hat{S}/\left(m_1^2 + m_2^2\right)$. The full template is:

$$a_1 = a_1^0 \cdot a_1^S \ , \tag{E.4}$$

$$a_1^0 = d_0^{a_1} \frac{1 + d_1^{a_1}\nu + d_2^{a_1}\nu^3}{1 + d_3^{a_1}\nu} \ , \tag{E.5}$$

$$a_1^S = \frac{1 + d_4^{a_1}\hat{S}_n + d_5^{a_1}\hat{S}_n^2 + d_6^{a_1}\hat{S}_n^3 + d_7^{a_1}\hat{S}_n^4}{1 + d_8^{a_1}\hat{S}_n + d_9^{a_1}\hat{S}_n^2 + d_{10}^{a_1}\hat{S}_n^3} \ . \tag{E.6}$$

The fitted coefficients take the values of a_1^0 are:

$$\begin{aligned} d_0^{a_1} &= \ \ 0.26132647 & d_1^{a_1} &= -4.90302367 \\ d_2^{a_1} &= 20.67036124 & d_3^{a_1} &= -3.17109808 \ . \end{aligned}$$

Note these coefficients have been fitted to waveforms for which $\chi_2 = \pm 0.01$ was set and χ_1 was chosen such that $\hat{S}_n = 0$. This will be the case for all of the following non-spinning factor fits.

The fitted coefficients of a_1^S are:

$$\begin{aligned} d_4^{a_1} &= -3.082861 & d_5^{a_1} &= 2.169948 \\ d_6^{a_1} &= -0.636353 & d_7^{a_1} &= 0.741419 \\ d_8^{a_1} &= -2.843896 & d_9^{a_1} &= 2.709697 \\ d_{10}^{a_1} &= -0.832894 & & . \end{aligned}$$

a_2 is fitted in a factorized form as well. Additionally, it holds an explicit depends of a_2^S on ν.

$$a_2 = a_2^0 \cdot a_2^S \ , \tag{E.7}$$

$$a_2^0 = d_0^{a_2} \frac{1 + d_1^{a_2}\nu + d_2^{a_2}\nu^3}{1 + d_3^{a_2}\nu} \ , \tag{E.8}$$

$$a_2^S = \frac{1 + d_4^{a_2}\hat{S}_n + d_5^{a_2}\hat{S}_n^2 + d_6^{a_2}\hat{S}_n^3 + d_7^{a_2}\hat{S}_n^4}{1 + d_8^{a_2}\hat{S}_n + d_9^{a_2}\hat{S}_n^2 + d_{10}^{a_2}\hat{S}_n^3} \ , \tag{E.9}$$

$$d_i^{a_2} = d_{i,0}^{a_2}\left(1 + d_{i,1}^{a_2}\nu\right) \ , \ for \ i = 4, ..., 10 \ . \tag{E.10}$$

The fitted coefficients of a_2^0 are:

$$\begin{aligned} d_0^{a_2} &= \ \ 1.03364144 & d_1^{a_2} &= -3.46191440 \\ d_2^{a_2} &= -7.86652243 & d_3^{a_2} &= -3.96268815 \ . \end{aligned}$$

The fitted coefficients of a_2^S are:

$$\begin{aligned} d_{4,0}^{a_2} &= \ \ 0.036452 & d_{4,1}^{a_2} &= -64.360789 \\ d_{5,0}^{a_2} &= \ \ 0.275707 & d_{5,1}^{a_2} &= -34.573145 \\ d_{6,0}^{a_2} &= -0.113951 & d_{6,1}^{a_2} &= \ \ 0 \\ d_{7,0}^{a_2} &= -2.531304 & d_{7,1}^{a_2} &= -7.691661 \\ d_{8,0}^{a_2} &= -1.025824 & d_{8,1}^{a_2} &= \ \ 4.237539 \\ d_{9,0}^{a_2} &= \ \ 0.593579 & d_{9,1}^{a_2} &= \ \ 1.661809 \\ d_{10,0}^{a_2} &= -0.939736 & d_{10,1}^{a_2} &= -6.333442 \ . \end{aligned}$$

$d_{6,1}^{a_2}$ was set to 0 prior to the evaluation of the fit to improve the convergence of the fit.

E.3 $q \geq 4$ sector

a_1 for $q \geq 4$ has an additional new feature. The explicit ν dependence is fitted through $x_\nu = \nu - 0.16$. The full template is:

$$a_1 = a_1^0 \cdot a_1^S \ , \tag{E.11}$$

$$a_1^0 = e_0^{a_1} \frac{1 + e_1^{a_1}\nu + e_2^{a_1}\nu^3}{1 + e_3^{a_1}\nu} \ , \tag{E.12}$$

$$a_1^S = \frac{1 + e_4^{a_1}\hat{S}_n + e_5^{a_1}\hat{S}_n^2 + e_6^{a_1}\hat{S}_n^3 + e_7^{a_1}\hat{S}_n^4}{1 + e_8^{a_1}\hat{S}_n + e_9^{a_1}\hat{S}_n^2 + e_{10}^{a_1}\hat{S}_n^3} \ , \tag{E.13}$$

$$e_i^{a_1} = e_{i,0}^{a_1}\frac{1 + e_{i,1}^{a_1}x_\nu}{1 + e_{i,2}^{a_1}x_\nu}, \ for \ i = 4, ..., 10 \ . \tag{E.14}$$

The fitted a_1^0 coefficients are:

$$e_0^{a_1} = 0.341803 \qquad e_1^{a_1} = -1.350488$$
$$e_2^{a_1} = -6.353357 \qquad e_3^{a_1} = 2.216156 \ .$$

The coefficients of a_1^S are fitted in 2 steps. First, for $q = 4$ and second, an extrapolated fit from there. The coefficients $e_{i,0}^{a_1}$ have been fitted to $q = 4$:

$$e_{4,0}^{a_1} = -2.287721 \qquad e_{5,0}^{a_1} = -0.598451$$
$$e_{6,0}^{a_1} = 0.766069 \qquad e_{7,0}^{a_1} = 1.857169$$
$$e_{8,0}^{a_1} = -2.035234 \qquad e_{9,0}^{a_1} = 0.836427$$
$$e_{10,0}^{a_1} = 0.297476 \qquad .$$

The remaining coefficients model the extrapolation of the spin dependence to larger mass ratios and are:

$$e_{4,1}^{a_1} = 7.650946 \qquad e_{4,2}^{a_1} = 7.106992$$
$$e_{5,1}^{a_1} = -60.630748 \qquad e_{5,2}^{a_1} = -69.630357$$
$$e_{6,1}^{a_1} = 47.114247 \qquad e_{6,2}^{a_1} = 5.733002$$
$$e_{7,1}^{a_1} = -12.905707 \qquad e_{7,2}^{a_1} = 5.045688$$
$$e_{8,1}^{a_1} = 3.515869 \qquad e_{8,2}^{a_1} = 1.564146$$
$$e_{9,1}^{a_1} = 0.642864 \qquad e_{9,2}^{a_1} = 2.947890$$
$$e_{10,1}^{a_1} = 31.023038 \qquad e_{10,2}^{a_1} = 1.829543 \ .$$

a_2 is fitted similarly with the template:

$$a_2 = a_2^0 \cdot a_2^S \ , \tag{E.15}$$

$$a_2^0 = e_0^{a_2} \frac{1 + e_1^{a_2}\nu + e_2^{a_2}\nu^3}{1 + e_3^{a_2}\nu} \ , \tag{E.16}$$

$$a_2^S = \frac{1 + e_4^{a_2}\hat{S}_n + e_5^{a_2}\hat{S}_n^2 + e_6^{a_2}\hat{S}_n^3 + e_7^{a_2}\hat{S}_n^4}{1 + e_8^{a_2}\hat{S}_n + e_9^{a_2}\hat{S}_n^2} \ , \tag{E.17}$$

$$e_i^{a_2} = e_{i,0}^{a_2} \frac{1 + e_{i,1}^{a_2} x_\nu}{1 + e_{i,2}^{a_2} x_\nu}, \ for\ i = 4, ..., 9 \ . \tag{E.18}$$

The fitted a_2^0 coefficients are:

$$e_0^{a_2} = 0.929192 \qquad e_1^{a_2} = 1.334263$$
$$e_2^{a_2} = -26.389790 \qquad e_3^{a_2} = -1.289984 \ .$$

The coefficients of a_2^S are fitted in 2 steps as well. The coefficients $e_{i,0}^{a_2}$ have been fitted to $q = 4$:

$$e_{4,0}^{a_2} = -0.886561 \qquad e_{5,0}^{a_2} = -1.953955$$
$$e_{6,0}^{a_2} = 1.366537 \qquad e_{7,0}^{a_2} = 0.950212$$
$$e_{8,0}^{a_2} = -2.531000 \qquad e_{9,0}^{a_2} = 1.723991 \ .$$

The remaining coefficients model the extrapolation of the spin dependence to larger mass ratios and are:

$$e_{4,1}^{a_2} = 15.871482 \qquad e_{4,2}^{a_2} = 5.066190$$
$$e_{5,1}^{a_2} = 7.168498 \qquad e_{5,2}^{a_2} = 6.709490$$
$$e_{6,1}^{a_2} = 18.583382 \qquad e_{6,2}^{a_2} = 5.764512$$
$$e_{7,1}^{a_2} = -14.038564 \qquad e_{7,2}^{a_2} = -17.126231$$
$$e_{8,1}^{a_2} = 6.387917 \qquad e_{8,2}^{a_2} = 3.438456$$
$$e_{9,1}^{a_2} = 8.867098 \qquad e_{9,2}^{a_2} = 2.910938 \ .$$

Appendix F

Numerical Relativity waveform tables

This appendix is devoted to listing details of the NR catalog utilized in this work. The spinning sector of the *calibration* set is given in Tab. F.1 – F.4. The spinning sector of the *validation* set is given in Tab. F.5 – F.13. The non-spinning sector of both sets is given in Tab. F.14 – F.15. The columns of the tables show from left to right:

(i) The waveform number with respect to all the waveforms used in this work.

(ii) The ID with respect to the `SXS` catalog [7].

(iii) (q, χ_1, χ_2) mass-ratio and dimensionless spin parameters. In the case of non-spinning waveforms solely the mass-ratio q.

(iv) $(\nu, \hat{S})$ symmetric mass-ratio and the EOB spin-parameter $\hat{S}$. In the case of non-spinning waveforms solely the symmetric mass-ratio ν.

(iv) The number of orbits $N_{\rm orb}$ between the reference time and the peak of the $\ell = m = 2$ mode.

(v) The eccentricity in units 10^{-3}. As for many waveforms only an upper limit of the eccentricity was given we have chosen to use this upper limit as a conservative estimate of the eccentricity.

`SXS` (vi) $\delta\phi^{\rm NR}_{\rm mrg}$, the accumulated phase difference between the two highest levels of resolution available, from the reference time up until merger. Given in units of rad.

(vii) $\bar{F}_{\rm NR/NR}$, the NR/NR unfaithfulness, eq. (A.12), computed between the two highest level of resolution available. Given in units of %.

`BAM` (vi) $r_{\rm ext}$, the radius of waveform extraction chosen.

Table F.1: This table list all `SXS` waveforms with at least one non-zero spin and equal-mass in the *calibration* set.

#	id	(q, χ_1, χ_2)	$\left(\nu, \hat{S}\right)$	$N_{\rm orb}$	$\varepsilon[10^{-3}]$	$\delta\phi^{\rm NR}_{\rm mrg}$ [rad]	$\bar{F}_{\rm NR/NR}$ [%]
1	`BBH:0178`	$(1, +0.9942, +0.9942)$	$(0.25, +0.5)$	23.91	1.8000	$+0.0127$	0.0066
2	`BBH:0177`	$(1, +0.9893, +0.9893)$	$(0.25, +0.5)$	24.61	2.0000	-0.0162	0.0021
3	`BBH:0172`	$(1, +0.9794, +0.9794)$	$(0.25, +0.49)$	24.63	1.1276	-0.1560	0.0022
4	`BBH:0157`	$(1, +0.9496, +0.9496)$	$(0.25, +0.47)$	24.49	0.1483	-0.1286	0.0027
5	`BBH:0160`	$(1, +0.8997, +0.8997)$	$(0.25, +0.45)$	24.09	0.4442	-0.0865	0.0118
6	`BBH:0153`	$(1, +0.8498, +0.8498)$	$(0.25, +0.42)$	23.71	0.8694	..	..
7	`BBH:0230`	$(1, +0.8, +0.8)$	$(0.25, +0.4)$	23.35	0.1219	$+0.1060$	0.0016
8	`BBH:0228`	$(1, +0.6, +0.6)$	$(0.25, +0.3)$	22.05	0.3081	-0.2269	0.0080
9	`BBH:0150`	$(1, +0.2, +0.2)$	$(0.25, +0.1)$	18.48	0.2714	$+0.0664$	0.0027
10	`BBH:0149`	$(1, -0.2, -0.2)$	$(0.25, -0.1)$	15.65	0.1604	$+0.0649$	0.0037
11	`BBH:0148`	$(1, -0.44, -0.44)$	$(0.25, -0.22)$	13.94	0.0350	-0.1144	0.0013
12	`BBH:0215`	$(1, -0.6, -0.6)$	$(0.25, -0.3)$	24.96	0.1975	-0.2331	0.0040
13	`BBH:0154`	$(1, -0.8, -0.8)$	$(0.25, -0.4)$	12.61	0.6400	-0.0138	0.0036
14	`BBH:0212`	$(1, -0.8, -0.8)$	$(0.25, -0.4)$	28.15	0.2318	$+0.1907$	0.0032
15	`BBH:0159`	$(1, -0.8996, -0.8996)$	$(0.25, -0.45)$	12.33	0.8100	-0.0679	0.0069
16	`BBH:0156`	$(1, -0.949, -0.949)$	$(0.25, -0.47)$	11.22	0.7671	$+0.1668$	0.0055
17	`BBH:0232`	$(1, +0.8998, +0.5)$	$(0.25, +0.35)$	22.34	0.2839	-0.1349	0.0073
18	`BBH:0225`	$(1, +0.8, +0.4)$	$(0.25, +0.3)$	22.21	0.3625	-0.2321	0.0014
19	`BBH:0229`	$(1, +0.65, +0.25)$	$(0.25, +0.23)$	22.48	0.3121	-0.2027	0.0053
20	`BBH:0231`	$(1, +0.8998, 0)$	$(0.25, +0.22)$	22.47	0.0340	-0.2667	0.0046
21	`BBH:0227`	$(1, +0.6, 0)$	$(0.25, +0.15)$	22.45	0.3209	-0.2282	0.0052
22	`BBH:0005`	$(1, +0.5, 0)$	$(0.25, +0.12)$	29.61	0.2355	-0.1223	0.0592
23	`BBH:0219`	$(1, +0.8998, -0.5)$	$(0.25, +0.1)$	20.93	0.3404	-0.0954	0.0076
24	`BBH:0221`	$(1, +0.8, -0.4)$	$(0.25, +0.1)$	22.10	0.2855	-0.1602	0.0053
25	`BBH:0223`	$(1, +0.3, 0)$	$(0.25, +0.08)$	22.83	..	$+0.0017$	0.1520
26	`BBH:0213`	$(1, -0.8, +0.8)$	$(0.25, 0)$	20.90	0.1435	-0.1251	0.0040
27	`BBH:0211`	$(1, -0.8997, +0.8998)$	$(0.25, 0)$	21.58	0.2801	-0.2333	0.0027
28	`BBH:0217`	$(1, -0.6, +0.6)$	$(0.25, 0)$	21.28	0.1926	-0.1533	0.0048
29	`BBH:0218`	$(1, +0.5, -0.5)$	$(0.25, 0)$	28.21	0.0720	-0.1185	0.2160
30	`BBH:0222`	$(1, -0.3, 0)$	$(0.25, -0.08)$	23.17	0.0540	$+0.1129$	0.1598
31	`BBH:0224`	$(1, -0.8, +0.4)$	$(0.25, -0.1)$	21.65	0.2727	-0.1912	0.0020
32	`BBH:0226`	$(1, -0.8997, +0.5)$	$(0.25, -0.1)$	22.33	0.2809	-0.2728	0.0018
33	`BBH:0004`	$(1, -0.5, 0)$	$(0.25, -0.12)$	29.19	0.3802	-0.0769	0.0189
34	`BBH:0216`	$(1, -0.6, 0)$	$(0.25, -0.15)$	22.94	0.2766	-0.2353	0.0040
35	`BBH:0214`	$(1, -0.62, -0.25)$	$(0.25, -0.22)$	23.21	0.2089	-0.1904	0.0010
36	`BBH:0210`	$(1, -0.8997, 0)$	$(0.25, -0.22)$	23.71	0.1567	-0.0818	0.0024
37	`BBH:0220`	$(1, -0.8, -0.4)$	$(0.25, -0.3)$	24.67	0.1158	-0.1330	0.0040
38	`BBH:0209`	$(1, -0.8997, -0.5)$	$(0.25, -0.35)$	26.49	0.1539	$+0.1350$	0.0010

Table F.2: This table list all `SXS` waveforms with at least one non-zero spin and unequal-mass in the *calibration* set. Part I, listing waveforms with mass-ratios $q \leq 3$.

#	id	(q, χ_1, χ_2)	$\left(\nu, \hat{S}\right)$	$N_{\rm orb}$	$\varepsilon[10^{-3}]$	$\delta\phi^{\rm NR}_{\rm mrg}$ [rad]	$\bar{F}_{\rm NR/NR}$ [%]
39	`BBH:0306`	$(1.3, +0.9612, -0.899)$	$(0.2455, +0.14)$	11.3344	1.3506	-0.1093	0.0031
40	`BBH:0013`	$(1.5, +0.5, 0)$	$(0.24, +0.18)$	23.4984	0.1357	..	..
41	`BBH:0025`	$(1.5, +0.5, -0.5)$	$(0.24, +0.1)$	21.8575	0.0550	-0.1641	0.0278
42	`BBH:0019`	$(1.5, -0.5, +0.5)$	$(0.24, -0.1)$	19.9375	0.0491	$+0.0966$	0.0213
43	`BBH:0016`	$(1.5, -0.5, 0)$	$(0.24, -0.18)$	29.7855	0.4267	-0.0093	0.0009
44	`BBH:0257`	$(2, +0.8498, +0.8498)$	$(0.2222, +0.47)$	24.1193	0.1139	-0.0213	0.0024
45	`BBH:0256`	$(2, +0.6, +0.6)$	$(0.2222, +0.33)$	23.1240	0.0779	-0.0469	0.0068
46	`BBH:0253`	$(2, +0.5, +0.5)$	$(0.2222, +0.28)$	28.1387	0.0490	-0.0109	0.0040
47	`BBH:0251`	$(2, +0.3, +0.3)$	$(0.2222, +0.17)$	23.0196	0.0510	-0.0935	0.0037
48	`BBH:0240`	$(2, -0.3, -0.3)$	$(0.2222, -0.17)$	23.1078	0.0450	$+0.0636$	0.0614
49	`BBH:0238`	$(2, -0.5, -0.5)$	$(0.2222, -0.28)$	31.4030	0.0640	-0.0630	0.1110
50	`BBH:0235`	$(2, -0.6, -0.6)$	$(0.2222, -0.33)$	23.8374	0.0610	-0.0738	0.0048
51	`BBH:0234`	$(2, -0.85, -0.8496)$	$(0.2222, -0.47)$	27.2911	0.0374	$+0.0393$	0.0049
52	`BBH:0258`	$(2, +0.8713, -0.8495)$	$(0.2222, +0.3)$	21.2744	0.1817	-0.0824	0.0061
53	`BBH:0255`	$(2, +0.6, 0)$	$(0.2222, +0.27)$	22.3143	0.0379	$+0.0250$	0.0023
54	`BBH:0254`	$(2, +0.6, -0.6)$	$(0.2222, +0.2)$	22.0411	0.0522	$+0.0136$	0.0009
55	`BBH:0248`	$(2, +0.13, +0.8497)$	$(0.2222, +0.15)$	22.2757	0.0763	-0.1057	0.0030
56	`BBH:0250`	$(2, +0.3, 0)$	$(0.2222, +0.13)$	22.6909	0.0540	-0.0904	0.0045
57	`BBH:0249`	$(2, +0.3, -0.3)$	$(0.2222, +0.1)$	22.7597	0.0440	-0.0828	0.0057
58	`BBH:0252`	$(2, +0.37, -0.8494)$	$(0.2222, +0.07)$	21.6622	0.3509	$+0.2098$	0.0029
59	`BBH:0247`	$(2, 0, +0.6)$	$(0.2222, +0.07)$	21.6482	0.1320	-0.1635	0.0041
60	`BBH:0246`	$(2, 0, +0.3)$	$(0.2222, +0.03)$	21.4548	66.0000	$+0.3219$	0.0081
61	`BBH:0245`	$(2, 0, -0.3)$	$(0.2222, -0.03)$	22.1939	0.0400	$+0.0421$	0.0226
62	`BBH:0244`	$(2, 0, -0.6)$	$(0.2222, -0.07)$	22.0958	0.0336	-0.1980	0.0010
63	`BBH:0239`	$(2, -0.37, +0.8497)$	$(0.2222, -0.07)$	21.5943	0.0571	$+0.2464$	0.0005
64	`BBH:0242`	$(2, -0.3, +0.3)$	$(0.2222, -0.1)$	22.5985	0.0490	-0.0164	0.0260
65	`BBH:0241`	$(2, -0.3, 0)$	$(0.2222, -0.13)$	22.6575	0.0510	-0.0636	0.0129
66	`BBH:0243`	$(2, -0.13, -0.8495)$	$(0.2222, -0.15)$	22.2092	0.2245	-0.2301	0.0006
67	`BBH:0237`	$(2, -0.6, +0.6)$	$(0.2222, -0.2)$	21.1681	0.0370	$+0.1251$	0.0014
68	`BBH:0236`	$(2, -0.6, 0)$	$(0.2222, -0.27)$	22.0960	0.0948	$+0.0308$	0.0029
69	`BBH:0233`	$(2, -0.8713, +0.8497)$	$(0.2222, -0.3)$	20.5769	0.0961	$+0.1486$	0.0012
70	`BBH:0293`	$(3, +0.85, +0.8495)$	$(0.1875, +0.53)$	23.8799	0.1022	-0.1300	0.0046
71	`BBH:0291`	$(3, +0.6, +0.6)$	$(0.1875, +0.37)$	22.7550	0.0397	-0.1730	0.0010
72	`BBH:0286`	$(3, +0.5, +0.5)$	$(0.1875, +0.31)$	23.5058	0.0610	$+0.0367$	0.0022
73	`BBH:0283`	$(3, +0.3, +0.3)$	$(0.1875, +0.19)$	22.9428	0.0510	-0.0352	0.0032
74	`BBH:0270`	$(3, -0.3, -0.3)$	$(0.1875, -0.19)$	22.3406	0.0366	-0.0006	0.0038
75	`BBH:0267`	$(3, -0.5, -0.5)$	$(0.1875, -0.31)$	22.8962	0.0590	$+0.0338$	0.0058
76	`BBH:0264`	$(3, -0.6, -0.6)$	$(0.1875, -0.37)$	22.0717	0.2819	$+0.1772$	0.0024
77	`BBH:0260`	$(3, -0.85, -0.8494)$	$(0.1875, -0.53)$	24.5257	0.3523	$+0.2350$	0.0004
78	`BBH:0290`	$(3, +0.6, +0.4)$	$(0.1875, +0.36)$	22.5790	0.1140	-0.0164	0.0032
79	`BBH:0292`	$(3, +0.73, -0.8493)$	$(0.1875, +0.36)$	21.7414	0.1521	$+0.0590$	0.0009
80	`BBH:0289`	$(3, +0.6, 0)$	$(0.1875, +0.34)$	23.0495	0.2296	-0.2081	0.0005

Table F.3: This table list all `SXS` waveforms with at least one non-zero spin and unequal-mass in the *calibration* set. Part II, listing waveforms with mass-ratios $q \geq 3$.

#	id	(q, χ_1, χ_2)	$\left(\nu, \hat{S}\right)$	$N_{\rm orb}$	$\varepsilon[10^{-3}]$	$\delta\phi^{\rm NR}_{\rm mrg}$ [rad]	$\bar{F}_{\rm NR/NR}$ [%]
81	`BBH:0288`	$(3, +0.6, -0.4)$	$(0.1875, +0.31)$	21.9643	0.2097	-0.2395	0.0006
82	`BBH:0287`	$(3, +0.6, -0.6)$	$(0.1875, +0.3)$	22.7030	0.0718	$+0.0163$	0.0053
83	`BBH:0174`	$(3, +0.5, 0)$	$(0.1875, +0.28)$	34.3933	0.2952	$+0.2481$	0.1040
84	`BBH:0285`	$(3, +0.4, +0.6)$	$(0.1875, +0.26)$	22.0723	0.1220	-0.1738	0.0013
85	`BBH:0045`	$(3, +0.5, -0.5)$	$(0.1875, +0.25)$	20.6343	0.6618	..	..
86	`BBH:0280`	$(3, +0.27, +0.8495)$	$(0.1875, +0.2)$	22.1099	0.0790	-0.0860	0.0052
87	`BBH:0284`	$(3, +0.4, -0.6)$	$(0.1875, +0.19)$	21.9538	0.1151	$+0.0367$	0.0005
88	`BBH:0282`	$(3, +0.3, 0)$	$(0.1875, +0.17)$	22.9026	0.0580	-0.0210	0.0011
89	`BBH:0281`	$(3, +0.3, -0.3)$	$(0.1875, +0.15)$	22.7014	0.0480	-0.0379	0.0027
90	`BBH:0279`	$(3, +0.23, -0.8494)$	$(0.1875, +0.08)$	21.0503	0.1136	$+0.0198$	0.0010
91	`BBH:0278`	$(3, 0, +0.6)$	$(0.1875, +0.04)$	21.9491	0.1976	-0.2538	0.0015
92	`BBH:0277`	$(3, 0, +0.3)$	$(0.1875, +0.02)$	22.1864	0.0480	-0.0326	0.0029
93	`BBH:0276`	$(3, 0, -0.3)$	$(0.1875, -0.02)$	22.1734	..	-0.0130	0.0028
94	`BBH:0275`	$(3, 0, -0.6)$	$(0.1875, -0.04)$	21.4036	0.1062	$+0.0948$	0.0008
95	`BBH:0274`	$(3, -0.23, +0.8497)$	$(0.1875, -0.08)$	21.2795	0.2141	$+0.1244$	0.0018
96	`BBH:0272`	$(3, -0.3, +0.3)$	$(0.1875, -0.15)$	22.1789	0.0510	-0.0051	0.0035
97	`BBH:0271`	$(3, -0.3, 0)$	$(0.1875, -0.17)$	22.0431	0.0490	-0.0340	0.0014
98	`BBH:0269`	$(3, -0.4, +0.6)$	$(0.1875, -0.19)$	20.8371	0.1165	$+0.1110$	0.0017
99	`BBH:0273`	$(3, -0.27, -0.8493)$	$(0.1875, -0.2)$	21.5046	0.1867	$+0.1087$	0.0027
100	`BBH:0268`	$(3, -0.4, -0.6)$	$(0.1875, -0.26)$	21.4250	0.1555	$+0.0793$	0.0016
101	`BBH:0036`	$(3, -0.5, 0)$	$(0.1875, -0.28)$	31.4671	0.5330	-0.0150	0.0010
102	`BBH:0263`	$(3, -0.6, +0.6)$	$(0.1875, -0.3)$	20.5094	0.2052	$+0.0774$	0.0009
103	`BBH:0266`	$(3, -0.6, +0.4)$	$(0.1875, -0.31)$	21.2988	0.1705	-0.1800	0.0003
104	`BBH:0262`	$(3, -0.6, 0)$	$(0.1875, -0.34)$	21.0470	0.2031	-0.1718	0.0002
105	`BBH:0261`	$(3, -0.73, +0.8495)$	$(0.1875, -0.36)$	21.1482	1.1000	$+0.0594$	0.0016
106	`BBH:0265`	$(3, -0.6, -0.4)$	$(0.1875, -0.36)$	22.0040	0.0880	-0.2962	0.0008
107	`BBH:0110`	$(5, +0.5, 0)$	$(0.1388, +0.35)$	23.8397	0.4125	..	..
108	`BBH:0060`	$(5, -0.5, 0)$	$(0.1388, -0.35)$	22.8094	3.4344	..	..
109	`BBH:0208`	$(5, -0.9, 0)$	$(0.1389, -0.63)$	49.5728	0.5090	-2.0018	0.0385
110	`BBH:0202`	$(7, +0.6, 0)$	$(0.1094, +0.46)$	60.8335	0.0959	-0.0908	0.0048
111	`BBH:0203`	$(7, +0.4, 0)$	$(0.1094, +0.3)$	57.3589	0.0144	-1.3040	0.0095
112	`BBH:0205`	$(7, -0.4, 0)$	$(0.1094, -0.3)$	43.6451	0.0672	-0.8000	0.0040
113	`BBH:0207`	$(7, -0.6, 0)$	$(0.1094, -0.46)$	34.6589	0.1743	$+0.1340$	0.0011
114	`BBH:0065`	$(8, +0.5, 0)$	$(0.0987, +0.4)$	33.5938	3.7400	$+0.3529$	0.0189
115	`BBH:0064`	$(8, -0.5, 0)$	$(0.0987, -0.4)$	18.2981	0.4998	-0.3465	0.0338
116	`BBH:1375`	$(8, -0.9004, 0)$	$(0.0988, -0.71)$	26.6545	1.1129	..	..

Table F.4: This table list the 16 `BAM` waveforms with at least one non-zero spin of the *calibration* set.

#	id	(q, χ_1, χ_2)	$\left(\nu, \hat{S}\right)$	$N_{\rm orb}$	$\varepsilon[10^{-3}]$	$r_{\rm ext}$
117	`BAM`	$(2, +0.75, +0.75)$	$(0.2222, +0.42)$	12.2855	4.4000	95
118	`BAM`	$(2, +0.5, +0.5)$	$(0.2222, +0.28)$	13.9746	1.2000	100
119	`BAM`	$(3, -0.5, -0.5)$	$(0.1875, -0.31)$	10.5346	1.0000	100
120	`BAM`	$(4, +0.75, +0.75)$	$(0.16, +0.51)$	15.4571	4.0000	100
121	`BAM`	$(4, +0.5, +0.5)$	$(0.16, +0.34)$	13.5333	3.6000	100
122	`BAM`	$(4, +0.25, +0.25)$	$(0.16, +0.17)$	12.0059	2.4000	100
123	`BAM`	$(4, -0.25, -0.25)$	$(0.16, -0.17)$	10.0061	1.0000	100
124	`BAM`	$(4, -0.5, -0.5)$	$(0.16, -0.34)$	9.6086	1.0000	100
125	`BAM`	$(4, -0.75, -0.75)$	$(0.16, -0.51)$	8.3831	0.8000	100
126	`BAM`	$(8, +0.85, +0.85)$	$(0.0988, +0.68)$	17.7168	0.0000	100
127	`BAM`	$(8, -0.85, -0.85)$	$(0.0988, -0.68)$	4.2467	0.5000	100
128	`BAM`	$(8, +0.8, 0)$	$(0.0988, +0.63)$	11.7887	4.9000	100
129	`BAM`	$(18, +0.8, 0)$	$(0.0499, +0.72)$	11.7559	0.0000	100
130	`BAM`	$(18, +0.4, 0)$	$(0.0499, +0.36)$	11.6451	1.8000	100
131	`BAM`	$(18, -0.4, 0)$	$(0.0499, -0.36)$	7.6889	0.5000	100
132	`BAM`	$(18, -0.8, 0)$	$(0.0499, -0.72)$	7.4415	0.5000	100

Table F.5: This table shows the `SXS` waveforms with approximately equal-mass ($\nu > 0.2485$) and at least one non-zero spin in the *validation* set. Part I.

#	id	(q, χ_1, χ_2)	$\left(\nu, \hat{S}\right)$	$N_{\rm orb}$	$\varepsilon[10^{-3}]$	$\delta\phi^{\rm NR}_{\rm mrg}$ [rad]	$\bar{F}_{\rm NR/NR}$ [%]
133	`BBH:1124`	$(1, +0.998, +0.998)$	$(0.25, +0.5)$	24.8752	0.8701	..	..
134	`BBH:0158`	$(1, +0.9695, +0.9695)$	$(0.25, +0.48)$	23.9199	0.5376	-0.1377	0.0031
135	`BBH:0176`	$(1, +0.9596, +0.9596)$	$(0.25, +0.48)$	23.6711	0.7982	-0.1821	0.0065
136	`BBH:0155`	$(1, +0.8, +0.8)$	$(0.25, +0.4)$	23.3269	0.5051	-0.0479	0.0035
137	`BBH:1477`	$(1, +0.8, +0.8)$	$(0.25, +0.4)$	19.7056	0.0974	$+0.0882$	0.0037
138	`BBH:0328`	$(1, +0.8, +0.8)$	$(0.25, +0.4)$	19.6887	0.1123	$+0.0976$	0.0034
139	`BBH:2104`	$(1, +0.8, +0.8)$	$(0.25, +0.4)$	22.8590	0.2704	-0.0375	0.0033
140	`BBH:0175`	$(1, +0.75, +0.75)$	$(0.25, +0.37)$	22.4926	3.5386	$+0.3758$	0.0030
141	`BBH:0152`	$(1, +0.6, +0.6)$	$(0.25, +0.3)$	21.8026	0.4272	-0.0498	0.0047
142	`BBH:2102`	$(1, +0.6, +0.6)$	$(0.25, +0.3)$	22.0345	0.1629	-0.0236	0.0007
143	`BBH:1123`	$(1, +0.5, +0.5)$	$(0.25, +0.25)$	20.5204	0.6331	-0.0821	0.0033
144	`BBH:1122`	$(1, +0.44, +0.44)$	$(0.25, +0.22)$	20.8795	0.3727	-0.2461	0.0031
145	`BBH:1134`	$(1, -0.44, -0.44)$	$(0.25, -0.22)$	8.5884	0.1394	-0.0108	0.0025
146	`BBH:1135`	$(1, -0.44, -0.44)$	$(0.25, -0.22)$	9.5239	0.2957	$+0.0025$	0.0047
147	`BBH:1144`	$(1, -0.44, -0.44)$	$(0.25, -0.22)$	14.4435	8.2117	-0.0318	0.0054
148	`BBH:0151`	$(1, -0.6, -0.6)$	$(0.25, -0.3)$	14.1702	0.4800	-0.0316	0.0022
149	`BBH:2089`	$(1, -0.6, -0.6)$	$(0.25, -0.3)$	24.6948	0.1182	$+0.0192$	0.0072
150	`BBH:1475`	$(1, -0.8, -0.8)$	$(0.25, -0.4)$	14.7348	0.6336	$+0.3502$	0.0026
151	`BBH:2086`	$(1, -0.8, -0.8)$	$(0.25, -0.4)$	27.6225	0.2960	$+0.0299$	0.0033
152	`BBH:0329`	$(1, -0.8005, -0.8)$	$(0.25, -0.4)$	14.6608	0.4020	$+0.0586$	0.0020
153	`BBH:1137`	$(1, -0.9692, -0.9692)$	$(0.25, -0.48)$	11.4049	0.4313	$+0.0190$	0.0021
154	`BBH:1481`	$(1, +0.8, +0.73)$	$(0.25, +0.38)$	19.5871	0.0640	$+0.1565$	0.0032
155	`BBH:2106`	$(1, +0.8998, +0.5)$	$(0.25, +0.35)$	22.3954	0.0221	$+0.0589$	0.0064
156	`BBH:1497`	$(1, +0.68, +0.67)$	$(0.25, +0.34)$	19.5347	0.5408	$+0.2185$	0.0032
157	`BBH:1495`	$(1, +0.78, +0.53)$	$(0.25, +0.33)$	19.4806	0.5575	$+0.2610$	0.0058
158	`BBH:2099`	$(1, +0.8, +0.4)$	$(0.25, +0.3)$	21.9856	0.0788	$+0.0559$	0.0048
159	`BBH:0394`	$(1, +0.6, +0.4)$	$(0.25, +0.25)$	18.7477	0.0661	-0.0998	0.0023
160	`BBH:1496`	$(1.16, +0.8, +0.03)$	$(0.2487, +0.24)$	18.6343	0.1039	-0.1859	0.0008
161	`BBH:2103`	$(1, +0.65, +0.25)$	$(0.25, +0.23)$	21.6974	0.0965	$+0.0563$	0.0022
162	`BBH:2105`	$(1, +0.8997, 0)$	$(0.25, +0.22)$	21.6971	0.1954	-0.0191	0.0002
163	`BBH:1503`	$(1, +0.73, +0.14)$	$(0.25, +0.22)$	18.5877	0.7405	$+0.2193$	0.0028
164	`BBH:1501`	$(1, +0.75, +0.09)$	$(0.25, +0.21)$	18.5604	0.7164	$+0.3254$	0.0040
165	`BBH:0326`	$(1, +0.8, 0)$	$(0.25, +0.2)$	18.4268	0.3255	-0.0580	0.0056
166	`BBH:1507`	$(1, +0.5, +0.29)$	$(0.25, +0.2)$	18.6017	0.4355	$+0.2739$	0.0032
167	`BBH:1376`	$(1.01, +0.25, +0.5)$	$(0.25, +0.19)$	19.5992	0.5848	$+0.0299$	0.0035
168	`BBH:0544`	$(1.08, 0, +0.69)$	$(0.2496, +0.16)$	18.2157	0.1142	$+0.0369$	0.0021
169	`BBH:2101`	$(1, +0.6, 0)$	$(0.25, +0.15)$	21.7281	0.0724	$+0.0719$	0.0039
170	`BBH:2095`	$(1, +0.8, -0.4)$	$(0.25, +0.1)$	21.2800	0.1571	$+0.0545$	0.0006
171	`BBH:0418`	$(1, +0.4, 0)$	$(0.25, +0.1)$	17.8067	0.0830	$+0.1507$	0.0041
172	`BBH:2093`	$(1, +0.8997, -0.5)$	$(0.25, +0.1)$	21.0059	0.1374	$+0.0339$	0.0018
173	`BBH:2097`	$(1, +0.3, 0)$	$(0.25, +0.07)$	21.6499	0.0608	$+0.0935$	0.0014
174	`BBH:1502`	$(1, +0.7, -0.42)$	$(0.25, +0.07)$	17.7053	0.1067	$+0.1935$	0.0026
175	`BBH:0518`	$(1.1, -0.14, +0.43)$	$(0.2493, +0.06)$	17.5772	0.1262	-0.0530	0.0012

Table F.6: This table shows the `SXS` waveforms with approximately equal-mass ($\nu > 0.2485$) and at least one non-zero spin in the *validation* set. Part II.

#	id	(q, χ_1, χ_2)	$\left(\nu, \hat{S}\right)$	$N_{\rm orb}$	$\varepsilon[10^{-3}]$	$\delta\phi^{\rm NR}_{\rm mrg}$ [rad]	$\bar{F}_{\rm NR/NR}$ [%]
176	`BBH:1352`	$(1.15, +0.71, -0.67)$	$(0.2488, +0.06)$	14.1426	0.0830	-0.1244	0.0013
177	`BBH:1114`	$(1, +0.2, 0)$	$(0.25, +0.05)$	17.1729	0.0519	..	..
178	`BBH:0366`	$(1, +0.2, 0)$	$(0.25, +0.05)$	17.4831	0.1527	$+0.1471$	0.0027
179	`BBH:0376`	$(1, +0.6, -0.4)$	$(0.25, +0.05)$	17.4690	0.3620	-0.1507	0.0013
180	`BBH:0370`	$(1, +0.4, -0.2)$	$(0.25, +0.05)$	17.4752	0.0789	$+0.0254$	0.0006
181	`BBH:1506`	$(1, +0.46, -0.32)$	$(0.25, +0.03)$	17.4223	0.5729	$+0.2054$	0.0023
182	`BBH:1476`	$(1, -0.8, +0.8)$	$(0.25, 0)$	17.2858	0.1815	$+0.3550$	0.0045
183	`BBH:2085`	$(1, -0.8996, +0.8997)$	$(0.25, 0)$	20.9333	0.0826	$+0.0842$	0.0021
184	`BBH:2087`	$(1, -0.8, +0.8)$	$(0.25, 0)$	20.9499	0.0440	$+0.0571$	0.0007
185	`BBH:2091`	$(1, -0.6, +0.6)$	$(0.25, 0)$	21.3166	0.0446	$+0.0740$	0.0019
186	`BBH:0304`	$(1, -0.5, +0.5)$	$(0.25, 0)$	27.8687	0.0650	-0.0374	0.0014
187	`BBH:2092`	$(1, +0.5, -0.5)$	$(0.25, 0)$	27.1687	0.0477	$+0.0284$	0.0028
188	`BBH:0327`	$(1, -0.8, +0.8)$	$(0.25, 0)$	17.1166	0.1007	$+0.0517$	0.0042
189	`BBH:0330`	$(1, -0.8005, +0.8)$	$(0.25, 0)$	17.1110	0.1500	$+0.0995$	0.0005
190	`BBH:1513`	$(1.15, -0.1, 0)$	$(0.2488, -0.03)$	23.0477	0.1235	$+0.5110$	0.0051
191	`BBH:0459`	$(1, -0.4, +0.2)$	$(0.25, -0.05)$	16.8421	0.0650	-0.1320	0.0023
192	`BBH:0447`	$(1, -0.6, +0.4)$	$(0.25, -0.05)$	16.8472	0.2242	-0.1259	0.0054
193	`BBH:1351`	$(1.03, -0.23, 0)$	$(0.25, -0.06)$	12.8464	0.2221	$+0.1636$	0.0005
194	`BBH:2096`	$(1, -0.3, 0)$	$(0.25, -0.07)$	22.1277	0.2636	$+0.1078$	0.0005
195	`BBH:1509`	$(1, -0.24, -0.1)$	$(0.25, -0.09)$	16.6398	0.5219	$+0.1105$	0.0014
196	`BBH:2100`	$(1, -0.8996, +0.5)$	$(0.25, -0.1)$	21.6573	0.0715	$+0.0693$	0.0017
197	`BBH:2098`	$(1, -0.8, +0.4)$	$(0.25, -0.1)$	21.5719	0.1550	$+0.1126$	0.0044
198	`BBH:0415`	$(1, -0.4, 0)$	$(0.25, -0.1)$	16.5057	0.5098	-0.1718	0.0021
199	`BBH:1499`	$(1, -0.75, +0.34)$	$(0.25, -0.1)$	16.5204	0.4727	$+0.1788$	0.0021
200	`BBH:1498`	$(1.03, +0.22, -0.78)$	$(0.25, -0.13)$	16.3149	0.5239	$+0.0433$	0.0093
201	`BBH:2090`	$(1, -0.6, 0)$	$(0.25, -0.15)$	22.3993	0.0623	-0.0285	0.0036
202	`BBH:0436`	$(1, -0.4, -0.2)$	$(0.25, -0.15)$	16.1984	0.5864	-0.1123	0.0019
203	`BBH:0585`	$(1, -0.6, 0)$	$(0.25, -0.15)$	16.2423	0.3059	-0.0298	0.0009
204	`BBH:0325`	$(1, -0.8, 0)$	$(0.25, -0.2)$	15.9157	0.2440	$+0.0200$	0.0022
205	`BBH:2088`	$(1, -0.62, -0.25)$	$(0.25, -0.22)$	23.2528	0.0803	$+0.0274$	0.0016
206	`BBH:2084`	$(1, -0.8997, 0)$	$(0.25, -0.22)$	23.1546	0.1050	-0.0177	0.0031
207	`BBH:1500`	$(1, -0.77, -0.2)$	$(0.25, -0.24)$	15.6588	0.4126	$+0.1222$	0.0012
208	`BBH:0462`	$(1, -0.6, -0.4)$	$(0.25, -0.25)$	15.5965	0.5654	-0.1030	0.0025
209	`BBH:2094`	$(1, -0.8, -0.4)$	$(0.25, -0.3)$	24.6859	0.1082	-0.1382	0.0009
210	`BBH:1492`	$(1, -0.8, -0.47)$	$(0.25, -0.32)$	15.2146	0.7066	$+0.1782$	0.0009
211	`BBH:2083`	$(1, -0.8997, -0.5)$	$(0.25, -0.35)$	25.8994	0.1105	-0.1156	0.0067

Table F.7: This table shows the SXS waveforms with unequal-mass and at least one non-zero spin in the *validation* set. Part I.

#	id	(q, χ_1, χ_2)	$\left(\nu, \hat{S}\right)$	N_{orb}	$\varepsilon[10^{-3}]$	$\delta\phi^{\mathrm{NR}}_{\mathrm{mrg}}$ [rad]	$\bar{F}_{\mathrm{NR/NR}}$ [%]
212	BBH:0626	(1.17, −0.8277, +0.73)	(0.2484, −0.09)	10.9579	0.0979	−0.0496	0.0061
213	BBH:0311	(1.19, +0.42, +0.38)	(0.2482, +0.2)	16.8055	0.1275	+0.0568	0.0019
214	BBH:0312	(1.2, +0.4, −0.48)	(0.2479, +0.02)	13.5938	0.3678	−0.0487	0.0046
215	BBH:0523	(1.2, −0.2, −0.47)	(0.248, −0.16)	16.1744	0.1346	+0.1686	0.0012
216	BBH:1353	(1.22, +0.33, −0.44)	(0.2476, +0.01)	13.6731	0.1515	−0.2410	0.0013
217	BBH:0309	(1.22, +0.33, −0.44)	(0.2475, +0.01)	14.0816	29.3240	+0.3544	0.0103
218	BBH:0305	(1.22, +0.33, −0.44)	(0.2475, +0.01)	13.7709	0.8382	−0.2457	0.0015
219	BBH:0318	(1.22, +0.33, −0.44)	(0.2475, +0.01)	12.3868	0.1088	+0.0056	0.0018
220	BBH:0319	(1.22, +0.33, −0.44)	(0.2475, +0.01)	12.5774	9.5765	−0.1374	0.0096
221	BBH:0313	(1.22, +0.38, −0.52)	(0.2476, 0)	13.4606	0.3643	−0.0218	0.0035
222	BBH:0314	(1.23, +0.31, −0.46)	(0.2474, 0)	13.4131	0.1054	+0.0955	0.0021
223	BBH:0307	(1.23, +0.32, −0.58)	(0.2474, −0.02)	11.2821	0.4279	−0.1700	0.0016
224	BBH:0507	(1.25, +0.8, +0.4)	(0.247, +0.33)	19.2477	0.0492	−0.0446	0.0043
225	BBH:0409	(1.25, +0.4, +0.8)	(0.247, +0.28)	19.0811	0.5530	+0.4135	0.0058
226	BBH:1490	(1.25, +0.41, +0.76)	(0.247, +0.28)	19.0150	0.5153	−0.2690	0.0026
227	BBH:0525	(1.25, +0.8, −0.4)	(0.247, +0.17)	18.1613	0.0978	−0.0110	0.0008
228	BBH:0486	(1.25, 0, +0.8)	(0.247, +0.16)	18.3046	0.1302	+0.5147	0.0024
229	BBH:0559	(1.25, −0.2, +0.8)	(0.247, +0.1)	17.9270	0.0860	+0.5519	0.0035
230	BBH:0591	(1.25, 0, +0.4)	(0.247, +0.08)	17.7346	0.5561	+0.3277	0.0028
231	BBH:0475	(1.25, −0.4, +0.8)	(0.247, +0.03)	17.5411	0.2125	+0.6229	0.0036
232	BBH:0465	(1.25, +0.6, −0.8)	(0.247, +0.03)	17.2130	0.1104	+0.1557	0.0010
233	BBH:1223	(1.25, +0.38, −0.46)	(0.247, +0.03)	16.4422	0.6707	+0.4807	0.0034
234	BBH:0503	(1.25, −0.6, +0.8)	(0.247, −0.03)	17.8042	0.2713	+0.5742	0.0017
235	BBH:0464	(1.25, 0, −0.4)	(0.247, −0.08)	16.6696	0.1334	+0.0221	0.0013
236	BBH:0535	(1.25, +0.2, −0.8)	(0.247, −0.1)	16.4933	0.4965	+0.0183	0.0023
237	BBH:1487	(1.25, −0.8, +0.51)	(0.2468, −0.15)	16.4172	0.6620	+0.3609	0.0022
238	BBH:0398	(1.25, 0, −0.8)	(0.247, −0.16)	16.1057	0.1052	+0.0427	0.0036
239	BBH:0377	(1.25, −0.8004, +0.4)	(0.247, −0.17)	16.8055	0.0697	+0.1819	0.0017
240	BBH:0386	(1.25, −0.2, −0.8)	(0.247, −0.22)	15.7385	0.2341	−0.0317	0.0012
241	BBH:0466	(1.25, −0.8004, −0.4)	(0.247, −0.33)	15.6628	0.6737	+0.3469	0.0006
242	BBH:0438	(1.25, −0.6, −0.8)	(0.247, −0.34)	15.5757	0.1831	+0.4975	0.0021
243	BBH:0315	(1.27, +0.32, −0.56)	(0.2464, 0)	13.2377	0.4605	−0.0745	0.0011
244	BBH:1493	(1.28, 0, +0.8)	(0.2462, +0.16)	18.2944	0.5462	−0.1611	0.0029
245	BBH:1508	(1.28, +0.3, −0.07)	(0.2463, +0.08)	17.6905	0.1619	+0.3529	0.0057
246	BBH:1474	(1.28, +0.72, −0.8)	(0.2462, +0.07)	17.4878	0.2141	+0.0671	0.0025
247	BBH:1505	(1.33, −0.1, +0.55)	(0.245, +0.07)	17.8158	0.5458	+0.5601	0.0021
248	BBH:1471	(1.33, −0.78, −0.8)	(0.245, −0.4)	14.7453	0.3099	+0.5592	0.0009
249	BBH:1482	(1.39, −0.58, +0.8)	(0.2435, −0.06)	17.7124	0.1146	+0.5314	0.0016
250	BBH:0625	(1.4, −0.71, +0.22)	(0.243, −0.2)	14.5338	0.2969	+0.0946	0.0046
251	BBH:1473	(1.45, +0.7, +0.79)	(0.2416, +0.38)	20.0089	0.0789	+0.3752	0.0060
252	BBH:1511	(1.47, +0.03, −0.1)	(0.241, 0)	12.9084	0.1650	+0.1356	0.0024
253	BBH:1146	(1.5, +0.95, +0.9493)	(0.24, +0.5)	24.8558	0.2451	−0.1625	0.0446
254	BBH:0441	(1.5, +0.6, +0.8)	(0.24, +0.34)	19.5122	0.0978	−0.1389	0.0034
255	BBH:0385	(1.5, +0.8, 0)	(0.24, +0.29)	19.0432	0.0569	+0.1450	0.0016
256	BBH:0372	(1.5, +0.8, −0.4)	(0.24, +0.22)	18.5367	0.0340	−0.0514	0.0025

Table F.8: This table shows the `SXS` waveforms with unequal-mass and at least one non-zero spin in the *validation* set. Part II.

#	id	(q, χ_1, χ_2)	$\left(\nu, \hat{S}\right)$	$N_{\rm orb}$	$\varepsilon[10^{-3}]$	$\delta\phi^{\rm NR}_{\rm mrg}$ [rad]	$\bar{F}_{\rm NR/NR}$ [%]
257	`BBH:0009`	$(1.5, +0.5, 0)$	$(0.24, +0.18)$	16.5553	0.0950	..	..
258	`BBH:0361`	$(1.5, 0, +0.8)$	$(0.24, +0.13)$	18.2273	0.0828	-0.1191	0.0025
259	`BBH:0369`	$(1.5, +0.6, -0.8)$	$(0.24, +0.09)$	17.6312	0.6193	$+0.3635$	0.0026
260	`BBH:0440`	$(1.5, 0, +0.4)$	$(0.24, +0.06)$	17.7528	0.6448	$+0.2463$	0.0014
261	`BBH:0392`	$(1.5, -0.2, +0.8)$	$(0.24, +0.06)$	17.7915	0.1732	-0.1267	0.0024
262	`BBH:0579`	$(1.5, +0.4, -0.8)$	$(0.24, +0.02)$	17.1681	0.1731	$+0.2433$	0.0022
263	`BBH:0404`	$(1.5, 0, -0.8)$	$(0.24, -0.13)$	16.3364	0.2054	$+0.4135$	0.0032
264	`BBH:0012`	$(1.5, -0.5, 0)$	$(0.24, -0.18)$	18.3843	0.0596	-0.0689	0.0068
265	`BBH:0014`	$(1.5, -0.5, 0)$	$(0.24, -0.18)$	22.3801	0.0403	$+0.1597$	0.0561
266	`BBH:0101`	$(1.5, -0.5, 0)$	$(0.24, -0.18)$	29.5191	2.5157	..	..
267	`BBH:0437`	$(1.5, -0.2, -0.8)$	$(0.24, -0.2)$	15.9208	0.4417	$+0.5762$	0.0019
268	`BBH:0397`	$(1.5, -0.8005, -0.4)$	$(0.24, -0.35)$	15.1362	0.3270	$+0.3178$	0.0017
269	`BBH:0499`	$(1.52, +0.01, +0.74)$	$(0.2392, +0.12)$	18.1953	0.1718	$+0.1801$	0.0041
270	`BBH:1470`	$(1.52, -0.73, -0.79)$	$(0.2394, -0.39)$	14.8268	0.5134	$+0.0917$	0.0035
271	`BBH:1479`	$(1.55, -0.56, -0.8)$	$(0.2384, -0.33)$	15.1981	0.2308	$+0.4428$	0.0016
272	`BBH:1480`	$(1.55, -0.8, -0.3)$	$(0.2384, -0.34)$	15.2383	0.5352	$+0.4378$	0.0035
273	`BBH:0519`	$(1.57, +0.64, +0.41)$	$(0.2379, +0.3)$	19.2173	0.0873	-0.2563	0.0048
274	`BBH:1488`	$(1.6, -0.33, +0.75)$	$(0.237, -0.01)$	17.6966	0.1815	$+0.0664$	0.0061
275	`BBH:1491`	$(1.66, +0.2, -0.7)$	$(0.2346, -0.02)$	17.0597	0.2663	-0.0262	0.0020
276	`BBH:0529`	$(1.7, 0, +0.53)$	$(0.2333, +0.07)$	17.9701	0.0492	$+0.1170$	0.0035
277	`BBH:0510`	$(1.71, -0.02, -0.75)$	$(0.2328, -0.11)$	16.5467	0.2528	-0.2075	0.0044
278	`BBH:1465`	$(1.7, -0.79, +0.77)$	$(0.233, -0.2)$	16.3485	0.1282	-0.2375	0.0038
279	`BBH:0388`	$(1.75, +0.8, +0.4)$	$(0.2314, +0.38)$	19.7492	0.6847	-0.1235	0.0034
280	`BBH:0501`	$(1.75, +0.6, +0.8)$	$(0.2314, +0.35)$	19.8571	0.4487	-0.0852	0.0063
281	`BBH:0552`	$(1.75, +0.8, -0.4)$	$(0.2314, +0.27)$	19.0140	0.0930	-0.1956	0.0016
282	`BBH:0435`	$(1.75, +0.4, +0.8)$	$(0.2314, +0.27)$	19.3303	0.1007	-0.1591	0.0029
283	`BBH:0566`	$(1.75, +0.2, +0.8)$	$(0.2314, +0.19)$	18.7708	0.3194	-0.1644	0.0041
284	`BBH:0488`	$(1.75, +0.6, -0.8)$	$(0.2314, +0.14)$	18.6404	0.4740	-0.0395	0.0040
285	`BBH:0382`	$(1.75, 0, +0.8)$	$(0.2314, +0.1)$	18.2795	0.3617	-0.0908	0.0017
286	`BBH:0451`	$(1.75, 0, +0.4)$	$(0.2314, +0.05)$	17.8566	0.0829	$+0.0133$	0.0022
287	`BBH:0550`	$(1.75, -0.2, +0.8)$	$(0.2314, +0.02)$	17.7834	0.1276	-0.0566	0.0021
288	`BBH:0473`	$(1.75, +0.2, -0.8)$	$(0.2314, -0.02)$	17.1561	0.2007	-0.1397	0.0019
289	`BBH:0371`	$(1.75, 0, -0.4)$	$(0.2314, -0.05)$	16.9743	0.7776	-0.1956	0.0060
290	`BBH:0423`	$(1.75, 0, -0.8)$	$(0.2314, -0.1)$	16.5558	0.3514	-0.1116	0.0008
291	`BBH:0355`	$(1.75, -0.6, +0.8)$	$(0.2314, -0.14)$	16.8654	0.5512	-0.1105	0.0015
292	`BBH:0414`	$(1.75, -0.4, -0.8)$	$(0.2314, -0.27)$	15.6249	0.2925	-0.3370	0.0038
293	`BBH:0402`	$(1.75, -0.8004, +0.4)$	$(0.2314, -0.27)$	16.0475	0.4541	-0.1049	0.0017
294	`BBH:0512`	$(1.75, -0.6, -0.8)$	$(0.2314, -0.35)$	15.1873	0.3508	-0.2491	0.0006
295	`BBH:0454`	$(1.75, -0.8006, -0.4)$	$(0.2314, -0.38)$	15.1309	0.0889	-0.2238	0.0011
296	`BBH:1510`	$(1.78, +0.03, +0.29)$	$(0.2305, +0.05)$	13.8311	0.3867	-0.0845	0.0018
297	`BBH:0545`	$(1.79, 0, -0.8)$	$(0.23, -0.1)$	16.6161	0.2192	-0.1857	0.0026
298	`BBH:1469`	$(1.85, +0.8, +0.67)$	$(0.2277, +0.42)$	20.6503	0.0250	$+0.0057$	0.0042
299	`BBH:0403`	$(1.88, 0, -0.05)$	$(0.2266, 0)$	17.4511	0.0662	$+0.0157$	0.0048
300	`BBH:0555`	$(1.9, 0, +0.53)$	$(0.2263, +0.06)$	18.0411	0.1155	-0.0744	0.0008
301	`BBH:1466`	$(1.9, +0.7, -0.8)$	$(0.226, +0.2)$	18.6924	0.1602	-0.0823	0.0015
302	`BBH:0368`	$(1.93, -0.05, +0.25)$	$(0.2247, 0)$	17.6389	0.0945	-0.0165	0.0015

Table F.9: This table shows the `SXS` waveforms with unequal-mass and at least one non-zero spin in the *validation* set. Part III.

#	id	(q,χ_1,χ_2)	$\left(\nu,\hat{S}\right)$	$N_{\rm orb}$	$\varepsilon[10^{-3}]$	$\delta\phi^{\rm NR}_{\rm mrg}$ [rad]	$\bar{F}_{\rm NR/NR}$ [%]
303	BBH:0580	$(1.93,+0.02,-0.78)$	$(0.2248,-0.08)$	16.7867	0.2788	-0.0720	0.0020
304	BBH:0530	$(1.95,0,+0.54)$	$(0.2241,+0.07)$	18.1093	0.2104	-0.0596	0.0015
305	BBH:1478	$(1.97,+0.8,+0.13)$	$(0.2232,+0.37)$	19.8240	0.6195	-0.1597	0.0047
306	BBH:1504	$(1.98,+0.25,+0.08)$	$(0.223,+0.12)$	18.2656	0.3277	$+0.1266$	0.0013
307	BBH:0482	$(2,-0.02,-0.13)$	$(0.2225,-0.02)$	17.9754	0.3742	$+0.0126$	0.0040
308	BBH:2131	$(2,+0.85,+0.8498)$	$(0.2222,+0.47)$	23.1890	0.2857	-0.2845	0.0011
309	BBH:0333	$(2,+0.8,+0.8)$	$(0.2222,+0.44)$	20.6856	0.6366	$+0.3275$	0.0115
310	BBH:2130	$(2,+0.6,+0.6)$	$(0.2222,+0.33)$	22.4793	0.2069	-0.2371	0.0032
311	BBH:2127	$(2,+0.5,+0.5)$	$(0.2222,+0.28)$	26.6115	0.0704	$+0.3188$	0.0102
312	BBH:0574	$(2,+0.4,+0.4)$	$(0.2222,+0.22)$	18.9940	0.4547	-0.1836	0.0016
313	BBH:2125	$(2,+0.3,+0.3)$	$(0.2222,+0.17)$	21.5845	0.0832	-0.1004	0.0017
314	BBH:2114	$(2,-0.3,-0.3)$	$(0.2222,-0.17)$	21.9376	0.0506	$+0.1410$	0.0021
315	BBH:0584	$(2,-0.4,-0.4)$	$(0.2222,-0.22)$	16.1090	0.4072	-0.3253	0.0027
316	BBH:2112	$(2,-0.5,-0.5)$	$(0.2222,-0.28)$	30.2460	0.0950	-0.2919	0.0031
317	BBH:2109	$(2,-0.6,-0.6)$	$(0.2222,-0.33)$	23.8427	0.2134	$+0.5404$	0.0015
318	BBH:0334	$(2,-0.8006,-0.8)$	$(0.2222,-0.44)$	15.2440	0.4419	$+0.3034$	0.0033
319	BBH:2108	$(2,-0.85,-0.8496)$	$(0.2222,-0.47)$	26.7728	0.1132	$+0.2301$	0.0068
320	BBH:2132	$(2,+0.8713,-0.8496)$	$(0.2222,+0.3)$	21.2802	0.3036	-0.3758	0.0039
321	BBH:0410	$(2,+0.6,0)$	$(0.2222,+0.27)$	19.1585	0.0369	-0.0817	0.0047
322	BBH:2129	$(2,+0.6,0)$	$(0.2222,+0.27)$	21.6406	0.0930	-0.2838	0.0016
323	BBH:0513	$(2,+0.6,-0.4)$	$(0.2222,+0.22)$	18.7680	0.3862	-0.0469	0.0030
324	BBH:2128	$(2,+0.6,-0.6)$	$(0.2222,+0.2)$	21.9947	0.1265	$+0.0760$	0.0051
325	BBH:2122	$(2,+0.13,+0.8496)$	$(0.2222,+0.15)$	21.7293	0.4362	$+0.4124$	0.0022
326	BBH:0448	$(2,+0.4,-0.4)$	$(0.2222,+0.13)$	18.2305	0.1345	-0.2608	0.0031
327	BBH:0399	$(2,+0.2,+0.4)$	$(0.2222,+0.13)$	19.0278	0.1255	-0.0364	0.0013
328	BBH:2124	$(2,+0.3,0)$	$(0.2222,+0.13)$	21.9927	0.0943	$+0.1157$	0.0014
329	BBH:2123	$(2,+0.3,-0.3)$	$(0.2222,+0.1)$	22.0045	0.2970	$+0.0823$	0.0021
330	BBH:0332	$(2,0,+0.8)$	$(0.2222,+0.09)$	18.3471	0.4964	-0.0808	0.0021
331	BBH:0599	$(2,+0.2,0)$	$(0.2222,+0.09)$	18.7836	0.5784	$+0.0118$	0.0027
332	BBH:2126	$(2,+0.37,-0.8496)$	$(0.2222,+0.07)$	21.1569	0.1032	$+0.2130$	0.0031
333	BBH:2121	$(2,0,+0.6)$	$(0.2222,+0.07)$	21.6921	0.1523	-0.1070	0.0017
334	BBH:0554	$(2,+0.2,-0.4)$	$(0.2222,+0.04)$	17.7079	0.0975	-0.2369	0.0029
335	BBH:0407	$(2,0,+0.4)$	$(0.2222,+0.04)$	17.8992	0.7705	-0.1603	0.0020
336	BBH:2120	$(2,0,+0.3)$	$(0.2222,+0.03)$	21.4284	0.0624	-0.4640	0.0013
337	BBH:2119	$(2,0,-0.3)$	$(0.2222,-0.03)$	21.4883	0.1871	$+0.2279$	0.0034
338	BBH:0375	$(2,0,-0.4)$	$(0.2222,-0.04)$	17.1322	0.6961	-0.3064	0.0013
339	BBH:0354	$(2,-0.2,+0.4)$	$(0.2222,-0.04)$	17.3865	0.1174	-0.1990	0.0006
340	BBH:2118	$(2,0,-0.6)$	$(0.2222,-0.07)$	22.2002	0.1064	$+0.0998$	0.0025
341	BBH:2113	$(2,-0.37,+0.8497)$	$(0.2222,-0.07)$	21.1137	0.2335	$+0.0176$	0.0012
342	BBH:1112	$(2,-0.2,0)$	$(0.2222,-0.09)$	16.8761	0.0505	..	..
343	BBH:0331	$(2,0,-0.8)$	$(0.2222,-0.09)$	16.7509	0.1533	-0.0024	0.0075
344	BBH:2116	$(2,-0.3,+0.3)$	$(0.2222,-0.1)$	21.2824	0.0377	$+0.1631$	0.0027
345	BBH:2115	$(2,-0.3,0)$	$(0.2222,-0.13)$	21.8903	0.0598	-0.1213	0.0038
346	BBH:0412	$(2,-0.2,-0.4)$	$(0.2222,-0.13)$	16.6145	0.8352	-0.6655	0.0018
347	BBH:2117	$(2,-0.13,-0.8496)$	$(0.2222,-0.15)$	22.3465	0.1189	-0.4815	0.0057
348	BBH:2111	$(2,-0.6,+0.6)$	$(0.2222,-0.2)$	21.2223	0.0383	-0.2196	0.0017

Table F.10: This table shows the `SXS` waveforms with unequal-mass and at least one non-zero spin in the *validation* set. Part IV.

#	id	(q, χ_1, χ_2)	$\left(\nu, \hat{S}\right)$	$N_{\rm orb}$	$\varepsilon[10^{-3}]$	$\delta\phi^{\rm NR}_{\rm mrg}$ [rad]	$\bar{F}_{\rm NR/NR}$ [%]
349	`BBH:2110`	$(2, -0.6, 0)$	$(0.2222, -0.27)$	22.0617	0.0556	-0.2713	0.0021
350	`BBH:0461`	$(2, -0.6, 0)$	$(0.2222, -0.27)$	16.4199	0.1519	-0.0076	0.0018
351	`BBH:0335`	$(2, -0.8005, +0.8)$	$(0.2222, -0.27)$	16.2627	0.7099	$+0.0043$	0.0012
352	`BBH:2107`	$(2, -0.8712, +0.8497)$	$(0.2222, -0.3)$	21.1942	0.1130	-0.4347	0.0012
353	`BBH:0387`	$(2, -0.6, -0.4)$	$(0.2222, -0.31)$	16.0241	0.6065	-0.0152	0.0022
354	`BBH:1148`	$(2.04, +0.43, +0.5)$	$(0.2208, +0.25)$	55.1780	0.4326	$+0.0443$	0.0048
355	`BBH:1147`	$(2.04, +0.43, -0.51)$	$(0.2208, +0.14)$	52.0651	0.1895	-0.9533	0.0094
356	`BBH:1494`	$(2.2, -0.47, -0.39)$	$(0.2146, -0.26)$	15.9926	0.2721	-0.2255	0.0025
357	`BBH:1467`	$(2.23, -0.56, +0.8)$	$(0.2137, -0.2)$	17.2545	0.5618	-0.0638	0.0051
358	`BBH:1459`	$(2.26, +0.76, +0.8)$	$(0.2127, +0.44)$	21.5007	0.6864	-0.4414	0.0112
359	`BBH:1468`	$(2.27, +0.51, +0.8)$	$(0.2124, +0.32)$	20.6638	0.4641	-0.3303	0.0068
360	`BBH:0631`	$(2.33, -0.13, -0.36)$	$(0.2103, -0.1)$	14.5709	0.0931	$+0.0608$	0.0036
361	`BBH:1453`	$(2.35, +0.8002, -0.78)$	$(0.2093, +0.32)$	20.2689	0.0360	$+0.0496$	0.0048
362	`BBH:1472`	$(2.37, -0.8, -0.12)$	$(0.2088, -0.4)$	15.4798	0.0937	-0.3256	0.0022
363	`BBH:1512`	$(2.4, +0.24, 0)$	$(0.2078, +0.12)$	22.9613	0.4823	-0.6255	0.0045
364	`BBH:1454`	$(2.45, -0.8, -0.73)$	$(0.2057, -0.47)$	15.4826	0.1984	-0.0135	0.0030
365	`BBH:1462`	$(2.63, -0.8, +0.51)$	$(0.1996, -0.38)$	16.0754	0.5980	-0.1760	0.0021
366	`BBH:1461`	$(2.88, -0.45, -0.8)$	$(0.1912, -0.3)$	16.3080	0.6354	-0.2885	0.0044
367	`BBH:1484`	$(2.9, -0.56, +0.3)$	$(0.1906, -0.3)$	17.0362	0.5345	-0.2043	0.0019
368	`BBH:1387`	$(2.98, +0.47, -0.36)$	$(0.188, +0.24)$	22.2480	0.1628	-0.1619	0.0026
369	`BBH:1456`	$(3, +0.74, +0.7)$	$(0.1877, +0.46)$	21.3281	0.4467	-0.1343	0.0123
370	`BBH:2163`	$(3, +0.6, +0.6)$	$(0.1875, +0.37)$	25.5841	0.1962	-0.2297	0.0029
371	`BBH:2158`	$(3, +0.5, +0.5)$	$(0.1875, +0.31)$	25.1335	0.0968	-0.1136	0.0089
372	`BBH:0047`	$(3, +0.5, +0.5)$	$(0.1875, +0.31)$	22.2615	0.4925	..	..
373	`BBH:2155`	$(3, +0.3, +0.3)$	$(0.1875, +0.19)$	23.2456	0.0965	-0.0703	0.0048
374	`BBH:2142`	$(3, -0.3, -0.3)$	$(0.1875, -0.19)$	21.0437	0.2741	$+0.0580$	0.0009
375	`BBH:0046`	$(3, -0.5, -0.5)$	$(0.1875, -0.31)$	13.9670	0.2173	..	..
376	`BBH:2139`	$(3, -0.5, -0.5)$	$(0.1875, -0.31)$	21.9678	0.0430	$+0.1670$	0.0029
377	`BBH:2136`	$(3, -0.6, -0.6)$	$(0.1875, -0.37)$	22.1288	0.2589	$+0.2913$	0.0020
378	`BBH:1151`	$(3, +0.7, +0.6)$	$(0.1875, +0.43)$	20.4047	0.0527	-0.3950	0.0093
379	`BBH:1152`	$(3, +0.7, +0.6)$	$(0.1875, +0.43)$	20.4006	0.0721	-0.2896	0.0079
380	`BBH:1382`	$(3, +0.7, +0.6)$	$(0.1875, +0.43)$	20.8126	9.0994	-0.3278	0.0072
381	`BBH:1150`	$(3, +0.7, +0.6)$	$(0.1875, +0.43)$	20.4691	0.9730	-0.5133	0.0088
382	`BBH:2162`	$(3, +0.6, +0.4)$	$(0.1875, +0.36)$	25.3936	0.2401	$+0.1817$	0.0020
383	`BBH:2161`	$(3, +0.6, 0)$	$(0.1875, +0.34)$	25.3306	0.1645	$+0.0554$	0.0052
384	`BBH:2160`	$(3, +0.6, -0.4)$	$(0.1875, +0.31)$	24.2444	0.1800	-0.0792	0.0058
385	`BBH:2159`	$(3, +0.6, -0.6)$	$(0.1875, +0.3)$	23.5837	0.0969	$+0.0942$	0.0034
386	`BBH:0031`	$(3, +0.5, 0)$	$(0.1875, +0.28)$	21.2242	0.0501	-0.0510	0.0244
387	`BBH:0041`	$(3, +0.5, 0)$	$(0.1875, +0.28)$	14.4106	0.0990	..	..
388	`BBH:2157`	$(3, +0.4, +0.6)$	$(0.1875, +0.26)$	24.5757	0.2450	-0.4904	0.0043
389	`BBH:2152`	$(3, +0.27, +0.8497)$	$(0.1875, +0.2)$	22.7604	0.0332	-0.0343	0.0047
390	`BBH:2156`	$(3, +0.4, -0.6)$	$(0.1875, +0.19)$	22.1396	0.2944	-0.0579	0.0009
391	`BBH:2154`	$(3, +0.3, 0)$	$(0.1875, +0.17)$	23.5527	0.0674	$+0.0199$	0.0081
392	`BBH:2153`	$(3, +0.3, -0.3)$	$(0.1875, +0.15)$	22.9692	0.0985	-0.0711	0.0013
393	`BBH:2151`	$(3, +0.23, -0.8493)$	$(0.1875, +0.08)$	21.0314	0.0542	-0.1003	0.0014
394	`BBH:2150`	$(3, 0, +0.6)$	$(0.1875, +0.04)$	21.3851	0.0861	-0.0961	0.0022

Table F.11: This table shows the `SXS` waveforms with unequal-mass and at least one non-zero spin in the *validation* set. Part V.

#	id	(q,χ_1,χ_2)	$\left(\nu,\hat{S}\right)$	$N_{\rm orb}$	$\varepsilon[10^{-3}]$	$\delta\phi^{\rm NR}_{\rm mrg}$ [rad]	$\bar{F}_{\rm NR/NR}$ [%]
395	`BBH:2149`	$(3,0,+0.3)$	$(0.1875,+0.02)$	21.3989	0.0780	$+0.1824$	0.0025
396	`BBH:2148`	$(3,0,-0.3)$	$(0.1875,-0.02)$	21.4080	0.2163	-0.2364	0.0049
397	`BBH:2147`	$(3,0,-0.6)$	$(0.1875,-0.04)$	21.4411	0.1130	-0.2911	0.0045
398	`BBH:2146`	$(3,-0.23,+0.8496)$	$(0.1875,-0.08)$	21.4812	0.3473	-0.0135	0.0038
399	`BBH:2144`	$(3,-0.3,+0.3)$	$(0.1875,-0.15)$	21.3457	0.0979	-0.1039	0.0032
400	`BBH:2143`	$(3,-0.3,0)$	$(0.1875,-0.17)$	21.0440	0.0242	-0.1665	0.0035
401	`BBH:2141`	$(3,-0.4,+0.6)$	$(0.1875,-0.19)$	20.8091	0.0699	$+0.1086$	0.0030
402	`BBH:2145`	$(3,-0.27,-0.8495)$	$(0.1875,-0.2)$	21.8265	0.1132	-0.1552	0.0044
403	`BBH:2140`	$(3,-0.4,-0.6)$	$(0.1875,-0.26)$	21.9437	0.1044	-0.7785	0.0019
404	`BBH:0038`	$(3,-0.5,0)$	$(0.1875,-0.28)$	14.7221	0.1000	..	..
405	`BBH:0039`	$(3,-0.5,0)$	$(0.1875,-0.28)$	21.8496	3.0069	..	..
406	`BBH:0040`	$(3,-0.5,0)$	$(0.1875,-0.28)$	8.8088	0.9107	..	..
407	`BBH:2135`	$(3,-0.6,+0.6)$	$(0.1875,-0.3)$	20.9400	0.1234	$+0.1837$	0.0026
408	`BBH:2138`	$(3,-0.6,+0.4)$	$(0.1875,-0.31)$	21.0642	0.1551	$+0.1148$	0.0020
409	`BBH:2134`	$(3,-0.6,0)$	$(0.1875,-0.34)$	21.3713	0.0310	-0.2258	0.0023
410	`BBH:2133`	$(3,-0.73,+0.8495)$	$(0.1875,-0.36)$	20.5436	0.1903	$+0.3355$	0.0023
411	`BBH:2137`	$(3,-0.6,-0.4)$	$(0.1875,-0.36)$	22.5091	0.1557	-0.3807	0.0019
412	`BBH:1172`	$(3,-0.7,-0.6)$	$(0.1875,-0.43)$	17.4246	0.0714	-0.3701	0.0021
413	`BBH:1170`	$(3,-0.7,-0.6)$	$(0.1875,-0.43)$	17.6633	9.7234	-0.3025	0.0021
414	`BBH:1171`	$(3,-0.7,-0.6)$	$(0.1875,-0.43)$	17.7321	2.1688	-0.2922	0.0024
415	`BBH:1173`	$(3,-0.7,-0.6)$	$(0.1875,-0.43)$	17.6095	0.0931	-0.2016	0.0013
416	`BBH:1174`	$(3,-0.7,-0.6)$	$(0.1875,-0.43)$	17.6302	0.0560	-0.2199	0.0004
417	`BBH:1175`	$(3,-0.7,-0.6)$	$(0.1875,-0.43)$	17.6034	0.0529	-0.2782	0.0022
418	`BBH:1485`	$(3.1,+0.35,-0.4)$	$(0.1846,+0.18)$	19.9371	0.5472	$+0.4004$	0.0046
419	`BBH:1446`	$(3.15,-0.8,+0.78)$	$(0.1828,-0.42)$	16.6309	0.4757	-0.5731	0.0047
420	`BBH:1447`	$(3.16,+0.74,+0.8)$	$(0.1826,+0.47)$	21.5506	0.7076	..	..
421	`BBH:1483`	$(3.17,+0.56,-0.2)$	$(0.1824,+0.31)$	20.9944	0.2982	$+0.3873$	0.0059
422	`BBH:1457`	$(3.25,+0.54,+0.8)$	$(0.18,+0.36)$	21.5910	0.5016	$+0.1098$	0.0095
423	`BBH:0317`	$(3.33,+0.52,-0.45)$	$(0.1777,+0.29)$	45.8194	0.8090	-0.6215	0.0040
424	`BBH:1489`	$(3.46,+0.3,-0.17)$	$(0.1738,+0.17)$	19.4817	0.2610	..	..
425	`BBH:1452`	$(3.64,+0.8,-0.43)$	$(0.169,+0.47)$	22.3615	0.1467	..	..
426	`BBH:1486`	$(3.72,+0.43,-0.03)$	$(0.167,+0.26)$	21.1556	0.1944	-0.5611	0.0038
427	`BBH:1458`	$(3.8,-0.06,+0.8)$	$(0.1649,0)$	18.7812	0.2951	-1.1364	0.0047
428	`BBH:1936`	$(4,-0.8,-0.8)$	$(0.16,-0.54)$	15.4264	0.4739	$+0.2498$	0.0091
429	`BBH:2014`	$(4,+0.8,+0.4)$	$(0.16,+0.53)$	23.5340	0.4193	..	..
430	`BBH:1938`	$(4,+0.4,+0.8)$	$(0.16,+0.29)$	21.8293	0.4565	-1.2430	0.0102
431	`BBH:1417`	$(4,+0.4,+0.5)$	$(0.16,+0.28)$	78.9983	0.0420	$+1.1516$	0.0565
432	`BBH:1937`	$(4,+0.4,0)$	$(0.16,+0.26)$	20.3573	0.4157	-0.3860	0.0031
433	`BBH:1942`	$(4,+0.4,-0.8)$	$(0.16,+0.22)$	19.8476	0.0370	-1.0339	0.0078
434	`BBH:1907`	$(4,0,+0.8)$	$(0.16,+0.03)$	19.9013	0.3965	-0.0364	0.0072
435	`BBH:2013`	$(4,0,+0.4)$	$(0.16,+0.02)$	19.7302	0.0903	-0.3687	0.0023
436	`BBH:2036`	$(4,0,-0.4)$	$(0.16,-0.02)$	19.1937	0.1487	$+0.2866$	0.0035
437	`BBH:1911`	$(4,0,-0.8)$	$(0.16,-0.03)$	18.9277	0.0849	-0.0922	0.0070
438	`BBH:1962`	$(4,-0.4,+0.8)$	$(0.16,-0.22)$	17.8848	0.2271	-0.7077	0.0039
439	`BBH:1961`	$(4,-0.4,0)$	$(0.16,-0.26)$	17.1221	0.2005	$+0.0155$	0.0011
440	`BBH:1418`	$(4,-0.4,-0.5)$	$(0.16,-0.28)$	65.5016	0.2177	$+1.1166$	0.0526

Table F.12: This table shows the `SXS` waveforms with unequal-mass and at least one non-zero spin in the *validation* set. Part VI.

#	id	(q, χ_1, χ_2)	$\left(\nu, \hat{S}\right)$	$N_{\rm orb}$	$\varepsilon[10^{-3}]$	$\delta\phi^{\rm NR}_{\rm mrg}$ [rad]	$\bar{F}_{\rm NR/NR}$ [%]
441	BBH:1966	$(4, -0.4, -0.8)$	$(0.16, -0.29)$	16.4605	0.0830	−0.9591	0.0020
442	BBH:1932	$(4, -0.8, +0.8)$	$(0.16, -0.48)$	16.5617	0.5770	−0.6471	0.0021
443	BBH:2018	$(4, -0.8, +0.4)$	$(0.16, -0.5)$	16.3809	0.7924	−0.5072	0.0021
444	BBH:1931	$(4, -0.8, 0)$	$(0.16, -0.51)$	15.3484	0.0739	−0.4649	0.0004
445	BBH:2040	$(4, -0.8, -0.4)$	$(0.16, -0.53)$	15.1353	0.3243	−0.3889	0.0006
446	BBH:1451	$(4.06, +0.31, -0.8)$	$(0.1587, +0.17)$	20.2972	0.1871	−0.6438	0.0070
447	BBH:1450	$(4.07, -0.28, -0.8)$	$(0.1584, -0.21)$	17.8045	0.5048	−1.1502	0.0020
448	BBH:1449	$(4.19, -0.8002, -0.34)$	$(0.1557, -0.53)$	15.1708	0.4271	−0.5360	0.0026
449	BBH:1434	$(4.37, +0.8, +0.8)$	$(0.1516, +0.56)$	24.1808	0.3177	..	..
450	BBH:1445	$(4.67, -0.5, +0.8)$	$(0.1452, -0.31)$	17.1449	0.6327	−0.7205	0.0058
451	BBH:1463	$(4.98, +0.61, +0.24)$	$(0.1393, +0.43)$	22.4088	0.4400	+0.2576	0.0032
452	BBH:0061	$(5, +0.5, 0)$	$(0.1388, +0.35)$	34.2689	4.2423	..	..
453	BBH:0109	$(5, -0.5, 0)$	$(0.1388, -0.35)$	14.2349	1.3126	..	..
454	BBH:1111	$(5, -0.9, 0)$	$(0.1389, -0.62)$	8.9056	0.5800	+0.1885	0.0071
455	BBH:1428	$(5.52, -0.8002, -0.7)$	$(0.13, -0.59)$	15.4075	0.3549	−1.0081	0.0066
456	BBH:1440	$(5.64, +0.77, +0.3)$	$(0.128, +0.56)$	24.0226	0.6962	−0.7863	0.0055
457	BBH:1443	$(5.68, +0.4, -0.74)$	$(0.1273, +0.28)$	21.2462	0.3166	−0.9964	0.0064
458	BBH:1432	$(5.84, +0.66, +0.8)$	$(0.1248, +0.5)$	23.7073	0.1893	−1.3306	0.0192
459	BBH:1438	$(5.87, +0.13, +0.8)$	$(0.1244, +0.1)$	20.5844	0.3179	−1.0427	0.0081
460	BBH:1444	$(5.94, -0.06, -0.76)$	$(0.1234, -0.06)$	19.7323	0.2126	−1.9529	0.0164
461	BBH:1437	$(6.04, +0.8, +0.15)$	$(0.122, +0.6)$	24.7986	0.2370	−0.9783	0.0141
462	BBH:1425	$(6.12, -0.8, +0.67)$	$(0.1208, -0.58)$	15.7926	0.2328	−1.6995	0.0098
463	BBH:1436	$(6.28, 0, -0.8)$	$(0.1185, 0)$	20.1015	0.4722	−0.3709	0.0142
464	BBH:1424	$(6.46, -0.66, -0.8)$	$(0.116, -0.5)$	15.5688	0.2226	−2.9472	0.0134
465	BBH:1439	$(6.48, +0.72, -0.32)$	$(0.1158, +0.53)$	24.0557	0.6145	..	..
466	BBH:1464	$(6.53, -0.05, -0.32)$	$(0.1151, -0.05)$	20.2563	0.7350	−0.0651	0.0057
467	BBH:1442	$(6.59, -0.7, -0.18)$	$(0.1144, -0.54)$	15.5149	0.5355	−0.6941	0.0018
468	BBH:1435	$(6.59, -0.79, +0.07)$	$(0.1144, -0.6)$	16.0754	0.3766	−1.2265	0.0081
469	BBH:1448	$(6.95, -0.48, +0.52)$	$(0.11, -0.36)$	17.1456	0.2625	..	..
470	BBH:0204	$(7, +0.4, 0)$	$(0.1094, +0.3)$	87.3919	0.0268	−3.4007	0.0434
471	BBH:0206	$(7, -0.4, 0)$	$(0.1094, -0.3)$	72.1627	0.0613	−2.2059	0.0171
472	BBH:1427	$(7.41, -0.61, -0.73)$	$(0.1048, -0.48)$	15.8739	0.4001	−1.2677	0.0050
473	BBH:1429	$(7.75, -0.2, -0.78)$	$(0.1012, -0.17)$	18.4554	0.0668	−0.5538	0.0049
474	BBH:1421	$(7.8, -0.6, +0.8)$	$(0.1006, -0.47)$	16.5496	0.7512	+0.1973	0.0046
475	BBH:1422	$(7.95, -0.8, -0.46)$	$(0.0992, -0.64)$	15.7759	0.1931	−0.7723	0.0060
476	BBH:1419	$(8, -0.8, -0.8)$	$(0.0988, -0.64)$	14.7190	0.4369	..	..
477	BBH:1441	$(8, +0.6, -0.48)$	$(0.0988, +0.46)$	24.2874	0.1958	..	..
478	BBH:1426	$(8, +0.48, +0.75)$	$(0.0988, +0.4)$	23.9987	0.3326	−0.7854	0.0378
479	BBH:1430	$(8, +0.28, -0.75)$	$(0.0988, +0.22)$	22.7065	0.1184	−1.1552	0.0302
480	BBH:1460	$(8, +0.12, +0.1)$	$(0.0988, +0.1)$	22.2531	0.2232	+0.3258	0.0030
481	BBH:1431	$(8, +0.08, -0.78)$	$(0.0988, +0.05)$	21.4002	0.5339	−1.9878	0.0153
482	BBH:1455	$(8, -0.4, 0)$	$(0.0988, -0.31)$	17.8110	0.3867	+0.0479	0.0023
483	BBH:0114	$(8, -0.5, 0)$	$(0.0987, -0.4)$	18.2319	1.7048	..	..
484	BBH:1423	$(8, -0.6, -0.75)$	$(0.0988, -0.49)$	16.8959	0.5557	−0.5687	0.0103
485	BBH:1433	$(8, -0.74, +0.2)$	$(0.0988, -0.58)$	16.4276	0.5132	−0.3390	0.0037
486	BBH:1420	$(8, -0.8, +0.8)$	$(0.0988, -0.62)$	16.1997	0.3312	+0.1364	0.0094

Table F.13: This table shows the `SXS` waveforms with an extremely long inspiral of between 139 and 147 orbits in the *validation* set.

#	id	(q, χ_1, χ_2)	$\left(\nu, \hat{S}\right)$	N_{orb}	$\varepsilon[10^{-3}]$	$\delta\phi^{\mathrm{NR}}_{\mathrm{mrg}}$ [rad]	$\bar{F}_{\mathrm{NR/NR}}$ [%]
487	`BBH:1412`	$(1.63, +0.4, -0.3)$	$(0.2357, +0.11)$	144.9269	0.4450	-4.2211	0.7295
488	`BBH:1413`	$(1.41, +0.5, +0.4)$	$(0.2428, +0.24)$	145.0944	0.1000	-7.0980	1.1856
489	`BBH:1414`	$(1.83, -0.5, +0.4)$	$(0.2285, -0.16)$	143.0923	1.6000	-5.4034	0.8919
490	`BBH:1415`	$(1.5, +0.5, +0.5)$	$(0.24, +0.26)$	147.2969	0.0430	-8.3376	1.5238
491	`BBH:1416`	$(1.78, -0.4, -0.4)$	$(0.2303, -0.22)$	139.0149	1.7000	-5.1125	0.5986

Table F.14: Non-spinning `SXS` and `BAM` data. The waveforms #526 – #547 form the non-spinning sector of the *calibration* set. While waveforms #548 – #570 represent all waveforms in the non-spinning sector of the *validation* set with a mass-ratio $q < 2$.

#	id	q	ν	N_{orb}	$\varepsilon[10^{-3}]$	$\delta\phi^{\text{NR}}_{\text{mrg}}$ [rad]	$\bar{F}_{\text{NR/NR}}$ [%]
492	`BBH:0180`	1	0.2500	27.8299	0.0511	+0.0259	0.0035
493	`BBH:0007`	1.5	0.2400	28.6965	0.4338	+0.0232	0.0020
494	`BBH:0169`	2	0.2222	14.9957	0.1000	+0.0074	0.0032
495	`BBH:0259`	2.5	0.2041	27.8710	0.0490	−0.0490	0.0050
496	`BBH:0030`	3	0.1875	17.6735	2.1213	−0.0295	0.0030
497	`BBH:0167`	4	0.1600	14.9332	0.0950	+0.0407	0.0057
498	`BBH:0295`	4.5	0.1488	27.0334	0.0267	−0.0965	0.0066
499	`BBH:0056`	5	0.1389	28.1856	0.4985	−0.1654	0.0158
500	`BBH:0296`	5.5	0.1302	27.1419	0.0330	−0.1691	0.0177
501	`BBH:0166`	6	0.1224	20.9629	0.0420	..	..
502	`BBH:0297`	6.5	0.1156	18.9546	0.0590	−0.0124	0.0069
503	`BBH:0298`	7	0.1094	18.9115	0.0400	−0.0044	0.0023
504	`BBH:0299`	7.5	0.1038	19.3106	0.0560	−0.0254	0.0013
505	`BBH:0063`	8	0.0988	25.1734	0.2880	−0.4132	0.0754
506	`BBH:0300`	8.5	0.0942	17.8944	0.0600	−0.0095	0.0037
507	`BBH:0301`	9	0.0900	18.1073	0.0570	+0.0087	0.0014
508	`BBH:0302`	9.5	0.0862	18.2937	0.0540	−0.0280	0.0039
509	`BBH:0185`	9.99	0.0827	23.7637	0.2928	−0.0509	0.0033
510	`BBH:0303`	10	0.0826	18.4270	0.0560	−0.1486	0.0045
511	`BAM`	4	0.1600	11.0449	1.4000	$r_{\text{ext}} = 100$	
512	`BAM`	10	0.0826	6.7622	0.8000	$r_{\text{ext}} = 100$	
513	`BAM`	18	0.0499	6.5094	1.3000	$r_{\text{ext}} = 100$	
514	`BBH:0001`	1	0.2500	27.7156	0.2569	..	..
515	`BBH:0066`	1	0.2500	27.6928	0.0643	..	..
516	`BBH:0067`	1	0.2500	27.7168	0.2365	..	..
517	`BBH:0068`	1	0.2500	27.8923	1.9465	..	..
518	`BBH:0070`	1	0.2500	27.6958	0.0459	..	..
519	`BBH:0071`	1	0.2500	27.6918	0.0610	..	..
520	`BBH:0072`	1	0.2500	27.6775	0.1462	..	..
521	`BBH:0073`	1	0.2500	27.5006	1.8770	..	..
522	`BBH:0086`	1	0.2500	27.7854	1.1708	..	..
523	`BBH:0090`	1	0.2500	32.0416	1.0254	..	..
524	`BBH:0389`	1	0.2500	17.1684	0.0892	+0.1455	0.0028
525	`BBH:1132`	1	0.2500	53.3421	0.7700	+0.6849	0.0192
526	`BBH:1153`	1	0.2500	39.6892	1.0400	+0.6347	0.0051
527	`BBH:1154`	1	0.2500	39.7730	0.0568	+0.5822	0.0071
528	`BBH:1155`	1	0.2500	39.7773	0.0490	+0.6307	0.0077
529	`BBH:0198`	1.2	0.2479	18.8232	0.2044	+0.0686	0.0030
530	`BBH:0310`	1.22	0.2475	13.5178	0.7880	−0.0402	0.0046
531	`BBH:1143`	1.25	0.2469	9.1879	0.1016	−0.3291	0.0062
532	`BBH:0008`	1.5	0.2400	20.8423	1.5862	−0.0758	0.0663
533	`BBH:0093`	1.5	0.2400	28.4823	2.3821	..	..
534	`BBH:0593`	1.5	0.2400	17.3162	0.0676	+0.2927	0.0039
535	`BBH:0194`	1.52	0.2394	18.6350	0.8020	−0.0298	0.0042
536	`BBH:1354`	1.83	0.2284	19.6238	0.0479	−0.3128	0.0010

Table F.15: The waveforms listed here represent all non-spinning waveforms in the *validation* set with a mass-ratio $q \geq 2$.

#	id	q	ν	N_{orb}	$\varepsilon[10^{-3}]$	$\delta\phi^{\text{NR}}_{\text{mrg}}$ [rad]	$\bar{F}_{\text{NR/NR}}$ [%]
537	`BBH:1222`	2	0.2222	27.5621	0.0623	+0.0526	0.0032
538	`BBH:0184`	2	0.2222	14.3278	0.0760	−0.0738	0.0039
539	`BBH:1166`	2	0.2222	39.4852	0.3876	−0.6920	0.0033
540	`BBH:1164`	2	0.2222	39.4971	1.2541	−0.0050	0.0010
541	`BBH:1165`	2	0.2222	39.5694	1.5612	−0.0533	0.0043
542	`BBH:1167`	2	0.2222	39.6251	0.3762	−0.0746	0.0027
543	`BBH:0201`	2.32	0.2106	19.0579	0.1406	−0.1260	0.0028
544	`BBH:0191`	2.5	0.2038	21.2360	0.7580	+0.1004	0.0036
545	`BBH:1221`	3	0.1875	25.8495	0.0390	+0.7166	0.0016
546	`BBH:0168`	3	0.1875	14.1701	0.0870	+0.0526	0.0022
547	`BBH:0183`	3	0.1875	14.5139	0.0630	−0.0814	0.0029
548	`BBH:1177`	3	0.1875	13.6732	2.6360	..	..
549	`BBH:1178`	3	0.1875	13.7628	0.1401	..	..
550	`BBH:1179`	3	0.1875	13.7675	0.0870	+0.0060	0.0020
551	`BBH:2265`	3	0.1875	64.9230	0.0689	+0.9661	0.0046
552	`BBH:0200`	3.27	0.1793	19.2608	0.4137	−0.1165	0.0013
553	`BBH:0193`	3.5	0.1729	18.6896	0.0390	−0.1776	0.0016
554	`BBH:0294`	3.5	0.1728	27.3567	0.0434	+0.1486	0.0102
555	`BBH:1906`	4	0.1600	19.3709	0.1472	+0.1092	0.0014
556	`BBH:0182`	4	0.1600	14.6056	0.0680	−0.0715	0.0049
557	`BBH:1220`	4	0.1600	25.4856	0.1037	−1.1501	0.0030
558	`BBH:0190`	4.5	0.1488	19.1304	0.0350	−0.2568	0.0012
559	`BBH:0054`	5	0.1389	14.7581	3.5135	+0.0511	0.0024
560	`BBH:0055`	5	0.1389	23.0954	0.2565	..	..
561	`BBH:0107`	5	0.1389	27.9706	2.3614	−0.1168	0.0095
562	`BBH:0112`	5	0.1389	23.0307	1.2412	..	..
563	`BBH:0187`	5.04	0.1382	18.3448	0.0460	−0.1198	0.0012
564	`BBH:0197`	5.52	0.1298	19.2079	0.2200	−0.2170	0.0011
565	`BBH:0181`	6	0.1225	25.3711	0.0791	−0.0572	0.0007
566	`BBH:0192`	6.58	0.1145	20.1365	0.0502	−0.2813	0.0020
567	`BBH:0188`	7.19	0.1072	21.3575	0.1609	−0.1357	0.0022
568	`BBH:0195`	7.76	0.1011	19.7015	0.2243	+0.0174	0.0040
569	`BBH:0186`	8.27	0.0963	23.1928	0.6700	−0.0843	0.0014
570	`BBH:0199`	8.73	0.0922	21.8602	0.0677	+0.1694	0.0089
571	`BBH:0189`	9.17	0.0887	24.1621	0.0817	−0.1516	0.0015
572	`BBH:1108`	9.2	0.0884	27.7155	0.1477	−0.2201	0.0032
573	`BBH:0196`	9.66	0.0850	22.3934	0.2629	−0.1411	0.0045
574	`BBH:1107`	10	0.0826	29.4820	1.1603	−0.1118	0.0010

Bibliography

[1] Einstein Telescope sensitivities. `http://www.et-gw.eu/index.php/etsensitivities`.

[2] Gravitational Wave Open Science Center. `https://www.gw-openscience.org/`.

[3] `http://gwcenter.icrr.u-tokyo.ac.jp/en/`. KAGRA, Large-scale Cryogenic Gravitational Wave Telescope Project.

[4] KAGRA observatory. `https://gwcenter.icrr.u-tokyo.ac.jp/en/`.

[5] The Sensitivity of the Advanced LIGO Detectors at the beginning of Gravitational Wave Astronomy. `https://www.ligo.org/science/Publication-O1Noise/index.php`.

[6] `https://dcc.ligo.org/LIGO-T1800235/public`.

[7] SXS Gravitational Waveform Database. `https://data.black-holes.org/waveforms/index.html`.

[8] Advanced LIGO anticipated sensitivity curves. `https://dcc.ligo.org/cgi-bin/DocDB/ShowDocument?docid=2974`. LIGO Document T0900288-v3.

[9] `http://www.ego-gw.it/`, . Virgo/EGO, European Gravitational Observatory.

[10] Advanced Virgo. `http://public.virgo-gw.eu/advanced-virgo/`, .

[11] Updated Advanced LIGO sensitivity design curve. `https://dcc.ligo.org/LIGO-T1800044/public`. LIGO Document T1800044-v5.

[12] `https://bitbucket.org/eob_ihes/teobresums/src/master/`. TEOBResumS code.

[13] B. P. Abbott et al. Observation of Gravitational Waves from a Binary Black Hole Merger. *Phys. Rev. Lett.*, 116(6):061102, 2016. doi: 10.1103/PhysRevLett.116.061102.

[14] B. P. Abbott et al. Binary Black Hole Mergers in the first Advanced LIGO Observing Run. *Phys. Rev.*, X6(4):041015, 2016. doi: 10.1103/PhysRevX.6.041015.

[15] B. P. Abbott et al. GW150914: First results from the search for binary black hole coalescence with Advanced LIGO. *Phys. Rev. D*, 93(12):122003, 2016. doi: 10.1103/PhysRevD.93.122003.

[16] B. P. Abbott et al. Tests of general relativity with GW150914. *Phys. Rev. Lett.*, 116(22): 221101, 2016. doi: 10.1103/PhysRevLett.116.221101,10.1103/PhysRevLett.121.129902. [Erratum: Phys. Rev. Lett.121,no.12,129902(2018)].

[17] B. P. Abbott et al. Properties of the Binary Black Hole Merger GW150914. *Phys. Rev. Lett.*, 116(24):241102, 2016. doi: 10.1103/PhysRevLett.116.241102.

[18] B. P. Abbott et al. GW170608: Observation of a 19-solar-mass Binary Black Hole Coalescence. *Astrophys. J.*, 851(2):L35, 2017. doi: 10.3847/2041-8213/aa9f0c.

[19] B. P. Abbott et al. GW170814: A Three-Detector Observation of Gravitational Waves from a Binary Black Hole Coalescence. *Phys. Rev. Lett.*, 119(14):141101, 2017. doi: 10.1103/PhysRevLett.119.141101.

[20] B. P. Abbott et al. GW170104: Observation of a 50-Solar-Mass Binary Black Hole Coalescence at Redshift 0.2. *Phys. Rev. Lett.*, 118(22):221101, 2017. doi: 10.1103/PhysRevLett.118.221101.

[21] B. P. Abbott et al. A gravitational-wave standard siren measurement of the Hubble constant. *Nature*, 2017. doi: 10.1038/nature24471.

[22] B. P. Abbott et al. GWTC-1: A Gravitational-Wave Transient Catalog of Compact Binary Mergers Observed by LIGO and Virgo during the First and Second Observing Runs. 2018.

[23] B. P. Abbott et al. GWTC-1: A Gravitational-Wave Transient Catalog of Compact Binary Mergers Observed by LIGO and Virgo during the First and Second Observing Runs. 2018.

[24] B. P. Abbott et al. Tests of General Relativity with GW170817. *Phys. Rev. Lett.*, 123(1):011102, 2019. doi: 10.1103/PhysRevLett.123.011102.

[25] B. P. Abbott et al. Binary Black Hole Population Properties Inferred from the First and Second Observing Runs of Advanced LIGO and Advanced Virgo. *Astrophys. J. Lett.*, 882(2):L24, 2019. doi: 10.3847/2041-8213/ab3800.

[26] B. P. Abbott et al. Tests of General Relativity with the Binary Black Hole Signals from the LIGO-Virgo Catalog GWTC-1. 2019.

[27] R. Abbott et al. Tests of General Relativity with Binary Black Holes from the second LIGO-Virgo Gravitational-Wave Transient Catalog. 10 2020.

[28] R. Abbott et al. GWTC-2: Compact Binary Coalescences Observed by LIGO and Virgo During the First Half of the Third Observing Run. 10 2020.

[29] T. D. Abbott et al. Improved analysis of GW150914 using a fully spin-precessing waveform Model. *Phys. Rev.*, X6(4):041014, 2016. doi: 10.1103/PhysRevX.6.041014.

[30] F. Acernese et al. Advanced Virgo: a second-generation interferometric gravitational wave detector. *Class. Quant. Grav.*, 32(2):024001, 2015. doi: 10.1088/0264-9381/32/2/024001.

[31] P. Ajith, M. Boyle, D. A. Brown, B. Brügmann, L. T. Buchman, et al. The NINJA-2 catalog of hybrid post-Newtonian/numerical-relativity waveforms for non-precessing black-hole binaries. *Class.Quant.Grav.*, 29:124001, 2012. doi: 10.1088/0264-9381/29/12/124001.

[32] S. Akcay, L. Barack, T. Damour, and N. Sago. Gravitational self-force and the effective-one-body formalism between the innermost stable circular orbit and the light ring. *Phys. Rev.*, D86:104041, 2012. doi: 10.1103/PhysRevD.86.104041.

[33] S. Akcay, R. Gamba, and S. Bernuzzi. Hybrid post-Newtonian effective-one-body scheme for spin-precessing compact-binary waveforms up to merger. *Phys. Rev. D*, 103(2):024014, 2021. doi: 10.1103/PhysRevD.103.024014.

[34] M. Alcubierre. *Introduction to 3+1 Numerical Relativity.* Oxford University Press, 2008.

[35] A. Arvanitaki, M. Baryakhtar, and X. Huang. Discovering the QCD Axion with Black Holes and Gravitational Waves. *Phys. Rev. D*, 91(8):084011, 2015. doi: 10.1103/PhysRevD.91.084011.

[36] A. Arvanitaki, M. Baryakhtar, S. Dimopoulos, S. Dubovsky, and R. Lasenby. Black Hole Mergers and the QCD Axion at Advanced LIGO. *Phys. Rev. D*, 95(4):043001, 2017. doi: 10.1103/PhysRevD.95.043001.

[37] B. Aylott et al. Status of NINJA: The Numerical INJection Analysis project. *Class. Quant. Grav.*, 26:114008, 2009. doi: 10.1088/0264-9381/26/11/114008.

[38] S. Babak, A. Taracchini, and A. Buonanno. Validating the effective-one-body model of spinning, precessing binary black holes against numerical relativity. *Phys. Rev.*, D95(2):024010, 2017. doi: 10.1103/PhysRevD.95.024010.

[39] S. Balmelli and P. Jetzer. Effective-one-body Hamiltonian with next-to-leading order spin-spin coupling. *Phys. Rev.*, D91:064011, 2015. doi: 10.1103/PhysRevD.91.064011.

[40] L. Barack. Gravitational self force in extreme mass-ratio inspirals. *Class.Quant.Grav.*, 26:213001, 2009. doi: 10.1088/0264-9381/26/21/213001.

[41] L. Barack, T. Damour, and N. Sago. Precession effect of the gravitational self-force in a Schwarzschild spacetime and the effective one-body formalism. *Phys.Rev.*, D82:084036, 2010. doi: 10.1103/PhysRevD.82.084036.

[42] E. Barausse, A. Buonanno, and A. Le Tiec. The complete non-spinning effective-one-body metric at linear order in the mass ratio. *Phys.Rev.*, D85:064010, 2012. doi: 10.1103/PhysRevD.85.064010.

[43] T. Baumgarte and S. Shapiro. *Numerical Relativity.* Cambridge University Press, Cambridge, 2010.

[44] T. Bayes, Rev. An essay toward solving a problem in the doctrine of chances. *Phil. Trans. Roy. Soc. Lond.*, 53:370–418, 1764. doi: 10.1098/rstl.1763.0053.

[45] S. Bernuzzi and A. Nagar. Binary black hole merger in the extreme-mass-ratio limit: a multipolar analysis. *Phys. Rev.*, D81:084056, 2010. doi: 10.1103/PhysRevD.81.084056.

[46] E. Berti, V. Cardoso, and C. M. Will. On gravitational-wave spectroscopy of massive black holes with the space interferometer LISA. *Phys. Rev.*, D73:064030, 2006. doi: 10.1103/PhysRevD.73.064030.

[47] E. Berti, V. Cardoso, and A. O. Starinets. Quasinormal modes of black holes and black branes. *Class. Quant. Grav.*, 26:163001, 2009. doi: 10.1088/0264-9381/26/16/163001.

[48] D. Bini and T. Damour. Analytical determination of the two-body gravitational interaction potential at the fourth post-Newtonian approximation. *Phys.Rev.*, D87(12):121501, 2013. doi: 10.1103/PhysRevD.87.121501.

[49] J. Blackman, S. E. Field, C. R. Galley, B. Szilágyi, M. A. Scheel, M. Tiglio, and D. A. Hemberger. Fast and Accurate Prediction of Numerical Relativity Waveforms from Binary Black Hole Coalescences Using Surrogate Models. *Phys. Rev. Lett.*, 115(12):121102, 2015. doi: 10.1103/PhysRevLett.115.121102.

[50] J. Blackman, S. E. Field, M. A. Scheel, C. R. Galley, D. A. Hemberger, P. Schmidt, and R. Smith. A Surrogate Model of Gravitational Waveforms from Numerical Relativity Simulations of Precessing Binary Black Hole Mergers. *Phys. Rev.*, D95(10):104023, 2017. doi: 10.1103/PhysRevD.95.104023.

[51] L. Blanchet. Gravitational Radiation from Post-Newtonian Sources and Inspiralling Compact Binaries. *Living Rev. Relativity*, 17:2, 2014. doi: 10.12942/lrr-2014-2.

[52] L. Blanchet, S. L. Detweiler, A. Le Tiec, and B. F. Whiting. High-Order Post-Newtonian Fit of the Gravitational Self-Force for Circular Orbits in the Schwarzschild Geometry. *Phys.Rev.*, D81:084033, 2010. doi: 10.1103/PhysRevD.81.084033.

[53] A. Bohé et al. Improved effective-one-body model of spinning, nonprecessing binary black holes for the era of gravitational-wave astrophysics with advanced detectors. *Phys. Rev.*, D95 (4):044028, 2017. doi: 10.1103/PhysRevD.95.044028.

[54] M. Boyle and A. H. Mroue. Extrapolating gravitational-wave data from numerical simulations. *Phys. Rev.*, D80:124045, 2009. doi: 10.1103/PhysRevD.80.124045.

[55] M. Boyle et al. The SXS Collaboration catalog of binary black hole simulations. *Class. Quant. Grav.*, 36(19):195006, 2019. doi: 10.1088/1361-6382/ab34e2.

[56] D. Brown, S. Fairhurst, B. Krishnan, R. A. Mercer, R. K. Kopparapu, L. Santamaria, and J. T. Whelan. Data formats for numerical relativity waves. 9 2007.

[57] B. Bruegmann, J. A. Gonzalez, M. Hannam, S. Husa, U. Sperhake, and W. Tichy. Calibration of Moving Puncture Simulations. *Phys. Rev.*, D77:024027, 2008. doi: 10.1103/PhysRevD.77.024027.

[58] B. Brügmann, W. Tichy, and N. Jansen. Numerical simulation of orbiting black holes. *Phys. Rev. Lett.*, 92:211101, 2004. doi: 10.1103/PhysRevLett.92.211101.

[59] L. T. Buchman, H. P. Pfeiffer, M. A. Scheel, and B. Szilagyi. Simulations of non-equal mass black hole binaries with spectral methods. *Phys. Rev.*, D86:084033, 2012. doi: 10.1103/PhysRevD.86.084033.

[60] A. Buonanno and T. Damour. Effective one-body approach to general relativistic two-body dynamics. *Phys. Rev.*, D59:084006, 1999. doi: 10.1103/PhysRevD.59.084006.

[61] A. Buonanno and T. Damour. Transition from inspiral to plunge in binary black hole coalescences. *Phys. Rev.*, D62:064015, 2000. doi: 10.1103/PhysRevD.62.064015.

[62] B. Carter. Axisymmetric Black Hole Has Only Two Degrees of Freedom. *Phys. Rev. Lett.*, 26:331–333, 1971. doi: 10.1103/PhysRevLett.26.331.

[63] G. Carullo, G. Riemenschneider, K. W. Tsang, A. Nagar, and W. Del Pozzo. GW150914 peak frequency: a novel consistency test of strong-field General Relativity. *Class. Quant. Grav.*, 36 (10):105009, 2019. doi: 10.1088/1361-6382/ab185e.

[64] K. S. T. Charles W. Misner and J. A. Wheeler. *Gravitation.* W. H. Freeman and Company, San Francisco, 1973.

[65] K. Chatziioannou et al. On the properties of the massive binary black hole merger GW170729. *Phys. Rev.*, D100(10):104015, 2019. doi: 10.1103/PhysRevD.100.104015.

[66] D. Chiaramello and A. Nagar. Faithful analytical effective-one-body waveform model for spin-aligned, moderately eccentric, coalescing black hole binaries. *Phys. Rev. D*, 101(10):101501, 2020. doi: 10.1103/PhysRevD.101.101501.

[67] T. Chu, H. P. Pfeiffer, and M. A. Scheel. High accuracy simulations of black hole binaries:spins anti-aligned with the orbital angular momentum. *Phys. Rev.*, D80:124051, 2009. doi: 10.1103/PhysRevD.80.124051.

[68] T. Chu, H. Fong, P. Kumar, H. P. Pfeiffer, M. Boyle, D. A. Hemberger, L. E. Kidder, M. A. Scheel, and B. Szilagyi. On the accuracy and precision of numerical waveforms: Effect of waveform extraction methodology. *Class. Quant. Grav.*, 33(16):165001, 2016. doi: 10.1088/0264-9381/33/16/165001.

[69] N. J. Cornish and T. B. Littenberg. BayesWave: Bayesian Inference for Gravitational Wave Bursts and Instrument Glitches. *Class. Quant. Grav.*, 32(13):135012, 2015. doi: 10.1088/0264-9381/32/13/135012.

[70] R. Cotesta, A. Buonanno, A. Bohé, A. Taracchini, I. Hinder, and S. Ossokine. Enriching the Symphony of Gravitational Waves from Binary Black Holes by Tuning Higher Harmonics. *Phys. Rev.*, D98(8):084028, 2018. doi: 10.1103/PhysRevD.98.084028.

[71] T. Damour. Coalescence of two spinning black holes: An effective one- body approach. *Phys. Rev.*, D64:124013, 2001. doi: 10.1103/PhysRevD.64.124013.

[72] T. Damour. Gravitational Self Force in a Schwarzschild Background and the Effective One Body Formalism. *Phys. Rev.*, D81:024017, 2010. doi: 10.1103/PhysRevD.81.024017.

[73] T. Damour and A. Gopakumar. Gravitational recoil during binary black hole coalescence using the effective one body approach. *Phys. Rev.*, D73:124006, 2006. doi: 10.1103/PhysRevD.73.124006.

[74] T. Damour and A. Nagar. Faithful Effective-One-Body waveforms of small-mass-ratio coalescing black-hole binaries. *Phys. Rev.*, D76:064028, 2007. doi: 10.1103/PhysRevD.76.064028.

[75] T. Damour and A. Nagar. Comparing Effective-One-Body gravitational waveforms to accurate numerical data. *Phys. Rev.*, D77:024043, 2008. doi: 10.1103/PhysRevD.77.024043.

[76] T. Damour and A. Nagar. New effective-one-body description of coalescing nonprecessing spinning black-hole binaries. *Phys.Rev.*, D90(4):044018, 2014. doi: 10.1103/PhysRevD.90.044018.

[77] T. Damour and A. Nagar. A new analytic representation of the ringdown waveform of coalescing spinning black hole binaries. *Phys.Rev.*, D90:024054, 2014. doi: 10.1103/PhysRevD.90.024054.

[78] T. Damour, P. Jaranowski, and G. Schaefer. On the determination of the last stable orbit for circular general relativistic binaries at the third postNewtonian approximation. *Phys. Rev.*, D62:084011, 2000. doi: 10.1103/PhysRevD.62.084011.

[79] T. Damour, P. Jaranowski, and G. Schaefer. Dimensional regularization of the gravitational interaction of point masses. *Phys. Lett. B*, 513:147–155, 2001. doi: 10.1016/S0370-2693(01)00642-6.

[80] T. Damour, P. Jaranowski, and G. Schäfer. Effective one body approach to the dynamics of two spinning black holes with next-to-leading order spin-orbit coupling. *Phys.Rev.*, D78:024009, 2008. doi: 10.1103/PhysRevD.78.024009.

[81] T. Damour, B. R. Iyer, and A. Nagar. Improved resummation of post-Newtonian multipolar waveforms from circularized compact binaries. *Phys. Rev.*, D79:064004, 2009. doi: 10.1103/PhysRevD.79.064004.

[82] T. Damour, A. Nagar, and S. Bernuzzi. Improved effective-one-body description of coalescing nonspinning black-hole binaries and its numerical-relativity completion. *Phys.Rev.*, D87:084035, 2013. doi: 10.1103/PhysRevD.87.084035.

[83] W. Del Pozzo and A. Nagar. Analytic family of post-merger template waveforms. *Phys. Rev.*, D95(12):124034, 2017. doi: 10.1103/PhysRevD.95.124034.

[84] T. Dietrich et al. Matter imprints in waveform models for neutron star binaries: Tidal and self-spin effects. *Phys. Rev.*, D99(2):024029, 2019. doi: 10.1103/PhysRevD.99.024029.

[85] A. Einstein. Approximative Integration of the Field Equations of Gravitation. *Sitzungsber. Preuss. Akad. Wiss. Berlin (Math. Phys.)*, 1916:688–696, 1916.

[86] H. Estellés, S. Husa, M. Colleoni, D. Keitel, M. Mateu-Lucena, C. García-Quirós, A. Ramos-Buades, and A. Borchers. Time domain phenomenological model of gravitational wave subdominant harmonics for quasi-circular non-precessing binary black hole coalescences. 12 2020.

[87] H. Estellés, A. Ramos-Buades, S. Husa, C. García-Quirós, M. Colleoni, L. Haegel, and R. Jaume. IMRPhenomTP: A phenomenological time domain model for dominant quadrupole gravitational wave signal of coalescing binary black holes. 4 2020.

[88] E. E. Flanagan and S. A. Hughes. Measuring gravitational waves from binary black hole coalescences: 2. The Waves' information and its extraction, with and without templates. *Phys. Rev. D*, 57:4566–4587, 1998. doi: 10.1103/PhysRevD.57.4566.

[89] J. A. González, U. Sperhake, B. Brügmann, M. Hannam, and S. Husa. Total recoil: the maximum kick from nonspinning black-hole binary inspiral. *Phys. Rev. Lett.*, 98:091101, 2007. doi: 10.1103/PhysRevLett.98.091101.

[90] E. Harms, S. Bernuzzi, A. Nagar, and A. Zenginoglu. A new gravitational wave generation algorithm for particle perturbations of the Kerr spacetime. *Class.Quant.Grav.*, 31:245004, 2014. doi: 10.1088/0264-9381/31/24/245004.

[91] J. Hartung and J. Steinhoff. Next-to-leading order spin-orbit and spin(a)-spin(b) Hamiltonians for n gravitating spinning compact objects. *Phys. Rev.*, D83:044008, 2011. doi: 10.1103/PhysRevD.83.044008.

[92] J. Hartung and J. Steinhoff. Next-to-next-to-leading order post-Newtonian spin-orbit Hamiltonian for self-gravitating binaries. *Annalen Phys.*, 523:783–790, 2011. doi: 10.1002/andp.201100094.

[93] J. Healy and C. O. Lousto. Hangup effect in unequal mass binary black hole mergers and further studies of their gravitational radiation and remnant properties. *Phys. Rev. D*, 97(8):084002, 2018. doi: 10.1103/PhysRevD.97.084002.

[94] J. Healy, P. Laguna, and D. Shoemaker. Decoding the final state in binary black hole mergers. *Class. Quant. Grav.*, 31(21):212001, 2014. doi: 10.1088/0264-9381/31/21/212001.

[95] J. Healy, C. O. Lousto, and Y. Zlochower. Nonspinning binary black hole merger scenario revisited. *Phys. Rev.*, D96(2):024031, 2017. doi: 10.1103/PhysRevD.96.024031.

[96] J. Healy, C. O. Lousto, Y. Zlochower, and M. Campanelli. The RIT binary black hole simulations catalog. *Class. Quant. Grav.*, 34(22):224001, 2017. doi: 10.1088/1361-6382/aa91b1.

[97] J. Healy, C. O. Lousto, J. Lange, R. O'Shaughnessy, Y. Zlochower, and M. Campanelli. Second RIT binary black hole simulations catalog and its application to gravitational waves parameter estimation. *Phys. Rev. D*, 100(2):024021, 2019. doi: 10.1103/PhysRevD.100.024021.

[98] D. A. Hemberger, G. Lovelace, T. J. Loredo, L. E. Kidder, M. A. Scheel, B. Szilágyi, N. W. Taylor, and S. A. Teukolsky. Final spin and radiated energy in numerical simulations of binary black holes with equal masses and equal, aligned or anti-aligned spins. *Phys. Rev.*, D88:064014, 2013. doi: 10.1103/PhysRevD.88.064014.

[99] I. Hinder, A. Buonanno, M. Boyle, Z. B. Etienne, J. Healy, et al. Error-analysis and comparison to analytical models of numerical waveforms produced by the NRAR Collaboration. *Class.Quant.Grav.*, 31:025012, 2013. doi: 10.1088/0264-9381/31/2/025012.

[100] I. Hinder, L. Kidder, H. Pfeiffer, M. Scheel, M. Boyle, D. Hemberger, G. Lovelace, and B. Szilagyi. Binary black-hole simulation sxs:bbh:1375, Apr. 2018. URL `https://doi.org/10.5281/zenodo.1215769`.

[101] S. Husa, S. Khan, M. Hannam, M. Pürrer, F. Ohme, X. Jiménez Forteza, and A. Bohé. Frequency-domain gravitational waves from nonprecessing black-hole binaries. I. New numerical waveforms and anatomy of the signal. *Phys. Rev.*, D93(4):044006, 2016. doi: 10.1103/PhysRevD.93.044006.

[102] M. Isi and A. J. Weinstein. Probing gravitational wave polarizations with signals from compact binary coalescences. 2017.

[103] W. Israel. Event horizons in static vacuum space-times. *Phys. Rev.*, 164:1776–1779, 1967. doi: 10.1103/PhysRev.164.1776.

[104] W. Israel. Event horizons in static electrovac space-times. *Commun. Math. Phys.*, 8:245–260, 1968. doi: 10.1007/BF01645859.

[105] K. Jani, J. Healy, J. A. Clark, L. London, P. Laguna, and D. Shoemaker. Georgia Tech Catalog of Gravitational Waveforms. *Class. Quant. Grav.*, 33(20):204001, 2016. doi: 10.1088/0264-9381/33/20/204001.

[106] E. T. Jaynes. *Probability Theory: The Logic of Science.* CUP, 2003. ISBN 9780521592710. URL `http://www.cambridge.org/au/academic/subjects/physics/theoretical-physics-and-mathematical-physics/probability-theory-logic-science?format=HB&isbn=9780521592710`.

[107] X. Jiménez-Forteza, D. Keitel, S. Husa, M. Hannam, S. Khan, and M. Pürrer. Hierarchical data-driven approach to fitting numerical relativity data for nonprecessing binary black holes with an application to final spin and radiated energy. *Phys. Rev.*, D95(6):064024, 2017. doi: 10.1103/PhysRevD.95.064024.

[108] D. Keitel et al. The most powerful astrophysical events: Gravitational-wave peak luminosity of binary black holes as predicted by numerical relativity. *Phys. Rev.*, D96(2):024006, 2017. doi: 10.1103/PhysRevD.96.024006.

[109] S. Khan, S. Husa, M. Hannam, F. Ohme, M. Pürrer, X. Jiménez Forteza, and A. Bohé. Frequency-domain gravitational waves from nonprecessing black-hole binaries. II. A phenomenological model for the advanced detector era. *Phys. Rev.*, D93(4):044007, 2016. doi: 10.1103/PhysRevD.93.044007.

[110] S. Khan, F. Ohme, K. Chatziioannou, and M. Hannam. Including higher order multipoles in gravitational-wave models for precessing binary black holes. 2019.

[111] P. Kumar, K. Barkett, S. Bhagwat, N. Afshari, D. A. Brown, G. Lovelace, M. A. Scheel, and B. Szilágyi. Accuracy and precision of gravitational-wave models of inspiraling neutron star-black hole binaries with spin: Comparison with matter-free numerical relativity in the low-frequency regime. *Phys. Rev. D*, 92(10):102001, 2015. doi: 10.1103/PhysRevD.92.102001.

[112] L. Lindblom, B. J. Owen, and D. A. Brown. Model Waveform Accuracy Standards for Gravitational Wave Data Analysis. *Phys.Rev.*, D78:124020, 2008. doi: 10.1103/PhysRevD.78.124020.

[113] L. London. Notes on the spheroidal harmonic multipole moments of gravitational radiation. 6 2020.

[114] L. London, S. Khan, E. Fauchon-Jones, X. J. Forteza, M. Hannam, S. Husa, C. Kalaghatgi, F. Ohme, and F. Pannarale. First higher-multipole model of gravitational waves from spinning and coalescing black-hole binaries. *Phys. Rev. Lett.*, 120(16):161102, 2018. doi: 10.1103/PhysRevLett.120.161102.

[115] G. Lovelace, M. Scheel, and B. Szilagyi. Simulating merging binary black holes with nearly extremal spins. *Phys.Rev.*, D83:024010, 2011. doi: 10.1103/PhysRevD.83.024010.

[116] G. Lovelace, M. Boyle, M. A. Scheel, and B. Szilagyi. Accurate gravitational waveforms for binary-black-hole mergers with nearly extremal spins. *Class. Quant. Grav.*, 29:045003, 2012. doi: 10.1088/0264-9381/29/4/045003.

[117] G. Lovelace et al. Nearly extremal apparent horizons in simulations of merging black holes. *Class. Quant. Grav.*, 32(6):065007, 2015. doi: 10.1088/0264-9381/32/6/065007.

[118] G. Lovelace et al. Modeling the source of GW150914 with targeted numerical-relativity simulations. *Class. Quant. Grav.*, 33(24):244002, 2016. doi: 10.1088/0264-9381/33/24/244002.

[119] M. Maggiore. *Gravitational Waves. Vol. 1: Theory and Experiments.* Oxford Master Series in Physics. Oxford University Press, 2007. ISBN 9780198570745, 9780198520740. URL `http://www.oup.com/uk/catalogue/?ci=9780198570745`.

[120] M. Maggiore. *Gravitational Waves. Vol. 2: Astrophysics and Cosmology.* Oxford University Press, 3 2018. ISBN 978-0-19-857089-9.

[121] A. Matas et al. Aligned-spin neutron-star–black-hole waveform model based on the effective-one-body approach and numerical-relativity simulations. *Phys. Rev. D*, 102(4):043023, 2020. doi: 10.1103/PhysRevD.102.043023.

[122] A. K. Mehta, P. Tiwari, N. K. Johnson-McDaniel, C. K. Mishra, V. Varma, and P. Ajith. Including mode mixing in a higher-multipole model for gravitational waveforms from nonspinning black-hole binaries. 2019.

[123] F. Messina, A. Maldarella, and A. Nagar. Factorization and resummation: A new paradigm to improve gravitational wave amplitudes. II: the higher multipolar modes. *Phys. Rev.*, D97 (8):084016, 2018. doi: 10.1103/PhysRevD.97.084016.

[124] M. Millhouse, N. J. Cornish, and T. Littenberg. Bayesian reconstruction of gravitational wave bursts using chirplets. *Phys. Rev.*, D97(10):104057, 2018. doi: 10.1103/PhysRevD.97.104057.

[125] Y. Mino, M. Sasaki, and T. Tanaka. Gravitational radiation reaction to a particle motion. *Phys.Rev.*, D55:3457–3476, 1997. doi: 10.1103/PhysRevD.55.3457.

[126] A. H. Mroue, M. A. Scheel, B. Szilagyi, H. P. Pfeiffer, M. Boyle, et al. A catalog of 174 binary black-hole simulations for gravitational-wave astronomy. *Phys.Rev.Lett.*, 111:241104, 2013. doi: 10.1103/PhysRevLett.111.241104.

[127] A. Nagar. Effective one body Hamiltonian of two spinning black-holes with next-to-next-to-leading order spin-orbit coupling. *Phys.Rev.*, D84:084028, 2011. doi: 10.1103/PhysRevD.84.084028.

[128] A. Nagar and P. Rettegno. Efficient effective one body time-domain gravitational waveforms. *Phys. Rev.*, D99(2):021501, 2019. doi: 10.1103/PhysRevD.99.021501.

[129] A. Nagar and A. Shah. Factorization and resummation: A new paradigm to improve gravitational wave amplitudes. *Phys. Rev.*, D94(10):104017, 2016. doi: 10.1103/PhysRevD.94.104017.

[130] A. Nagar, T. Damour, and A. Tartaglia. Binary black hole merger in the extreme mass ratio limit. *Class. Quant. Grav.*, 24:S109–S124, 2007. doi: 10.1088/0264-9381/24/12/S08.

[131] A. Nagar, T. Damour, C. Reisswig, and D. Pollney. Energetics and phasing of nonprecessing spinning coalescing black hole binaries. *Phys. Rev.*, D93(4):044046, 2016. doi: 10.1103/PhysRevD.93.044046.

[132] A. Nagar, G. Riemenschneider, and G. Pratten. Impact of Numerical Relativity information on effective-one-body waveform models. *Phys. Rev.*, D96(8):084045, 2017. doi: 10.1103/PhysRevD.96.084045.

[133] A. Nagar, G. Pratten, G. Riemenschneider, and R. Gamba. A Multipolar Effective One Body Model for Non-Spinning Black Hole Binaries. 2019.

[134] A. Nagar, G. Riemenschneider, G. Pratten, P. Rettegno, and F. Messina. Multipolar effective one body waveform model for spin-aligned black hole binaries. *Phys. Rev. D*, 102(2):024077, 2020. doi: 10.1103/PhysRevD.102.024077.

[135] A. Nagar et al. Time-domain effective-one-body gravitational waveforms for coalescing compact binaries with nonprecessing spins, tides and self-spin effects. *Phys. Rev.*, D98(10):104052, 2018. doi: 10.1103/PhysRevD.98.104052.

[136] S. Ossokine et al. Multipolar Effective-One-Body Waveforms for Precessing Binary Black Holes: Construction and Validation. *Phys. Rev. D*, 102(4):044055, 2020. doi: 10.1103/PhysRevD.102.044055.

[137] Y. Pan, A. Buonanno, R. Fujita, E. Racine, and H. Tagoshi. Post-Newtonian factorized multipolar waveforms for spinning, non-precessing black-hole binaries. *Phys.Rev.*, D83:064003, 2011. doi: 10.1103/PhysRevD.83.064003.

[138] E. Poisson and C. M. Will. *Gravity: Newtonian, Post-Newtonian, Relativistic.* Cambridge University Press, Cambridge, 2014. doi: 10.1017/CBO9781139507486.

[139] E. Poisson, A. Pound, and I. Vega. The Motion of point particles in curved spacetime. *Living Rev.Rel.*, 14:7, 2011.

[140] F. Pretorius. Evolution of binary black hole spacetimes. *Phys. Rev. Lett.*, 95:121101, 2005. doi: 10.1103/PhysRevLett.95.121101.

[141] T. C. Quinn and R. M. Wald. An Axiomatic approach to electromagnetic and gravitational radiation reaction of particles in curved space-time. *Phys.Rev.*, D56:3381–3394, 1997. doi: 10.1103/PhysRevD.56.3381.

[142] M. A. Scheel, M. Giesler, D. A. Hemberger, G. Lovelace, K. Kuper, M. Boyle, B. Szilágyi, and L. E. Kidder. Improved methods for simulating nearly extremal binary black holes. *Class. Quant. Grav.*, 32(10):105009, 2015. doi: 10.1088/0264-9381/32/10/105009.

[143] P. Schmidt, I. W. Harry, and H. P. Pfeiffer. Numerical Relativity Injection Infrastructure. 3 2017.

[144] B. F. Schutz. Determining the Hubble Constant from Gravitational Wave Observations. *Nature*, 323:310–311, 1986. doi: 10.1038/323310a0.

[145] D. Shoemaker. URL `https://dcc.ligo.org/cgi-bin/DocDB/ShowDocument?docid=2974`.

[146] H. Tagoshi, C. K. Mishra, A. Pai, and K. G. Arun. Parameter estimation of neutron star-black hole binaries using an advanced gravitational-wave detector network: Effects of the full post-Newtonian waveform. *Phys. Rev. D*, 90(2):024053, 2014. doi: 10.1103/PhysRevD.90.024053.

[147] S. H. *et al.* Sensitivity studies for third-generation gravitational wave observatories. *Classical and Quantum Gravity*, 28(9):094013, apr 2011. doi: 10.1088/0264-9381/28/9/094013. URL `https://doi.org/10.1088/0264-9381/28/9/094013`.

[148] J. Thornburg. The Capra Research Program for Modelling Extreme Mass Ratio Inspirals. *GW Notes*, 5:3–53, 2011.

[149] V. Varma, S. E. Field, M. A. Scheel, J. Blackman, L. E. Kidder, and H. P. Pfeiffer. Surrogate model of hybridized numerical relativity binary black hole waveforms. 2018.

[150] V. Varma, S. E. Field, M. A. Scheel, J. Blackman, D. Gerosa, L. C. Stein, L. E. Kidder, and H. P. Pfeiffer. Surrogate models for precessing binary black hole simulations with unequal masses. *Phys. Rev. Research.*, 1:033015, 2019. doi: 10.1103/PhysRevResearch.1.033015.

[151] R. M. Wald. *General relativity.* The University of Chicago Press, Chicago, 1984. ISBN 0-226-87032-4 (hardcover), 0-226-87033-2 (paperback).

[152] R. M. Wald. *General Relativity.* Chicago Univ. Pr., Chicago, USA, 1984. doi: 10.7208/chicago/9780226870373.001.0001.

[153] J. Weber. Detection and Generation of Gravitational Waves. *Phys. Rev.*, 117:306–313, 1960. doi: 10.1103/PhysRev.117.306.

[154] J. M. Weisberg, J. H. Taylor, and L. A. Fowler. GRAVITATIONAL RADIATION FROM PULSAR PSR-1913+16. (IN GERMAN). *Spektrum Wiss.*, 12:53–61, 1981.

[155] R. Weiss. Interferometric gravitational wave detectors. In *12th Conference on General Relativity and Gravitation*, pages 331–339, 1989.